UNIVERSITY OF CALIFORNIA

Los Angeles

Ultra-High Accelerating Gradients in Radio-Frequency Cryogenic Copper Structures

A dissertation submitted in partial satisfaction
of the requirements for the degree
Doctor of Philosophy in Physics

by

Alexander David Cahill

2017

ABSTRACT OF THE DISSERTATION

Ultra-High Accelerating Gradients in
Radio-Frequency Cryogenic Copper Structures

by

Alexander David Cahill
Doctor of Philosophy in Physics
University of California, Los Angeles, 2017
Professor James Rosenzweig, Chair

Normal conducting radio-frequency (rf) particle accelerators have many applications, including colliders for high energy physics, high-intensity synchrotron light sources, non-destructive testing for security, and medical radiation therapy. In these applications, the accelerating gradient is an important parameter. Specifically for high energy physics, increasing the accelerating gradient extends the potential energy reach and is viewed as a way to mitigate their considerable cost. Furthermore, a gradient increase will enable for more compact and thus accessible free electron lasers (FELs).

The major factor limiting larger accelerating gradients is vacuum rf breakdown. Basic physics of this phenomenon has been extensively studied over the last few decades. During which, the occurrence of rf breakdowns was shown to be probabilistic, and can be characterized by a breakdown rate.

The current consensus is that vacuum rf breakdowns are caused by movements of crystal defects induced by periodic mechanical stress. The stress may be caused by pulsed surface heating and large electric fields. A compelling piece of evidence that supports this hypothesis is that accelerating structures constructed from harder materials exhibit larger accelerating gradients for similar breakdown rates.

One possible method to increase sustained electric fields in copper cavities is to cool them to temperatures below 77 K, where the rf surface resistance and coefficient of thermal

expansion decrease, while the yield strength (which correlates with hardness) and thermal conductivity increase. These changes in material properties at low temperature increases metal hardness and decreases the mechanical stress from exposure to rf electromagnetic fields. To test the validity of the improvement in breakdown rate, experiments were conducted with cryogenic accelerating cavities in the Accelerator Structure Test Area (ASTA) at SLAC National Accelerator Laboratory.

A short 11.4 GHz standing wave accelerating structure was conditioned to an accelerating gradient of 250 MV/m at 45 K with 10^8 rf pulses. At gradients greater than 150 MV/m I observed a degradation in the intrinsic quality factor of the cavity, Q_0. I developed a model for the change in Q_0 using measured field emission currents and rf signals. I found that the Q_0 degradation is consistent with the rf power being absorbed by strong field emission currents accelerated inside the cavity. I measured rf breakdown rates for 45 K and found $2 * 10^{-4}/pulse/meter$ when accounting for any change in Q_0. These are the largest accelerating gradients for a structure with similar breakdown rates.

The final chapter presents the design of an rf photoinjector electron source that uses the cryogenic normal conducting accelerator technology: the TOPGUN. With this cryogenic rf photoinjector, the beam brightness will increase by over an order of a magnitude when compared to the current photoinjector for the Linac Coherent Light Source (LCLS). When using the TOPGUN as the source for an X-ray Free Electron Laser, the higher brightness would allow for a decrease in the required length of the LCLS undulator by more than a factor of two.

The dissertation of Alexander David Cahill is approved.

Robert N. Candler

Troy A. Carter

Pietro Musumeci

James Rosenzweig, Committee Chair

University of California, Los Angeles

2017

For Mom and Dad, who always inspire me.

Table of Contents

List of Figures

List of Tables

Acknowledgments

First, I need to thank my friends in the UCLA graduate school who all helped me get to this point of which there are too many to count. I know that we will all continue to succeed in the future, and keep in touch!

Second, to all of my colleagues at UCLA who taught me how to function in accelerator physics. In particular: Atsushi Fukasawa, Oliver Williams, and Brendan O'Shea helped me in the beginning of my time at PBPL. To the rest of PBPL, thanks for the support and for the BBQs that were a good excuse to not accomplish anything on a Friday.

To my colleagues at SLAC, you all made me feel as though I fitted in when I showed up out of the blue. I would in particular like to mention those who supported and helped me with my experiments at ASTA: John Eichner, Victor Rey, Joe Olszewski, Jim Lewandowski, John Van Pelt, Matt Franzi, Paul Welander, Brandown Weatherford, Stephen Weathersby, Charles Yoneda, Matt Boyce, Zenghai Li, Emilio Nanni, Aaron Tremaine, Craig Burkhart, Dian Yeremian, Mike Gonzales, and Queenie Huang. Also those who consulted on and designed all of my projects: Gordon Bowden, Ann Sy, Diana Gamzina, Charlie Markusen, and Andy Haase. And then there was the UED group who graciously shared the ASTA space even though I blast their detectors with X-rays.

To the collaborators in the TOPGUN initiative: Cecile Limborg, Sami Tantawi, Renkai Li, Jared Maxson, Bruno Spataro, Pietro Musumeci, Claudio Emma, Ariel Nause, Ryan Roussel, Riccardo Pompili, and Giovanni Castorina who helped support my work as we all work to make this idea a success.

Finally, I need to thank the advisers that I have had, and I have been quite lucky in mine. Stephon Alexander, who made physics an enjoyable experience at Haverford College. James Rosenzweig, who supported my work and is always full of brilliant ideas. Valery Dolgashev, who taught me the nitty gritty details of how to run accelerator systems.

To all those who have supported me along the way, this accomplishment would not have been possible without you.

Vita

2011	B.S. (Physics), Haverford College, Haverford, PA.
2011	Robert Finkelstein Fellowship, , Los Angeles, California.
2012	M.S. (Physics), UCLA, Los Angeles, California.
2015	Science Graduate Student Researcher Fellowship, Department of Energy.
2011–present	Graduate Student Researcher, UCLA, Los Angeles, California.
2015–present	Researching remotely at SLAC, Menlo Park, CA.

Publications

Cahill et al. *Dynamically Changing Quality Factor in a Copper Cryogenic Cavity.* In preparation.

Cahill et al. *Ultra-High RF Surface Electric Fields in a Copper Cryogenic Cavity.* In preparation.

Cahill et al. *TopGun: An Ultra-High Gradient Cryogenic RF Photoinjector.* Nucl. Instrum. and Meth. A 865 105-108 (2017).

Cahill et al. *Ultra-High Gradient Breakdown Rates in X-Band Cryogenic Normal Conducting RF Accelerating Cavities.* In Proc. of IPAC 2017 4395-4398.

Cahill et al. *Optimization of Beam Dynamics for an S-Band Ultra-High Gradient Photoinjector.* In Proc. of IPAC 2017 1626-1629.

Cahill et al. *High Gradient S-Band Cryogenic Accelerating Structure for RF Breakdown Studies.* In Proc. of NAPAC 2016 991-994.

Cahill et al. *Quality Factor in High Power Tests of Cryogenic Copper Accelerating Cavities.* In Proc. of NAPAC 2016 987-990.

Cahill et al. *Measurements of Copper RF Surface Resistance at Cryogenic Temperatures for Applications to X-Band and S-Band Accelerators.* In Proc. of IPAC 2016 477-480.

Cahill et al. *Automated Design for Standing Wave Electron Photoguns: TOPGUN RF Design.* In Proc. of IPAC 2016 3999-4003.

Cahill et al. *TM01 Mode Launcher for Use in High Brightness Photoguns.* In Proc. of IPAC 2016 491-494.

Cahill et al. *Simulations for the high gradient, low emittance supergun RF photoinjector.* In Proc. of LINAC 2014 391-394.

Nomenclature

Abbreviations

Ag	Silver
ASE	Anomalous skin effect
ASTA	Accelerator Structure Test Area
BDR	Breakdown Rate
BNL	Brookhaven National Lab
C	Carbon
C-band	4-8 GHz
CAD	Computer aided design
CEA	the French Alternative Energies and Atomic Energy Commission
CERN	European Organization for Nuclear Research
CLIC	Compact Linear Collider
Cr	Chromium
Cu	Copper
CW	Continuous wave
DESY	Deutsches Elektronen-Synchrotron
DLW	disk-loaded waveguide
DTL	Drift-tube linac
FEL	Free electron laser
FNAL	Fermi National Accelerator Laboratory
GLC	Global Linear Collider
H	Hydrogen
HG	High gradient
ILC	International Linear Collider
INFN	National Institute for Nuclear Physics
IR	Infrared
KEK	High Energy Research Organization

LANL	Lawrence Berkeley National Laboratory
LANL	Los Alamos National Laboratory
LCLS	Linac Coherent Light Source
LEP	Large ELectron-Positron Collider
LHC	Large Hadron Collider
linac	Linear accelerator
Nb	Niobium
NLC	Next Linear Collider
NSE	Normal skin effect
O	Oxygen
QE	Quantum Efficiency
RF	Radio-frequency
RMS	Root Mean Square
S-band	2-4 GHz
SMA	SubMiniature version A
SW	Standing wave
TE	Transverse electric
TM	Transverse magnetic
TW	Traveling wave
UCLA	University of California, Los Angeles
UED	Eltra-fast electron diffraction
VNA	Vector network analyzer
WKB	Wentzel-Kramers-Brillouin
X-band	8-12 GHz
XFEL	X-ray free electron laser
Zr	Zirconium

Symbols

α	Attenuation constant
α_D	Thermal Diffusivity, $\frac{k_c}{\rho c_{\mathcal{E}}}$

α_T	Coefficient of thermal expansion, $\frac{1}{L}\frac{dL}{dT}$
β	Coupling constant, $\frac{Q_0}{Q_E}$
β_c	Velocity beta, $\frac{v}{c}$
δ	RF skin depth
ϵ_0	Vacuum permittivity, $5.53 \times 10^{-5} e/V \cdot m$
ϵ_n	Normalized emittance
ϵ_x	Emittance in x plane
Γ	Reflection coefficient
γ	Lorentz factor, $\sqrt{1-\beta_c^2}^{-1}$
λ	Wavelength, $\frac{2\pi}{k}$
$\mathcal{L}$	Luminosity
μ_0	Vacuum Permeability, $4\pi \times 10^{-7} T/A$
ω	Angular frequency
ω_p	Plasma frequency
ϕ	RF phase
ρ	Density function
σ_c	DC electrical conductivity
τ_f	Filling Time
B_e	5-D electron beam brightness, $\frac{2I}{\epsilon_n^2}$
c	Speed of light, $2.998 \times 10^8 m/s$
$c_\mathcal{E}$	Specific heat capacity
E	Electric field
e	Elementary charge, $1.602 \times 10^{-19} C$
f	frequency, $\frac{\omega}{2\pi}$
G	Accelerating gradient
H	Magnetic field
I	Current
i	$\sqrt{-1}$
J	Current Density

k	Wave number
k_B	Boltzmann's constant, $8.617 \times 10^{-5} eV/K$
K_c	THermal conductivity
L	Length of accelerating cell
l	Electron mean free path
m_e	Electron mass, $3.11 \times 10^{-31} kg$
P	Power
p	Particle momentum
q	Particle charge
Q_0	Internal quality factor
Q_E	External quality factor
Q_e	Beam total charge
Q_T	Total quality factor, $\left(\frac{1}{Q_0} + \frac{1}{Q_E}\right)^{-1}$
R_s	Surface resistance
r_s	Shunt impedance
S	Poynting vector, $\vec{E} \times \vec{H}$
T	Temperature
t	Time
T_{rf}	Transit time factor
V	Voltage
v	Particle velocity
v_f	Fermi velocity
v_g	Group velocity, $\frac{\partial \omega}{\partial k}$
v_p	Phase velocity, $\frac{\omega}{k}$
W	Energy of a particle
Z	Shunt impedance per unit length
Z_0	Vacuum impedance, $\sqrt{\frac{\mu_0}{\epsilon_0}}$

CHAPTER 1

Introduction to Normal Conducting Radio-Frequency Linear Accelerators

Accelerating structures have many uses, in light sources, high energy physics discovery machines, security scanning, and medical radiation therapy. There are two central schemes to accelerate particles to high energies that have been used for many decades, circular and linear machines. In electron circular machines, such as the LEP, the particles are continuously accelerated for every revolution around the circle. However, a significant percentage of the beam energy, nearly 20% in the case of LEP, is radiated away from accelerating around bends every revolution [1]. This makes reaching very high energies with electrons impractical in a circular scheme. In linear machines, the beam travels in a straight line. As such, no energy is lost to synchrotron radiation from accelerating in a circle, though synchrotron radiation is still a problem in some bunch compression schemes that use bending magnets [2]. However, since the particle beam is only accelerated once through the structure, the final energy is limited by the length of the machine. Therefore, to reach a given particle energy, one requires a linear accelerator structure (linac) with a given gradient, G, and total length, L. Any increase in available operating gradients then decreases the required length of linac. This places immense importance on reaching extremely large accelerating gradients to create more practical and cheaper accelerator machines.

1.1 Historical Development of Radio-Frequency Linacs

The first proposal for a particle accelerator that would use time-dependent fields was laid out by Gustav Ising [3]. The design presented would accelerate the particle beam by pulsed

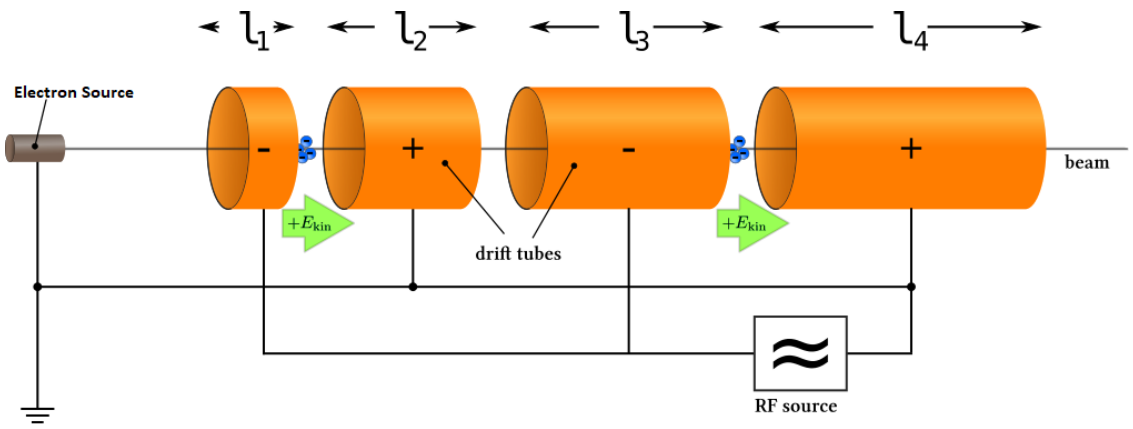

Figure 1.1: A diagram of a Widerøe Linac. The electrodes have alternating voltages applied to accelerate electron beam. The lengths of the electrodes are adjusted so the particle beam is always in phase with the accelerating voltage [5].

voltages across vacuum gaps that were created by spark discharges. This concept was never implemented but did inspire Rolf Widerøe to propose and demonstrate the first rf linear accelerator.

Widerøe designed a predecessor to the drift-tube linac (DTL) that operated at 1 MHz and successfully accelerated potassium ions to 50 keV [4]. The Widerøe linac consists of a series of hollow electrodes that the beam travels through, an example of which is depicted in Figure 1.1. Alternating electrodes are connected to the positive and negative terminal of an alternating radio-frequency (rf) voltage source. The particles are accelerated when passing across the voltage difference that is maintained in the gaps between electrodes. The length of the electrodes is set such that particles arrive at the vacuum gaps at the same phase as an accelerating voltage difference. As the particle gains energy and velocity, the length of the electrodes increases along the length of the accelerator. The voltage applied was 25 kV, less than the final energy of the particles, and Widerøe was able to reach a beam energy larger than the applied voltage for the first time. This success was an instrumental step that inspired David Sloan and Ernest Lawrence to build a linear accelerator composed of 30 drift tube sections, expanding the concept to a higher energy scale. The applied voltage for this longer accelerator was 42 kV at 10 MHz and the beam of mercury ions reached a final energy

of 1.26 MeV [6].

As final beam energies increased, and the target of the acceleration changed to lighter particles, protons and electrons, drift-tube linacs became impractical. As the speeds of the particles approach the speed of light, the lengths of the electrodes in the accelerator become long, requiring the frequency of operation to approach values on the order of a GHz. At these frequencies the geometry of the drift-tubes would operate similar to an antenna, becoming lossy and inefficient [7]. The solution that the accelerator community arrived at was to enclose the linac in a high-Q resonant cavity. Luis Alvarez and coworkers at the University of California, Berkeley created such a structure, the DTL, which operates similarly to the Widerøe linac[8]. This design was used to accelerate protons from 4 to 32 MeV with an operating frequency of 200 MHz at the Berkeley proton linear accelerator [9].

For electrons, William Hansen and coworkers at Stanford University decided to use an array of coupled pillbox-cavities with holes for the beam to traverse between them [10]. Another way to conceptualize this accelerator, is that the boundaries between the pillbox cavities act as periodic elements in a waveguide that create reflections to slow down the phase velocity of a propagating electromagnetic wave. When designed correctly, the accelerated particle beam travels synchronously with the wave and is accelerated. This concept is known as the disk-loaded waveguide type linac (DLW) [7] and the technology was used to accelerate electrons to 1 GeV in 220 feet [11]. Figure 1.2 shows an example of the DLW used in the BeV Stanford Accelerator. Eventually this cavity would be developed into the accelerating structures of the 3 km SLAC linac, which operates at 2.856 GHz [12], sections of which are still in use today.

1.2 RF Acceleration

I will now consider the energy gained by a particle that travels across an rf gap as shown in Figure 1.3. This gap could be between two electrodes in a DTL or between two irises in a

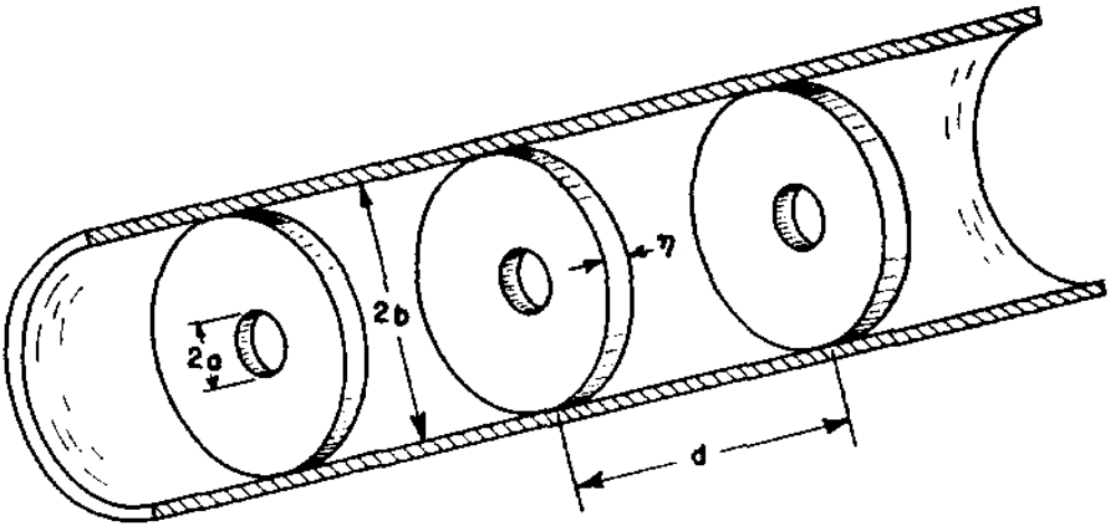

Figure 1.2: A diagram of an early DLW linac used in the BeV Stanford Accelerator, image from [11]. In this diagram a is the iris radius, b is the outer radius, η is the iris width, and d is the iris spacing.

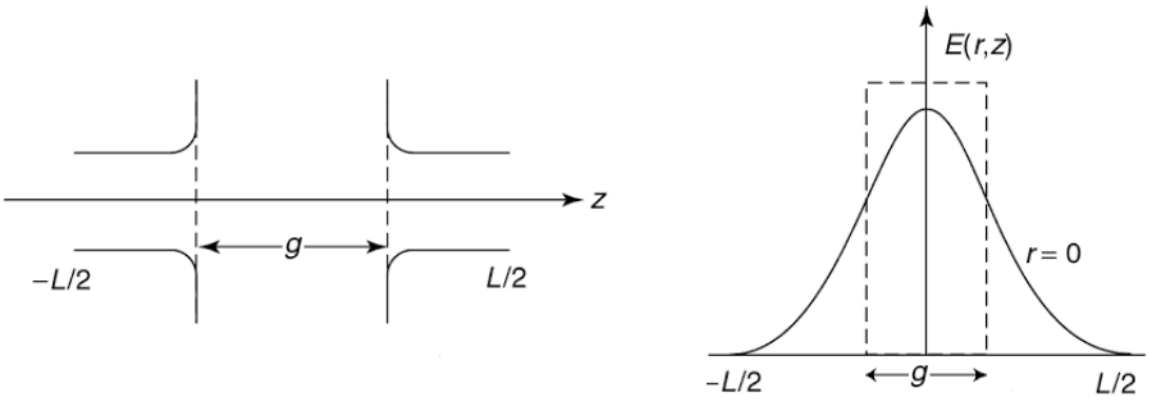

(a) (b)

Figure 1.3: (a)Representation of a gap of length g with (b) an arbitrary electric field along the axis, where a charged particle would travel along the z-axis. The length L will be the periodic length of the accelerating structure. Image from [7]

DLW. The energy gained by a particle, ΔW, traveling along the axis is:

$$\Delta W = q \int_{-L/2}^{L/2} E_{rf}(z) \cos(\omega t(z) + \phi) dz, \tag{1.1}$$

where at $t = 0$, ϕ is the phase of the field relative to the crest, ω is the angular frequency of the rf field, E_{rf} is the field inside the rf gap, L is length that the particle travels (this is the periodic length of the linac), q is the charge of the particle, and $t(z)$ is the time the particle is at position z along the axis. In most cases of accelerating electrons, the velocity is essentially $\beta_c = v_e/c \approx 1$. Then $t(z) = k_{rf} z$, with k_{rf} as the wavenumber of the rf field. Next, I will assume that the electric field is an even function across $z = 0$. Then I define:

$$\begin{aligned} V_0 &= \int_{-L/2}^{L/2} E_{rf}(z) dz = E_0 L \\ T_{rf} &= \frac{\int_{-L/2}^{L/2} E_{rf}(z) \cos(k_{rf} z) dz}{V_0} \end{aligned} \tag{1.2}$$

Where E_0 is the average electric field amplitude, V_0 is the rf voltage change across the gap, and T_{rf} is the transit-time factor. T_{rf} essentially quantifies how much the fields are bunched to the center of the rf gap if $\beta_c = 1$. Equations 1.1 and 1.2 can be combined to find:

$$\Delta W = q E_0 T_{rf} L \cos\phi; \tag{1.3}$$

known as the Panofsky equation. $G \equiv E_0 T_{rf}$ is defined as the accelerating gradient.

1.2.1 Figures of Merit

The linacs that have been presented here can be considered resonant cavities composed of imperfect conductors. Power to create rf electromagnetic fields is inputted in through coupling holes, and power is lost to ohmic losses in the cavity walls, or through radiation out of the same coupling holes. There are several defined quantities that are important to the design and operation of linacs. The first to be considered are the intrinsic and external quality factors, Q_0 and Q_E, defined as:

$$\begin{aligned} Q_0 &= \frac{\omega U}{P_{cav}} \\ Q_E &= \frac{\omega U}{P_{ext}}, \end{aligned} \tag{1.4}$$

where U is the stored energy per periodic unit cell in a linac, and P_{cav} and P_{ext} are the average powers lost to the cavity walls and out of the coupling holes respectively. The total quality factor, Q_T, incorporating both the power lost to ohmic losses and to the external coupling is:

$$Q_T = \frac{\omega U}{P_{ext} + P_{cav}} = \left(\frac{1}{Q_E} + \frac{1}{Q_0} \right)^{-1} \tag{1.5}$$

The coupling factor, β, is defined to be:

$$\beta = \frac{Q_0}{Q_E}, \tag{1.6}$$

then $Q_T = Q_0/(1+\beta)$.

The shunt impedance, r_s and effective shunt impedance, r, of a cavity are:

$$\begin{aligned} r_s &= \frac{V_0^2}{P_{cav}} \\ r &= \frac{(V_0 T_{rf})^2}{P_{cav}} = r_s T_{rf}^2 \end{aligned} \tag{1.7}$$

The shunt impedance measures the efficiency of generating voltage per power lost, while the effective shunt impedance is specifically the voltage that an accelerated particle experiences. I also define the shunt impedance per unit length $Z = r_s/L$, and the effective shunt impedance per unit length is ZT_{rf}^2. Increasing ZT_{rf}^2 serves to maximize the energy gained by a particle per unit of power supplied to the cavity, an important parameter in linac design.

A final parameter that is important for linac design to be introduced here is the r/Q, a ratio that measures the efficiency of acceleration per unit of stored energy. This parameter, r over Q, is a function only of the cavity geometry, not of the surface properties of the cavity material.

1.2.1.1 Frequency Scaling of RF Parameters

Linacs can operate at many different rf frequencies, thus it will be insightful to consider how the parameters that define the accelerators change as we change the frequency of a cavity. I will assume for this exercise that the fields inside the linacs are held constant on change of frequency. As the frequency changes, the physical dimensions scale with the wavelength,

λ_{rf}. The frequency dependence of the rf surface resistance is derived in Section A

$$R_s \propto \begin{cases} f_{rf}^{1/2} & \text{Near 300 K} \\ f_{rf}^{1/3} & \text{Below 30 K.} \end{cases} \tag{1.8}$$

In between 45 K and 300 K the dependence transitions smoothly between 1/2 and 1/3. When the fields are held constant, the stored energy per unit cell scales with the volume, and the power lost to the cavity walls scales with the surface area times the rf surface resistance.

Then the scaling of Q_0 is

$$Q_0 = \frac{\omega U}{P_{cav}} \propto \begin{cases} f_{rf}^{-1/2} & \text{Near 300 K} \\ f_{rf}^{-2/3} & \text{Below 30 K..} \end{cases} \tag{1.9}$$

Another interesting scaling to mention is the ratio of Q_0 at 300 K to the Q_0 at 30 K, which scales with $f_{rf}^{-1/6}$. Therefore, the improvement in cavity parameters by decreasing the temperature is larger at lower frequencies.

The effective shunt impedance per unit length scales as:

$$ZT^2 = \frac{(E_0 T)^2 L}{P_{cav}} \propto \begin{cases} f_{rf}^{1/2} & \text{Near 300 K} \\ f_{rf}^{1/3} & \text{Below 30 K..} \end{cases} \tag{1.10}$$

Using the scaling of ZT^2 and Q_0 we find their ratio ZT^2/Q_0 scales as f_{rf} for both 300 K and for 30 K. This is as predicted, since the ratio of shunt impedance to Q_0 is independent of the cavity properties.

1.2.2 Traveling Wave and Standing Wave Structures

1.2.2.1 Traveling Wave

Traveling wave (TW) structures are broadband DLW type linacs, in which the power flows through each cell successively. The iris spacing is chosen to match the phase velocity of the rf field with the velocity of the accelerated particle. The phase advance per cell is defined as $\Delta\phi = k_{rf} L$. The choice for phase advance that nearly maximizes shunt impedance is $2\pi/3$

rad/cell. The group velocity, $v_g = d\omega/dk$, defines the speed at which the electromagnetic wave traverses the linac. As the rf power traverses the cells, energy is dissipated due to ohmic losses. If the v_g is constant throughout the structure, the electric fields will decrease exponentially along the length of the structure, with dependence:

$$\begin{aligned} \frac{dE_z(z)}{dz} &= -\alpha(z)E_z(z) \\ \alpha &= \frac{\omega}{2v_g Q_0}. \end{aligned} \tag{1.11}$$

Structures are where v_g is constant are called constant-impedance, and have the same iris radii along the structure.

The attenuation can be corrected for, keeping the electric fields constant, by tapering the iris radius, leading to smaller values of v_g at the end of the structure. If the v_g is made to decrease linearly along the structure with the correct initial and final values, then the electric field amplitude can be held constant along the structure, known as a constant-gradient linac.

The amount of time that it takes to bring the electric fields to the nominal value in a TW structure with constant input rf power is:

$$\tau_{TW} = \int_0^{N_{cell}L} \frac{1}{v_g(z)} dz, \tag{1.12}$$

where N_{cell} is the number of cells in the linac. Figure 1.4 shows a constant impedance TW wave structure, where the fields (represented by the color intensity) decrease along the length.

1.2.2.2 Standing Wave

Standing wave (SW) structures are narrow-band devices where each cell of the linac fills with electromagnetic energy concurrently. SW linacs commonly operate in the π mode, where the phase advance per unit cell is 180 degrees. Then, if each cell length is designed to be π/k_{rf} a particle traveling with $\beta_c = 1$ will always experience an accelerating field. Figure 1.4 depicts a SW linac with coupling between the cavities on the outer radius. Coupling between cells can also be accomplished through the irises.

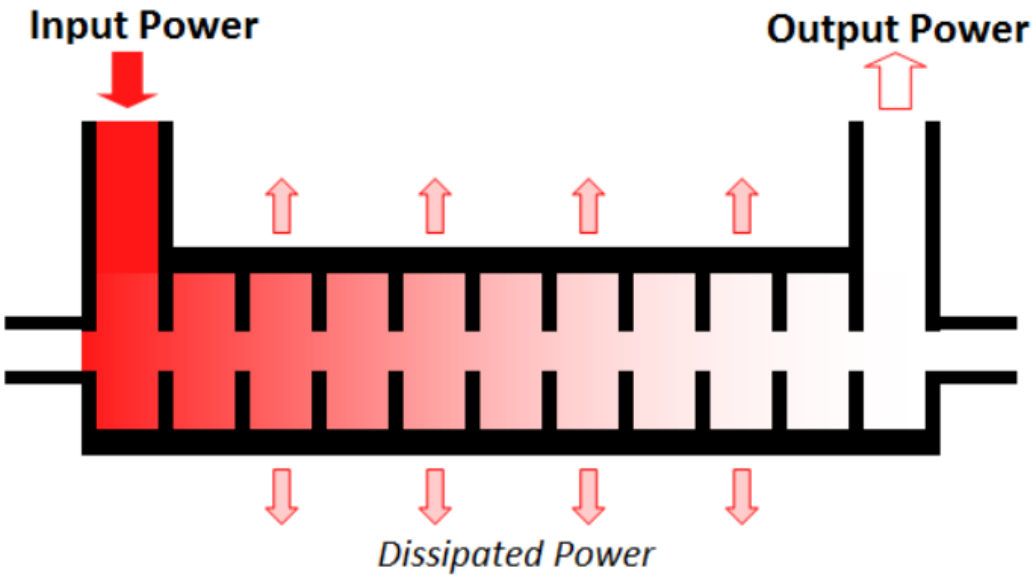

(a)

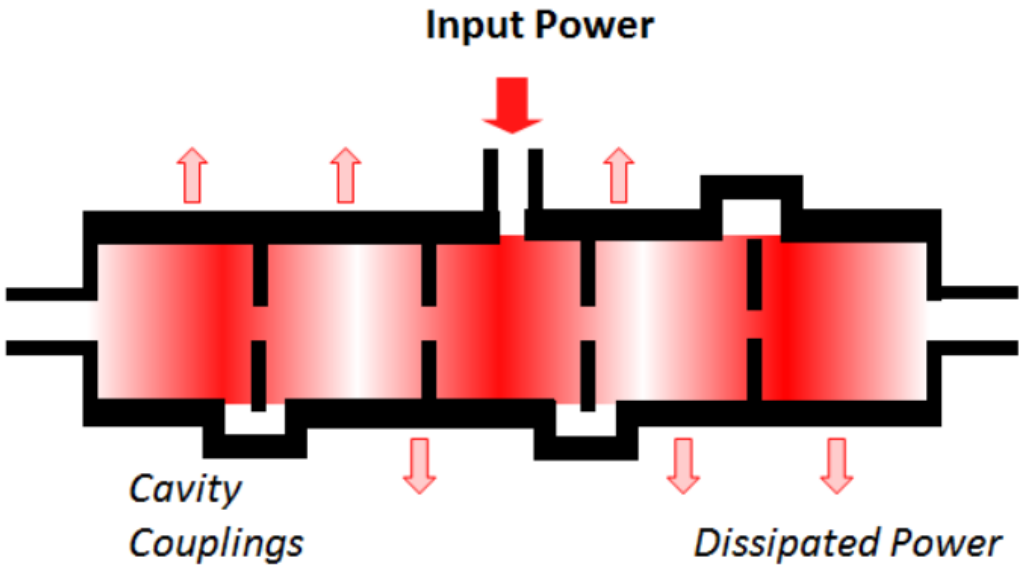

(b)

Figure 1.4: Conceptual diagrams of a (a) TW and (b) SW linac. In a TW linac the rf power flows from the input to the output, and is attenuated along the structure. In a SW linac, the input rf power creates a stationary wave. Power is lost to resistive losses in the walls or is reflected out of the input port. Image courtesy [13].

The differential equation that defines the time-dependence of energy in a SW structure is

$$\frac{dU(t)}{dt} = -\frac{\omega U(t)}{Q_T}. \tag{1.13}$$

The solution for an initial stored energy $U(t=0) = 0$ and constant input power, becomes

$$U(t) = U_0 \left(1 - \exp\left(\frac{-\omega t}{Q_T}\right)\right), \tag{1.14}$$

where U_0 is an asymptotic value of the stored energy, where the input rf power equals the power lost. The filling time for electric fields, where $E_0 \propto \sqrt{U}$, in a SW cavity is:

$$\tau_f = \frac{2Q_0}{\omega(1+\beta)} \tag{1.15}$$

Further discussion of temporal behavior of SW linacs is included in C.

1.2.3 Comparison to Superconducting Linacs

So far, we have considered normal-conducting structures, however, linacs can also be constructed using superconducting materials. For cavities of the same geometry, the rf surface resistance of superconducting materials versus copper is a factor of $10^5 - 10^6$ smaller, and thus the Q_0 is proportionately larger. The superconductor that is most often used for linac manufacturing is Nb, which has a relatively large critical temperature of 9.2 K. Operating temperature for the Nb superconducting linacs is usually 1.8 to 4.2 K. At these temperatures, the Carnot efficiency [14] and the mechanical inefficiency of cryogenic refrigerators [15] combine to a create a ratio of power spent to removed power from the cold system of 1000. Combining the increase Q_0 and the penalty in removing power from the cold accelerator leads 2-3 orders of magnitude improvement in rf efficiency for superconducting linacs over normal-conducting ones.

However, superconducting accelerators have other limitations. The accelerating gradient is limited by the super-heating critical H-field, which in Nb is near 1800 G at 2 K[16]. Above these magnetic fields, the material will become normal-conducting and lose any advantages for its use. Practically, this limits accelerating gradients to $\tilde{5}5$ MV/m, however, work has

been ongoing to extend to higher levels through use of alternate materials and geometries [17–19]. The other disadvantage for superconducting cavities is the extremely long fill times, due to large Q_0, during which time the particles cannot be accelerated. This disadvantage is often mitigated by operating in multi-bunch mode or even continuous wave (CW) operation, where the amount of wasted time during filling and decaying is reduced by launching multiple beams each time the cavity is filled.

Superconducting and normal conducting acceleration both have their advantages, the main ones being: high gradient and no need for the complex cryogenic infrastructure in normal conducting, and high efficiency for superconducting. The differences make design considerations of the two types of linacs divergent, and they have different optimal applications.

1.3 RF Photoinjectors as Electron Sources

For many applications of electron acceleration, the quality of the delivered beam is important, such as large densities of the beam in high-energy colliders to increase luminosity [20], and intense very cold beams to create free-electron lasers (FELs) [21]. Liouville's Theorem states that conservative forces acting on a system of particles do not change the momentum or space density along physical trajectories [22]. This means that beam densities cannot be increase using accelerators. Therefore, the electron beam density at creation is crucial. This places a large importance on the design and operation of the electron sources.

1.3.1 Design of Electron Guns

RF electron sources, commonly known as rf electron guns, are constructed similarly to DLW type linacs and usually operate as SW cavities. The geometry consists of a given number of cells operating in the π mode each with length $\lambda_{rf}/2$, except for the initial cell, where the electron beam is created, which is shorter and has a wall on one end rather than an iris opening. This wall functions as the cathode for the electron gun, and the initial cell is referred to as the cathode cell, an example geometry is shown in Figure 1.5.

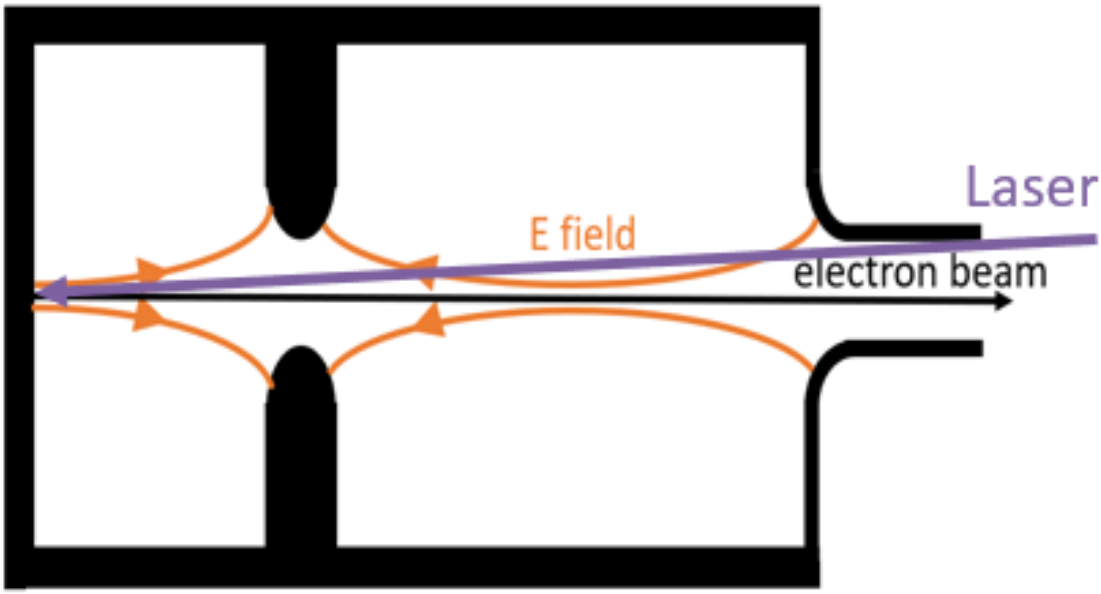

Figure 1.5: Geometry for an example electron gun. The cathode cell is on the left, and the electron beam travels to the right. The rf phase of the electric field changes by 180° between cells.

The length of the cathode cell is shorter to allow for phase slippage of the electron beam relative to the rf. Earlier we had said that electrons are traveling with $\beta = 1$ and travel synchronously with the rf accelerating mode. However, at the inception of the electron beam, $\beta < 1$ and the electrons fall behind the synchronous wave. The length of the cathode cell and initial phase of the electron beam creation relative to the rf crest, are chosen such that the electron beam will arrive at the first iris after the cathode cell as the rf reaches a null, and thus the electron beam will have arrived at an accelerating synchronous phase for the rest of the structure. When the electrons arrive at the first iris they essentially are traveling at the speed of light.

The choice of length for the cathode cell depends on the situation, where longer cathode cells, such as the $0.6\lambda_{rf}/2$ cell [23], was chosen to provide extra transverse rf focusing. While shorter cells can be chosen to increase the electric field gradient that electron beam experiences at inception, such as $0.4\lambda_{rf}/2$ in some cases [24, 25].

There are two types of commonly used methods for generating electrons in rf electron

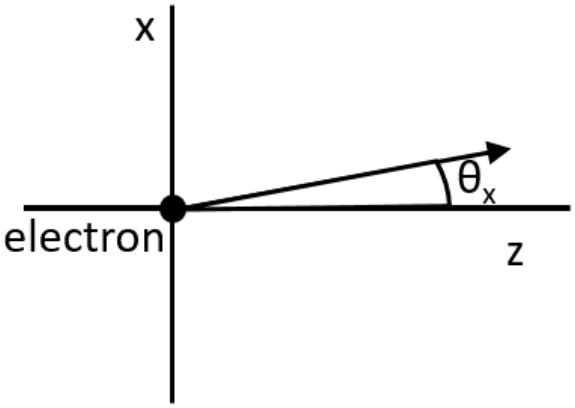

Figure 1.6: Diagram of electron traveling with angle θ_x relative to the z-axis. In most situations θ_x is small.

guns: photoelectric effect, and thermionic emission. Guns that use the photoelectric effect are known as photoinjectors, and operate with a laser pulse on the cathode that emits electrons. The number of electrons emitted depends on the intensity of the incident laser as well as the quantum efficiency (QE) of the photocathode at the wavelength of the laser. Photo emission will cease either when the laser pulse ends, or electron emission is prohibited by the space charge forces of previously emitted electrons. A disadvantage of photoinjectors is the requirement of a relatively complex full laser system combined with the rf system. Thermionic emission is commonly accomplished by heating a cathode, and then the rf field combined with the large temperature electrons will emit electrons into the gun. One disadvantage of thermionic emission is the large transverse motion of electrons directly after emission, due to the large temperatures.

1.3.2 Relevant Theory

In accelerator physics, it is common to use paraxial rays for descriptions of particles in accelerators. Longitudinal momentum, designated to be along the z-axis defined by the linac accelerating axis, is significantly larger than the perpendicular transverse momentums. In addition, it is simpler to consider the system as a function of space, rather than time, as we can understand best the position of a particle along the accelerating system.

In this description we define, θ_x, as depicted in Figure 1.6:

$$\tan\theta_x = \frac{p_x}{p_z}, \tag{1.16}$$

with an analogous equation for the y-direction. We will use the notation $x' = \frac{dx}{dz}$. In the limit that $p_x << p_z$, then

$$x' = \tan\theta_x \sim \theta_x \sim \sin\theta_x. \tag{1.17}$$

When considering phase for the transverse dimensions, the variables x, x', y, and y', are often used rather than the explicit momentums $p_x = p_z x'$ and $p_y = p_z y'$. We will use this formalism in the following definitions.

1.3.2.1 Emittance and Brightness

Next, we will consider two properties of electron beams that are often used as figures of merit for rf photoinjectors. The emittance of a beam is a measure of the area in phase space that it occupies. The brightness of a beam is instead a measure of the density in phase space. The definition of the normalized RMS emittance in units of π mm-mrad is

$$\epsilon_x = \beta\gamma\sqrt{< x^2 >< x'^2 > - < xx' >^2} = \frac{p_z}{m_p c}\sqrt{< x^2 >< x'^2 > - < xx' >^2}, \tag{1.18}$$

where m_p is the mass of the particle, $\gamma = 1/\sqrt{1 - v^2/c^2}$, and the expected values in the definition are

$$\begin{aligned} < x^2 > &= \frac{\int_V x^2 \rho(x, x', y, y', z, p_z) dV}{\int_V \rho(x, x', y, y', z, p_z) dV}, \\ < x'^2 > &= \frac{\int_V x'^2 \rho(x, x', y, y', z, p_z) dV}{\int_V \rho(x, x', y, y', z, p_z) dV}, \\ < xx' > &= \frac{\int_V xx' \rho(x, x', y, y', z, p_z) dV}{\int_V \rho(x, x', y, y', z, p_z) dV}, \end{aligned} \tag{1.19}$$

where $\rho(x, x', y, y', z, p_z)$ is the density function for particles in phase space and V is the volume of the 6-D phase space. There are analogous definitions for the other two axes directions. The emittance in each direction is not necessarily conserved, since the shape of the density function can change, possibly increasing one emittance and decreasing another, sometimes called emittance exchange [26]. This can lead to asymmetric beams where $\epsilon_{n,x} >>$

$\epsilon_{n,y}$ [27], which may have applications in certain accelerator schemes [28, 29]. However, if there is no coupling between the three systems (x, x'), (y, y'), and (z, p_z) then each emittance will be a conserved quantity according to Liouville's theorem [22].

The 5-D brightness is defined as

$$B_e = \frac{2I}{\epsilon_n^2}, \tag{1.20}$$

where $I = Q_e/\sigma_z$ is the current of the beam, Q_e is the charge, and σ_z is the bunch length in the z-direction. As we are often dealing with cylindrically symmetric systems where $\epsilon_x = \epsilon_y$, I will define $\epsilon_n = \sqrt{\epsilon_x^2 + \epsilon_y^2}$ as the transverse normalized emittance.

1.3.2.2 Emittance Compensation

An important aspect of beam dynamics in rf photoinjectors is emittance compensation, where the emittance of the beam grows to a large value before the original small emittance is recovered. This action does not violate Liouville's theorem, as will be explained.

Emittance compensation was first described in [30]. In this theory to understand emittance compensation, the electron beam is considered to be composed of a multitude of slices in the longitudinal direction. Each slice can be considered to have its own small emittance, which is represented as an ellipse in phase space, and originally these ellipses are aligned. As the beam travels along the beamline, each slice may have different space-charge forces or transverse kicks from the accelerator acting upon it, and then each slice will rotate in phase space around the origin. As the slices become misaligned in phase space, the emittance of the entire beam, considering all the slices, will grow, even as the emittance of each slice remains small. This situation is depicted in Figure 1.7. The beam can be made to pass through a solenoid lens, which applies a kick, after which the slices will rotate and drift back to alignment. When the slices are aligned, the emittance returns to the original small value.

This increase and subsequent decrease of the emittance does not violate Liouville's theorem, since the actual phase-space density of the beam is not changing. The transverse emittance of the full beam is temporarily larger, but can be restored to the smaller original value by realigning the slices. Thus, the action is a rotation in phase space, not a change in

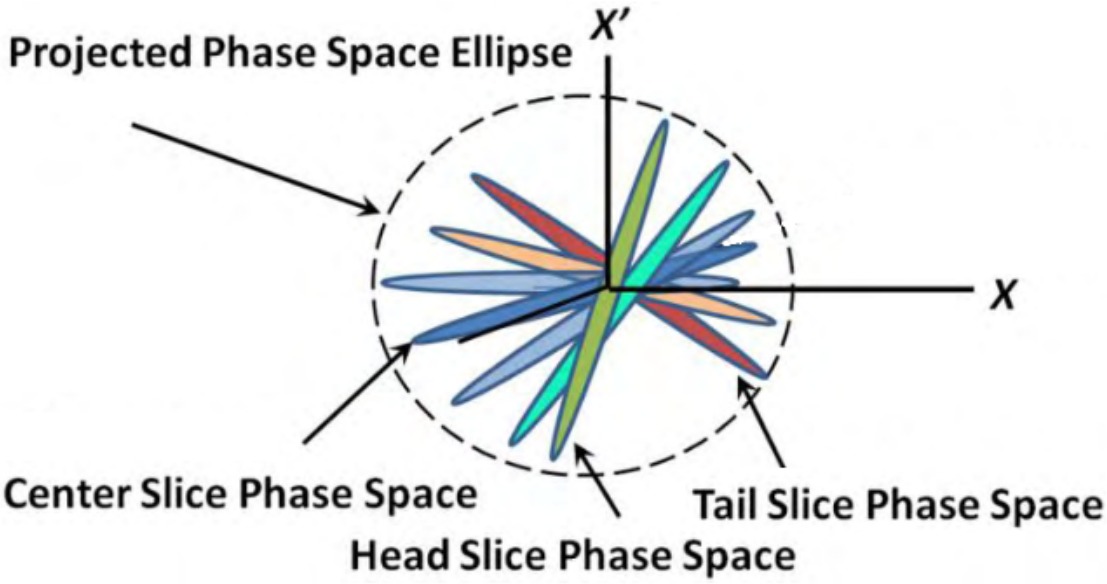

Figure 1.7: Slices of an electron beam in phase space that are misaligned. The emittance of the whole beam is the area of the large dashed circle. The emittance of a single slice is small, the area of a small colored ellipse. Image from [31]

density.

The theory was further expanded in [32], with the idea of an invariant envelope. In this case the compensation, the restoration of the small initial emittance, is performed by solenoid channel focusing, and the beam is launched with an appropriate radius for the strength of the solenoid. Each slice of the beam will oscillate around an equilibrium radius with a given frequency related to the plasma frequency. By careful choice of the solenoid strength and beam radius, the frequency of oscillation in each slice will be the same, and thus these oscillations will cause a similar oscillation in the beam emittance.

These oscillations can be "frozen" by accelerating the beam, since the plasma frequency is proportional to $1/\gamma^2$. If the beam is accelerated when the emittance is at a minimum, the small emittance can be maintained. This emittance compensation scheme was optimized [33] and then empirically measured in [34], which is shown in Figure 1.8.

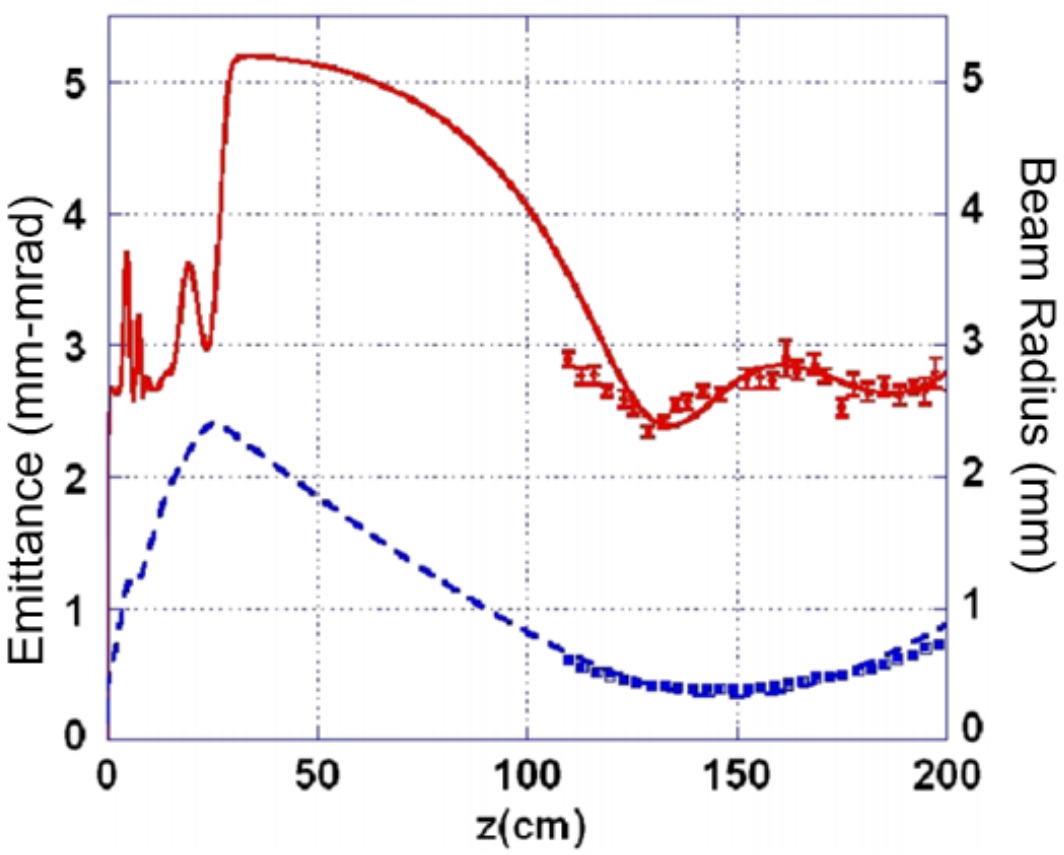

Figure 1.8: Measurements (points) of the double emittance maximum, compared to beam dynamic simulations (lines). Red is rms normalized emittance, Blue is the rms beam radius. After 100 cm the oscillatory behavior of the emittance is clear [34].

1.3.2.3 Space-Charge-Limited Emission

As electrons are emitted from the surface of a cathode, the space-charge forces limit the current densities that can be reached with a photoinjector. In the limit of a pancake beam aspect ratio (the longitudinal direction is short relative to the transverse dimensions), the charge density is [35, 36]:

$$|J| \sim \frac{e\epsilon_0 E_0^2}{m_e c}. \tag{1.21}$$

This limit is taken where the space-charge constant $\alpha_{SC} \equiv \sigma_b/\epsilon_0 E_0 << 1$ where σ_b is the beam surface charge density. In this case the current density is reached without drawing the maximum charge from the cathode. In the case where $\alpha_{SC} \sim 1$, the maximum charge is extracted, and the scaling is [37]

$$|J| \sim 2\epsilon_0 \sqrt{\frac{2e}{m_e R}} E_0^{3/2}. \tag{1.22}$$

1.3.3 Examples of Photoinjectors

The first rf photoinjector was designed and operated at LANL, and consisted of a single cathode cell at L-Band. This led quickly to development of a 1.5 cell S-band rf photoinjector for the ATF at BNL [38]. RF power was brought into the gun by a side-coupling scheme through the walls of both cells. Next, was the development of the BNL/SLAC/UCLA S-band photoinjector [39, 40]. In this design, the side-coupling from the rf source was only to the full-cell, with the cathode cell coupled to the full cell. This design is the basis for many photoinjectors [41–45], one of which, the LCLS gun, is shown in Figure 1.9. The coupling port was changed to the full cell alone to reduce peak pulsed heating, and the cathode cell was lengthened to make a 1.6 cell gun [46]. The LCLS is near state-of the-art and I will include the gun parameters for future reference in Table 1.1.

There are other photoinjector designs that do not use the BNL/UCLA/SLAC model. Such as a 1.5 cell with both L-band and S-band versions is operated at DESY with an alternative coupling scheme. The rf fields are coupled in along the axis via a coaxial feed, with a "door-knob mode converter to connect the coaxial line to a rectangular waveguide [47]. An outlier in frequency range is a 144 MHz single cell rf operated at the CEA [48]. Then

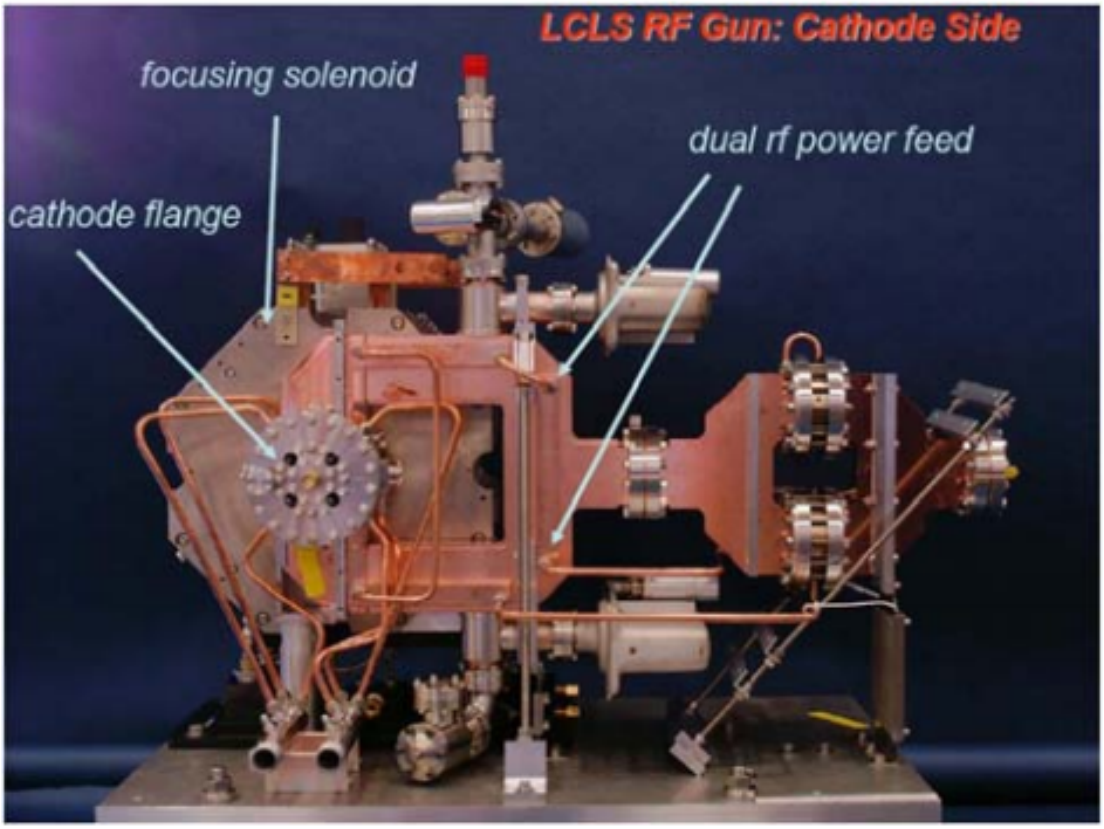

Figure 1.9: View of the LCLS gun from the cathode side [46]

Emittance (mm-mrad)	0.4-0.6
Bunch Charge (pC)	20-250
Bunch Length (mm)	0.25-0.65
Laser Spot Radius (mm)	0.3-0.9
Repetition Rate (Hz)	120
Pk. Surf. Elec. Fld. (MV/m)	120
Elec. Fld. at Launch (MV/m)	60

Table 1.1: Parameters for the LCLS photoinjector [46]

there are two notable guns that are significantly longer. First, the LANL/High-Brightness Accelerator FEL 5.5 cell L-band gun, where each cell is directly coupled to; the gun was successfully used for the regenerative amplifier FEL [49]. The other is a high-gradient X-band 5.6 cell gun at SLAC [50].

All the previous guns mentioned operate with low duty factors, with repetition rates on the order of 100 Hz. There are other cases where high duty factors are useful. The first was the 433 MHz Boeing/LANL 1.5 cell gun, with each cell powered independently [51]. The photoinjector achieved 25% duty factor, with 8.3 ms rf pulses at 30 Hz. The LANL/Advanced Energy Systems rf gun is a CW 700 MHz gun with 2.5 cells and a dummy cell added for extra vacuum pumping capabilities [52]. The gun that has been developed for LCLS-II is the Advanced Photoinjector Experiment very high frequency 1-cell gun that will deliver electron beams with up to a 1 MHz repetition rate with comparable emittances to the LCLS-I gun [53]. The gun is designed with larger surface area for better thermal management, and coupling is accomplished through inductive loops, rather than the typical ports of other electron guns.

1.4 Applications of Normal Conducting High-Gradient RF Technology

The original push for high gradient rf accelerating technology was for linear particle colliders used for high energy physics. In the present, this application for high gradient accelerators is still very important and accelerating gradient is one of the major factors that drives the cost of a full linear collider facility.

Normal conducting high gradient structures were planned to be used for the NLC/GLC, a 500 GeV center of mass electron positron collider on a 32 km footprint [54]. NLC/GLC would have used 11.424 GHz TW linacs to accelerate electron and positron beams to the desired energy. Later, NLC/GLC was absorbed into the ILC collaboration, which will instead operate with superconducting linacs, targeting a similar center of mass energy as a collider.

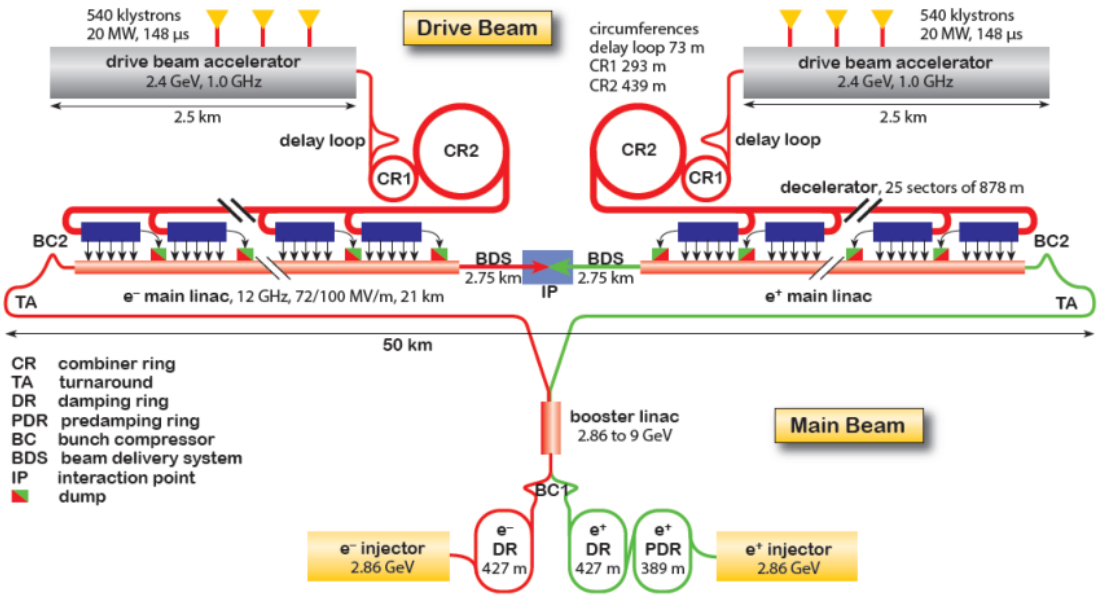

Figure 1.10: Schematic layout of CLIC. The drive beam delivers the rf power for the main linac. Image from [20].

The current proposal for a normal conducting linear collider is the Compact Linear Collider (CLIC) at CERN. Originally, the proposal called for 30 GHz structures, but has since been altered to 12 GHz TW linacs. The target initial center of mass energy is 380 GeV with possibility of upgrades all the way to 3 GeV. The initial energy stage is above the energy threshold for top pair production, and would serve as a precise top and Higgs boson measurement facility. The CLIC linac will be not be powered by traditional rf sources, but instead by a second linac. The second linac will accelerate a much higher charge beam, and then extract rf power to accelerate the main beam [55]. The total length of CLIC will be up to 48 km. A schematic is shown in Figure 1.10.

Accelerators are also used in many other applications such as inverse Compton scattering gamma ray sources [56–58], compact Free-Electron Lasers (FELs) [59, 60], compact medical linacs for electron and hadron therapy [61, 62], 4-th harmonic linearizers for FELs [63], compact cargo-scanning for security applications [64], rf deflectors [65–67], and rf undulators [68, 69].

I will describe a couple of these applications. In Compton backscattering sources, electron

beams in the 10's to 100's of MeVs are scattered off low energy photon beams. These interactions create very high energy photons in the keV to MeV range, and can be used as light sources. Linac-driven FELs generate X-rays when GeV scale electron beams travel through alternating magnetic fields, known as undulators. The so-called 4th generation light sources have enabled large step forwards in science involving multiple disciplines [70]. Many FELs have used superconducting linacs [71, 72] to teach higher duty factors. However, high gradient technology can serve to create the GeV scale beam in a more compact footprint when space is limited. In medical therapy, electron and hadron beams have shown the ability to treat cancers through radiation therapy. Electrons and hadrons deposit energy inside a body in a much more defined position than X-rays, so a similar dose to a tumor can be delivered with significantly less dosage to the surrounding tissue. These beams require beams on the order of 100s of MeVs. Linacs can create compact X-ray sources that can be used for scanning cargo, and are especially good at picking out radioactive materials [64], which have large atomic numbers.

1.4.1 Applications for Bright Beams

In 1.3.2.1 I mentioned that electron beam brightness is an important parameter for rf photoinjectors. I will demonstrate a scaling of the beam brightness with respect to the applied cathode peak surface electric field and show that higher gradients can lead to higher brightness. By combining equations 1.20 and 1.21:

$$B_e = \frac{2I}{\epsilon_x \epsilon_y} = \frac{2I}{\epsilon_n^2} = \frac{2J_{max} m_e c^2}{k_B T_c}, \tag{1.23}$$

where T_c is the effective cathode temperature, and $k_B T_c$ is the mean transverse energy of the electron beam directly after emission. If we substitute in the scaling of current density for pancake beams with $\alpha_{SC} < 1$, then

$$B_e \sim \frac{2ec\epsilon_0 (E_0 \sin\phi_{rf})^2}{k_B T_c}, \tag{1.24}$$

where ϕ_{rf} is the phase that the electron beam is created relative to the rf crest. We see that the brightness of a photoinjector scales with the square of the applied cathode electric field.

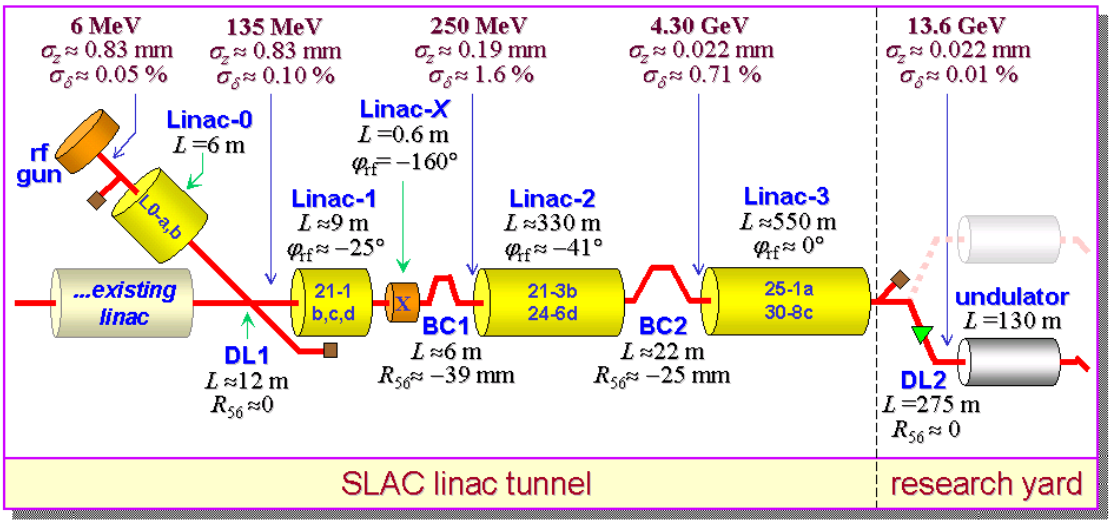

Figure 1.11: Schematic of LCLS. BC stands for bunch compressor. [75]

An application for high brightness electron sources is to FELs. The efficiency of the FEL process is significantly reduced when the emittance of the electron beam is greater than the emittance of the lasing photon beam, where the emittance of a photon beam is $\lambda_\gamma/4\pi$ [73]. Also, brightness of the electron beam determines the minimum wavelengths of the X-ray laser produced in the FEL process. Finally, the efficiency of the FEL, the transfer of energy from the electron beam to the laser, and the gain length, the length of undulator required for an e-fold increase in laser power, are dependent on $B_e^{1/3}$ and $B_e^{-1/3}$ respectively [35, 74]. The decreased gain length reduces cost and size, which can enable University-scale FELs increasing accessibility, or allow other uses for the freed space in current km-long XFELs [72, 75–79], such as LCLS, of which the beamline is shown in Figure 1.11.

Other applications for high brightness electron sources are wakefield accelerators and ultra-fast electron diffraction (UED) experiments. In dielectric beam-driven wakefield experiments [80–82], large currents are required to fit through small apertures to generate large wakefields. In UED, small emittance is required to reach higher resolutions, and more charge per shot allows for better image differentiation [83, 84].

I will outline the plan for an ultra-high gradient high brightness rf photoinjector in 5, also referenced in [24, 35].

CHAPTER 2

Physics of RF Breakdowns

There are a few phenomena in accelerating structures that limit HG operation in normal conducting linacs: rf vacuum breakdown, rf pulsed heating, and field emission currents. Of these, the main limitation of modern accelerating structures for reaching large operating accelerating gradients is vacuum rf breakdown. In this chapter I will introduce what a vacuum rf breakdown is, review the progress that has led to state of the art HG accelerators, and explain the current theoretical understanding behind the cause of rf breakdowns.

2.1 Field Emission Currents

Accelerating structures operating with large surface electric fields generate electron currents even when there are no beams present. These currents come from conduction electrons in the metal being promoted to freely propagating states by the large surface electric fields. The process is governed by quantum mechanical tunneling through the potential barrier that separates the electrons in the metal from the free propagating state in the vacuum. Field emission is both an important diagnostic and issue to overcome for normal operation of high gradient accelerators as well as an important component of the rf breakdown process.

These following steps are adapted from [85], which originally adapted the Fowler-Nordheim equation specifically to rf cavities. To find an equation to predict field emitted current, also known as dark current, I will first assume that the metal is described by a semi-infinite plane for $x \leq 0$. The potential barrier between the binding potential, V_m in the metal and the

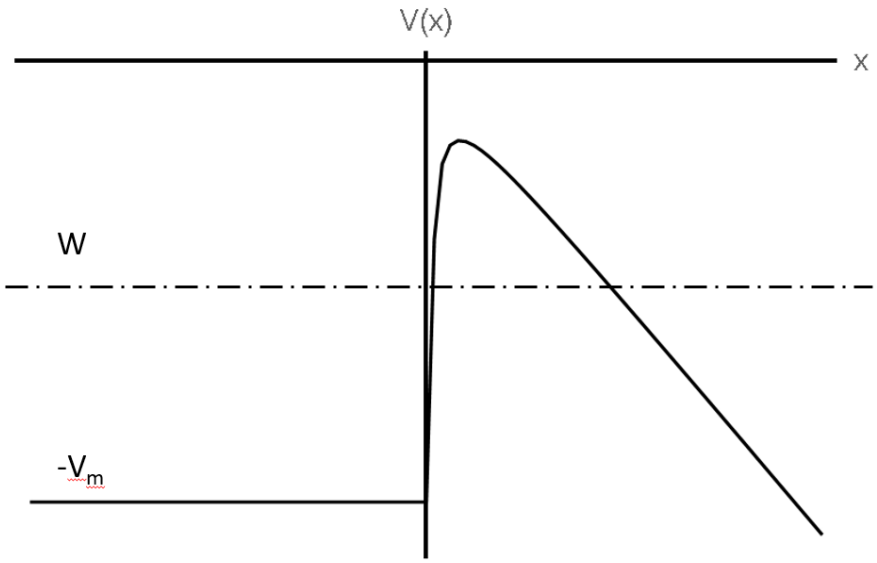

Figure 2.1: The potential barrier of an electron in a metal exposed to large electric field. Electrons quantum tunnel through the barrier into the vacuum.

vacuum in the presence of an electric field E_s is described by:

$$V(x) = \begin{cases} -V_m & x \leq 0 \\ -eE_s x - \frac{e^2}{16\pi\epsilon_0 x} & x > 0. \end{cases} \tag{2.1}$$

The first term for $x > 0$ is the effect of the applied electric field, and the second term is the classical screening energy of a perfectly conducting semi-infinite plane. This potential barrier is shown in Figure 2.1.

For this specific potential energy, the Schrödinger equation cannot be solved directly. Instead, a semi-classical WKB approximation is applied to find the probability of quantum tunneling for a given electron energy. The electrons in the metal are assumed to behave according to Fermi-Dirac statistics. Then the number of electrons in a given volume V_e, with specified momentum p, and energy W is:

$$dn = \frac{2V_e}{h^3} \frac{dp_x dp_y dp_z}{\exp \frac{W-\zeta}{k_B T} + 1}. \tag{2.2}$$

The flux of electrons incident on the metal surface from $x < 0$ can be found by integrating dn over p_y, and p_z. Finally, to find current density we integrate the escape probability for a

given energy over the flux of electrons for those energies. The result is:

$$J_{FN} = \frac{1.54 \times 10^{-6} \times 10^{-4.52\phi^{0.5}} E_s^2}{\phi} \exp\left[\frac{-6.53 \times 10^9 \phi^{1.5}}{E_s}\right], \tag{2.3}$$

where the following simplifications have been applied, the operating temperature is not close to the Fermi temperature of copper, and that the binding potential energy is larger than the electric field modification $V_m > \sqrt{e^3 E_s / 4\pi\epsilon_0}$.

Equation 2.3 applies only for applied DC electric fields. To find the current instead for an rf electric field, the current density is averaged over a single period, where the resulting form is:

$$\bar{J}_{FN} = \frac{5.7 \times 10^{-12} \times 10^{-4.52\phi^{0.5}} E_s^{2.5}}{\phi^{1.75}} \exp\left[\frac{-6.53 \times 10^9 \phi^{1.5}}{E_s}\right]. \tag{2.4}$$

The important aspect of this equation is the strong dependence of the current on surface electric field. As accelerating gradients are pushed higher with advances in engineering, then the field emitted current will become more of a factor in accelerating structures.

In experiments with real accelerating structures, the dark current is always larger than predicted by the rf Fowler-Nordheim equation. To explain this discrepancy, a field enhancement term, β_E, is added to the equation, directly multiplying the surface electric fields. β_E of a structure is found by plotting $I_{DC}/E_s^2.5$ vs $1/E_s$ on a log plot, then the slope is proportional to β. There are many proposed explanations for what could causes the field enhancement, such as: geometric imperfections in the surface, non-metallic inclusions in the surface [85], dielectric dust on the surface, or variations of the work function due to changing crystal structure [86]. The final equation for dark current from a given area of the surface, A_E, is:

$$\bar{I}_{FN} = \frac{5.7 \times 10^{-12} \times 10^{-4.52\phi^{0.5}} (\beta_E E_s)^{2.5} A_E}{\phi^{1.75}} \exp\left[\frac{-6.53 \times 10^9 \phi^{1.5}}{\beta_E E_s}\right]. \tag{2.5}$$

An example of a measurement of dark current compared to Fowler-Nordheim emission is shown in Figure 2.2.

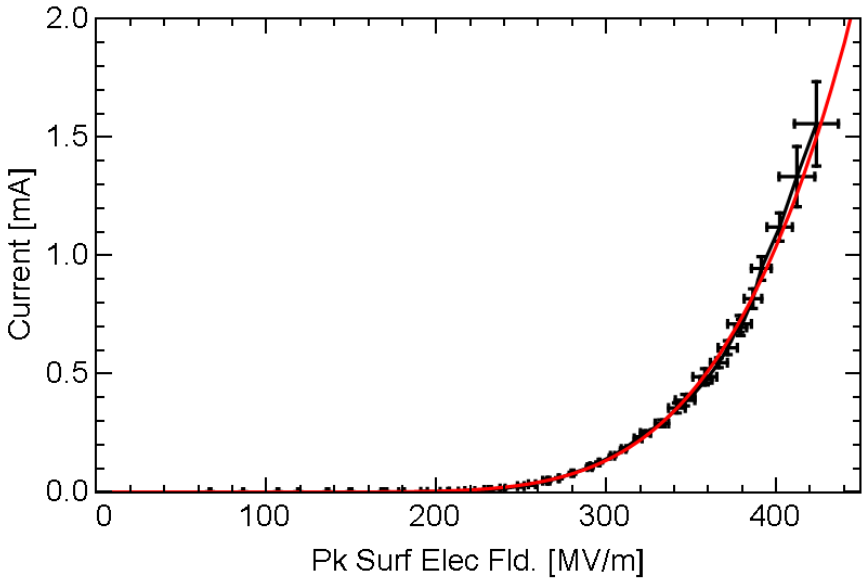

Figure 2.2: Measurement of dark current in an accelerating cavity and plot of Fowler-Nordheim emission for rf fields with $\beta = 20.6$.

2.2 Physical Description of an RF Breakdown Event

When operating an accelerating structure, the physical indicators of a vacuum rf breakdown are [87–90]:

- Elevated dark current, more than an order of magnitude larger than during normal operation,
- Increased X-ray production outside of the cavity,
- Elevated vacuum levels inside the cavity,
- Visible sparks when the interior of the accelerating structure can be seen. The spectral lines are mostly from neutral Cu atoms [87] and can last for several micro seconds,
- Mechanical vibrations in the bulk metal,
- Disrupted reflected rf signals from the structure, with much of the input rf signal is fully reflected.

Figure 2.3: Photograph of the iris of a SW accelerating structure where damage is clearly visible due to breakdowns. The breakdowns occur in large field regions on the surface of the metal. Image Courtesy of [91]

.

Post-mortem analysis of structures shows craters on the surface after being subjected to rf breakdowns, with damage visible to the eye as shown in Figure 2.3.

The current understanding of the physical mechanism that explains these consequences of breakdown is:

- A protrusion forms on the surface that enhances the surface electric field and field emission currents.
- As the protrusion emits field electrons and is exposed to the strong electric field, strong heating causes a thermal runaway that ablates the emitting tip [92].
- Neutral atoms, ions and electrons are released into the vacuum as the surface melts

and evaporates while under large electric fields, this is known as the onset phase [93].

- The high density of neutral atoms, ions, and electrons causes an avalanche ionization process, forming a plasma of ions. A quasi-neutral plasma sheath forms around the original emission site. The plasma sheath shields the space-charge forces of the emitted electrons, allowing large amounts of current to be released from the surface, on the order of 50 A from a single site [89]. Light is emitted from ion-electron recombination events. This period is known as the burning phase

- The still present electric field accelerates ions into the surface, damaging and melting the surface and releasing more ions and neutrals, continuing the process stated above. The pressure exerted by the ion bombardment is on the order of kAtms [94]. The damage caused by bombardment may create surface protrusions that will be the point of subsequent breakdowns. This final phase is known as the cratering phase.

- The bombardment of the cavity walls by electrons and ions will create X-rays through the bremsstrahlung process.

- The plasma formed inside the cavity becomes reflective to the incoming rf power.

- The plasma is extincted due to expansion cooling, causing an increase in vacuum pressure, that is subsequently removed by pumps.

This process is diagrammed in Figure 2.4

There is a difference in the breakdown process for TW and SW structures. In a SW structure, the plasma forms and the input rf signal is reflected quickly, on the order of a several ns. In TW structures, the rf signal is not fully reflected for 20-100 ns. In that time, more energy is absorbed by ion and electron beams [89, 95].

2.3 Review of High-Gradient RF Breakdown Experiments

In this section I will review the previous work on vacuum rf breakdown physics in DLW type linacs that have directly informed the experiments presented here. Special focus will

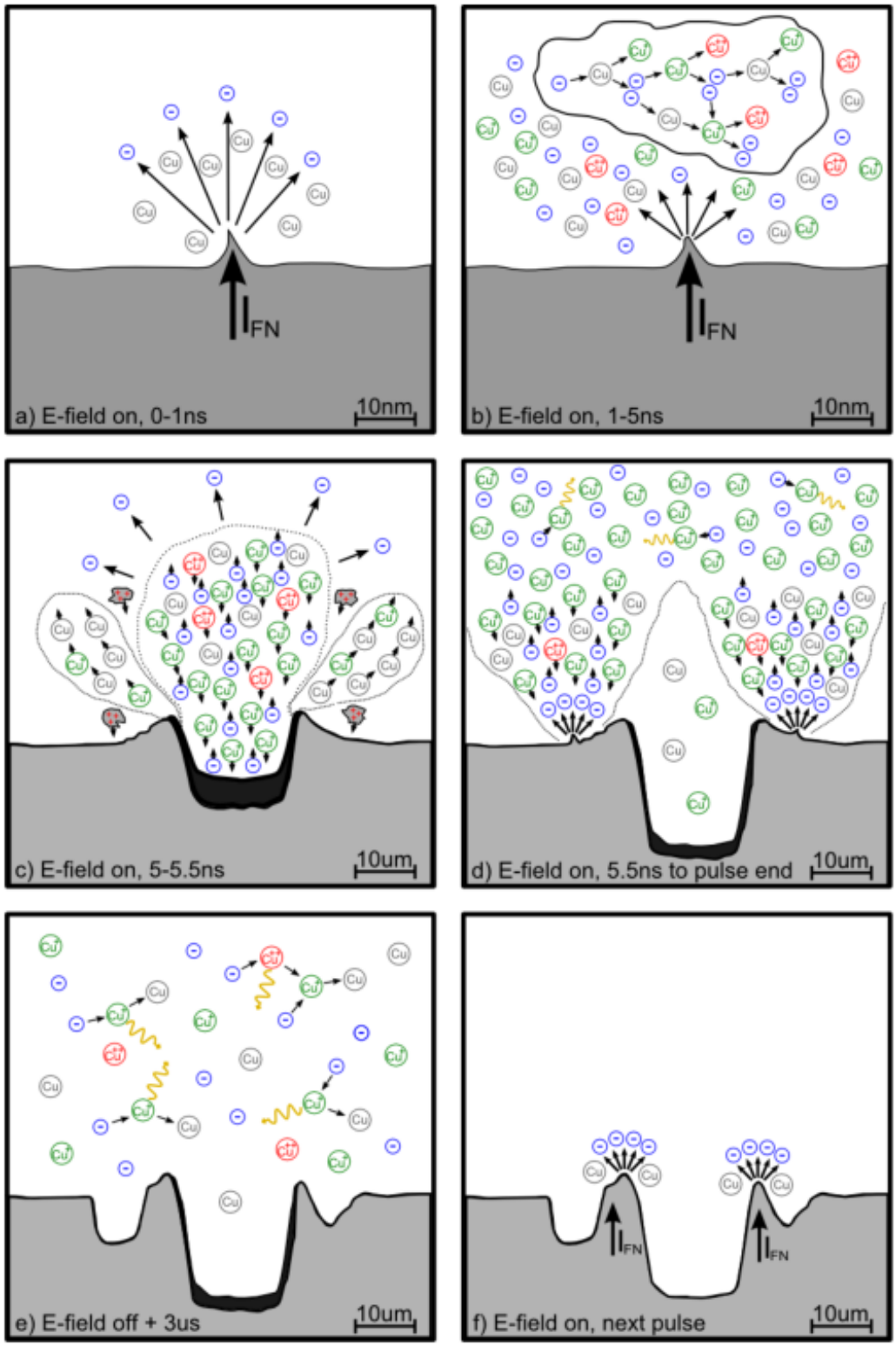

Figure 2.4: A depiction the life cycle of a vacuum rf breakdown from [93]. See text for details

be placed on the single cell SW structure program that this work is a part of.

2.3.1 Early Work on High-Gradient Systems

The Stanford Two-Mile Accelerator was the first large high energy linear accelerator, completed in 1967 [12]. The accelerating components for the beamline operate at S-band, 2.856 GHz, and are low-group velocity TW structures in the $2\pi/3$ mode. During the construction phase the highest gradient reached without obvious signs of breakdown was believed to be 46 MV/m, and the ratio of the accelerating gradient to the surface field is near 2.17 [85]. Normal operation however, is on the order of 20 MV/m accelerating gradient. Studies of SW DLW at SLAC investigated the possibilities of increasing the frequency and what effect that would have on accelerating gradients. Peak surface electric fields of 340 MV/m for 1.5 μs at S-band, 445 MV/m for 3.5 μs at C-band (5 GHz), and 572 MV/m for 3.8 μs at X-band (9.3 GHz) were reported. When the structures were examined after testing, significant damage was observed on the interior surfaces, most likely due to rf breakdowns. An empirical relation between maximum field and frequency was found to be $G \sim 195 \times f(GHz)^{1/2}$, where only the peak electric field and frequency would determine when rf breakdowns would limit operation [88]. In these experiments at SLAC, maximum achievable gradient was the specific goal of the tests, and structure damage, the physics of rf breakdown, and heavy beam loading by dark current were not fully considered.

In Novosibirsk, results were published for a single C-band structure at 5.6 GHz that reached 160 MV/m peak surface electric fields for a 2 μs pulse length [96]. In these experiments, the surface electric fields were limited by beam loading from dark current, rather than from vacuum rf breakdown. Beam loading of a structure is when input rf power to the accelerating structure is absorbed by charged particles when they are accelerated. Since the amount of dark current is so strongly dependent on the surface electric field, once enough dark current is created to absorb a significant portion of the rf power, any further power increase creates significantly more current that absorbs significantly more power. This process limits the accelerating gradient of a structure, where past that gradient all input rf power

goes to the dark current. This phenomenon is not common in accelerating structures, where rf breakdown is usually the initial barrier to increasing the accelerating gradient.

Another important discovery from these early experiments was the beginning in understanding the process of conditioning. Once a structure has been manufactured and installed into the experimental setup, the maximum gradient achievable will be relatively low. However, over a period of operational time, during which the cavity is being pulsed with rf power, the maximum sustainable gradient will increase, and the amount of field emitted current will decrease. During rf breakdowns, puffs of H, CH_4, H_2O, CO, and CO_2 gases were detected. This led to the hypothesis that rf breakdowns remove adsorbed gases and surface dielectric impurities, causing some of the increase in sustainable gradient during the processing period. Techniques were also developed to safely process accelerating structures by decreasing the input rf power upon detection of a vacuum breakdown, followed by ramp up of the rf power back to the nominal level [97]. The theory is to increase the electric field at current emitters, such as surface protrusions or included impurities, and remove them without causing unnecessary surface damage. If this process is rushed, where too many breakdowns occur in a row, the surface of the cavity can be badly damaged, reducing the maximum sustainable accelerating gradients.

2.3.2 Research in Breakdown Physics of TW structures for NLC/GLC

A collaboration formed between groups at SLAC, FNAL, CERN, and KEK to work on accelerating structures for the NLC and GLC. The final design report of the accelerator specified a target of 65 MV/m accelerating gradients with an X-band operating frequency of 11.424 GHz and a pulse length of 400 ns [54]. Most of the structures tested were TW, operating in the $2\pi/3$ mode, constant gradient, and 1.8 m in length with 206 cells. To maintain a constant gradient the group velocity decreases from 12%c to 3%c along the length of the accelerating section [98]. During the development, breakdowns were detected in the initial structures at significantly lower accelerating gradients, as low as 50 MV/m, than predicted [99, 100]. When the structures were later dismantled, damage from rf breakdowns

was obvious on the input couplers, where the rf power was introduced to the accelerating structure.

During these studies the statistical nature of rf breakdowns was also discovered. The likelihood of an rf breakdown occurring in a given structure can be characterized by a probability, the breakdown rate (BDR) [101], defined as:

$$\text{BDR} = \frac{\text{Number of breakdowns}}{\text{Number of pulses} \times \text{Length}}. \tag{2.6}$$

rf breakdowns in TW structures are not completely independent. An initial breakdown can create a chain of subsequent breakdowns in the following short time period [102]. The secondary breakdowns can occur at significantly lower field levels, as the power is decreased quickly after an initial breakdown. Initial breakdowns are independent events and follow a Poisson distribution. A structure can then be characterized by a BDR only for initial breakdowns, and a total BDR for when all breakdowns are considered. Subsequently the BDR of initial breakdowns became one of the main quantitative requirements for characterizing the high gradient performance of linacs. For example, the NLC/GLC design goal for breakdown rate was set to 10^{-1} probability of a breakdown per hour in the entire accelerator for the target accelerating gradient of 65 MV/m.

To investigate the very large BDRs in the initial structures, a set of experiments was devised to test the dependence of rf breakdowns on the length and group velocity of the TW structures. First, two structures were tested with different lengths, but the same v_g profile, one was 20 cm long and the other 105 cm, where the initial 20 cm was identical to the shorter design. After processing, the two structures were found to have the same BDR [98]. Two other structures were then designed with differing v_g, one with a 5%c-3.3%c profile, the other with 3.3%c-1.6%c. The lower v_g structure processed to a gradient of 86 MV/m for a low BDR, and the larger v_g structure processed to 80 MV/m for a similar BDR. From the limited data available the collaboration proceeded to create structures with lower v_g and focus was shifted to higher order mode damping to limit short-range wakefields [103]. Evidence from these tests and further experiment at CERN supported the theory that lower v_g, and thus lower power flow, leads to lower BDRs [104]

In these structures the distribution of the breakdowns heavily weighted towards the input coupler. The design of the coupler at that time had very sharp edges, which enhance the electromagnetic fields creating points for rf breakdowns [101]. Development of smoothed out edges on the couplers, decreasing the surface magnetic field, as well as novel forms of coupling, such as the mode launcher [105], reduced rf breakdowns near the coupler in new structures [103].

BDR was shown to be dependent on both the accelerating gradient (G), and the rf pulse length (t_p), where the gradient for a constant breakdown rate was shown to be proportional to $t_p^{-1/6}$, and the BDR increased by a decade when the gradient was increased by 7 MV/m [106]. This result is similar to findings from CLIC researchers on their development of TW structures, which showed that the breakdown rate (BDR) is proportional to BDR [86]

$$\frac{BDR}{G^{30}t_p^5} = \text{constant}. \tag{2.7}$$

These scalings are true for TW structures only.

Finally, during the development of the NLC/GLC accelerating structures faster conditioning recipes were developed. Structures are initially exposed to very short rf pulses as the input rf power is gradually increased while keeping the rate of breakdowns constant as the structure conditions. When the rf breakdown rate does not decrease further at the rf power level, the rf pulse length is increased while the rf power is decreased to still maintain the constant breakdown rate. This process is continued until the breakdown rate no longer decreases with more pulses. This process was safer, causing less surface damage and allowing higher gradients than previous methods [106]. Most accelerating structures showed nearly steady breakdown rates after $10^5 - 10^7$ pulses [107].

2.3.3 State of the Art High-Gradient TW Structures for CLIC

The target for high gradient changed to the X-band CLIC parameters with 100 MV/m loaded gradient, 12 GHz, and a breakdown rate less than 4×10^{-7}/pulse/m of structure [20]. Early in the development of CLIC a review of previous experiments was conducted to attempt to determine parameters that scale with the BDR of accelerating structures [108]. A new phys-

ical quantity was found to correlate to the BDR across different structures. This quantity, known as the modified Poynting vector and is defined as:

$$S_c = \mathrm{Re}\left[\bar{S}\right] + g_c \cdot \mathrm{Im}\left[\bar{S}\right], \tag{2.8}$$

where $g_c = 1/6$ and $\bar{S} = 1/2|\vec{E} \times \vec{H}|$ is the time averaged Poynting vector. The Modified Poynting vector then becomes a powerful tool to reasonably predict the BDR of structures before they are constructed. Minimizing S_c and advances in fabrication methods [109, 110] has led to the establishment of structures that can operate with accelerating gradients up to 100 MV/m for structures with wakefield damping and up to 120 MV/m for undamped structures [86, 111]. A picture of a CLIC structure is shown in Figure 2.5 and the BDR of constructed CLIC test linacs is shown in Figure 2.6.

As these structures are designed to eventually accelerate beams of electrons, experiments were devised to determine whether the presence of an electron beam will influence the BDR. When the electron beam travels through an accelerating structure, energy is exchanged between the beam and the structure. Depending on the phase, energy can be absorbed by the beam or the beam can pass energy to the accelerating structure. The energy gained or lost by the accelerating structure will increase or decrease the accelerating gradient. The results of the experiment showed that beam loading, where the gradient is decreased, or anti-beam loading, where the gradient is increased, will affect the BDR in the accelerating structure. However, the change in the BDR is consistent with the change if the gradient was changed by differing input rf powers [112], therefore, the presence of a beam does not affect BDR outside of power exchange.

A later review of the conditioning process for structures at CERN showed that multiple structures conditioned at the same rate and to the same scaled gradients when considering the number of rf pulses applied, but not when compared versus the number of breakdowns that occurred [113]. These results imply that the rf pulse conditioning, rather than the effect of rf breakdowns, are processing the structure.

A study was performed on the statistics of rf breakdowns. There are two types of breakdowns, as alluded to before, initial breakdowns and secondary breakdowns [98]. The sec-

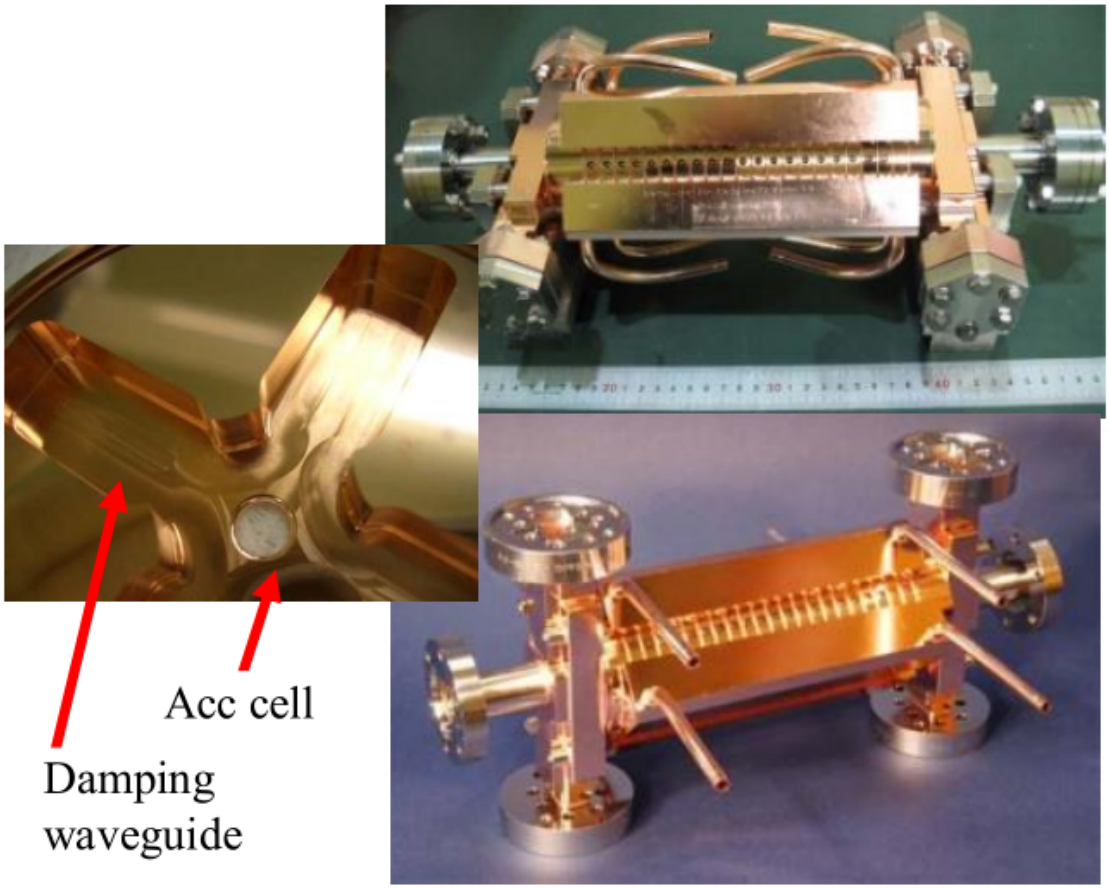

Figure 2.5: Photo of constructed CLIC TW linacs with wakefield damping. A full structure is constructed by combining many of the individual cells depicted on the left. The damping works by letting higher frequency rf power into the waveguides shown, while confining the desired accelerating mode. Image from [110]

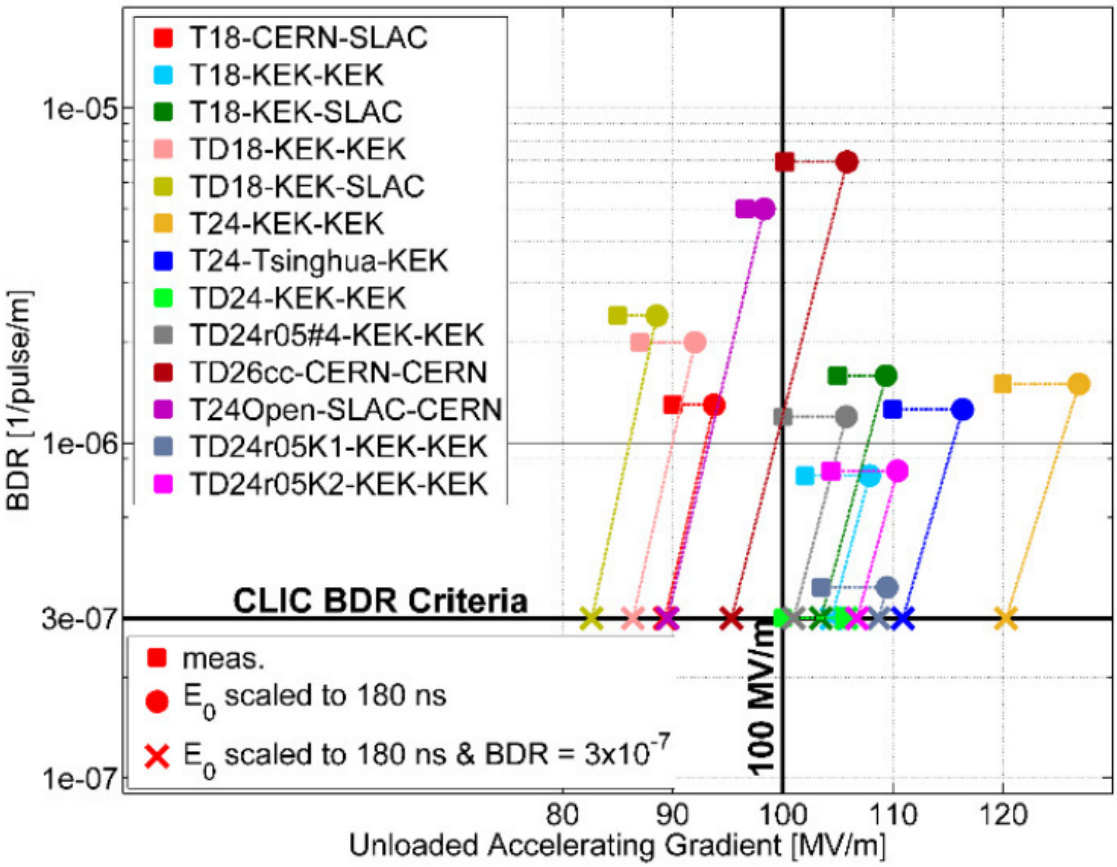

Figure 2.6: BDR for multiple tested CLIC structures. Image from [111]

ondary breakdowns occur in a chain that appears to be caused by the initial breakdown and occur within a short period of time after the initial breakdown, on the order of 30 seconds for 50 Hz operation. Also, pairs of breakdowns that are close temporally are also close spatially [114], further bolstering the evidence of a relationship between initial and secondary breakdowns. The distribution of breakdowns in time can be analyzed by a double Poisson distribution, where the probability density function (PDF) of number of pulses between breakdowns is defined as:

$$A\exp(-Cn) + B\exp(-Dn), \tag{2.9}$$

where C describes the initial breakdowns and the long-term part of the distribution and D describes secondary breakdowns that occur quickly after the previous breakdown. Typically for TW structures D is larger than C by about an order of magnitude. This study shows the existence of chains of breakdowns that appear to be caused by initial breakdowns [114]. This study was performed on TW structures so far, and in SW structures the number of secondary breakdowns is small, and the breakdowns essentially follow a single Poisson distribution [115].

2.3.4 Studies of RF Pulsed Heating

An important aspect of high gradient operation is the pulsed heating due to the magnetic field creating currents and then ohmic losses in the cavity walls. The temperature rises that are created cause thermal stress. Thus, the peak temperature always must be limited to avoid exceeding the yield strength and causing cracking damage inside the cavity[116]. I will cover a short overview of the theory and describe some experiments looking at the effects of pulse heating.

In our case we will assume that heat conduction and elasticity are uncoupled effects. This may not be true, particularly in high gradient situations where the peak temperature rise is near the operating temperatures, such as cryogenic accelerators. However, considering heat conduction separately will be adequate for our uses in this discussion.

I will consider a semi-infinite plane of a conductor with finite conductivity, subject to a

rf electromagnetic field. Then the power, P_{cav}, dissipated per unit area,A, on the surface is:

$$\frac{dP_{cav}}{dA} = \frac{1}{2}R_s(T)|H_{||}|^2, \tag{2.10}$$

where R_s is the rf surface resistance as described in A.2, and $H_{||}$ is the magnetic field parallel to the cavity surface. From A.2, the field decays exponentially into the bulk of the conductor. To find the distribution of temperature in x-direction and time, I include equation 2.10 with the heat equation, which gives:

$$\frac{\partial^2 T(x,t)}{\partial x^2} + \frac{R_s(T)|H_{||}|^2}{k_c(T)\delta(T)}e^{-2x/\delta(T)} = \frac{1}{\alpha_d(T)}\frac{\partial T(x,t)}{\partial t}, \tag{2.11}$$

where k_c is the thermal conductivity, δ is the rf skin depth that depends on the rf surface resistance, and α_d is the thermal diffusivity. The initial conditions are $T(x,0) = T_0$ and $\partial T(0,0)/\partial z = 0$. In the case of cryogenic accelerators, the thermal conductivity, thermal diffusivity, and rf surface resistance all vary quickly with temperature, and this equation cannot be solved analytically. However, to get a rough approximation, I will assume the physical properties are constant. I then can find the special case of the temperature rise on the surface for a square pulse of power dissipation with pulse length t_p. Following [116], by applying a Green's function for a semi-infinite slab and assuming the skin depth is significantly shorter than the diffusion length I find:

$$T(0,t) = T_0 + \frac{R_s|H_{||}|^2\sqrt{t_p}}{\rho c_{\mathcal{E}}\sqrt{\pi\alpha_d}} \tag{2.12}$$

The conclusion to take from this result is that the peak surface rf pulsed heating $\Delta T = (T(0,t) - T_0) \propto R_s|H_{||}|^2\sqrt{t_p}$.

Two experiments at SLAC were designed to test pulsed heating damage on metal disk samples. the first experiment, using a pillbox-like cavity, showed that cracking can occur in Cu structures when exposed to millions of pulses at pulsed heating temperatures above 80 K, showing that pulsed heating can be a significant problem for pulsed high gradient structures [117]. The second experiment used a cavity that was designed such that sample disks were not exposed to any surface electric fields, but had enhanced surface magnetic fields, where the structures were tested with maximum temperature rises of 110 K. The

results were that harder materials, such as non-annealed CuAg, CuCr, and CuZr, exhibited significantly less damage than annealed copper samples, and also damage was apparent when the temperature of peak pulse heating reached greater than 50 K [118]. In addition, a single crystal sample that exposed to pulsed heating was then tested for hardness. The result showed that the hardness increased in places where the pulsed heating was higher.

In another study, reported in [119], copper samples were prepared with the same heat treatment process as for accelerating structures, and then mechanically stressed for the same number of pulses as used for conditioning of accelerating structures. Comparison of the copper samples and autopsy of accelerating structures showed similar damage and mechanical hardening on the surface.

2.3.5 Review of SW Single-Cell Breakdown Physics Program at SLAC

A separate track of studies that focus on SW cavities to investigate the physics of rf breakdowns started as a collaboration between SLAC, KEK, and INFN [120]. This series of experiments seek to investigate the dependence of rf breakdowns on the geometry and materials of the accelerating cavities, ,which requires the construction of many expensive accelerating structures. To decrease the cost, a smaller single-cell design was chosen with a modular reusable TM_{01} mode launcher as the coupler [105]. The single-cell design is SW structure in the π mode with three cells, however the rf fields are twice as large in the middle cell. A rendering of an example single cell accelerating structure is shown in Figure 2.7. Because of the difference in electric field, nearly all of the rf breakdowns will occur in the central cell. The two outer cells are included so that the fields in the center cell mimic the field shape of a multi-cell linac [90, 123]. This experimental design has allowed for the testing of over 50 structures to date.

An early important study progressed with three geometries, each with varying iris radii. The varying size of the radii changes the ratio of the accelerating gradient to the maximum surface magnetic field and the shunt impedance. The results of the experiment showed that the rf breakdown rates for the three structures correlated with the peak surface magnetic

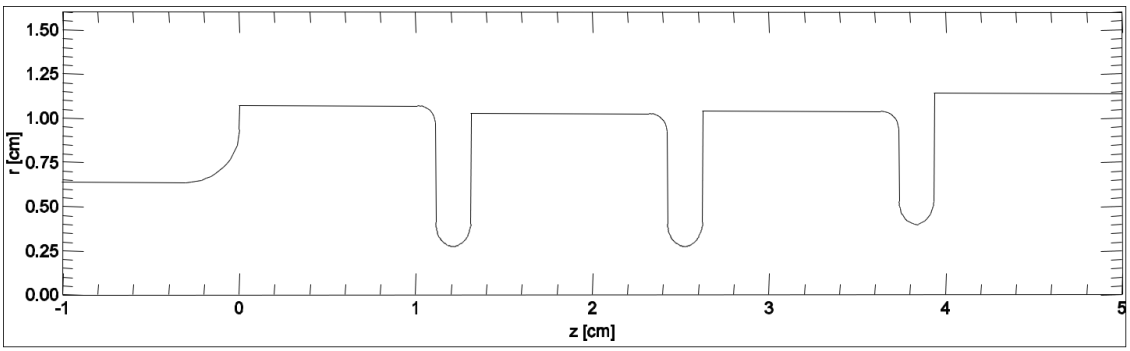

(a)

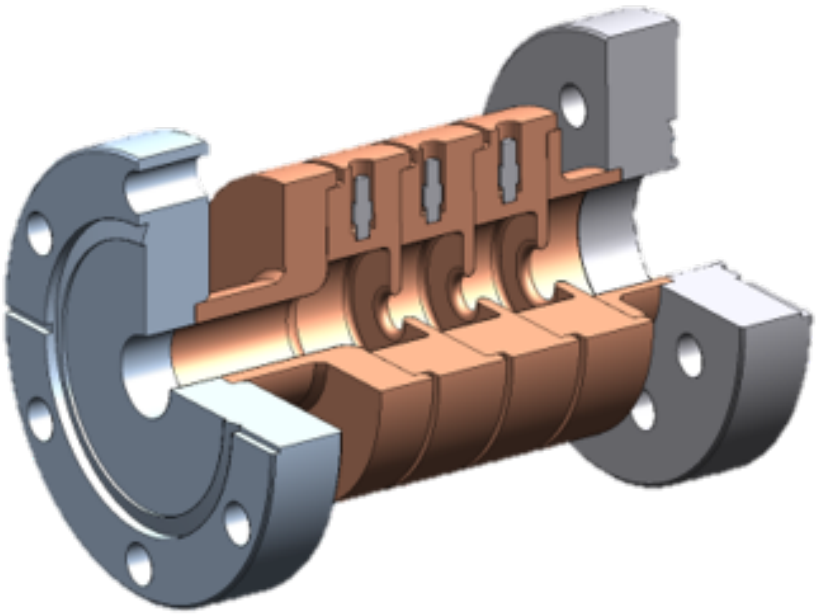

(b)

Figure 2.7: (a) Geometry of an example single cell accelerating cavity with cylindrical symmetry (b) A Solid Edge [121] 3D rendering of the same structure. Image courtesy [122]

field rather than the peak surface electric field when the rf pulse length was the same for all three geometries. Further investigation of one of the structures by varying the rf pulse length showed the correlation is specifically with the peak pulsed heating rather than the peak surface magnetic field in general [123]. These results are shown in Figure 2.8. A later review of the same data showed that the dependence of the BDR on pulse length is stronger than would be expected for a pulse heating dependence, however the difference is not significant [124]. In these same results it was discovered that $BDR \propto G^{46}$ in SW structures.

When the iris radii of single-cell structures are varied, the ratio of the modified Poynting vector and the peak pulsed heating stays relatively constant. To investigate the effect of the modified Poynting vector on rf breakdown rates, three single-cell geometries were designed so that they had varying ratios between the peak pulsed heating and the Poynting vector: one geometry that had the middle radius of the previous set of experiments, one geometry that was side coupled instead of on-axis coupled, and a different geometry was included that had been designed with rounded cells to reduce the peak pulsed heating [107, 125]. The side-coupled structure has an elevated breakdown rate compared to an on-axis coupled structure. However, in the results of this experiment the BDR of the three geometries correlates together with the modified Poynting vector than with the peak pulse heating [107] as evidenced in Figure 2.9. Also, when the structures were disassembled most of the locations of breakdown damage appeared to be located in areas of large Poynting vector, rather than areas of large peak surface magnetic field.

Another important result of single-cell structure tests was reproducibility. Identical structures of many single cell accelerating cavities were constructed and tested, and the multiple tests have been consistent with each other. In addition, results would be reproducible for identical structures created by different laboratories. Therefore, breakdown performance can be interpolated to new structures, and these results imply that structure geometry and material properties are the main input parameters when trying to predict breakdown performance [115].

Experiments were conducted testing copper alloys such as CuCr, CuZr, and CuAg as

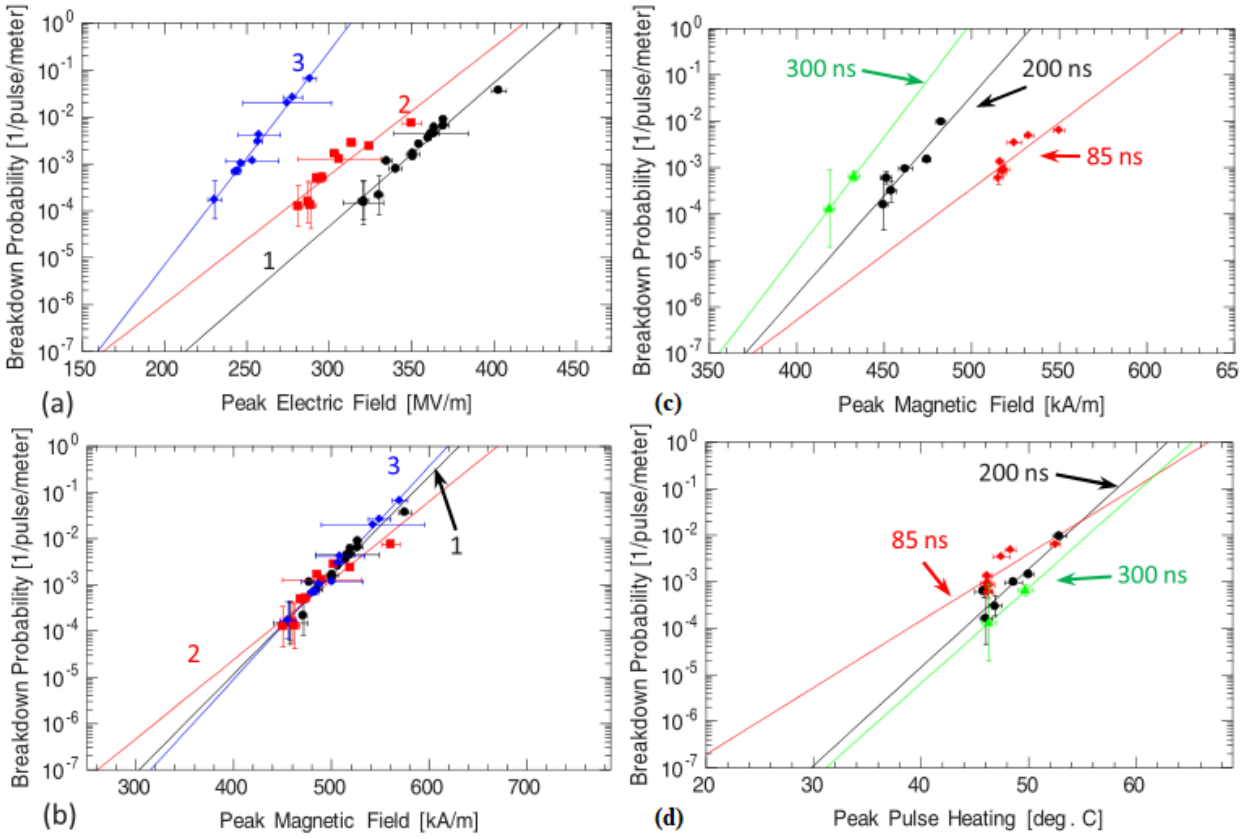

Figure 2.8: (a) BDR vs peak surface electric field and (b) BDR vs peak magnetic field for three structures with varying iris radii, which changes the shunt impedance of the structure, structures 1, 2, and 3 have increasing iris radii, and decreasing shunt impedance. (c) BDR vs peak surface magnetic field and (d) BDR vs peak rf pulsed heating for three different rf pulse lengths in the same accelerating structure. The BDR appears to correlate the strongest with the rf peak pulsed heating for all cases [123].

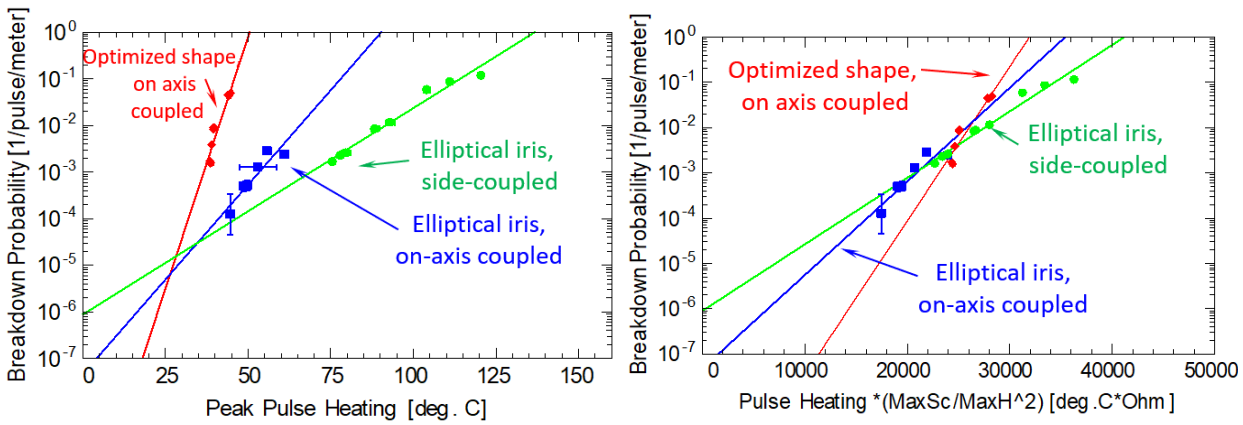

(a) (b)

Figure 2.9: BDR vs (a) peak pulsed heating and (b) modified Poynting vector. The BDR of three structures correlates better to Modified Poynting vector than to peak pulsed heating [107].

these alloys are harder than Cu, and the pulsed heating experiments showed less damage in these materials. All of these alloys showed similar performance to a similar Cu structure [115, 126]. Another structure was tested instead with a coating of TiN, which has been shown to decrease secondary electron emission [127]. This structure had lower gradient than soft Cu for a similar BDR [128].

The next step that was taken was to explore manufacturing single-cell cavities from harder materials. When a copper cavity is brazed, the metal is softened by the heat treatment. So, to avoid brazing, a special vacuum container was developed, in which the structures would be assembled by the cells being clamped together. Many materials have been tested with the clamped method: hard Cu, ultra-hard Cu, hard CuCr, hard CuZr, and hard CuAg. The hard qualifier means that the structure did not go through a heat treatment during manufacturing that would soften the material. The ultra-hard Cu was created by equal-channel angular extrusion pre-machining [129]. The results of this experiment showed that hard Cu and ultra-hard copper cavities performed similarly with up to 175 MV/m for BDR near 10^{-4} breakdown/pulse/m, but both were larger than the soft-Cu cavity that reached 150 MV/m, with similar breakdown rates [130]. Hard CuCr and CuCr performed worse

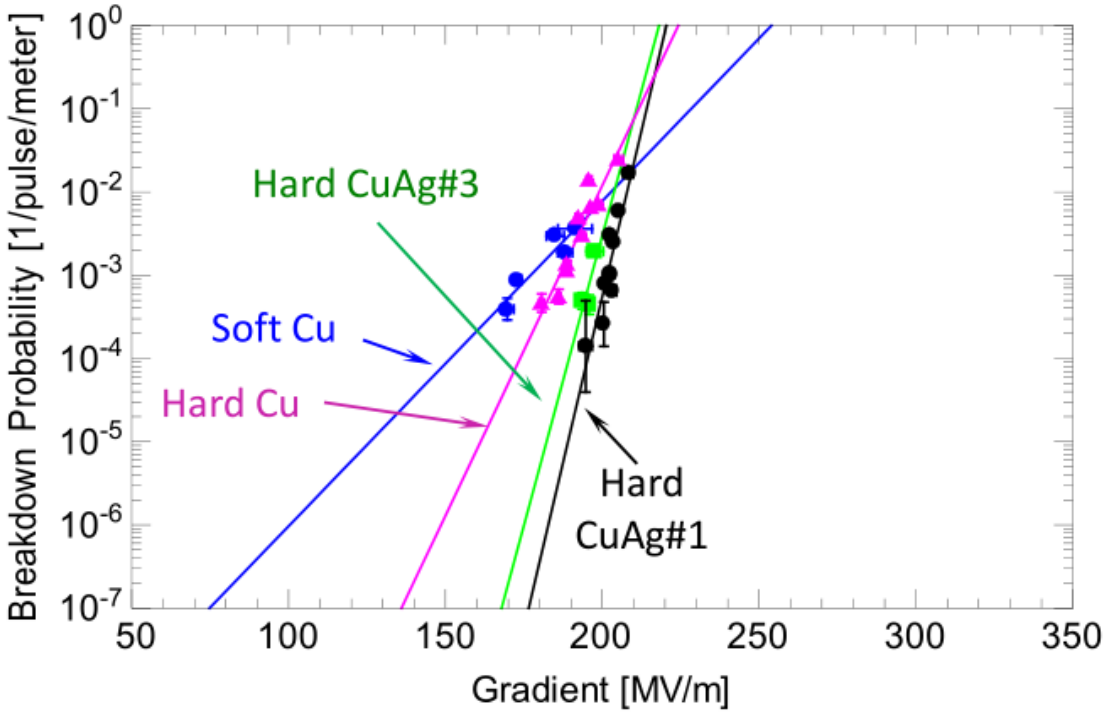

Figure 2.10: Summary of BDRs for hard Cu, hard Cu, and hard CuAg. Hard CuAg exhibits the largest gradients of all previously tested single cell accelerating structures for a constant BDR [91].

than soft Cu, with higher BDRs for similar gradients. It was hypothesized that material precipitated on the surface, creating favorable locations for rf breakdowns [126]. Of all the tested materials, the hard CuAg performs the best, with 200 MV/m accelerating gradients at similar breakdown rates to the 175 MV/m for hard Cu and 150 MV/m for soft Cu [91]. A summary of the performance in hard Cu and hard CuAg is compared to soft Cu is in Figure 2.10.

Another avenue for structure hardening that was pursued was to create clad structures, in which regions of high peak pulse heating and mechanical stress are made of harder materials such as stainless steel (SUS) and Mo, while the rest of the structure is Cu, as described in [131]. These structures are clamped together rather than brazed, which can cause stress at the bi-metal joints. Both tested clad structures performed worse than soft Cu. The hypothesis for the degraded performance is that the thermal cycling from the rf pulsed heating

cause stress at the bi-metal joints, decreasing quality and again increasing the BDR [132].

With the success of the hard Cu and hard CuAg experiments, further structures were developed to leverage the apparent advantage of harder materials. Alternative cell-joining technologies were developed and tested that allow assembly of practical accelerating structures without heat treatment, namely electroforming and electroplating [133, 134]. Both of these techniques with Cu have shown similar results to soft Cu so far; with problems remaining in the manufacturing process. Other alternative manufacturing schemes are forming structures from milled halves [135] or quadrants [136] that can then be welded, avoiding heat treatment. These structures also have shown gradients up to 125 MV/m compared to 150 MV/m in soft Cu for similar BDRs, and again require more development of the manufacturing techniques.

Finally, an alternative geometry was designed to test the dependence of BDR on magnetic fields, a dual-mode cavity was designed with independent electric and magnetic field control and fed by two klystrons[137]. The BDR was shown to strongly correlate with the strength of the magnetic field as the electric field was held constant [91].

2.4 Theoretical Developments in the Understanding of RF Breakdowns

A current theory is that vacuum rf breakdowns are caused by movements of crystal defects induced by periodic mechanical stress [138]. The model posits that dislocations form in the metal at locations of crystallographic defects and voids in the presence of large surface electric fields, E_s. The movement of these locations dislocations can lead to the necessary mass transport to cause protrusions on the copper surface of the cavity. Once a protrusion forms, field enhancement on the tip will create field emission and a thermal runaway that cause the tip to ablate into the vacuum, creating the plasma to cause a breakdown. The stress that causes the defect movement may be caused by pulsed surface heating, large electric fields on the metal surface, or other reasons. This theory predicts the empirical scaling of breakdown rate with respect to gradient, for room temperature structures with breakdown

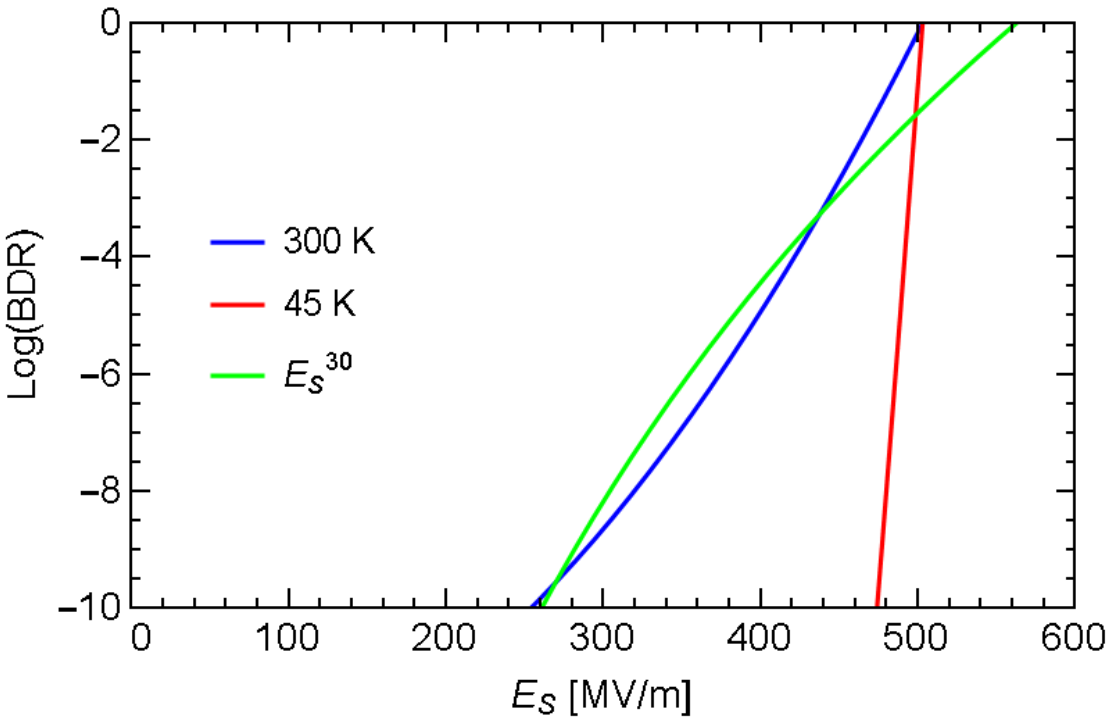

Figure 2.11: Dependence of BDR on the surface electric field E_S in the defect-stress model [138]. A BDR of 1 is if the structure breaks down every pulse. The empirical E_S^{30} scaling is also included for reference. The dependence of BDR on E_S becomes significantly steeper as the temperature is decreased.

rates on the order of $10^{-5} - 10^{-9}$/pulse/m with the following equation:

$$BDR \propto \exp\left(\frac{\epsilon_0 E_s^2 \Delta V}{k_B T}\right), \tag{2.13}$$

where k_B is the Boltzmann constant, ΔV is the relaxation volume of a defect, which depends on the material, T is the temperature, and ϵ_0 is the vacuum permittivity.

An intriguing consequence of this theory, is that the temperature dependence of the theory predicts that for low temperatures the dependence of BDR on T is larger as shown in Figure 2.11. If this consequence is true, then it may be possible to reach exceedingly large accelerating gradients with very low BDRs using cryogenic accelerators.

A DC experiment was designed to test breakdown thresholds at CERN. The system consists of a high voltage source that operates with a repetition rate of up to 1 kHz, and has a variable gap to increase the gradient applied to the metal samples. The breakdown

threshold for different materials varied strongly based on the crystal packing. This finding is consistent with the dislocation-stress model, where the packing with the lowest dislocation mobility showed tolerance for the largest surface electric fields, and high mobility metals had low thresholds [139].

Another group has shown that breakdown statistics for high gradient experiments using Cu can be described by a stochastic model of dislocation creation and depletion that depends on the applied surface electric field [140]. A vacuum breakdown event will occur when the dislocation population crosses a critical level, continuing in the process described above. If this theory is correct, it may be possible to detect precursors to a breakdown when the dislocation population has crossed across the critical level, but the vacuum breakdown has not yet occurred. The precursor may be extra field emission [141], but so far has not been detected.

CHAPTER 3

Cryogenic Normal Conducting Resonant Cavities

As was discussed in the previous chapter, decreasing dislocation mobility is currently hypothesized to decrease the BDR for a given accelerating gradient. One possible method to decrease the dislocation mobility is to decrease the operating temperature of the accelerating structure. At decreased temperatures the rf surface resistance and coefficient of thermal expansion, α_T, decrease, while the yield strength and thermal conductivity increase [142, 143]. The increase in hardness decreases the mobility of dislocations. Also, as the rf surface resistance decreases and thermal conductivity increases, the rf pulsed heating, equation 2.12, will decrease. Finally, since the thermal stress is proportional to $\alpha_T \Delta T$, then the thermal stress will decrease significantly as the coefficient of thermal expansion decreases along with the peak rf pulsed heating. The physical properties of cryogenic copper make it a very promising candidate for high gradient operation.

3.1 History of RF Cavities at Cryogenic Temperatures

Of these properties, the decrease in rf surface resistance has been studied the most with regard to resonant cavities. In cryogenic copper, the rf surface resistance is well described by the theory of anomalous skin effect (ASE) [144], which is shown in A.2. Measurements of the rf losses agree with this theory to within 10% at a range of frequencies: 1.17, 1.4, 3, 5.7, 9.3, 11.4, and 35 GHz [145–153]. These experiments used the Q_0 of resonant cavities at very low fields and sub Watt rf power to measure the rf surface resistance.

3.1.1 High Power Tests

There is little data on the sustainable electric fields of copper cavities at temperatures below 100 K with high input rf power, corresponding to surface electric fields greater than 75 MV/m. The results of an experiment at 9.3 GHz, 77 K, with 150-300 kW input peak power found surface electric fields up to 50 MV/m [151]. In another study conducted at 5.7 GHz, 20 K, showed surface fields up to 65 MV/m [147].

An experiment at 3 GHz, 77 K with surface electric fields up to 300 MV/m, however they also showed a decrease of Q_0 with increased fields [153]. In this experiment, two cavities were used with varying ratios of peak electric field to peak magnetic field. The authors report that the decrease in Q_0 is correlated with surface magnetic fields rather than the peak surface electric field. The explanation posited is the Q_0 decrease is possibly caused by multipactor discharge [154]. Multipactor is the process where electrons inside the cavity are accelerated into a wall, causing secondary electron emission.

In the experiments above, the breakdown rate was not considered. A study conducted at CERN attempted to show the relation between rf breakdown rate and decreased temperatures. Cavities with frequencies between 21 and 39 GHz showed no dependence of breakdown rates on temperature between 100 and 800 K [155].

To build on the previous results in the literature and with the end goal of specifically measuring BDR at cryogenic temperatures, a series of copper resonant cavities were devised. The first resonant cavity constructed, the TE dome cavity, was originally designed to be used in a superconducting material test bed, but has been also used to measure the low power properties of cryogenic copper. After the low temperature rf surface resistance of copper at 11.4 GHz was measured, a single cell cryogenic accelerating structure was devised, and multiple cavities were constructed. To extend the study of cryogenic breakdown physics to a lower frequency and to support the proposal of a 2.856 GHz cryogenic photoinjector 5, a S-band low power test cavity was constructed. Finally, a high power single cell S-band accelerating structure has been designed and is currently under construction. I will discuss the design and results from each of these resonant cavities in this following chapter.

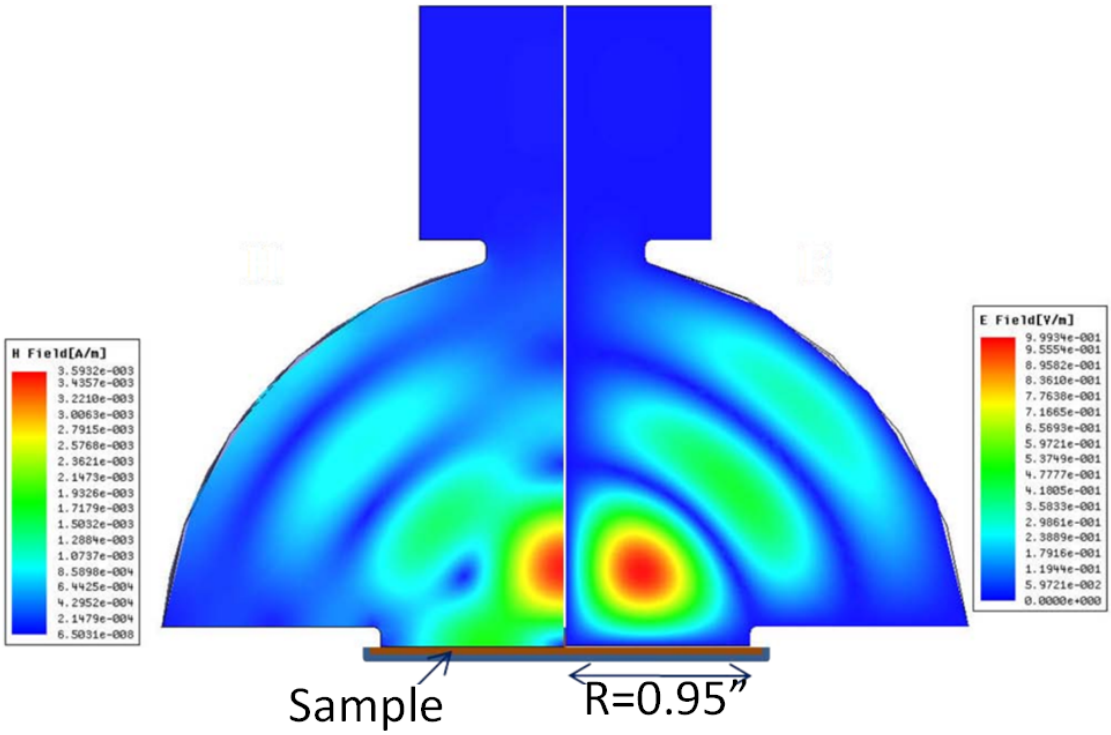

Figure 3.1: E (right half) and H (left half) field maps of the sample testing cavity. Detachable sample plate is located on the bottom of this picture [150].

3.2 TE Dome Cavity

This first cavity was originally designed to measure samples of superconducting materials. For that reason, a removable 3-in. diameter sample plate was used in the design to allow for testing of many samples. A hemispherical geometry operating in the TE_{013} mode was chosen. This specific electromagnetic mode has reduced electric field on the sample, to remove the likelihood of multipactor. This mode also avoids current flow across the gap between the sample and the rest of the cavity, which avoids issues of breakdown at these gaps. The fields and geometry of the TE dome cavity are shown in Figure 3.1. The TE dome cavity, and all subsequent structures will be assumed to be manufactured from copper with residual resistivity ratio of 400. Residual Resistivity Ratio (RRR) is the ratio of the resistivity of a copper sample at room temperature and at 4 K. RRR ranges from 40 to over 2000 for mostly pure copper samples.

The geometric factor, D_{Cav} of a resonant cavity is defined by

$$D_{\mathrm{Cav}} R_S = Q_0. \tag{3.1}$$

In this case specifically, a geometric factor can be defined each for the sample and the rest of the cavity separately. The separate geometric factors are then used to find the R_S of a sample, even when the sample and cavity are different materials. The equation describing the relations between R_s and D are:

$$Rs_{Cav} = \frac{1}{(\frac{1}{D_{Cav}} + \frac{1}{D_{Samp}})Q0_{ref}}, \tag{3.2}$$

$$Rs_{Samp} = D_{Samp}(\frac{1}{Q0_{Samp}} - \frac{Rs_{Cav}}{D_{Cav}}), \tag{3.3}$$

where $Q_{0,ref}$ is the Q_0 measured with a reference sample, with the same physical properties as the rest of the cavity, and $Q_{0,Samp}$ is the Q_0 of the cavity measured when a given sample is installed.

To maximize the effect of the sample on the cavity Q_0, the geometric factor of the sample was made larger than the geometric factor of the entire cavity: $D_{samp} = 3742, D_{Cav} = 1967$[150]. The value of the geometric factors were calculated using HFSS [156].

For measuring the Q_0 at cryogenic temperatures, the TE dome cavity was placed inside a cryostat and cooled down using a Cryomech PT415 cryorefrigerator, where the temperature could be reduced to near 3 K. The cavity was coupled to the external power source through a circular TM_{01} waveguide and a TM_{01} to TE_{01} mode converter [105]. Figure 3.2 shows the heat shield around the cavity and cryocooler before being lowered into the cryostat. A Keysight N5242A vector network analyzer (VNA) is connected directly to the mode converter and is used to measure the Q_0, Q_E, and f_0 of the resonant cavity at the given temperature. The method of deriving the properties of a cavity with a VNA is outlined in C.3.1. The Q_E of the system is near 310,000 and varies little with temperature, and f_0 is near 11.4 GHz at 4 K.

To scan Q_0 over temperature, the cavity is initially cooled to 3 K, and then heated using resistive heaters while the VNA records data every 0.1 K change.

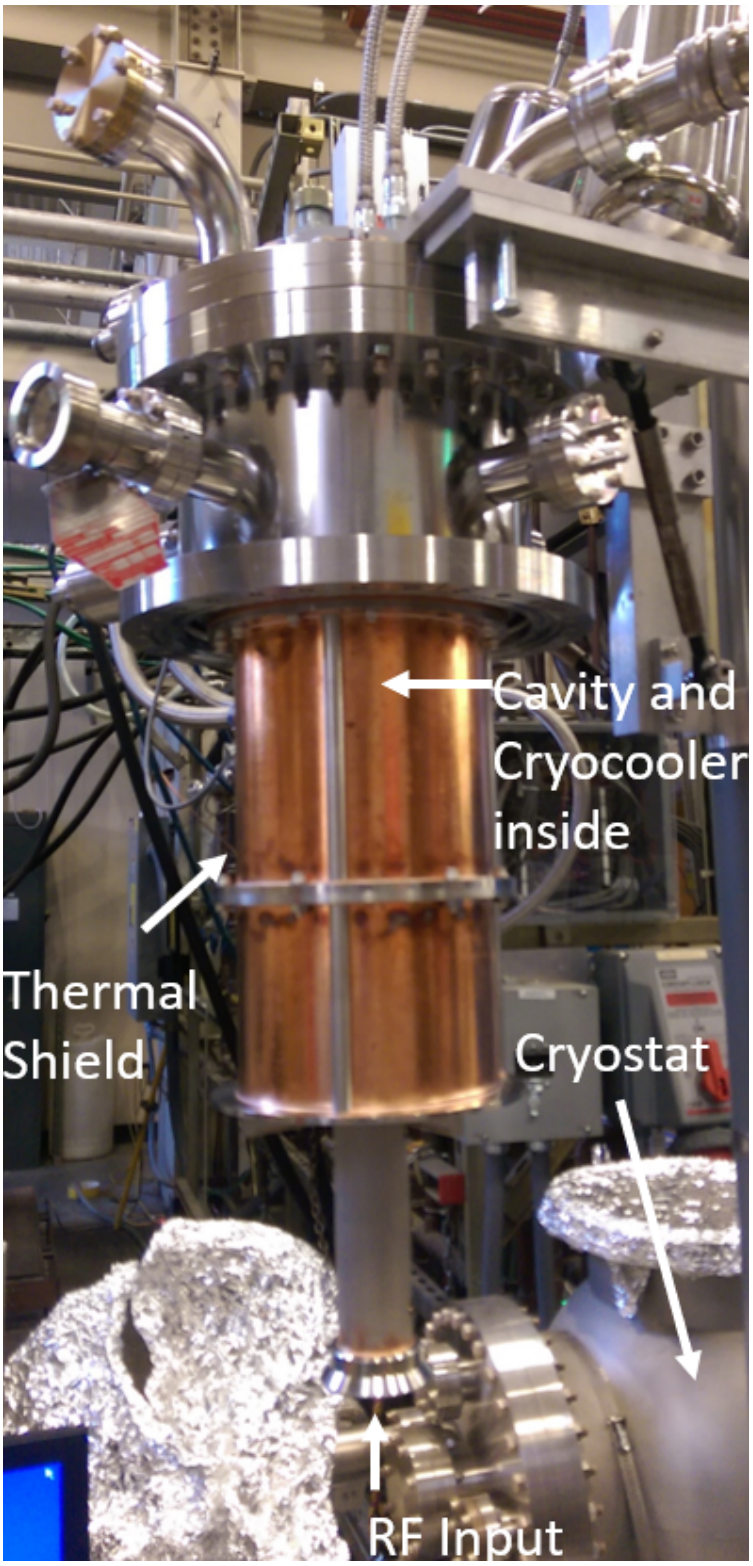

Figure 3.2: Picture of the heat shield around the cavity and cryocooler head before being lowered into the cryostat. Also shown are the input circular waveguide and cryostat.

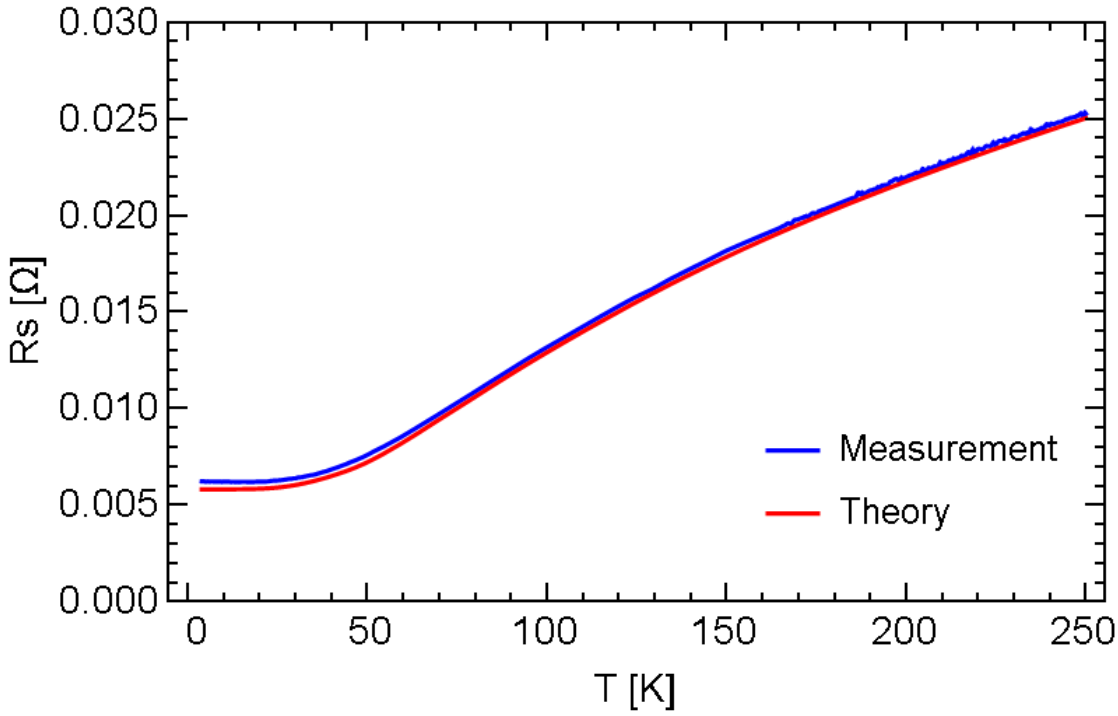

Figure 3.3: RF Surface resistance of the X-band accelerating cavity (blue), compared to theoretical value (red) calculated for copper with International Annealed Copper Standard (IACS) 100% and RRR=400.

3.2.1 Low Power Copper Measurements

Using data presented in [150], I analyzed the data to find R_S and compare to the ASE model. The results are shown in Figure 3.3. In this measurement, there is good agreement between the experimental and theoretically calculated determined R_s , with a slight increase in R_S at very low temperatures in the experimental values compared to the ASE theory.

3.2.2 High Purity Copper Samples

In 2010 four different samples were measured; a 6N (99.9999% pure) sample, two separate 7N (99.99999% pure) samples with large grains, and a 7N sample that was processed to have small grains. The first large grain 7N sample was tested and then chemically etched before being tested again. The calculated rf surface resistance for these samples, the reference sample, and the theoretical prediction for the rf surface resistance are included in Figure 3.4.

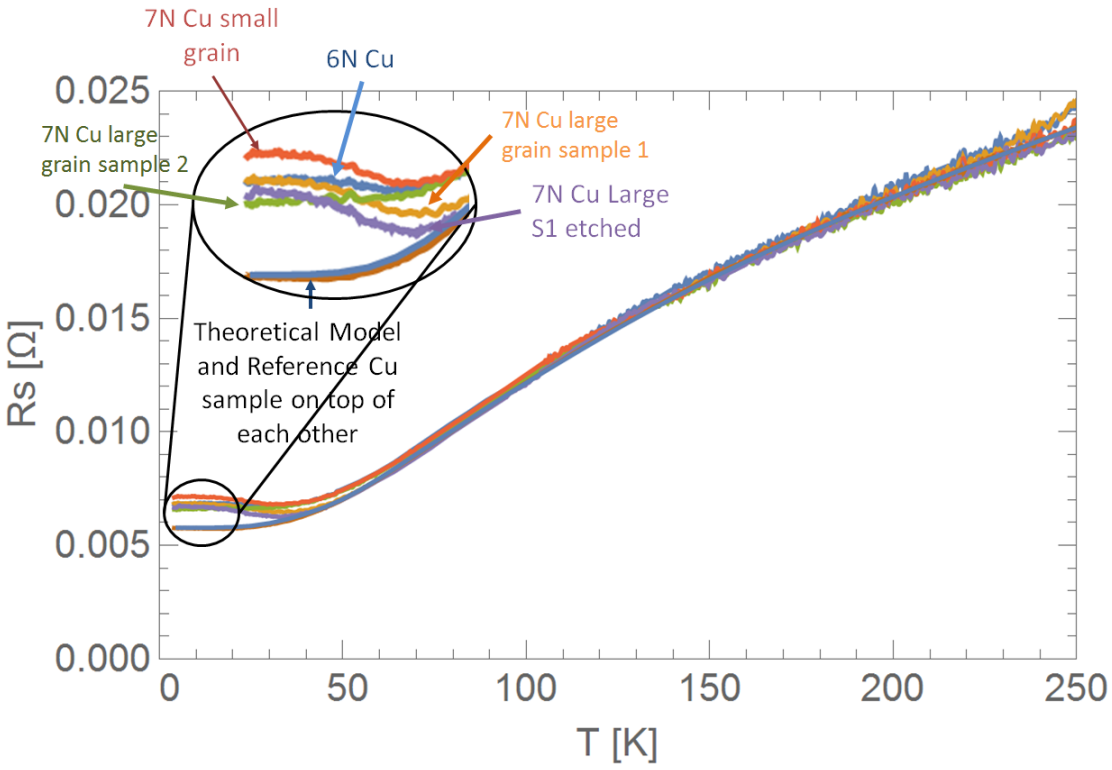

Figure 3.4: R_s of 5 measurements of high purity copper. Also included is the theoretical model for IACS 100% and RRR=400 and the reference sample of 4N Cu.

High purity copper samples are expected to have very large RRR values, leading to exceedingly small values of DC electrical resistance. However, in the ASE theory as the RRR of copper increases, the low temperature value of R_S does not rise significantly, as explained in A.2.2. In these results the high purity Cu samples actually have a larger rf surface resistance than the standard 4N (99.99% pure) Cu at low temperatures. There is also evidence of a minimum in the rf surface resistance around 33 K, after which, the rf surface resistance actually increases as the temperature decreases further. These results imply that another effect even past the ASE theory may occur as the electron mean free path becomes significantly long.

3.3 X-Band Single-Cell Cavity

With the data from the X-band TE dome cavity, an X-band cryogenic DLW accelerating structure was designed to continue the study of rf breakdown physics via the single cell SW cavity program. The shape of the cryogenic X-band single cell accelerating structure was based on the highest impedance structures from the single cell program described in 2.3.5, with elliptical irises with radius of 2.75 mm and thickness 2.0 mm. We use the same geometry to directly compare our room temperature results with those presented here.

RF power is coupled into the structure using a TM_{01} mode launcher [105]. For the design of the structure, we used properties of cryogenic copper measured in previous experiments [150]. The structure was designed to be critically coupled, $\beta = 1$, at 96 K with $Q_0 = 19,100$. At 45 K, the cryogenic cavity is over-coupled with $\beta = 2.12$, and at 293 K under-coupled with $\beta = 0.45$. The resonant frequency of the accelerating mode is 11.424 GHz at 150 K. Table 3.1 includes the calculated parameters for a periodic structure with the same dimensions of the cryogenic X-band structure for 45 K and 293 K. The measured parameters at 45 K are included in Table 3.2. The cryogenic cavity does not include a field probe, as they distort and amplify surface fields and degrade high power performance. To determine the electric fields we instead use the measured input rf power to the cavity (forward power), rf power reflected from the cavity, and signals from the current monitors which intercept the

Parameter	293 K	45 K
Q-Value	8,590	29,000
Shunt Impedance [MΩ/m]	102.891	347.39
H_{max} [MA/m]	0.736	0.736
E_{max} [MV/m]	507.8	507.8
E_{acc} [MV/m]	250	250
$H_{max}Z_0/E_{acc}$	1.093	1.093
Losses in a cell [MW]	7.97	2.36
Peak pulsed heating (150 ns) [K]	86.9	21.9
a [mm]	2.75	2.75
a/λ	0.105	0.105
iris thickness [mm]	2	2
Iris ellipticity	1.385	1.385

Table 3.1: Parameters of periodic accelerating structure with π phase advance per cell and dimensions of the Cryo-Cu-SLAC middle cell at 45 K and 293 K. Fields are normalized to $E_{acc} = 250$ MV/m for $f_0 = 11.424$ GHz. Peak pulsed heating is calculated for a pulse with 150 ns flat gradient.

field emission currents.

Two of these structures were constructed and tested, named 1C-SW-A2.75-T2.0-Cryo-Cu-SLAC-#1 and #2. Figure 3.5 shows the geometry and fields, and Figure 3.6 shows a measurement of the on-axis electric fields in 1C-SW-A2.75-T2.0-Cryo-Cu-SLAC-#2 using the bead-pull method (see [157]) on the second structure. Figure 3.7 is a picture of the bead-pull setup with 1C-SW-A2.75-T2.0-Cryo-Cu-SLAC-#2 and a mode launcher [105].

3.3.1 Experimental Setup

The cavity was placed inside a cryostat and cooled by a pulse tube cryocooler, the Cryomech PT-415. The cold head of the cryocooler was in thermal contact with the cavity. The input

Parameter	Value
f_0 [GHz]	11.4294
Q-Value	30,263
H_{max} [MA/m]	0.736
E_{max} [MV/m]	507.8
E_{acc} [MV/m]	250
Coupling β	1.97
Power lost in walls [MW]	3.46

Table 3.2: Measured parameters of full Cryo-Cu-SLAC-#2 shown in Figure 1. Fields are normalized to $E_{acc} = 250$ MV/m in the middle cell at 45 K.

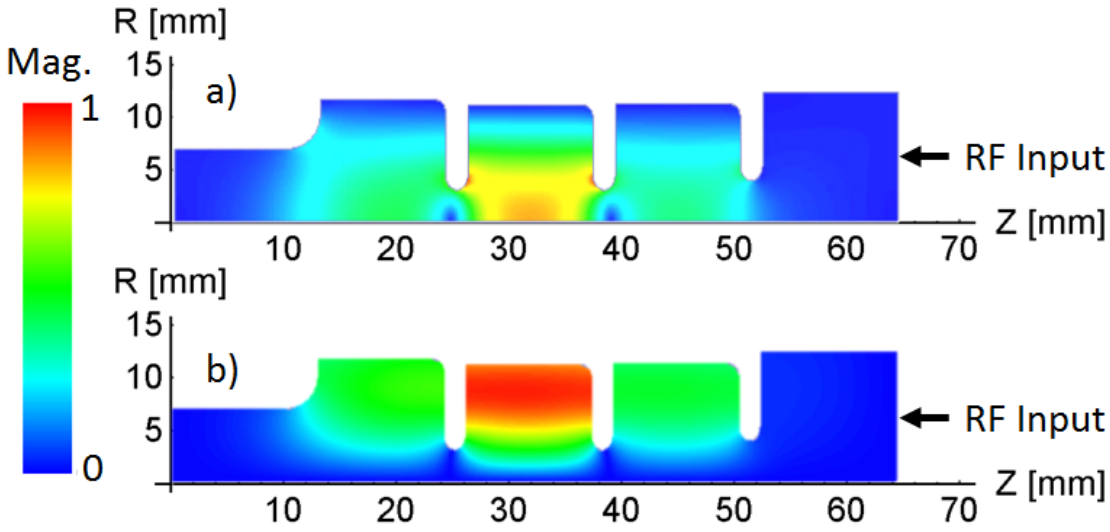

Figure 3.5: Electric and magnetic fields for the cryo cavity. The fields are scaled to 2.5 MW dissipated in the cavity. T=45 K and $Q_0 = 30,263$. a) shows the surface electric fields, with a maximum 400 MV/m. b) shows the surface magnetic fields, with a maximum 580 kA/m.

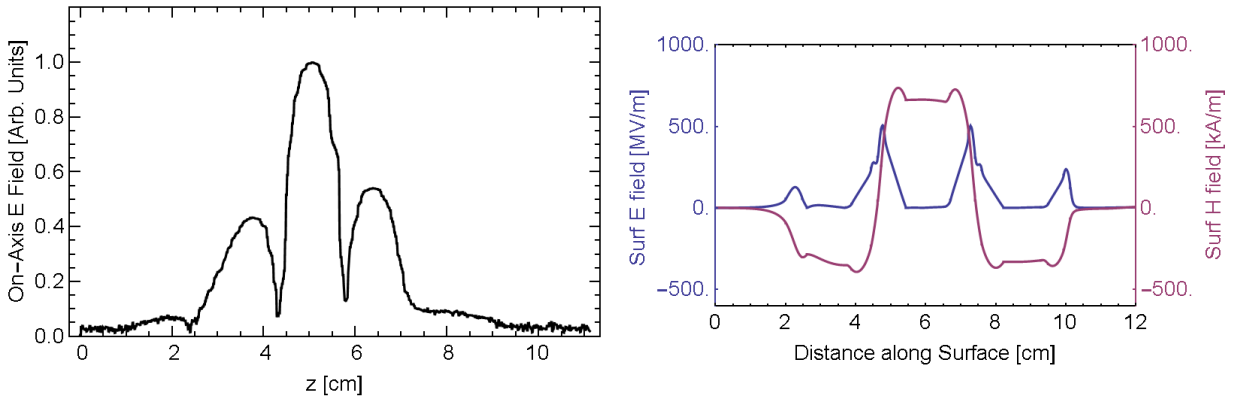

(a) (b)

Figure 3.6: (a) Measurement of the on-axis electric fields using the bead-pull method, scaled to the maximum on-axis value. (b) Surface electric and magnetic fields along the surface for the X-band cryo cavity, scaled to 250 MV/m maximum electric field on the axis.

waveguide was connected to the outside of the cryostat by the TM_{01} mode launcher [105].

For the first experiment, 1C-SW-A2.75-T2.0-Cryo-Cu-SLAC-#1 was connected to the mode launcher with two rf chokes in the circular waveguide as described in [158]. These rf chokes create a gap in the circular waveguide that functions as a thermal break, preventing heat conduction from the room temperature mode launcher to the cryogenic structure. However, the rf chokes also connected the vacuum inside the cryostat to that of the accelerating structure.

In the second experiment, the rf chokes were removed. In addition, the vacuum of the cryostat and 1C-SW-A2.75-T2.0-Cryo-Cu-SLAC-#2 were explicitly separated by brazing a thin piece of copper foil over the beam pipe of the cryogenic X-band cavity. A diagram and photo of the cryostat in the configuration for the second structure are included in Figures 3.8 and 3.9.

For low power measurements, I used a VNA, the Keysight N5242A. With the VNA we measured the dependence of the reflection coefficient on the rf frequency to find the rf parameters as described in C.3.1.

For high power measurements, the rf source was a SLAC 50 MW XL-4 klystron. We

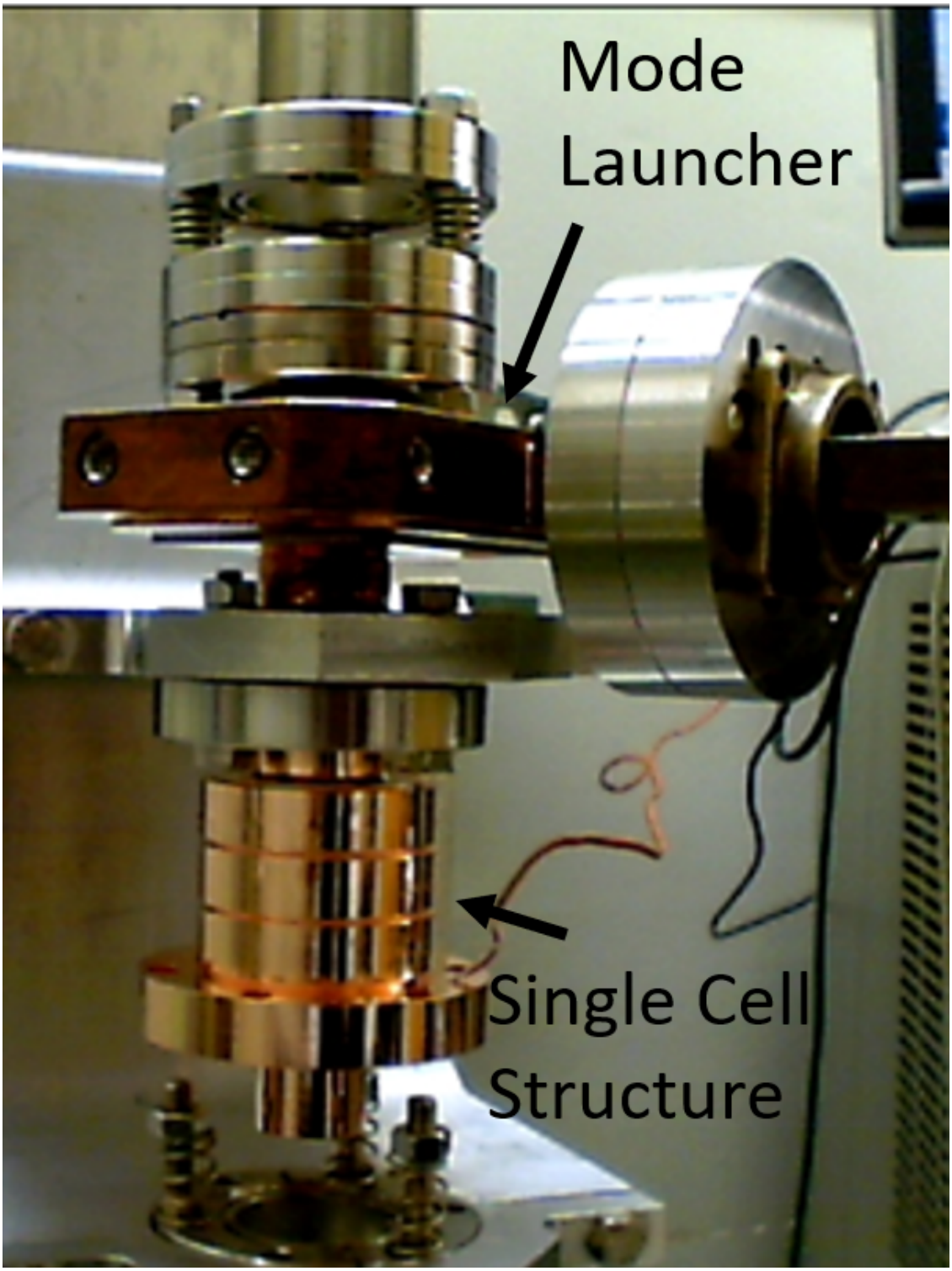

Figure 3.7: The setup of a bead-pull measurement with 1C-SW-A2.75-T2.0-Cryo-Cu-SLAC-#2 and a mode launcher.

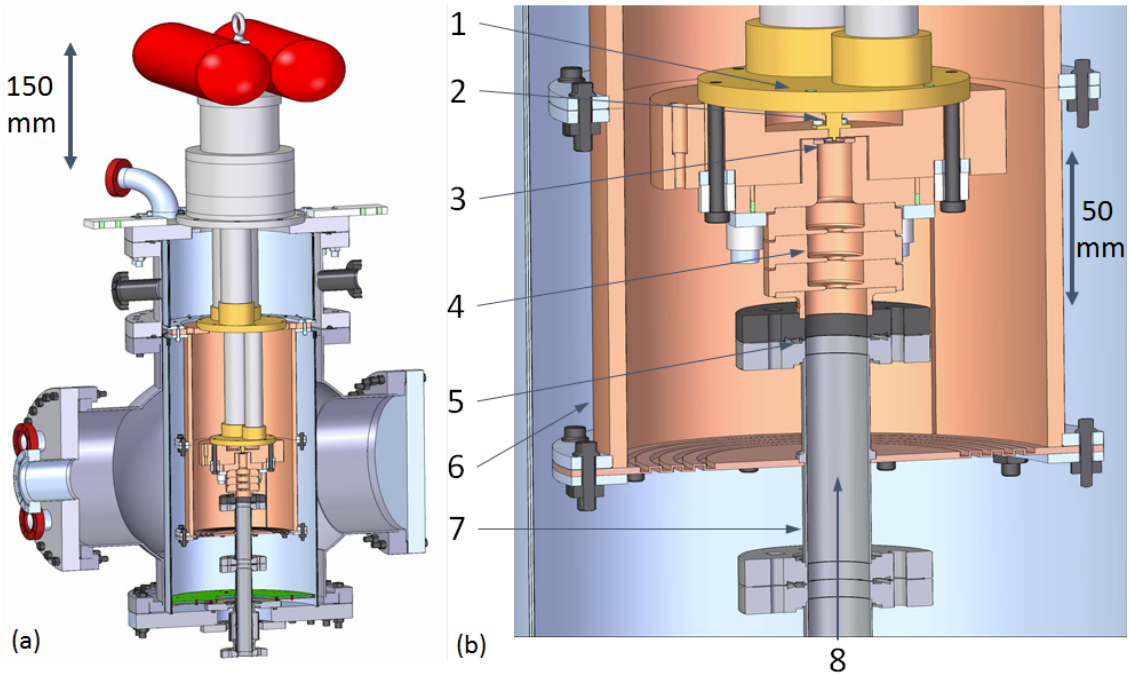

Figure 3.8: (a) Solid model of the cryostat and (b) zoom in on Cryo-Cu-SLAC-#2 in same model. 1 - Cold head of cryocooler; 2 - current monitor; 3 - brazed metal foil; 4 - Cryo-Cu-SLAC-#2; 5 - rf flange; 6 - thermal shield; 7 - Cu-plated stainless steel waveguide; 8 - rf input.

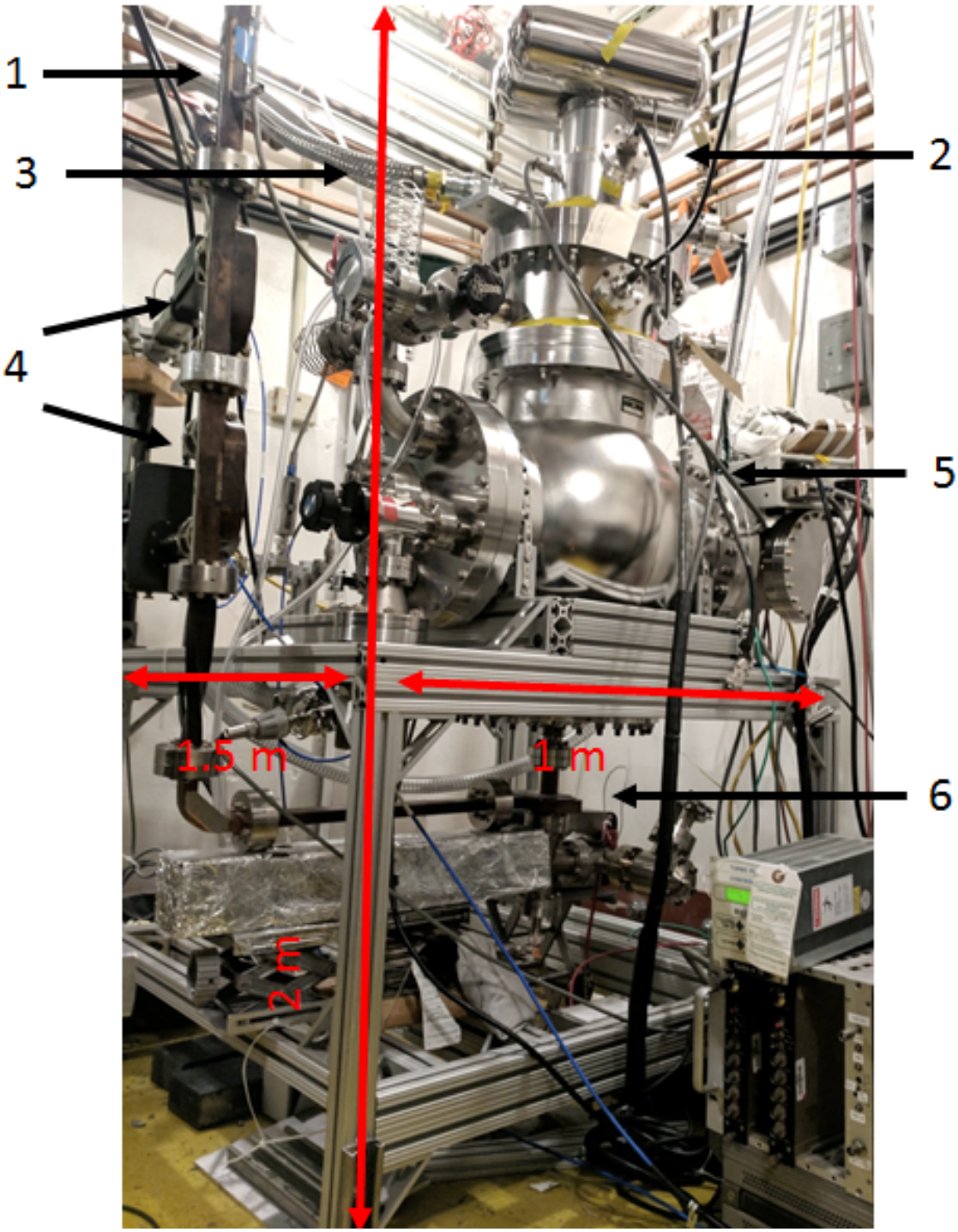

Figure 3.9: Photo of experimental setup: 1-WR90 waveguide towards the klystron; 2- pulse tube cooler; 3-helium lines; 4-WR90 directional couplers; 5-vacuum chamber of the cryostat; 6- TM_{01} mode launcher.

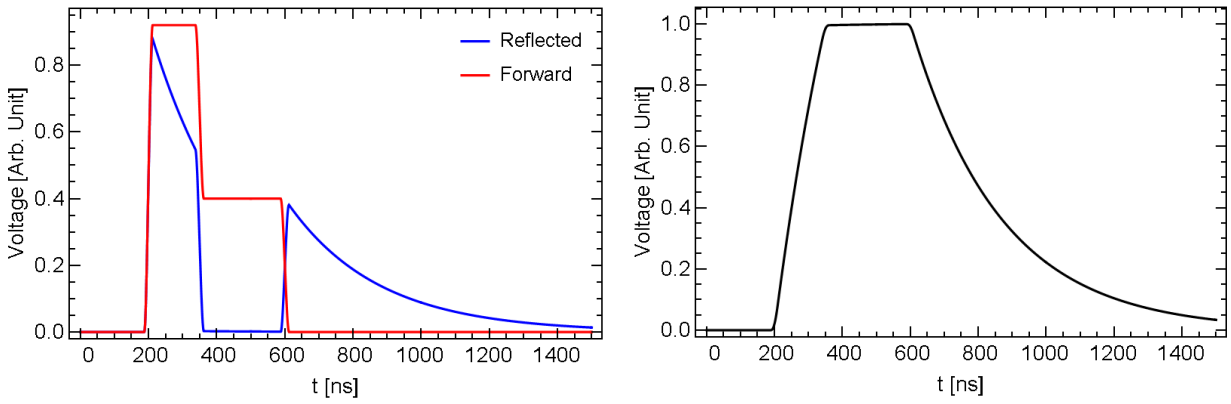

(a) (b)

Figure 3.10: An example of the rf pulse shaping for the cryogenic X-band structure with $Q_0 = 19,000$, $\beta = 1$, and $f_0 = 11.4$ GHz. (a) forward and reflected voltage (b) gradient inside the cavity is flat in time.

pulsed the rf with a repetition rate of 5, 10, or 30 Hz and pulse length up to 1.8 μs. The rf pulses are shaped in a specific way for this experiment. The initial 150 ns is at high power, and then afterwards the power level is designed to fall to a level of about 25% the previous power for the remainder of the rf pulse. The lower power level is chosen to match the rf power lost by the accelerating structure, and therefore the accelerating gradient remains constant during the second part. The rf pulse is shaped in this way for two reasons. First, this creates a more precise measurement of the BDR at specific gradients rather than a varying gradient. Second the ratio between the initial and secondary power levels is dependent on the Q_0, which adds a verification of the Q_0 measurement if the field is flat when it is expected to be. An example of this pulse shaping and the flat gradient is shown in Figure 3.10.

Figure 3.11 shows a diagram of the high power circuit. The klystron (item-7 in Figure 3.11) was connected to the cryostat by a network of WR90 waveguides, with a 3 dB hybrid (5) used to reduce large reflections to and from the klystron. The rf signals were sampled by two directional couplers (4) directly before the mode launcher. The forward and reflected signals were measured with a Keysight N1912A peak power meter (14) and downmixed to 115 MHz (15) to be read by a fast digitizer (13). Two current monitors (3) on both sides of the cavity intercepted the field emission electrons. One of the current monitors

was located below the mode launcher and is an Aluminum disc with a radius of 7.94 mm. The position of the other current monitor is shown in Figure 3.8 and is an Aluminum pin with radius 1.23 mm and length around 2.5 mm. These current monitors were connected via coaxial cables to the digitizer.

3.3.2 First Structure

The first structure, 1C-SW-A2.75-T2.0-Cryo-Cu-SLAC-#1, was tested at high power initially at room temperature. The BDR was much higher than in the previously tested soft copper structures. As the structure was tested at decreased temperature, the BDR did not appear to decrease[159]. Both of these results are shown in Figure 3.12.

As mentioned previously, the vacuum of the cryostat and the first structure were shared. It was speculated that gases in the cryostat may have contaminated the accelerating structure, causing an increased BDR.

Changes were then made to the experimental setup for 1C-SW-A2.75-T2.0-Cryo-Cu-SLAC-#2, as explained in the previous section. The minimal operating temperature is not as low, but the vacuum inside the accelerating structure is cleaner.

3.3.3 Low Power Measurements of Second Structure

We used the VNA to find the Q_0 from 10 to 250 K, the results are shown in Figure 3.13. The Q_0 at low temperatures is lower than expected when compared to the TE dome cavity data. This measurement occurred after 1C-SW-A2.75-T2.0-Cryo-Cu-SLAC-#2 had been processed to high power. To explain the differences in Q_0 between the modes, there may have been damage caused by high power operation, or the high-field surfaces may have been affected when the system was vented to perform the low power measurements. The different modes of 1C-SW-A2.75-T2.0-Cryo-Cu-SLAC-#2 had different increases in Q_0, with the π mode having the smallest increase and the $\pi/2$ mode having the largest. The π mode was the mode that was operated during high power tests, and would be the most affected by damage to the middle cell, and the $\pi/2$ mode, with little electric field in the middle cell,

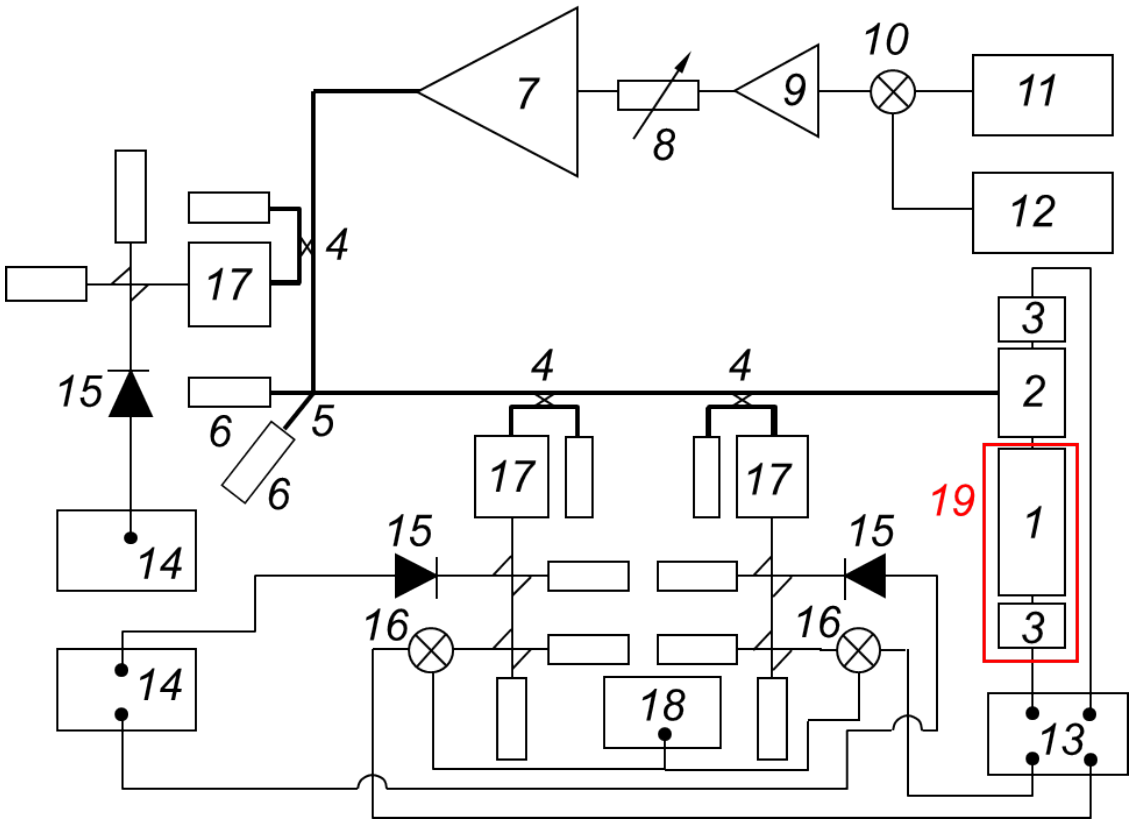

Figure 3.11: Schematic diagram of the experimental setup: 1 - Cryo-Cu-SLAC-#2; 2 - TM_{01} mode launcher; 3 - current monitors for field emission currents; 4 - high power directional couplers; 5 - waveguide 3 dB hybrid; 6 - high power loads; 7 - SLAC XL-5 X-band klystron; 8 - variable attenuator; 9 - booster traveling wave tube; 10 - mixer for klystron signal shaping; 11 - signal generator; 12 - arbitrary function generator; 13 - fast digitizer; 14 - peak power meter; 15 - probes of peak power meter; 16 - mixer for data acquisition; 17 - low pass filters; 18 - signal generator for data acquisition; 19 - cryostat envelope. Not numbered: cross guide directional couplers that couple signal between low pass filter (17) and probes (15) and (16) and low power rf loads which are connected to high power directional couplers (4) and cross guide directional couplers.

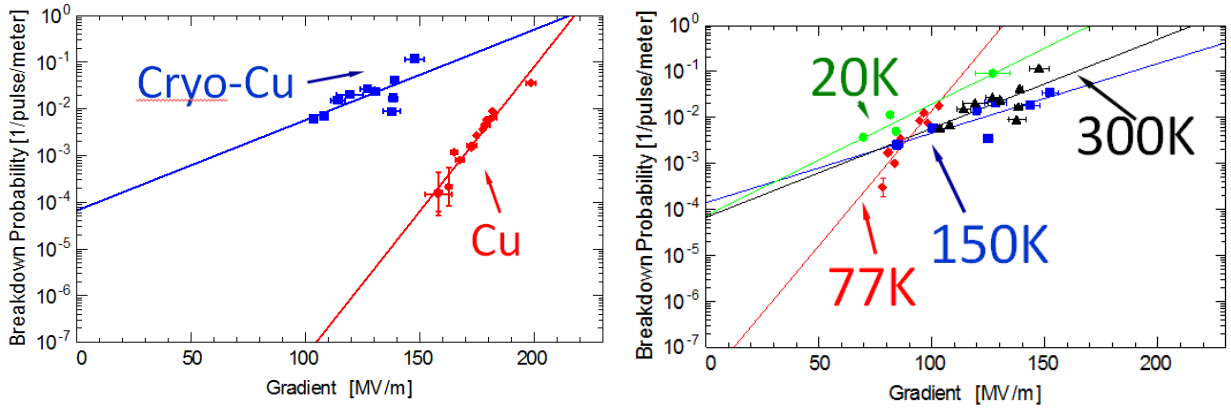

(a) (b)

Figure 3.12: (a) BDR of 1C-SW-A2.75-T2.0-Cryo-Cu-SLAC-#1 (blue) at room temperature compared to a previously tested soft copper structure (red). (b) BDR of 1C-SW-A2.75-T2.0-Cryo-Cu-SLAC-#1 at different temperatures.

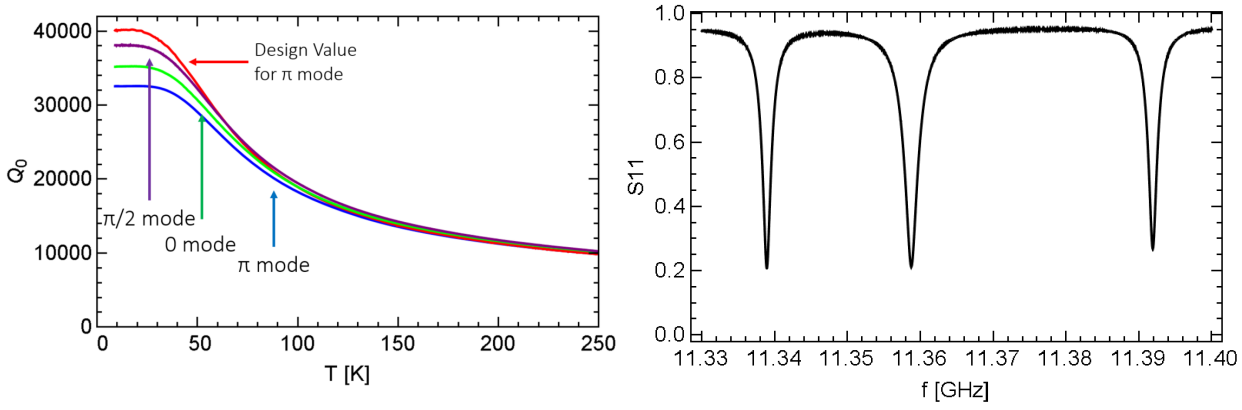

(a) (b)

Figure 3.13: (a) Q_0 for the three modes of 1C-SW-A2.75-T2.0-Cryo-Cu-SLAC-#2, and the design value for the π mode. (b) Measured S11 for all three modes of 1C-SW-A2.75-T2.0-Cryo-Cu-SLAC-#2 at room temperature measured by a VNA.

would be affected the least.

3.3.4 Improvement of Diagnostics and Model of RF System

As will be discussed at length in 4.1, the first high power results for 1C-SW-A2.75-T2.0-Cryo-Cu-SLAC-#2 exhibited unexplained behavior. The reflected signals from the accelerating structure could not be reconstructed properly using the Q_0 that was expected from the results of the TE dome cavity. In this section I will explain my first attempts to explain the discrepancy, by examining the rf circuit between the klystron and 1C-SW-A2.75-T2.0-Cryo-Cu-SLAC-#2, as well as the diagnostic equipment for measuring the rf signals.

The first step I took was to attempt a low power frequency scan of the reflection coefficient using the Klystron. The original idea was to recreate the VNA data without disconnecting the full rf circuit as needs to be done with the VNA. Klystrons are not designed for this use, and have shorter maximum pulse lengths than is ideal for this type of measurement. Another problem with this is the significant variation of the forward klystron pulse shape for different frequencies.

The method I used was to create an input square rf pulse with as long pulse length as possible, around 1 μs, and then scan the frequency. With the data taken from this scan, I divided reflected signal by the forward signal of the last 200 ns of the signal, where the resonant cavity reached near the asymptotic value. This value should correspond to the reflection coefficient of the resonant cavity.

The first test of the rf system I tried was to place attenuators of the same value on the two long coaxial lines that connected the reflected and forward ports of the directional coupler to the downmixers. I compared the klystron frequency scan with these attenuators included and not, shown in Figure 3.14. Since both signals are attenuated by the same value, the resulting ratio should be the same. Since there is a clear discrepancy between the two scans, this implies that there are reflections in the coax lines that are disrupting the rf signals.

The solution was to move the downmixers inside the concrete bunker directly adjacent to the cryostat, reducing the length of this coaxial line. In addition, I added isolators, one-

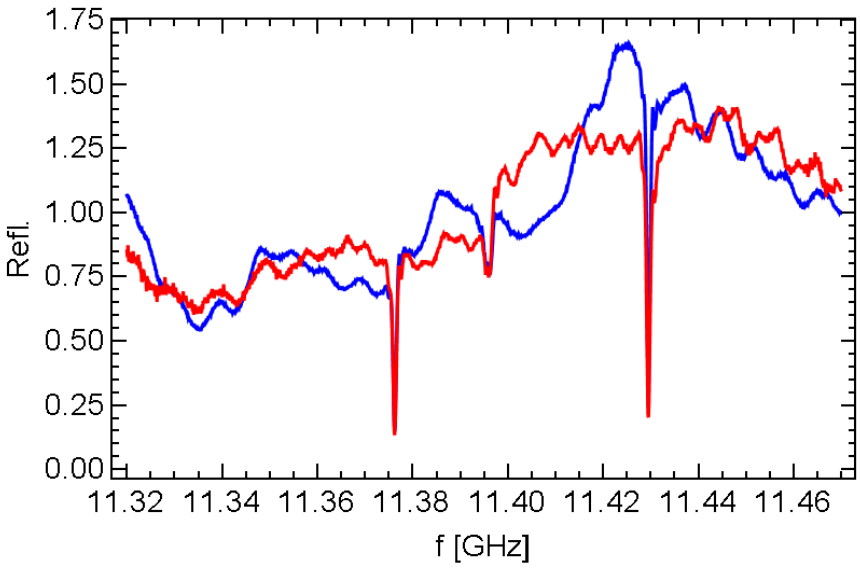

Figure 3.14: Comparison of klystron frequency scan with (blue) and without (red) attenuation between the directional coupler and downmixers. The discrepancy implies the existence of reflections in the coaxial lines.

way attenuators, that significantly reduce reflections. In addition, I added isolators to the coaxial lines that run from the downmixers to the digital scope, which reduced noise in the measurements. The final result after these improvements is shown in Figure 3.15. The data show that the klystron scan finds the same frequency for the modes of 1C-SW-A2.75-T2.0-Cryo-Cu-SLAC-#2, but the amplitudes are different, and it would be difficult to extract the rf parameters from this data.

The next step was to examine the rf components between the klystron and 1C-SW-A2.75-T2.0-Cryo-Cu-SLAC-#2. Initially I used the VNA to measure the accelerating cavity through the forward and reflected arms of the directional coupler without breaking vacuum and disconnecting any of the rf plumbing. This is different to the low power measurement above, which was conducted through the mode launcher when the rectangular waveguide was disconnected. The problem with the measurement is that the directional coupler has 46 dB attenuation each way, significantly increasing noise in the measurement. To attempt to fit this data, I created a model of the full rf circuit in a similar vein to the equivalent circuit models derived in C.3.1. The model is derived in C.5. With this model I was able

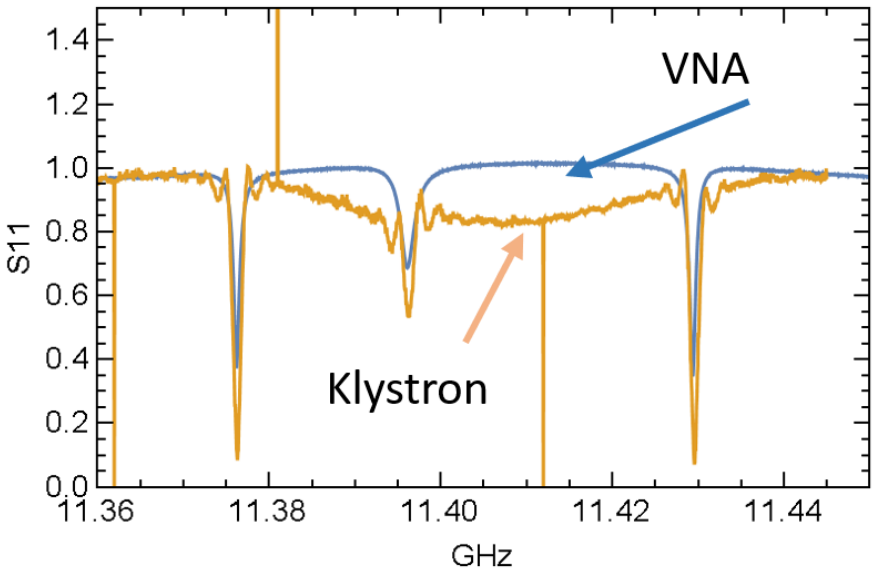

Figure 3.15: Frequency scan of the reflection coefficient using the klystron and VNA.

to accurately represent the data as shown Figure 3.16. This data fit uses the rf parameters from the previous cold test data.

Using the full rf system model I wanted to know if the rf circuit was altering our reflected signal reconstruction. I took a signal that I had measured from the forward port of the directional coupler. I then compared the reconstructed reflected signal from inputting this forward signal into the resonant cavity using the model from C, versus the reflected signal from the full rf system model that would also produce the same forward signal at the directional coupler. The comparison is shown in Figure 3.17. I found that the two reflected signals are nearly identical, and that the effects of the full rf circuit are essentially accounted for by using the forward signal at the directional coupler to recreate reflected signals.

To summarize, the reconstructed reflected signals are the same for the full rf system model and the simple resonant cavity model, and I could reconstruct the VNA scan of the resonant cavity through the directional coupler. These combined results imply that we understand any effects from the full high-power rf system from klystron to accelerating structure, and that the full system does not affect our measurements of Q_0.

The high-power data for 1C-SW-A2.75-T2.0-Cryo-Cu-SLAC-#2 is presented in chap-

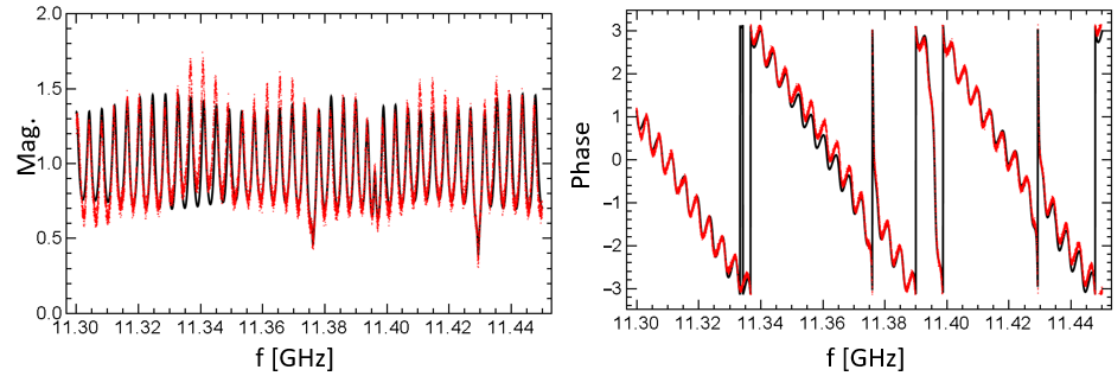

(a)

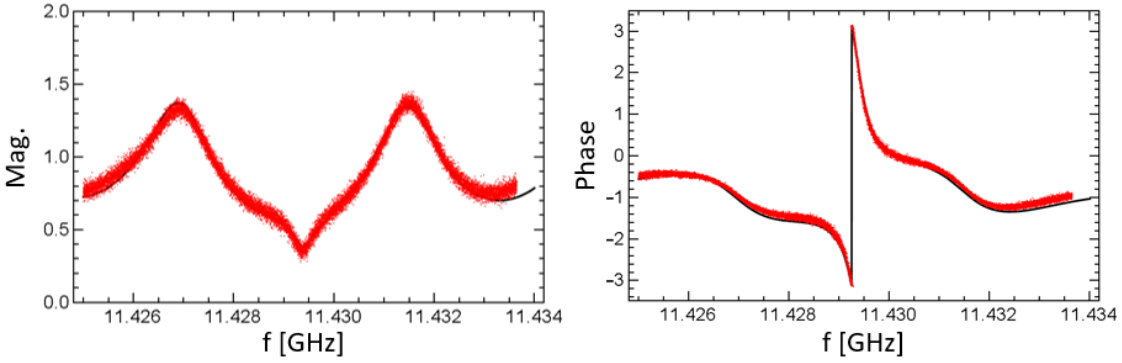

(b)

Figure 3.16: (a) VNA measurement of 1C-SW-A2.75-T2.0-Cryo-Cu-SLAC-#2 through the directional coupler (red) and a model of the full rf system (black). (b) Zoom in of the same data set around the π mode of 1C-SW-A2.75-T2.0-Cryo-Cu-SLAC-#2.

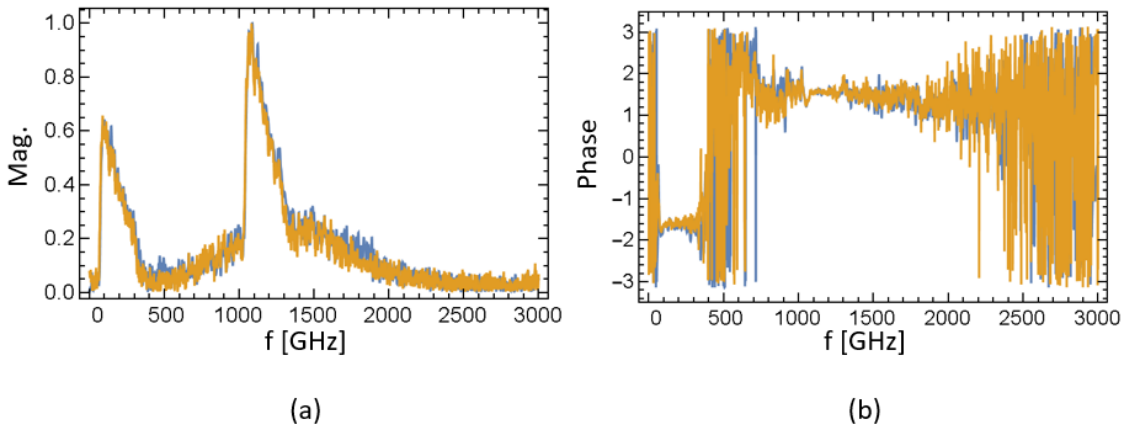

Figure 3.17: Comparison of a reflected pulse from the full rf system model (blue) and from the simple equivalent circuit model (orange), using the same forward rf signal. (a) is magnitude and (b) is the phase of the reflected signal. The differences are small enough that we will use the simple equivalent circuit model for our experiment.

ter 4.1.

3.4 S-Band Pillbox Cavity

An S-band resonant test cavity was designed to measure the low temperature R_S for copper at 2.856 GHz. This experiment was designed because of the proposal for a S-band cryogenic photoinjector, as described in Chapter 5.

The cavity design chosen for the S-band tests is a pillbox that was manufactured from two pieces of copper brazed together, which was chosen for simplicity and cost reasons. Half of the geometry is shown in Figure 3.18. The radius of the cavity was chosen so that the TM_{010} mode will be 2.586 GHz at 20 K. Due to thermal expansion, at room temperature the resonant frequency is 2.847 GHz.

The length of the cavity was chosen to be 48 mm due to space constraints in the cryostat. To remove degeneracy of the multipole modes we cut a groove in the outside radius that breaks the azimuthal symmetry. To couple rf into the cavity we used two separate antennas, one through the flat wall of the pillbox and the other in the outer diameter. In the first

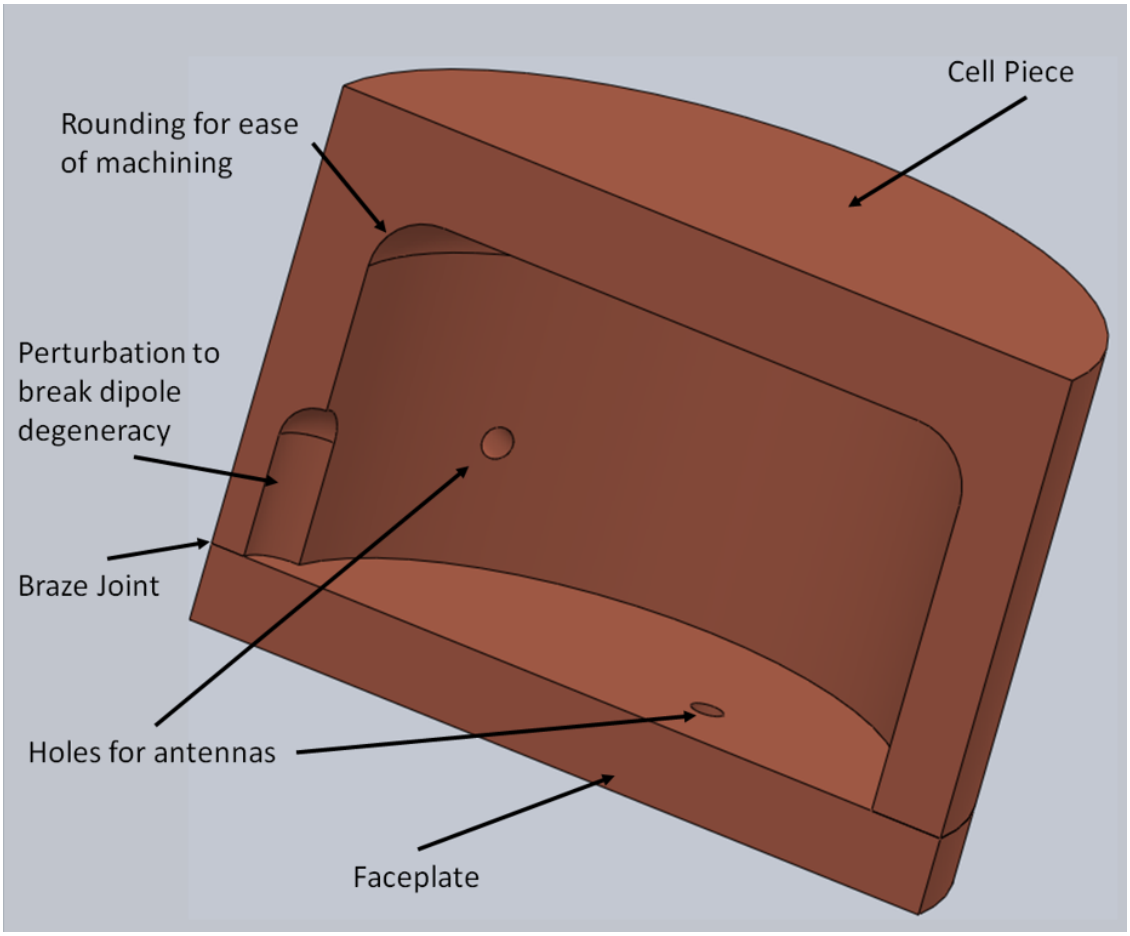

Figure 3.18: A Solidworks rendering of the ASE test cavity. The cavity is formed from two pieces, the cell piece and the faceplate. Coupling is accomplished by the two holes, which allow for antennae insertion. The notch in the side is to break the degeneracy of higher order multipole modes.

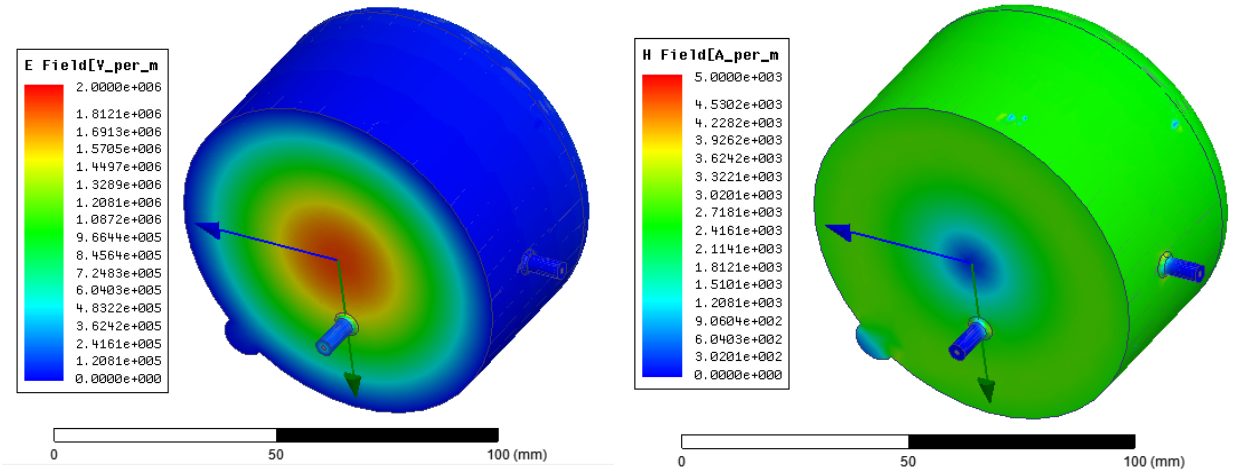

(a) (b)

Figure 3.19: Surface electric and magnetic TM_{010} fields of the S-band cavity. Fields are normalized to 1 mJ stored energy.

experiment we used only the antenna in the flat wall to couple to the TM_{010} mode. Since the other antenna does not couple to the TM_{010} mode, it has minimal little effect on the measurement.

The Q_0 of the cavity was designed to be 18,000 and the geometric factor was calculated to be $D_{\mathrm{Cav}} = 252$. The external coupling of the cavity was tuned by changing the length of the antenna and was designed to be close to critical coupling at cryogenic temperatures. The calculated surface electric and magnetic fields are shown in Figure 3.19. Two of the S-band cavities were manufactured from different copper stocks and by two separate machine shops, to show the reproducibility of the data. The first cavity was made at SLAC, and the second at UCLA.

The S-band cryo cavity was tested in the same cryostat used for the TE dome cavity. The antennae were connected to high voltage SMA feed-throughs to reach out of the cryostat, which then were connected to the VNA. Due to the SMA feed-through, the equivalent circuit was modified. The altered fitting model can be found in C.3.2. Temperature scans were conducted with the same method as described in the TE dome cavity section. Each cavity was tested separately. Figure 3.20 shows a picture of the S-band pillbox cryogenic cavity on

	SLAC Cav		UCLA Cav	
	4 K	293 K	4K	293 K
Q_0	82,931	17,184	83,066	17,375
Q_E	92,249	80,118	58,272	68,014
$f_0(GHz)$	2.855	2.845	2.856	2.846

Table 3.3: Measured rf parameters for the two S-band cryo test cavities.

the bench with the standard 3.5 mm SMA connections.

3.4.1 Low Power Measurements

RF parameters measured for both cavities at 4 K and room temperature are shown in Table 3.3. We see that the frequency for both cavities was within a few MHz of the design and that the measured Q_0 was lower than design by about 5%. Once the coupling antennas were tuned, the coupling beta reached the design value of $\beta = 0.25$ at room temperature. The Q_E of both cavities varies with temperature. We speculate that this may be caused by the length of the coupling antenna with changing with temperature. The increase in Q_0 from room temperature to 4 K is measured to be 4.82 for the SLAC cavity and 4.78 for the UCLA cavity.

We performed temperature scans on both cavities, however, the scan on the UCLA cavity stopped after reaching 50 K due to problems with the network analyzer and we were not able to repeat the measurement. The cavity from SLAC warmed to 300 K. The measured values of Q_0, Q_E, and f_0 are included in Figure 3.21. We calculated the rf surface resistance using the geometric factor from the temperature scans, shown in Figure 3.22, compared to the theoretical value from the ASE model.

Again, there is a discrepancy between the measured R_S and the theoretical value. This may have to do with coupling through the antennae, where any effects due to the change in temperature were not considered.

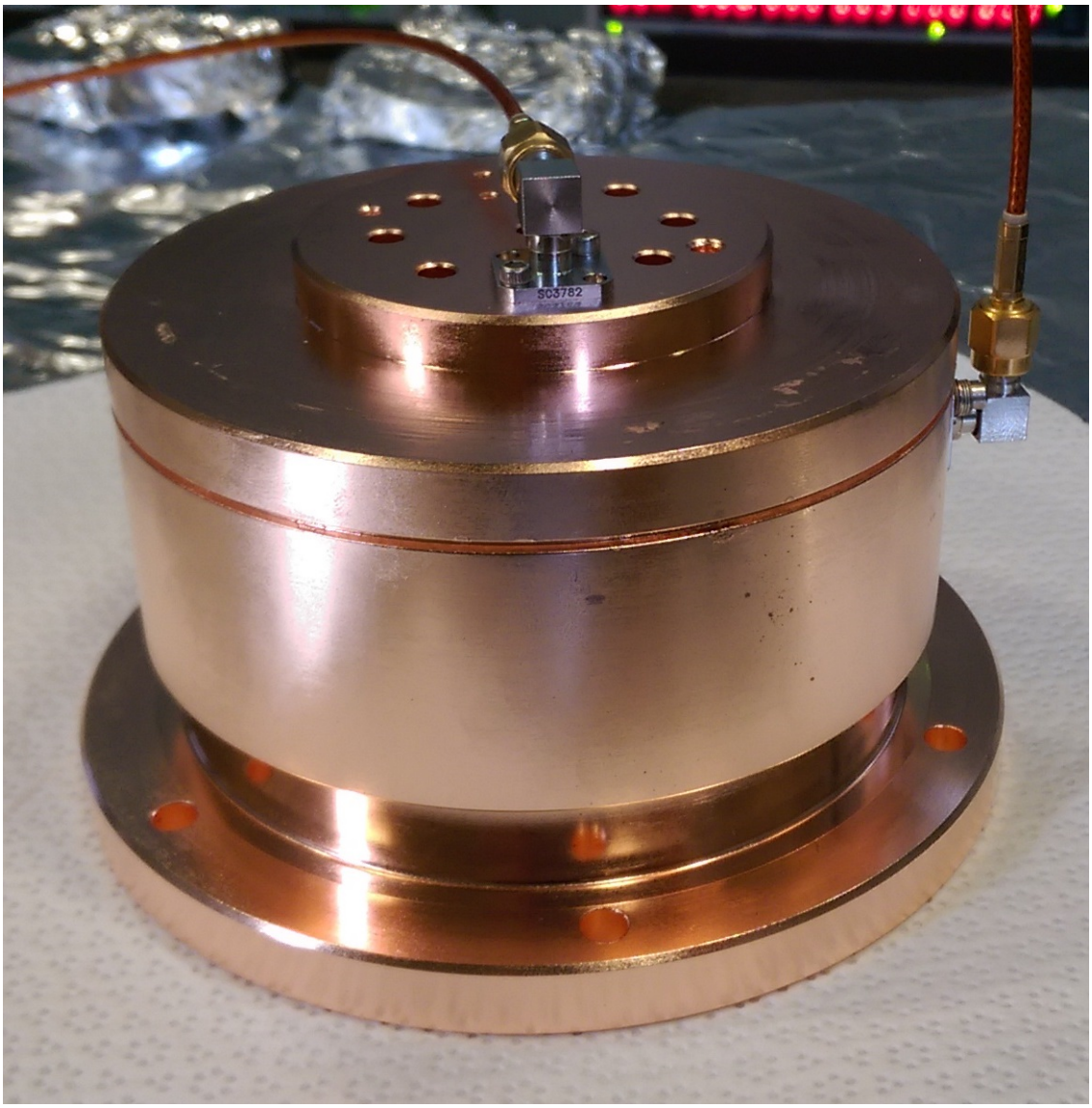

Figure 3.20: Picture of the S-band pillbox cavity

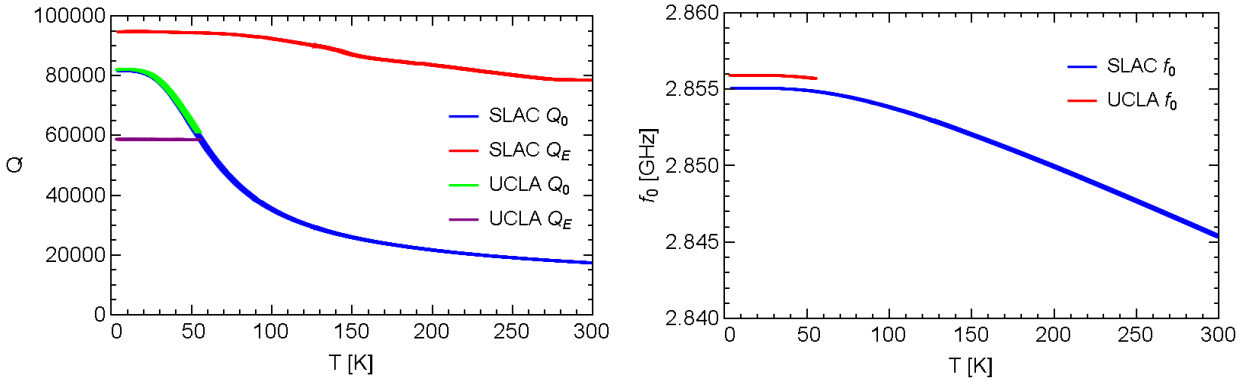

(a) (b)

Figure 3.21: Rf parameter measurements from the temperature scan. (a) shows the Q_0 and Q_E for both the SLAC and UCLA cavities. (b) shows the f_0. The thickness of the lines are the error bars from fitting to the VNA data.

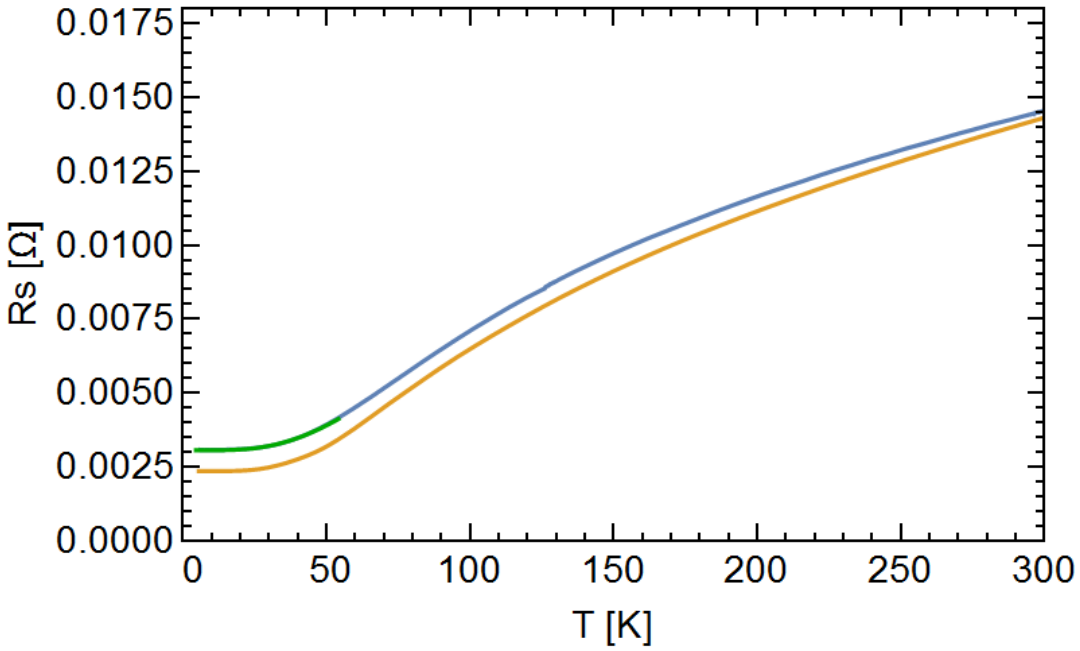

Figure 3.22: RF Surface resistance of S-band accelerating cavities, SLAC (blue) and UCLA (green) compared to theoretical value (yellow) for copper with IACS 95% and RRR=400.

3.4.2 Direct Skin Depth Measurement

As mentioned in B, the skin depth of a metal will change the resonant frequency of any cavity constructed from that metal. As the electromagnetic fields penetrate farther into the metal surfaces, the volume effectively becomes larger, decreasing the resonant frequency. I have calculated the change in frequency versus temperature due to the change in skin depth in two ways. First, using cavity perturbation theory, where frequency changes can be calculated for adding or subtracting small volumes to a resonant cavity [160]:

$$\frac{\omega_2 - \omega_1}{\omega_1} \sim \frac{\int_{\Delta V}(\mu_0|H|^2 - \epsilon_0|E|^2)dV}{\int_{\Delta V}(\mu_0|H|^2 + \epsilon_0|E|^2)dV}, \tag{3.4}$$

where ΔV is the volume of the cavity walls where the skin depth penetrates, ω_1 is the unperturbed frequency, and ω_2 is the frequency the cavity resonates at. For this exercise I will assume the pillbox cavity is a perfect cylinder, then the integration into the boundaries is possible to complete without the aid of a finite element electromagnetic solver. The dependence of the electric and magnetic fields on depth into the conductor is defined in A.2.1.

The second method to calculate the frequency shift is from the derivation of the differential equation that governs the fields inside the cavity B, where

$$\omega_2 = \frac{\omega_1}{\sqrt{1 + \zeta_{\mathrm{Im}}/Q_0}}, \tag{3.5}$$

where ζ_{Im} is defined in B.

Finally, the thermal expansion and contraction of the cavity shifts the frequency as the temperature changes as well. This frequency change should be accounted for to be able to measure the frequency change due only to changes in the skin depth. However, the uncertainty in measured values of the coefficient of thermal expansion, α_T, are significant, with relative errors in the percent range [143]. Since the change in frequency due to thermal expansion is around 10 MHz, while the frequency change due to skin depth is near 100 kHz, the percent error in α_T dominates the exercise.

The resulting calculations and experimental measurements from the SLAC cavity are shown in Figure 3.23. The measured frequency change is larger than either model, however, the behavior more closely matches the model from the differential equations in B.

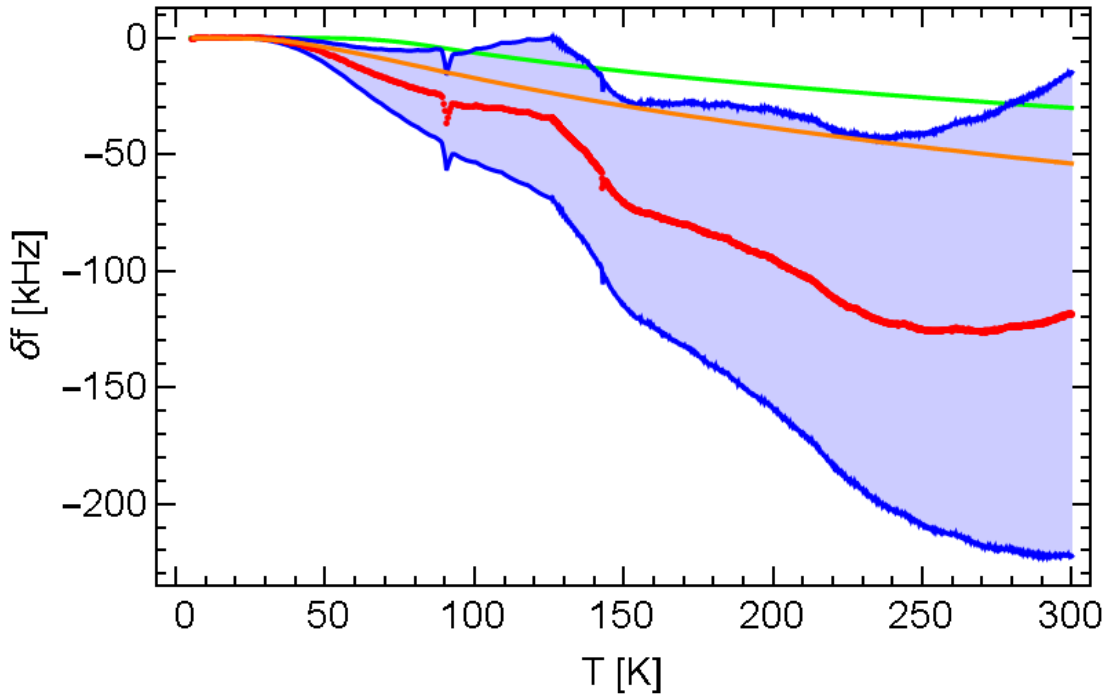

Figure 3.23: Measurements and estimates of the frequency change due to the change in rf skin depth. Blue is the measured frequency minus the expected frequency change due to thermal expansion. Red is the expected change based on the model from differential equations governing electromagnetic fields inside resonant cavities. Green is the expected change due to cavity perturbation theory. The error bands are from the error in the value of thermal coefficient of expansion.

3.5 Design for S-Band Single-Cell Cavity

With low power cryogenic copper R_S S-band data completed, I then created a design for a S-band cryogenic single cell copper accelerating structure. The approach and geometry are the same as the X-band single cell structures, discussed in 2.3.5 and 3.3, where most of the dimensions have been scaled up by a factor of 4. The ratio between the iris radius and the wavelength was kept the same: $0.105 = a_{\mathrm{Ir}}/\lambda_{\mathrm{rf}}$. The electric field along the axis will be designed to reach a peak in the center cell, twice that of the outer cells, as is standard for these designs.

The difference between the cryogenic S-band and cryogenic X-band single cell cavities are two-fold: the outer diameter of the cells in the S-band design are rounded to increase the Q_0 and reduce the peak surface magnetic field, and the S-band design is significantly overcoupled. The choice of the coupling value will be discussed later this chapter in 3.5.1.2.

A new S-Band TM_{01} mode launcher was designed that reduces the quadrupole component, which will convert the circular waveguide on the single cell cavity to the external TE_{01} rectangular waveguide. The Quadrupole free mode launcher will be discussed in chapter 5.3, as the mode launcher will also be used for the TOPGUN design.

3.5.1 Design Considerations

SUPERFISH[161], a 2D finite element electric field solver, was used to design the geometry of the S-band accelerator cavity, and verified with HFSS[156], a 3D finite element electric field solver. The automated SUPERFISH toolkit described in 5.1 and [162], was used to quickly optimize the design. The geometry and field maps are shown in Figure 3.24. The on-axis electric field and the surface electric and magnetic fields for the cavity in the π mode are shown in Figure 3.25.

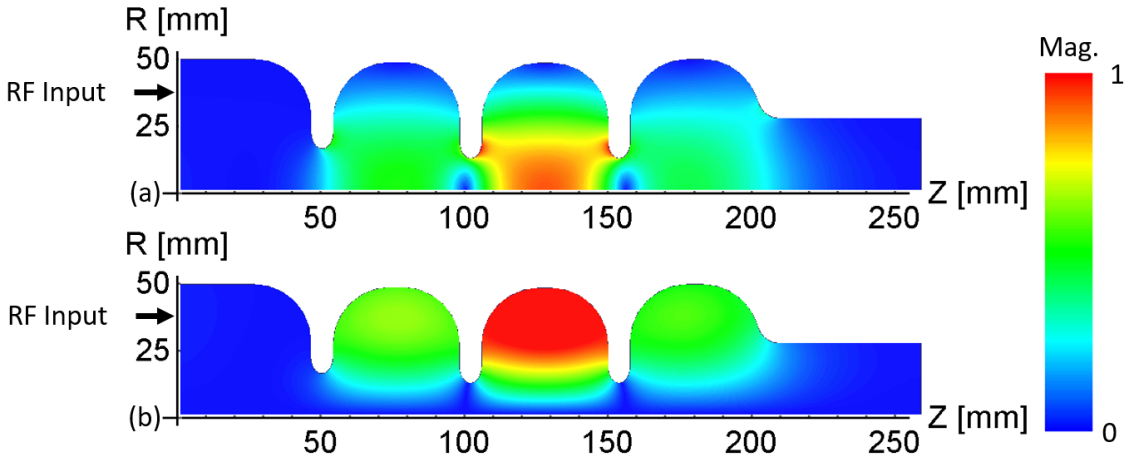

Figure 3.24: Geometry and fields of the cryogenic S-band accelerating cavity. The fields are scaled to 250 MV/m maximum field on axis. The maximum electric field is 267 MV/m and the maximum H field is 382 kA/m.

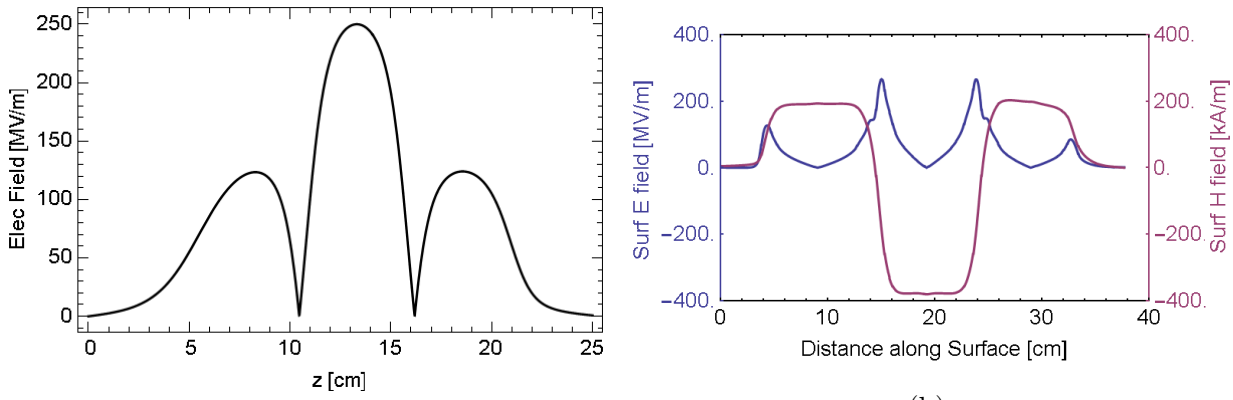

(a) (b)

Figure 3.25: (a) On-axis electric field (b) surface electric (blue) and magnetic (purple) fields all scaled to 250 MV/m maximum electric field on axis. Fields are calculated by SUPERFISH.

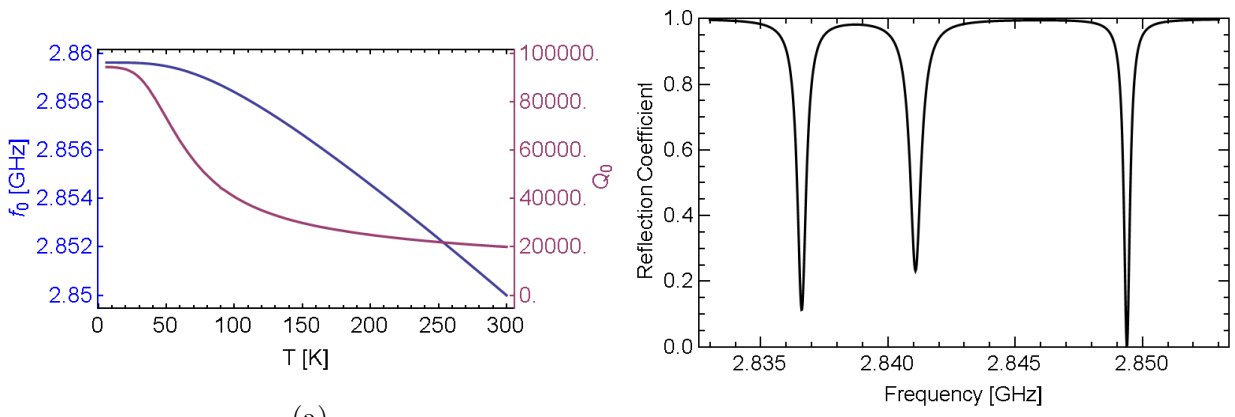

(a) (b)

Figure 3.26: (a)Expected temperature dependence of f_0 (blue) and Q_0 (purple) for the π mode frequency in the S-band cryogenic single cell structure. (b) Expected results from a frequency scan for the S-band single cell cavity from a network analyzer. Expected Q_0 is adapted from the S-band cryogenic pillbox results. Expected f_0 is from the expected thermal expansion of copper.

3.5.1.1 f_0 and Q_0

The SLAC 5045 S-band klystron can operate in the frequency range 2856 ± 10 MHz [163]. Therefore, the resonant frequency of the cavity must be within this bandwidth from room temperature to 20 K. The frequency of the π mode at 300 K was chosen to be 2.85 GHz. As the cavity is cooled to 20 K the frequency will increase to 2.86 GHz. The expected Q_0 dependence on temperature is taken from the results of the cryogenic pillbox S-band cavity. At cryogenic temperatures Q_0 will increase to more than 90,000. The predicted temperature dependence of the frequency and Q_0 for the π mode are shown in Figure 3.26, as well as the expected VNA measurement for all three modes of the accelerator.

3.5.1.2 Coupling

Because of the change in the Q_0, the rf coupling β will also increase by a factor of 4.7 from room temperature to cryogenic temperatures. We have chosen to use a 15 MW 3.5 μs klystron pulse for this experiment. We would like to choose a coupling that will allow the

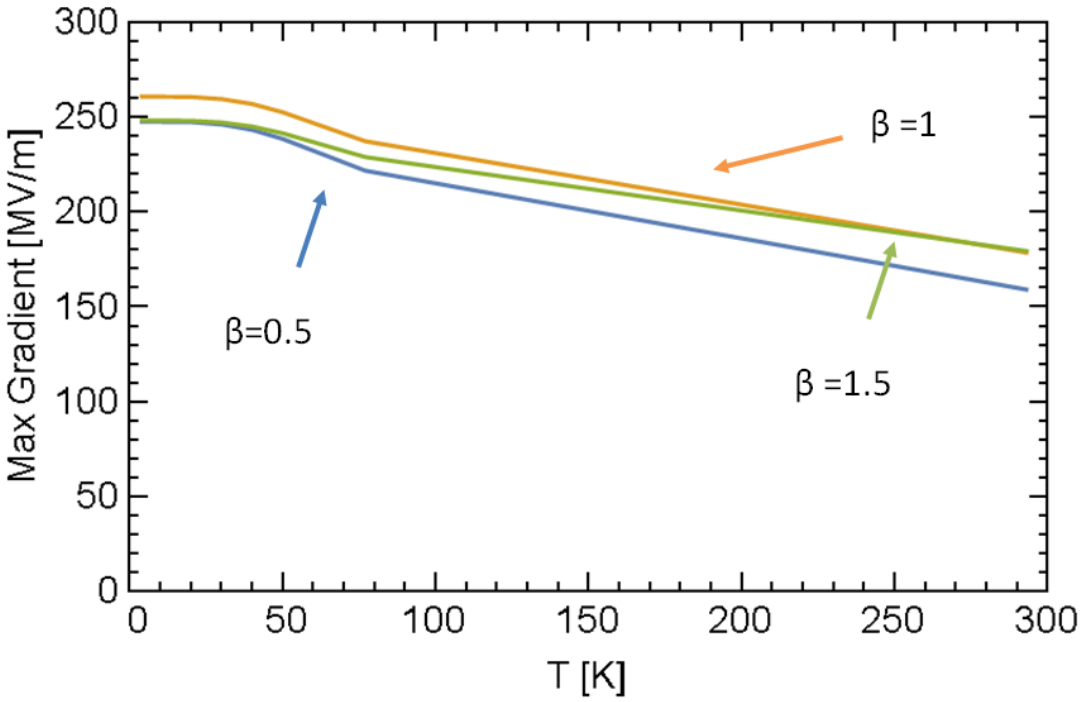

Figure 3.27: The max gradient reached at different temperatures for three different coupling betas at room temperature. Critical coupling was chosen, since it has the larger gradient achieved.

maximum possible accelerating gradient to be reached using these rf pulse parameters.

We calculated the expected gradients achieved by the S-band experimental set-up using the following equation,

$$G[\mathrm{t}] = \sqrt{\frac{4\beta Z \mathrm{P_{in}}}{(1+\beta)^2 L}} \left(1 - \mathrm{e}^{-\frac{2\pi f_0 (1+\beta) t}{2Q_0}}\right), \tag{3.6}$$

where G is the gradient in the central cell, $L = 0.13$ cm is the length of the cell, and Z is the effective shunt impedance of the middle cell. Figure 3.27 shows calculations for the accelerating gradient achievable at cryogenic temperatures for the given rf input pulse at three different choices of β at room temperature (the β will be larger by a factor of 4.7 at cryogenic temperatures) . From these results we have chosen the room temperature coupling to be $\beta = 1$.

Quality factor (Q_0)	19,989
π mode frequency f_0	2.85 GHz
Stored energy (U)	10.2 J
Shunt Impedance (Z)	57.4 MΩ/m
Max Magnetic Field (H_{max})	275 kA/m
Max Electric Field (E_{max})	195.8 MV/m
Losses in one cell	9.165 MW
$H_{max}Z_0/E_{acc}$	1.036
Coupling β	1.0

Table 3.4: RF properties for a periodic cell calculated at room temperature. Values are normalized to an accelerating gradient of 100 MV/m.

3.5.1.3 Final RF Parameters

We calculated parameters for the π mode of a periodic accelerating structure with the same dimensions as the middle cell of our cavity to give an effective shunt impedance and accelerating gradient for the middle cell. These rf parameters, calculated at room temperatures are contained in Table 3.4.

3.5.2 Thermal Considerations

As the cryogenic S-band single structure operates far below room temperature, thermal management is an important issue. The amount of heat that can be dissipated into the cavity is limited by the cryocooler, or else the operating temperatures will continually rise. I will consider the projected thermal load of the S-band cryogenic single cell accelerating structure when operating with large gradients.

Temp. (K)	4	20	30	40	50	77	300
Q_0	94,352	93,419	90,080	82,787	73,249	51,281	19,989
Coupling β	4.66	4.62	4.46	4.12	3.64	2.54	1
Pk. Elec. (MV/m)	261	261	260	257	253	237	179
Ener. Diss./Pulse (J)	8.45	8.51	8.80	9.46	10.59	14.46	27.06=7
ΔT (K)		8.62	7.52	7.92	9.61	17.67	24.84

Table 3.5: Coupling and Gradient reached at different temperatures for the S-band cryo accelerating structure. Also included are pulse heating and rf surface losses per pulse. Data for 15 MW 3.5 μs flat pulse

3.5.2.1 Heat Load in Accelerating Structure

To calculate the energy dissipated per pulse we used the equation

$$P_{\text{dissip}}[\text{t}] = \frac{\omega_0 U[t]}{Q_0}, \tag{3.7}$$

where the stored energy is calculated by SUPERFISH, and is proportional to the square of the electric field. We assume a square input rf pulse, and that the electric field inside the cavity charges and decays exponentially with the time constant 1.15. The magnitude of the electric field is defined by 3.6. To find the total energy dissipated, the power is integrated in time.

The pulse heating was calculated from the diffusion equation assuming the thermal properties of copper are static at the starting temperature of the pulse. This is a bad assumption for 4K, which was therefore not computed. For other temperatures this appears to be a good assumption, since the pulse heating is only on the order of $\Delta T = 10$ K , where the material properties of copper are relatively stable.

Table 3.5 shows the calculated gradient, power dissipation, and rf pulse heating for our S-band experiment. The cryocooler that we are using can remove around 40W at 10K, therefore this structure will be able to operate at a minimum of 1 Hz repetition rate.

3.5.2.2 Heat Load in Cylindrical Waveguide

A worry was that as the power travels through the circular waveguide, power would be lost as heat in the waveguide and be conducted back to the accelerating cavity. This is a calculation to show how much power is lost in the waveguide during high power operation, including forward rf power from the klystron and reflections from the cavity.

The waveguide is cylindrical with radius, $R = 1.81in = 45.974mm$. At first the surface resistance is left as a variable to allow for other waveguide materials. This derivation follows [164].

The rf will travel in the TM01 mode at 2.856 GHz where the cutoff wave number and β_{wg} are:

$$\begin{aligned} k_c &= \frac{2.405}{R} radians/m \\ \beta &= \sqrt{k^2 - k_c^2} \end{aligned} \tag{3.8}$$

The electromagnetic fields for this mode are

$$\begin{aligned} E_\rho &= -i\frac{\beta E_0}{k_c} J_n'(k_c\rho)\exp(-\imath\beta z) \\ H_\phi &= -i\frac{\omega\epsilon_0 E_0}{k_c} J_n'(k_c\rho)\exp(-\imath\beta z). \end{aligned} \tag{3.9}$$

From this we can calculate the power flow in the waveguide:

$$\begin{aligned} P &= \frac{1}{2} Re \int_A \vec{E}\times\vec{H}^*\cdot d\vec{a} \\ &= \pi(|E_0|^2 \frac{\beta\omega\epsilon_0 R^2}{2k_c^2} J_1^2(k_c R)). \end{aligned} \tag{3.10}$$

The power lost in the walls per unit length becomes

$$\begin{aligned} \frac{dP_{\text{wall}}}{dz} &= \frac{R_s}{2}\oint_l |n\times\vec{H}|^2 dl \\ &= R_s\pi R|E_0|^2\left(\frac{\omega\epsilon_0}{k_c}\right)^2 J_1(k_c R)^2 \end{aligned} \tag{3.11}$$

We can then define the attenuation constant in the waveguide:

$$\begin{aligned} \alpha_{\text{wg}} &\equiv \frac{1}{2P}\frac{dP_{\text{wall}}}{dz} \\ &= R_s\frac{\omega\epsilon_0}{\beta R}. \end{aligned} \tag{3.12}$$

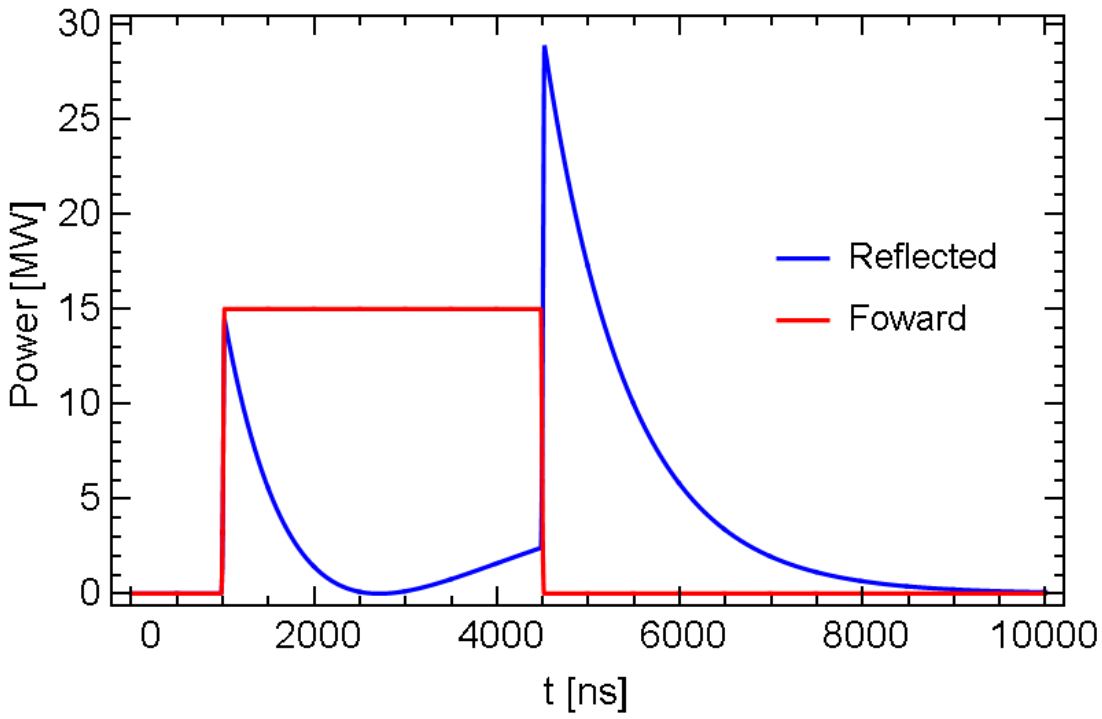

Figure 3.28: Power transmitted to and reflected from the cryogenic S-band cavity with $\beta = 4.66$ and $Q_0 = 93,419$. Blue is the reflected rf power and red is the input rf power.

Since α_{wg} is small, we can expand the exponential that gives the power deposited $P_{\text{wg}} = P_{in} 2\alpha_{\text{wg}} z$. Then for a 15 MW input pulse of 3.5 μs the power deposited is 12.33 Rs J/pulse/m.

We can use the time dependent equivalent circuit model from C.4 to calculate the reflected power from the cavity. Using the parameters for the system at 20 K, where $Q_0 = 93,419$ and $\beta = 4.66$ is the coupling of the system, then Figure 3.28 shows the reflected and input rf power.

The result of integrating the reflected rf power is 35.54 J/pulse is reflected back to the waveguide. Combining power lost in the waveguide from the input and reflected power gives the result, 20.56 R_s J/pulse/m.

Gordon Bowden incorporated this information into a model to calculate the temperature distribution along the waveguide from room temperature at the mode launcher. The result of the calculation show that 5.2 Watts will flow from the waveguide into the thermal shield of the cryocooler, when incorporating IR radiation from the environment and the pulse heating

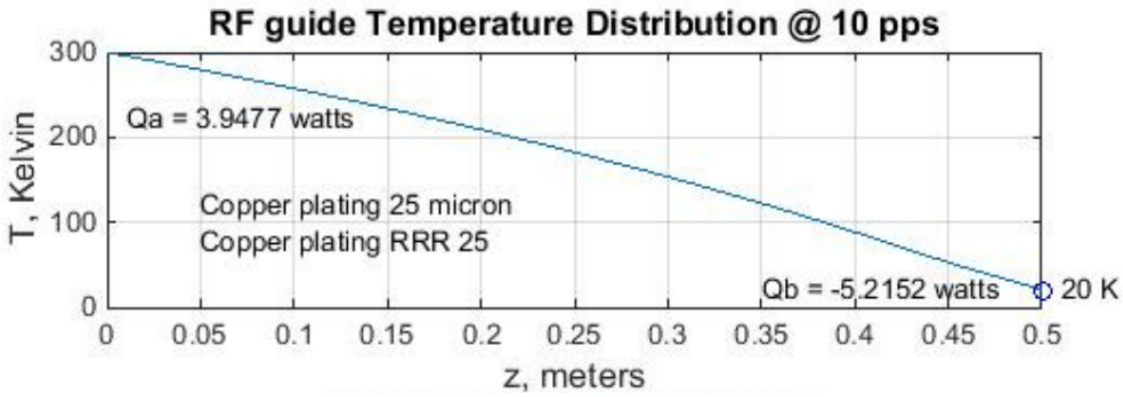

Figure 3.29: Temperature distribution of the circular waveguide assuming the end temperature are fixed. Heat input is from conduction via the room temperature mode launcher, IR radiation, and rf pulse heating of the waveguide [165]

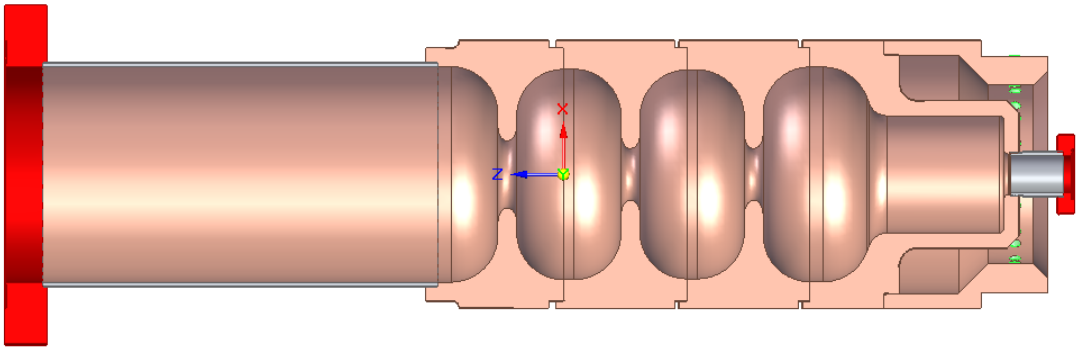

Figure 3.30: CAD model of the SW accelerating structure

of the waveguide, as seen in Figure 3.29 from [165]. This is an acceptable amount of heat that the cryocooler can handle, and the accelerating structure will generate significantly more heat and will limit operation first.

3.5.3 Mechanical Drawings

The mechanical engineers at SLAC (Diana Gamzina, Ann Sy, Charlie Markusen, Andy Haase, Charles Yoneda, and Gordon Bowden) worked with me to create drawings and engineering models for the S-band cryo single cell structure, Figure 3.30, and experimental setup, Figure 3.31. Manufacturing is now underway.

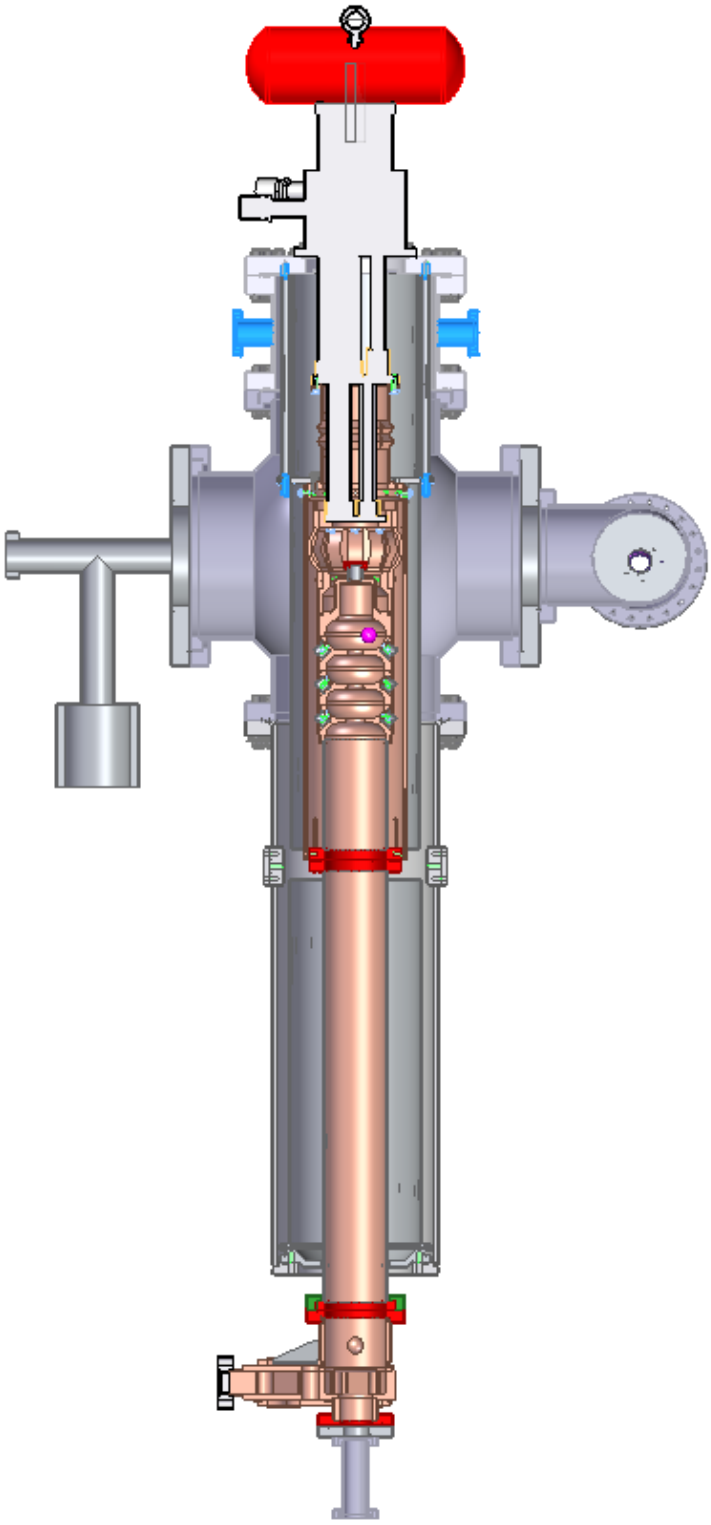

Figure 3.31: CAD model of full experimental setup, including the mode launcher, SW accelerating structure, cryocooler, and cryostat.

CHAPTER 4

High Power Tests of the Cryogenic X-Band Single Cell Structure

4.1 Degradation of Quality Factor in High-Power Tests

4.1.1 Evidence of Quality Factor Degradation

The initial data for 1C-SW-A2.75-T2.0-Cryo-Cu-SLAC-#2 showed unexpected behavior [159]. I will show an example pulse from this data set in Figure 4.1 at 45 K. In this pulse, the time constant is measured during the decay of the reflected rf signal and used to find Q_T. The measured Q_T from this pulse was $Q_{\mathrm{T}} = 7,531$. This value would correspond to a temperature of 133 K, according to the low power measurements with the VNA. The expected Q_T value at 45 K would be $Q_T = 10,183$.

To investigate this abnormally small Q_0, I conducted a systematic study of the accelerating structure. I measured the cavity for different pulse lengths: 100, 150, 200, 300, 400, 500, 650, and 800 ns flat gradient for a shaped rf pulse as described in Figure 3.10; different temperatures: 10, 25, 45, 77, 150, 293 K; different repetition rates: 5, 10, 30 Hz; and varying power levels, from the smallest measurable input rf power to the largest power before being limited by rf breakdowns. The number of rf power data points taken was between 40 and 50 for each specific combination of temperature, pulse length, and repetition rate. For each rf power data point, the down mixed rf signals and dark current signals were averaged over 100 consecutive pulses. At each data point, the rf pulse shape was corrected to create a flat gradient inside the cavity by linear feedback.

From these results, I found that for pulses where the peak surface electric field was less

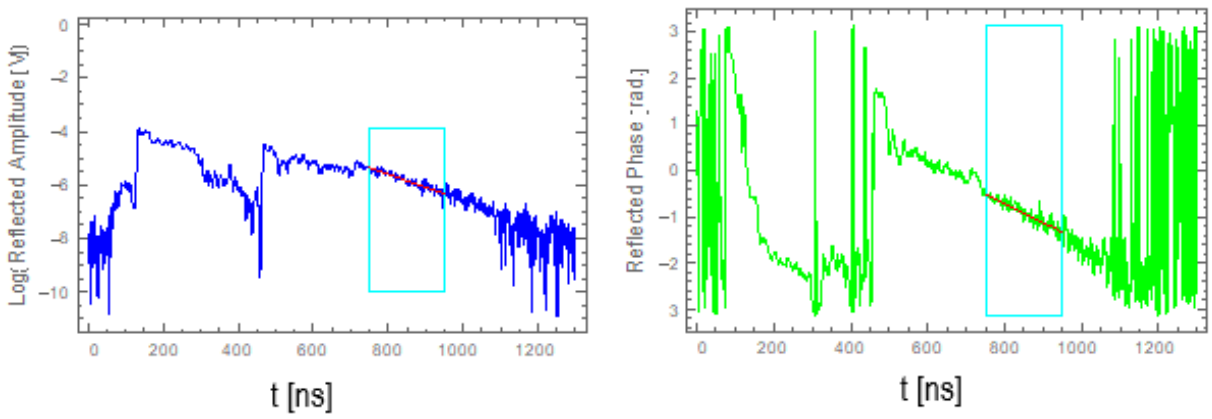

(a) (b)

Figure 4.1: (a) Log reflected magnitude and (b) phase for a high-power pulse from 1C-SW-A2.75-T2.0-Cryo-Cu-SLAC-#2. The box defines the range in time where the time constant is measured

than 300 MV/m, the equivalent circuit model well-described the data as described in C. Pulses with peak surface electric fields larger than this value showed discrepancies between the reconstructed and measured signals. Two example pulses, one with lower input rf power and surface electric fields < 300 MV/m and another pulse with higher input power are shown in Figure 4.2. Both of these example pulses had 400 ns flat gradient pulse length input power and were operate at 45 K and 10 Hz repetition rate. The expected rf parameters values at 45 K from VNA measurements are $Q_0 = 30,263$, $Q_E = 15,361$, and therefore the cavity is over-coupled with a $\beta = 1.97$.

4.1.2 Calculating Gradients with Dynamic Quality Factor

As mentioned in 3.3.1, there are two current monitors in the system. One current monitor is located on the mode launcher, far from the accelerating structure. The other current monitor is on the beam pipe of 1C-SW-A2.75-T2.0-Cryo-Cu-SLAC-#2, behind a brazed in piece of copper foil. The copper foil will stop low energy electrons. Measuring the dark current from each of the current monitors gives a different value for the field enhancement β_E. $\beta_E = 16.2 \pm 0.77$ for the current monitor on the structure and $\beta_E = 28.1 \pm 2.77$ for the

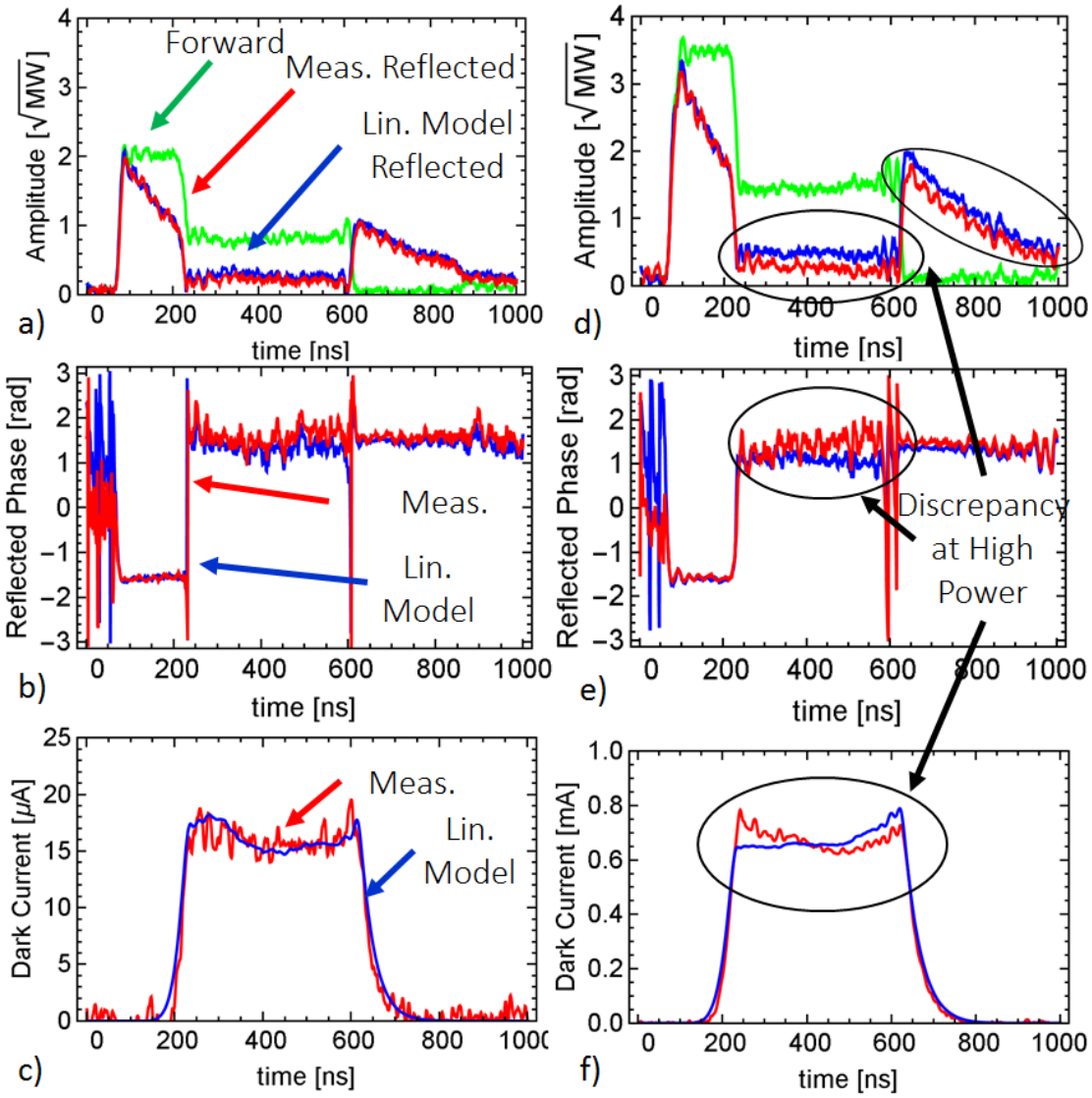

Figure 4.2: Measurement (red) and linear model (blue) for two pulses with flat gradient section of 400 ns of low (left) and high (right) power at 45 K and 10 Hz. The input rf pulse (green), begins at 50 ns and ends at 600 ns. The model agrees with the measured signal for $Q_0 = 30,263$ at low power ((a)-(c)). For high power ((d)-(f)), the linear model does not match the measured rf and dark current signals.

current monitor on the mode launcher. This β_E splitting may be caused by the geometry, the copper foil, or a combination of both.

In the data it became evident that the Q_0 and ω_0 of 1C-SW-A2.75-T2.0-Cryo-Cu-SLAC-#2 decrease during high power rf pulses, and return to their low power value before the subsequent pulse. I decided to calculate the electric field insdie the cavity, while allowing the Q_0 and ω_0 to vary in time. The time-dependence of these parameters would be found by fitting to the measured rf and dark current signals. The framework for calculating the electromagnetic fields inside a resonant cavity with changing rf parameters is derived inB, and I will use equation B.42. For this model, t_1 is defined as the beginning of the rf pulse, t_2 as the beginning of the flat part, and t_3 as the end of the flat part. This model will be termed the nonlinear model, while the equivalent circuit model is the linear model.

For fitting the model, I used dark current signals as the primary driver of the fit quality. The rf pulse is shaped to create a flat gradient for a portion of the pulse, and whether the resulting gradient is flat or not depends on the Q_0. Since the dark current is strongly dependent on the peak surface electric field, then any deviations from a flat gradient will be magnified. This allows a more accurate constraint of the Q_0 during the rf pulse than measuring the time constant.

To fit measurements to the nonlinear model using the dark currents, I first found the exact field enhancement factor β during each pulse. This removes any worry that β_E changing between pulses will affect the data. I find β_E for each pulse by fitting the exponential growth of the dark current to the calculated electric fields from t_1 to t_2. I use the linear model for the field calculation and assumed β_E is constant during the rf pulse. Next, with the nonlinear model, I calculated the cavity fields and dark current, using the β_E I obtained. I found $Q_0(t)$ by matching the measured and calculated dark currents. Finally, I found $\omega_0(t)$ by similarly fitting the rf phase of the reflected signal.

I tested many functional dependencies for $\omega_0(t)$ and $Q_0(t)$ and found that the model shown in Figure 4.3(e) and (f) best describes the data. The initial value of $Q_0(t)$ is equal to its measured low power value and begins to decrease at time t_1 before becoming constant

again at time t_2 (Figure 4.3(e) and (f)). The Q_0 returns to its original value by the start of the next rf pulse; the enhanced losses are a reversible effect. However, in this experiment I cannot robustly determine exactly when the return to the initial value occurs. I find that the resonant frequency of the cavity changes over a longer time scale than $Q_0(t)$, where $\omega_0(t)$ begins to decrease at time t_1 and reaches a minimum value at time t_3 (Figure 4.3(e) and (f)(f)). As I cannot determine exactly when the ω_0 recovers to its initial value, I leave ω_0 at the minimum after t_3. In both cases, I have used a monotonic cubic spline between the starting and minimum value. I found that the measured reflected and dark current signals were well matched using the nonlinear model, as shown in Figure 4.3(e) and (f)(a)-(c). In Figure 4.3(d) shows the peak surface electric field calculated by both the linear and nonlinear models, where the difference in the maximum field is 6%, even though the Q_0 drops by 20%.

This procedure was applied to every measured rf pulse. The resulting changes in Q_0 for these measured pulses were analyzed for any trends.

4.1.3 Results of Dynamic Quality Factor Model

I found no dependence of the minimum values for Q_0 and ω_0 ($Q_0(t_2)$ and $\omega_0(t_3)$) on the repetition rate. Figure 4.4 shows an example of this, with the final Q_0 and ω_0 values for power scans at T=25 K, $t_p = 400$ ns, and the three repetition rates: 5, 10, and 30 Hz. This implies that average rf power does not affect the Q_0 degradation, since the heat deposited in the structure will change with the repetition rate.

I also found no dependence of the minimum values for Q_0 and ω_0 on the pulse length of the flat part of the gradient. This data set is shown in Figure 4.5 for T=45 K, and repetition rate 30 Hz. This independence of $Q_0(t_2)$ on pulse length is inconsistent with a hypothesis that the surface rf resistance increase is caused by pulsed rf surface heating, since the maximum temperature change due to the pulsed surface heating, and thus an increase in rf surface resistance, increases with the square root of the pulse length from equation 2.12.

I also examined the different behaviors of the Q_0 degradation for the different operational temperatures. Figure 4.6 summarizes all this data for pulse length of 400 ns and repetition

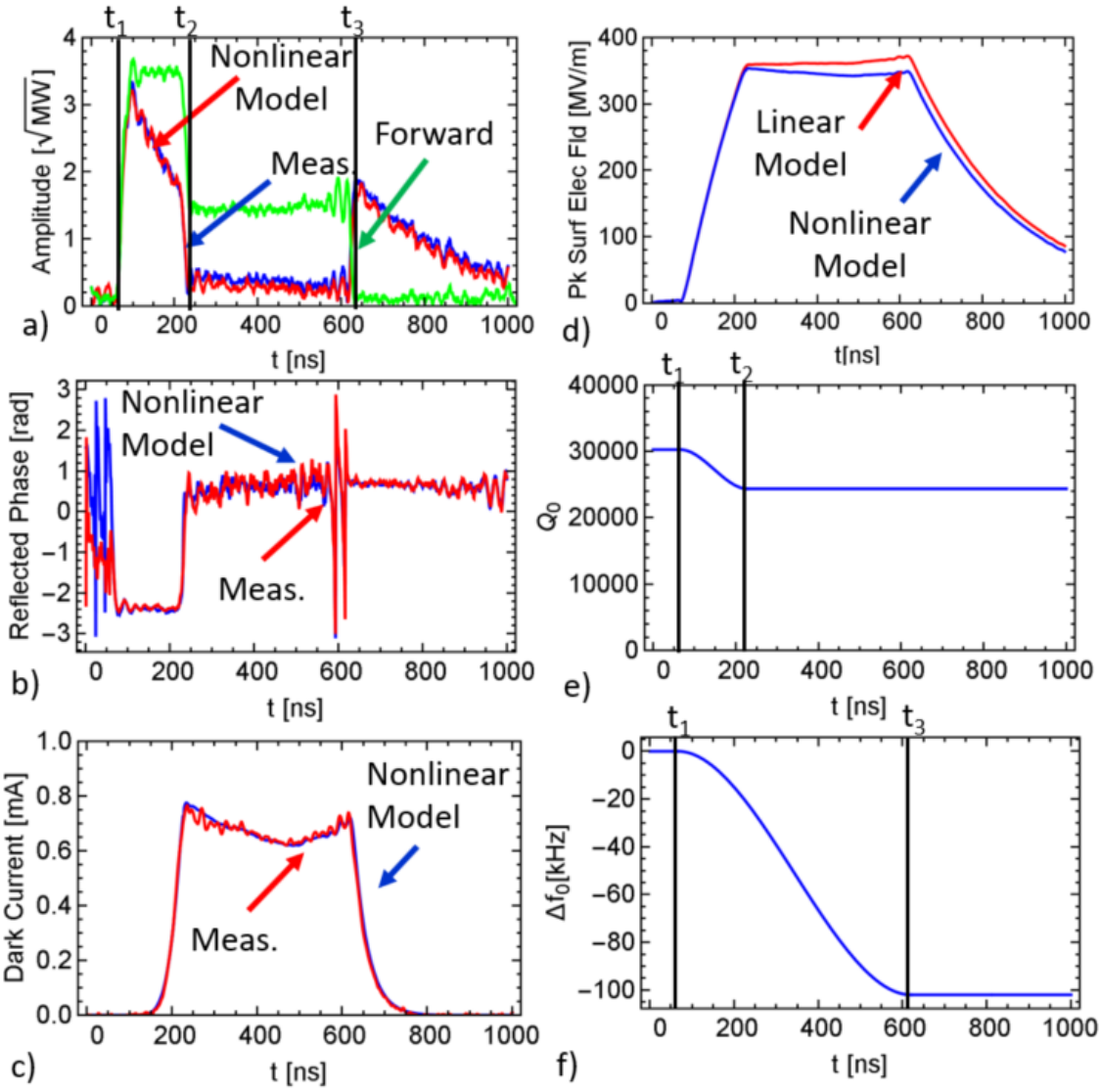

Figure 4.3: Measured data (red) for 45 K, also shown in Figure 4.2(d)-(f), and nonlinear model (blue) are plotted in (a)-(c). (d) shows the calculated gradient for linear and nonlinear models. (e) and (f) show the predicted change in $Q_0(t)$ and $f_0(t) = \omega_0(t)/2\pi$ respectively. Comparing the linear model in Figure 4.2(d)-(f) and the nonlinear model in Figure 4.3(a)-(c), the nonlinear model better predicts the data.

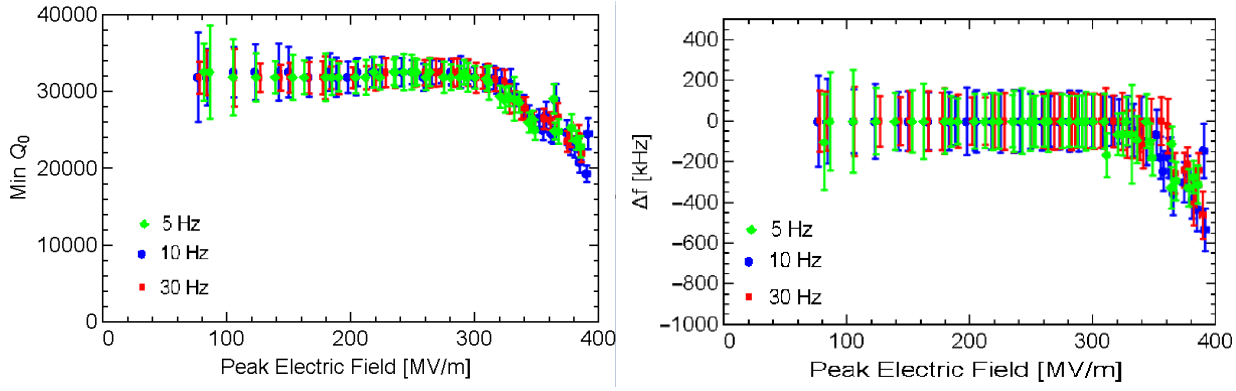

(a) (b)

Figure 4.4: (a) final Q_0 and (b) frequency shift for T=25 K, t_p = 400 ns, and repetition rates: 5, 10, and 30 Hz. There is no obvious difference between the three data sets.

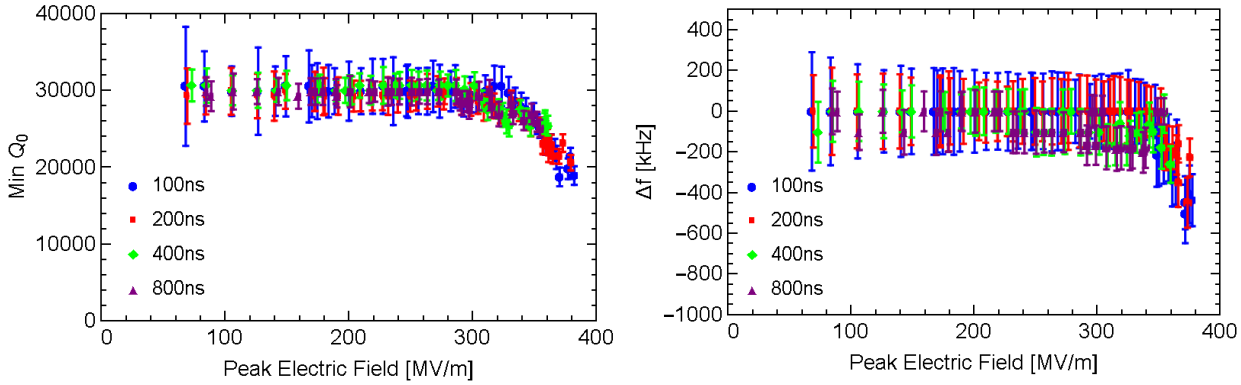

(a) (b)

Figure 4.5: (a) final Q_0 and (b) frequency shift for T=45 K, repetition rate 30 Hz for multiple pulse lengths. There is no obvious difference between the four data sets.

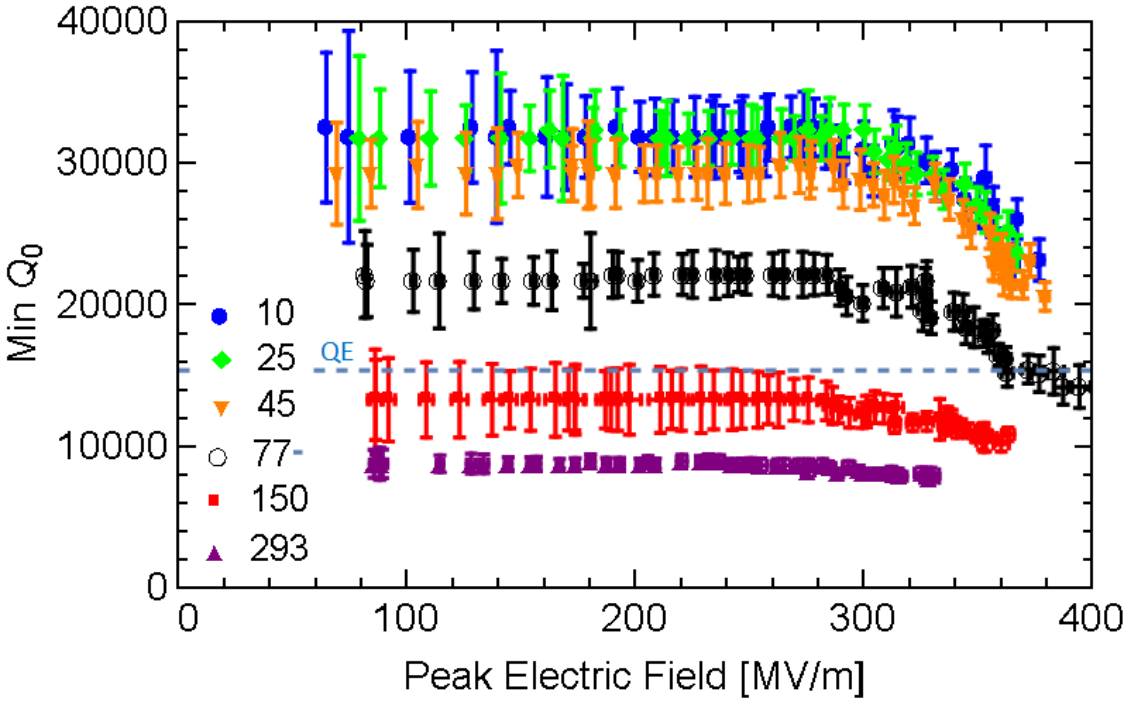

Figure 4.6: Final Q_0 value for all temperatures with $t_p = 400$ ns. Included is the dashed line that shows the value of Q_E.

rate of 30 Hz (except 10 K which is at 10 Hz, since the cryocooler cannot operate at 30 Hz for this temperature). At each temperature except room temperature, the Q_0 appears to start decreasing at the same peak surface electric field, near 300 MV/m. At room temperature, the Q_0 degradation is minimal and consistent with no change in the Q_0. I also include a plot of the final Q_0 value relative to the initial Q_0 value at the beginning of the rf pulse in Figure 4.7. In this plot we see more clearly that the change in Q_0 occurs near the same field level and is not dependent on the temperature.

4.1.4 Missing Power

Next, I quantify what we term the missing rf power, which is the difference between the power lost in the cavity calculated by the linear and nonlinear models, when the nonlinear model accurately describes the measured data. This value described the amount of extra power that disappears inside the structure, in addition to the normal power lost through resistive heating in the cavity walls for the unchanged Q_0 value. I find that the missing

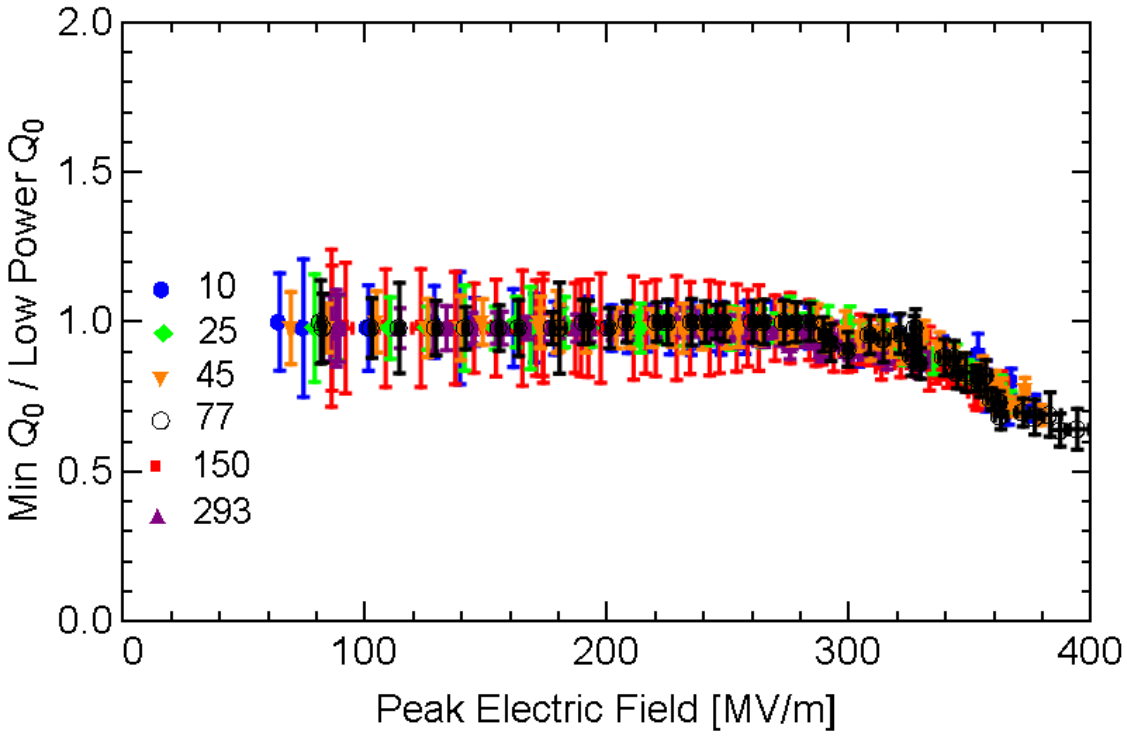

Figure 4.7: Final Q_0 value relative to initial value for all temperatures with $t_p = 400$ ns.

power correlates well with the measured magnitude of dark current, shown in Figure 4.8 for T=45 K.

The missing power also grows what appears to be linearly with the peak surface electric field. I show this dependence for temperatures between 10 K and 77 K, where again the change temperature does not change the behavior of the missing power. This data is summarized in Figure 4.9.

With this data presented, I hypothesize that the degradation of Q_0 is caused by dark current beam loading, where field emitted electrons are accelerated by the electric field inside the cavity, and absorb power, which is then seen as missing from the rf system. The amount of power in dark current would then be correlated with the amount of dark current. In addition, the amount of dark current has an exponential dependence on the peak surface electric field, and thus the power in the dark current should have a similar dependence.

The beam loading could also be the responsible for the behavior of $\omega_0(t)$, by what is called the reactive component modifying the rf phase of the fields inside the cavity, which

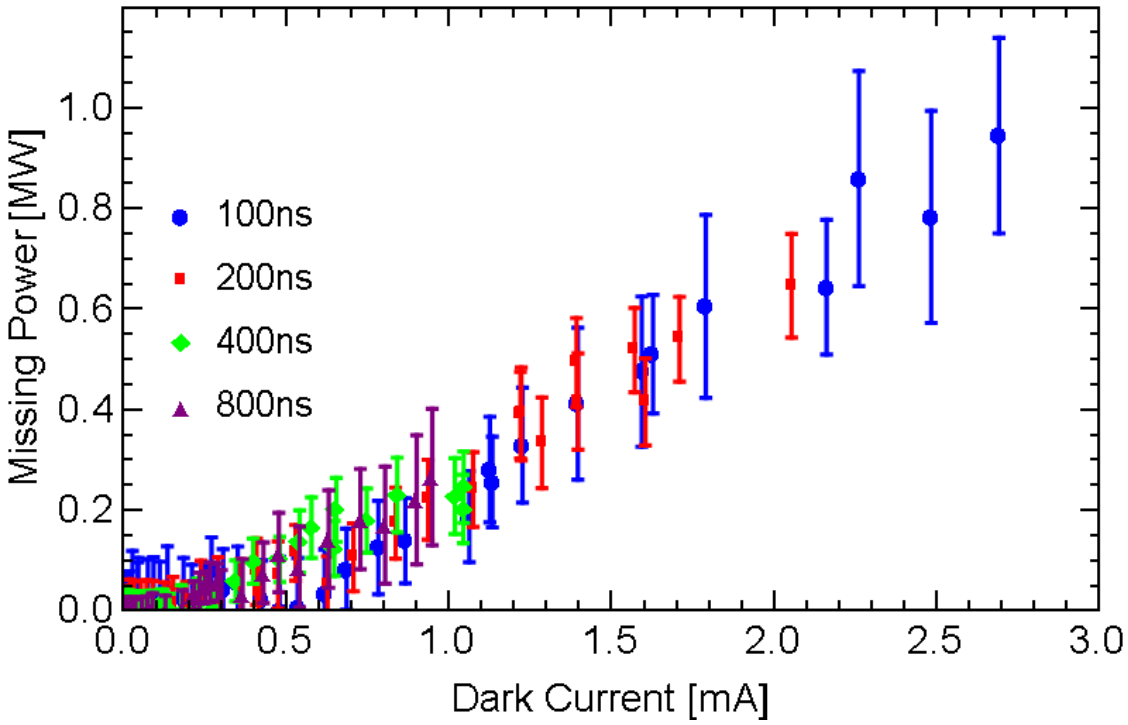

Figure 4.8: Missing power in the accelerating cavity versus the measured amplitude of dark current for different rf input pulse lengths and T=45 K. The missing power is the difference between what we measured as the power lost to the cavity walls, and what would have been lost to the walls in the linear model. The measured missing power is correlated with the amplitude of the dark current.

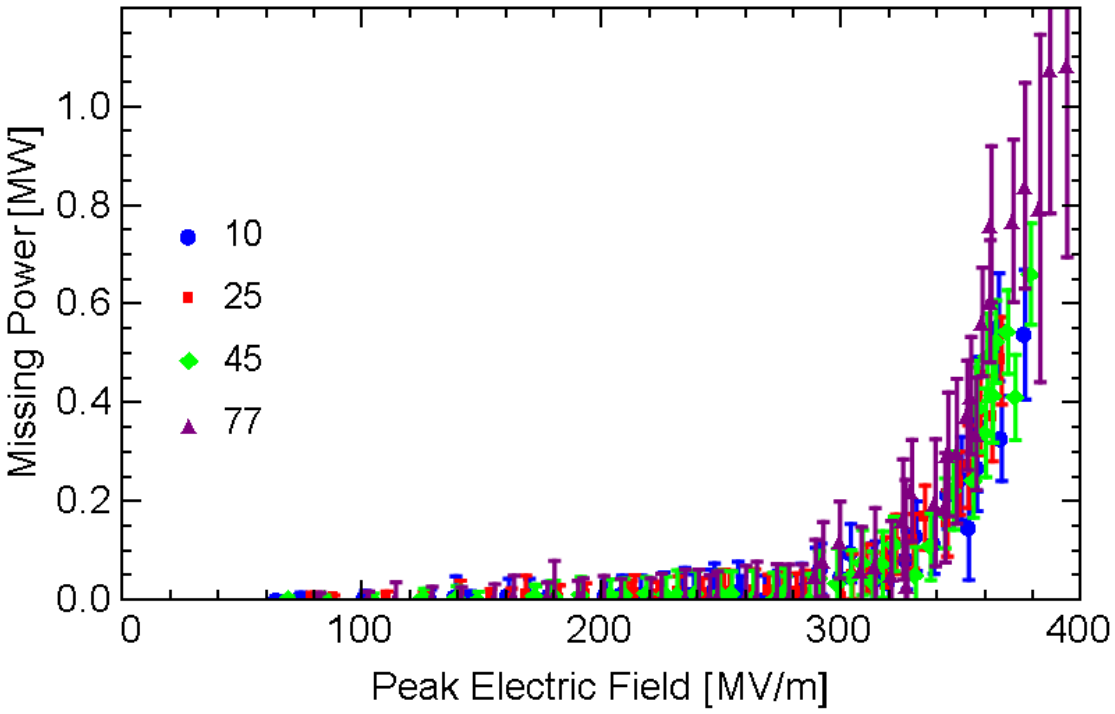

Figure 4.9: Missing power in the accelerating cavity versus the peak surface electric field for different operating temperatures and $t_p = 200$ ns. The missing power is the difference between what we measured as the power lost to the cavity walls, and what would have been lost to the walls in the linear model. The measured missing power is correlated with the amplitude of the dark current.

would appear as a change of the resonant frequency [166].

To investigate the possibility of beam loading, we simulated field emitted electrons using a finite element electromagnetic and particle tracking code, ACE3P [167]. In the simulations, electrons were emitted uniformly from the cavity walls using the Fowler-Nordheim field emission model with $\beta = 25$ and work function $\phi = 4.2\ eV$ [85]. Particles lost in the walls or current monitors generated no secondary or elastically scattered electrons. The simulated electrons at the current monitors showed Fowler-Nordheim behavior, with the current strongly dependent on the applied electric field. The β_E measured from the simulated electrons at the monitors exhibited the same splitting between the two monitors and were consistent with the experimental values. This model does not consider the following: location and size of the emitters were not known, secondary and elastically scattered electrons are ignored, the work function is not precisely known, and ambient magnetic fields that can distort the beam.

In these simulations, we calculated the average energy of the field emitted electrons when they struck a wall or current monitor for a given accelerating gradient. Figure 4.10 shows the simulated values for the average field emitted electron energies along with a cubic interpolation. To compare measured missing power to these simulations, the power absorbed by the dark current was calculated by multiplying the measured dark current magnitude by the average electron energy corresponding to an analogous accelerating gradient and finally multiplying by a final scalar fitting constant. This final constant describes the percentage of field emitted electrons that reach the current monitors, and the final value is 0.0525%. The result of the simulation are included in Figure 4.11 and is consistent with the measured missing power for both the peak surface electric field and the dark current magnitude.

I end with the conclusion that the dominant factor causing the degradation of Q_0 is rf power absorbed by accelerated field emission currents, or dark current beam loading. Similar effects have been seen at high fields in room temperature cavities [168]. However, in the case of a cryogenic cavity the effect is more pronounced for two reasons. First, since the sustained surface electric fields are larger than typical room temperature experiments, more field emission currents are produced, greatly enhancing the beam loading. Second,

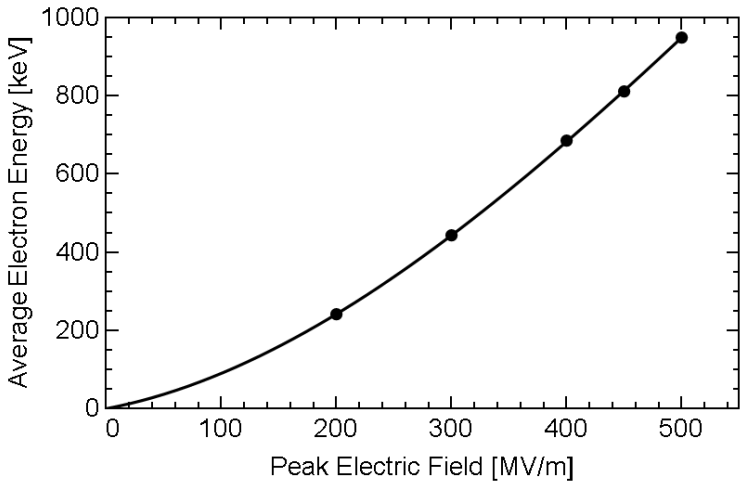

Figure 4.10: Simulated values for the average energy of field emitted electrons when they strike a wall or current monitor. The solid line is a cubic interpolation between the simulated points.

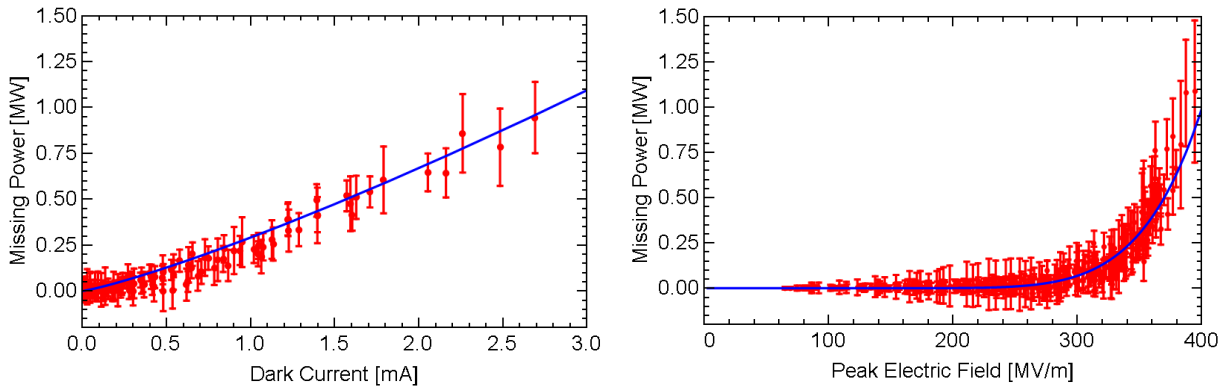

(a) (b)

Figure 4.11: Missing power plotted against the (a) dark current intensity and (b) peak surface electric field. Red points are measured data, and the blue lines are simulated trends.

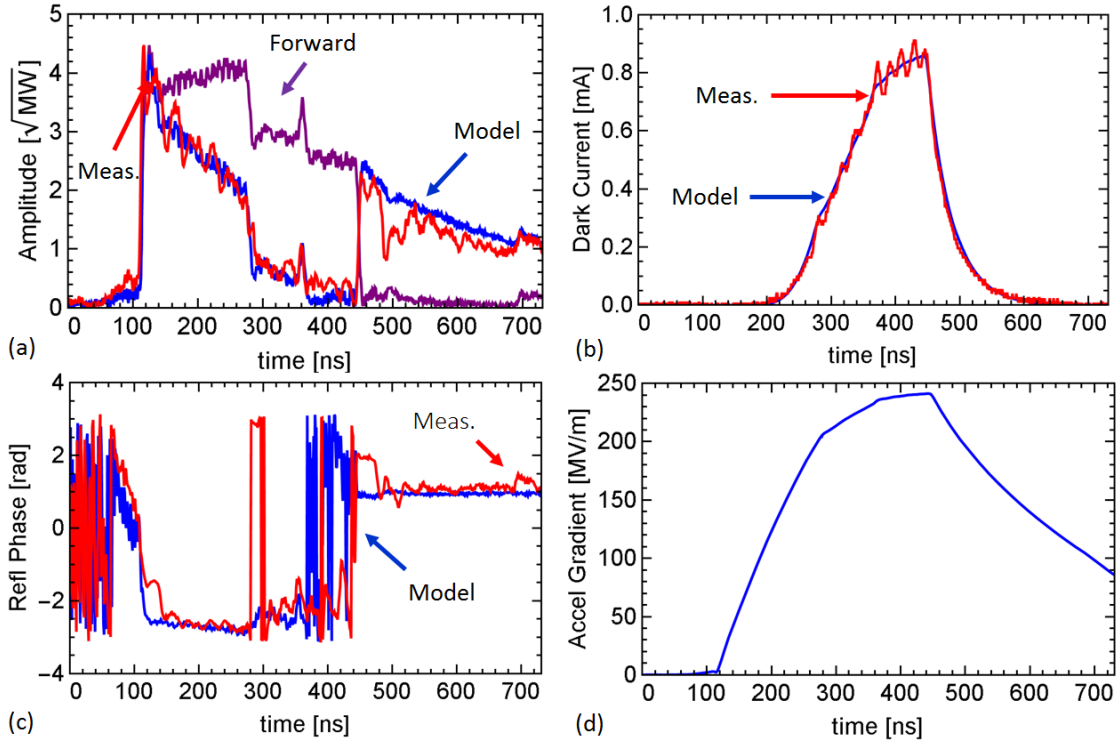

Figure 4.12: A Typical pulse from the data of 1C-SW-A2.75-T2.0-Cryo-Cu-SLAC-#2 at T=45 K.

since Q_0 is increased at cryogenic temperatures, the power lost due to beam loading is not overwhelmed by power lost to resistive losses. It is possible that other mechanisms of rf losses are also present, but due to the strong dependence of field emission current on surface fields, the effect of beam loading is observed to dominate in this experiment.

4.2 Breakdown Rates in the Cryogenic Accelerating Structure

Now that I can analyze data that has a non-constant Q_0, I can return to the high-power data mentioned at the beginning of this chapter and reprocess the results for a BDR. I used the same method as described in 4.1.2, and used the results of the low power measurements from 3.3.3 for the Q_0 at the beginning of the pulse. Figure 4.12 shows a typical pulse with the nonlinear model fits for the data set at T=45 K. In this example, the Q_0 starts at the low power value of $Q_0(0) = 30,410$ and decreases to 17,931. The average gradient over the

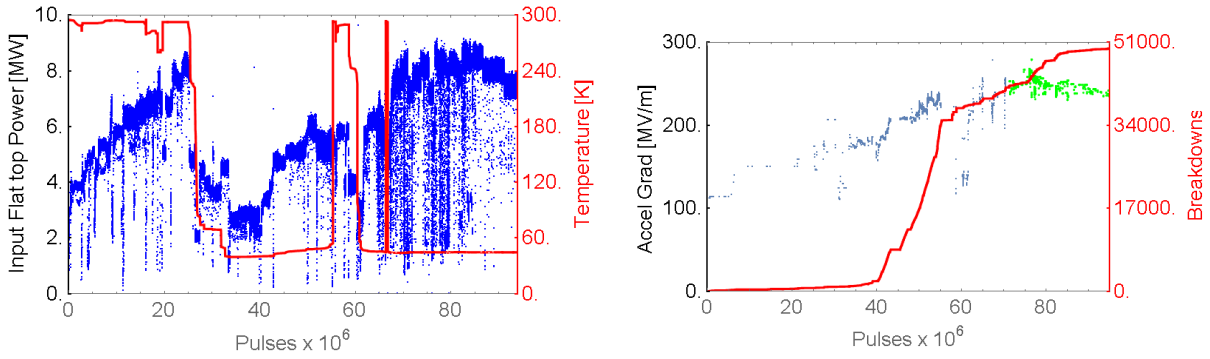

(a) (b)

Figure 4.13: The processing history for 1C-SW-A2.75-T2.0-Cryo-Cu-SLAC-#2. (a) Blue is the input flat power and red is the temperature. (b) Red is the cumulative number of recorded breakdowns. Blue is the gradient from the linear model at a breakdown while the structure is processing, and the green shows the calculated gradient from the nonlinear model during measurements of the rf breakdown rate, with 150 ns flat gradient

flat gradient section of the shaped rf pulse is calculated to be 237.9 ± 5.3 MV/m, down from the 248.0 MV/m if the Q_0 had remained constant at the low power value. The change in gradient is relatively small for two reasons: the external quality factor $Q_E = 15347$ is smaller Q_0 at this temperature and the decrease in Q_0 changes the coupling closer to critical $\beta = 1$. For the same power level, we would only expect the asymptotic accelerating gradient to increase by about 20 % for this drop in Q_0. Second, the forward rf pulse is optimized to create a flat gradient for the smaller Q_0. For this same pulse, a cavity where the Q_0 does not decrease would not reach the asymptotic gradient. Thus the average over where the gradient should be flat is instead an average over a growing function of gradient, and is lower than the asymptotic gradient.

Figure 4.13 shows the processing history of 1C-SW-A2.75-T2.0-Cryo-Cu-SLAC-#2, including the temperature, input rf power, number of breakdowns, and the accelerating gradient in the structure at the time. The structure was processed to high gradient before BDR measurements were conducted.

The structure was deemed to be processed enough for BDR statistics after 70 million

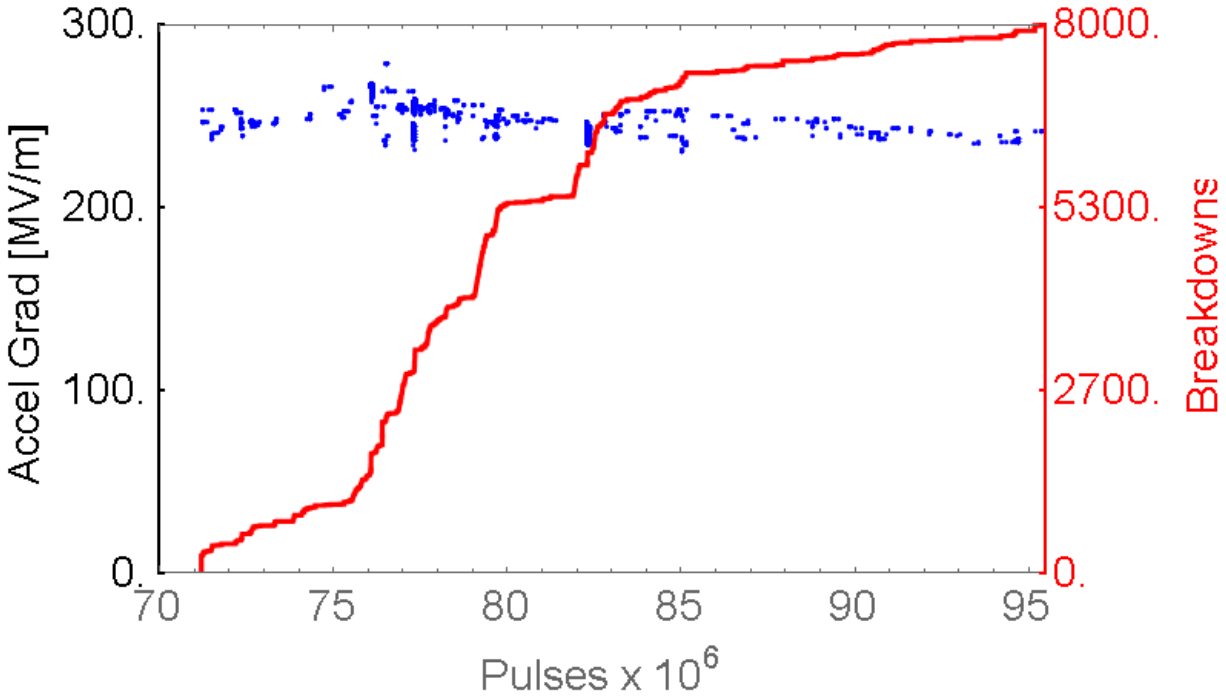

Figure 4.14: Cumulative Breakdowns and calculated accelerating gradient from the nonlinear model for the processed structure that is used to measure rf breakdown rates.

pulses and data taking continued up to 95 million pulses; Figure 4.14 shows a zoom in on this time period.

Breakdown rate was measured for periods of 1-3 million pulses where the gradient and rate of breakdowns were relatively constant. I measured both the first (or "trigger") BDR and the total BDR. The first breakdown rate only counts the rate of the trigger breakdowns, excluding breakdowns that are part of chain. Total breakdown rate counts all breakdowns, including the ones in breakdown chains.

The measured value for the first breakdown rate is 2×10^{-4} breakdowns/pulse/m at 250 MV/m and shaped pulse with 150 ns flat gradient. The total breakdown rate is 10^{-3} breakdowns/pulse/m for accelerating gradients of 250 MV/m at 150 ns pulse length. The 250 MV/m accelerating gradient corresponds to a 507 MV/m peak surface electric field for this accelerating structure. Figure 4.15 compares these rf breakdown rates to previous measurements in room temperature copper, hard copper, and hard CuAg accelerating structures

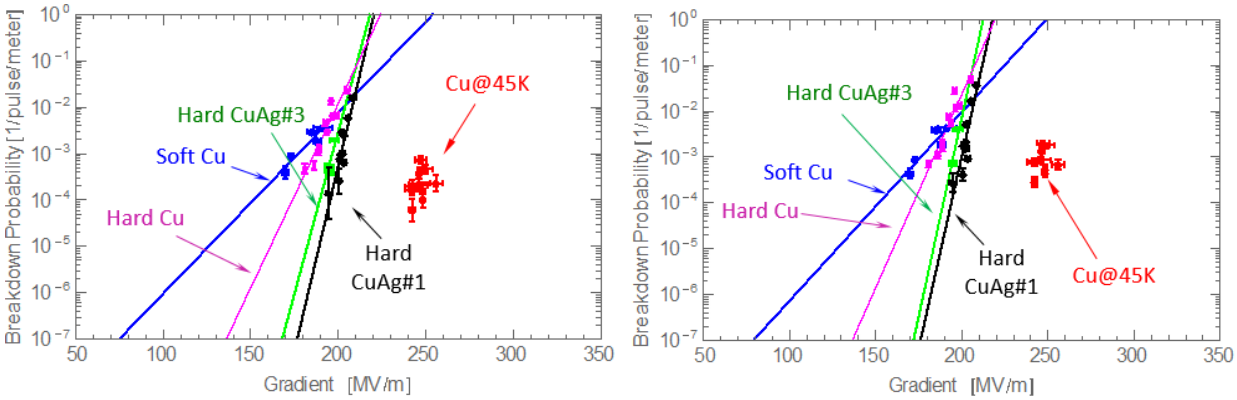

(a) (b)

Figure 4.15: Breakdown rate vs. gradient: top) first, trigger rf breakdowns; bottom) all rf breakdowns. For the breakdown probability $10^{-3} - 10^{-4}$ 1/pulse/m cryogenic structure clearly outperforms record data from hard CuAg obtained in initial stages of conditioning. CuAg on final stages of conditioning very similar to hard Cu.

of the same shape (2.75 mm aperture radius) [91].

In these results, cryogenic copper accelerating structures have lower BDR rates than comparable structures at room temperatures, and lower BDRs than even the hard CuAg structures that had been the state of the art for conventional copper structures. These results support the prevailing theory of rf breakdown physics that increasing the hardness and reducing stress of accelerating structures can continue to improve the operational gradients.

CHAPTER 5

Ultra-High Brightness Cryogenic Copper RF Photoinjector: TOPGUN

As stated in 1.4.1, the brightness of a photoinjector increases with the square of the surface electric field at the time the electron beam is created. The ultra-high operating gradients that have been shown to be attainable in cryogenic accelerating structures would enable a large leap in electron beam brightness. Combined with geometry modifications to bring the launch phase closer to rf crest, a LCLS gun replacement with over an order of magnitude increase in the electron beam brightness can be designed and created. The proposed cryogenic copper rf photoinjector has been dubbed the TOPGUN.

5.1 Automation in SUPERFISH

To complete the rf design of the TOPGUN photoinjector, I decided that automated optimization would be beneficial. This toolkit utilizes SUPERFISH [161], a 2D finite element electromagnetic simulation code, where the rf design was verified later by HFSS [156], a 3-D finitie element solver. SUPERFISH can solve geometric iterations more quickly, and so is used for the automatic optimization, while HFSS is only used as a final step. The optimizing toolkit is controlled through Mathematica. I will present the geometries that the toolkit can create, and then describe the steps that the optimization routine runs through.

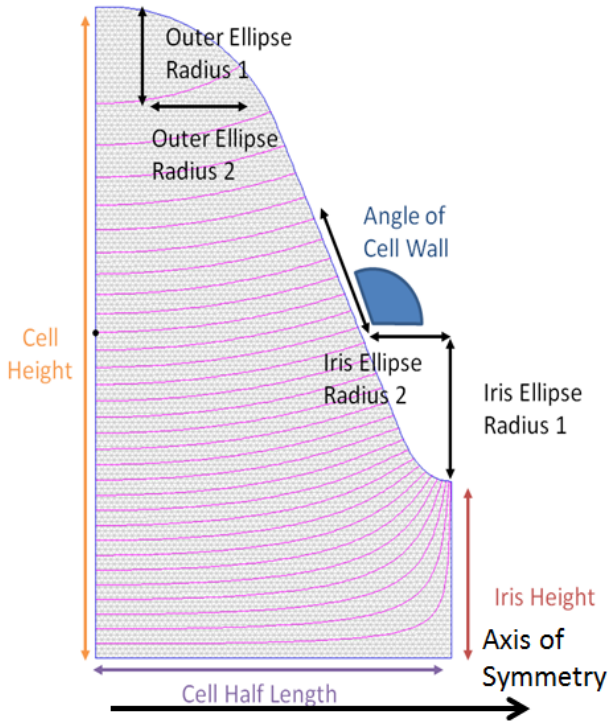

Figure 5.1: Figure showing the 8 independent variables for half of a cell of photogun geometry.

5.1.1 Geometry

This toolkit was designed to simulate general photoguns that can be constructed from one cathode cell and an arbitrary number of full cells fed by a cylindrical waveguide. The rf power is coupled to the gun through a cylindrical waveguide. To make the toolkit flexible, the geometry was made to be generic. The cathode cell is modeled as a generalized half-cell is constructed from 8 independent geometric variables, that are depicted in Figure 5.1, and includes a cathode back plate, which is assumed to be a copper wall for this exercise.

Full cells are constructed from two of the half cells back to back, giving 14 independent parameters (the cell height and cell half-length will be equal for each generalized half-cell). The cylindrical waveguide is connected to the last off the arbitrary number of full cells. Figure 5.2 shows an example of one full cell and the cylindrical waveguide.

This toolkit does not currently support re-entrant nose-cones. The geometry is otherwise flexible enough to be adapted to create the geometry of the single cell accelerating structure

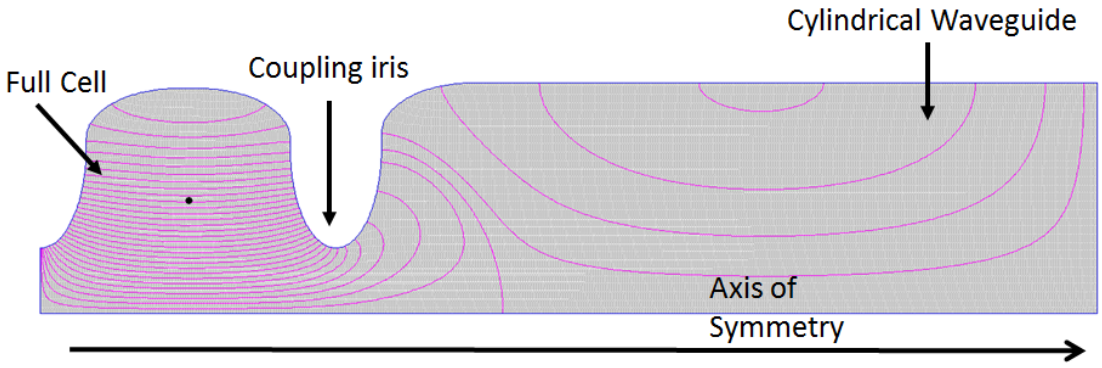

Figure 5.2: Figure showing one full cell and the cylindrical waveguide.

or standing wave linacs with an arbitrary number of cells.

5.1.2 Optimization Loop

The toolkit works in a loop, each time a geometric parameter of interested is changed or incremented a new tuned gun is created from the following steps.

5.1.2.1 Frequency Tuning

The first step in the optimization is to create a geometry with the correct frequency within a given tolerance. The method used here is to initially tune each cell to the desired frequency separately, with perfect H boundaries between cells. To do this, I used an iterative method, where the structure is first solved to find f_{calc}, and then the cell height (CH) is iterated as follows:

$$CH_{i+1} = CH_i \frac{f_{target}}{f_{calc}}. \tag{5.1}$$

This relatively crude method can reach a 0.001% tolerance band around the design frequency within a few iterations. After the process is complete for each cell in the geometry, the entire geometry should be close to the design frequency in the π mode.

5.1.2.2 Field Balance

At this point the next step in the optimization routine is to balance the electric field. For photoguns with a cathode cell and a single full cell, the arbitrary ratio between the max on-axis electric field can be controlled. In this toolkit, the ratio is controlled by decreasing or increasing the full cell height by a given percentage and changing the cathode cell height by the same percentage in the opposite direction. The percentage change is calculated from how far the electric field ratio is off the desired value. Using this method, the frequency of the overall photogun geometry will not shift significantly while changing the electric field balance ratio. This method has also been adopted to the single cell geometry, where the middle cell has twice the on-axis field of the outer cells, but the ratio of inner to outer cells can also be chosen arbitrarily.

After the field balancing, the frequency of the π mode may have been altered from the design value. In that case the structure is frequency tuned again by changing the cell height of all included cells simultaneously in the manner described by 5.1. I have found that this method does not significantly affect the field balance, but if greater accuracy is needed the field balance and whole structure frequency tuning can be iterated to reach closer to the design parameters.

5.1.2.3 Matching

The final step to finish the rf design is to match the rf cavity to the input waveguide with the design coupling coefficient, however, SUPERFISH does not calculate β directly. Instead, I infer the Q_E by simulating a resonator composed of the frequency tuned cavity combined with a shorted waveguide. If the length of the shorted waveguide is varied, then I can use an equivalent circuit to extract the Q_E from the variation of the resonant frequency of the combined resonator with changes in the shorted waveguide length.

In the equivalent circuit, the impedance (Z_C) and reflection (Γ_C) of the accelerating

cavity are:

$$\begin{aligned} Z_C(f) &= \frac{f_0}{2i(f-f_0)Q_E}, \\ \Gamma_C(f) &= \frac{Z_C(f)-1}{Z_C(f)+1}. \end{aligned} \tag{5.2}$$

Where f_0 is the resonant frequency of the cavity. The reflection (S_W) from a shorted waveguide of a given length l, cutoff frequency f_c, and ϕ the phase at the beginning of the waveguide:

$$\begin{aligned} \Gamma_W(f) &= -e^{2ilk(f)}e^{i\phi} \\ k(f) &= \frac{2\pi}{c}\sqrt{f^2-f_c^2}, \end{aligned} \tag{5.3}$$

SUPERFISH will find solutions where $\Gamma_W = \Gamma_C$, when the shorted waveguide and rf photogun reach a power exchange equilibrium. Figure 5.3 shows an example scan of waveguide length and the resulting resonant frequency.

Using this process, the coupling can be tuned to a desired value by changing the size of the coupling iris between the last cell and the waveguide. After the coupling is tuned, the field is again balanced, and frequency tuned, which does not change the coupling significantly.

5.1.2.4 Optimization

With these steps, a given set of geometric dimensions and desired rf parameters can be turned into a tuned, matched, and balanced rf photogun. At this point an optimization algorithm can be used to find the best values for the geometric dimensions that are not determined by the previous steps, namely the elliptical radii, and cell wall angle (the iris radius and cell lengths for TOPGUN are set before hand). I used this toolkit to find the largest r/Q for a 1.45 cell rf photogun, within the constraints of the TOPGUN design, of which the major constraint is that the maximum electric field should be on the cathode. The TOPGUN design is presented in the next section.

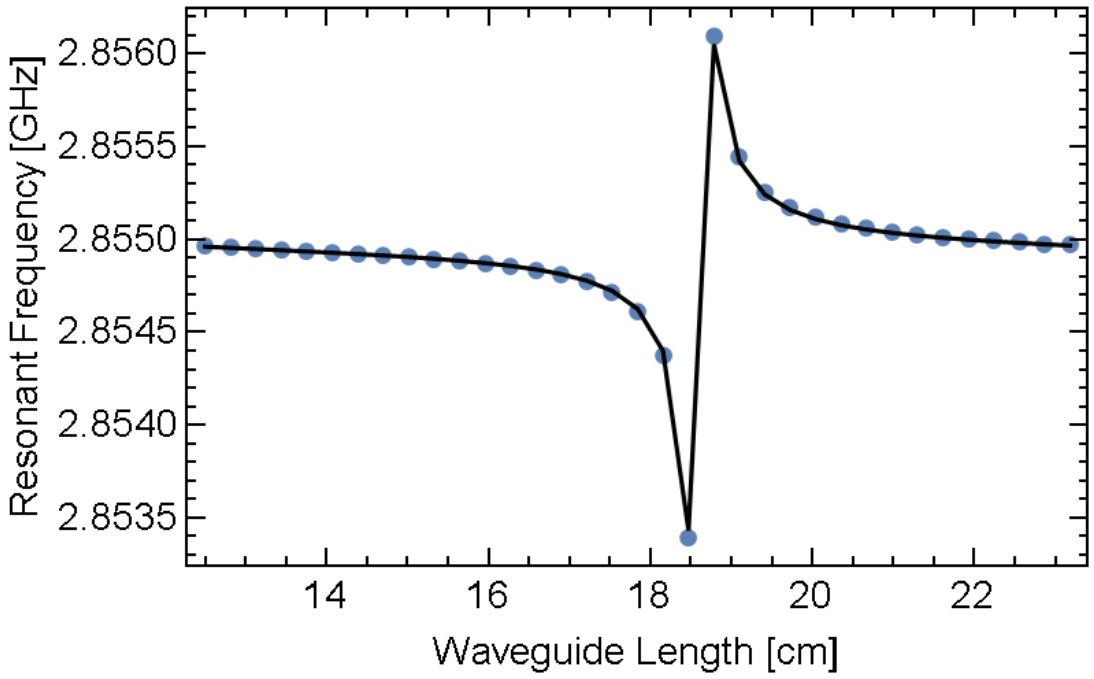

Figure 5.3: Graph shows resonant frequency versus waveguide length, with data from simulations as the blue points. The line is a fit to the data, used to find the Q_E of the system. The parameters for this example are $Q_E = 19,400$, $f_0 = 2.855$ GHz, and $\phi = 4.38$ rad.

5.2 TOPGUN RF Design

In this section I present the current S-Band design of the TOPGUN cryogenic copper rf photoinjector. Also included is a similar model for C-band as an alternative for different applications in 5.2.5. For this design, an increase in possible gradient of approximately a factor of two is assumed, where the TOPGUN is expected to operate with 250 MV/m on the cathode. The increase is based on a similar approximately factor of two increase seen from current operating X-band accelerators to the performance of the X-band cryogenic single cell accelerating structure. This assumption will be investigated in the future with the S-band single cell cryogenic experiment 3.5.

5.2.1 Design Considerations

I designed the TOPGUN photogun to be a drop-in replacement for the current LCLS photoinjector, which is a 1.6 cell S-band cavity[169]. Electrons at LCLS are launched around 60° away from the crest of the rf pulse, due to the length of the cathode cell, therefore the launch gradient is 60 MV/m. The TOPGUN design maximizes the launch gradient both by incorporating the increase in gradient from the cryogenic operating temperature and the design calls for the electron beam to be launched very near maximum electric field in the rf cycle.

To investigate the launch phase, ϕ_0, it can be approximated using the:

$$\alpha_\phi = \frac{2\pi e E_{\text{Cath}}}{f m_e c} \tag{5.4}$$

$$\pi/2 - \phi_0 \sim (2\alpha \sin\phi_0)^{-1}, \tag{5.5}$$

where c is the speed of light, E_{Cath} is the cathode electric field, m_e is the mass of an electron, and e is the charge of an electron [35]. The approximation for the launch phase in this equation is for a 0.5 cathode cell with length 0.5 $\lambda/2$. The launch phase of a cathode cell of length 0.6 $\lambda/2$ will be 20% further from crest, and a shorter cathode cell, the electron bunch can be launched closer to the rf crest.

With this information the following are design choices and considerations for the TOP-

GUN:

- I have chosen to set the cathode cell length to $0.45\lambda/2$. With the shortened cathode cell and larger applied cathode fields, the phase slippage of the electrons traversing the cathode cell is nearly ignorable, and electrons can be launched effectively on crest.

- The cathode cell is not shorter than $0.45\lambda/2$, because then the surface electric field on the first iris becomes larger than the cathode, increasing the likelihood of rf breakdowns. In addition, rf defocusing becomes more significant with short cathode cells, making beam size control and emittance compensation more challenging.

- TOPGUN will operate at 27 K. This choice is for two reasons: 27 K is in the liquid phase of neon, which is being considered considering as a coolant; and the rf surface resistance of copper reaches a knee and does not decrease significantly past $\sim$ 45 K A.2. In addition, since the rf surface resistance is nearly constant at this temperature, temperature changes from operation should not affect the performance of the photoinjector.

- Since removing power from the photogun at cryogenic temperatures is inefficient, the TOPGUN will be optimized to reduce average heating by increasing r/Q.

- The coupling will be accomplished by a TM_{01} mode launcher, similar to those used in the single cell SW structure experiments. Multiple advantages to this coupling scheme include: full cylindrical symmetry that removes multipole mode that spoil beam quality, simplified cooling, solenoid placement is not restricted by input waveguides, and removes edges on couplers in high field regions that can reduce high-field performance.

- The mode launcher also allows the room temperature coupling to be physically distanced from the cryogenic photoinjector, reducing heat conduction from the room temeprature mode launcher.

- The photogun will be strongly overcoupled to decrease the cavity filling time. This decreased fill time will minimize the required klystron pulse length to reach the target gradient, decreasing the average heating and BDR.

- TOPGUN is designed to operate at the rep rate of LCLS, 120 Hz[75] to be a drop-in replacement.
- The operational frequency is set to be $f_0 = 2.856$ GHz ($\lambda = 10.5$ cm), also the same as for the LCLS gun.
- Mode separation should be at least 15 MHz from the π mode to the 0 mode.

5.2.1.1 Coupling Factor

To reduce average heating and BDR, the rf pulse length to reach the design accelerating gradient should be minimized. A common method for accomplishing this goal is to overcouple the structure so that $\beta > 1$ and thus the cavity fill time decreases.

The rf power source is assumed to be a 5045 S-band 5045 klystron that outputs at least 50 MW with a flat pulse of up to $t_p = 3.5$ μs. The electric field on the cathode at the end of the rf pulse needs to be 250 MV/m by design. Increasing the coupling reduces the filling time of the accelerating cavity thus reducing the rf heating, but also decreases the asymptotic field reached. We calculated the final cathode gradient for a range of klystron pulse lengths and external couplings using Equation 3.6. Results of these calculations for three different klystron pulse lengths are shown in Figure 5.4. The minimum pulse length that produces 250 MV/m on the cathode is $t_p = 0.9$ μs. With this pulse length the optimal coupling at 27 K is $\beta = 10$ and $\beta = 2.15$ at room temperature.

Fortunately, a design of an overcoupled structure of $\beta = 2.15$ at room temperature does not require an overly large coupling iris compared to critically coupled structures; and some present photoinjector designs already operate near $\beta \sim 2$ [170, 171].

5.2.2 TOPGUN Fields and RF Parameters

Optimization to increase r/Q was performed by the toolkit described in 5.1 and subject to the constraints listed in 5.2.1. The resulting room temperature geometry and fields are presented in Figure 5.5 and Figure 5.6, the expected f_0 and Q_0 are shown in Figure 5.7, and

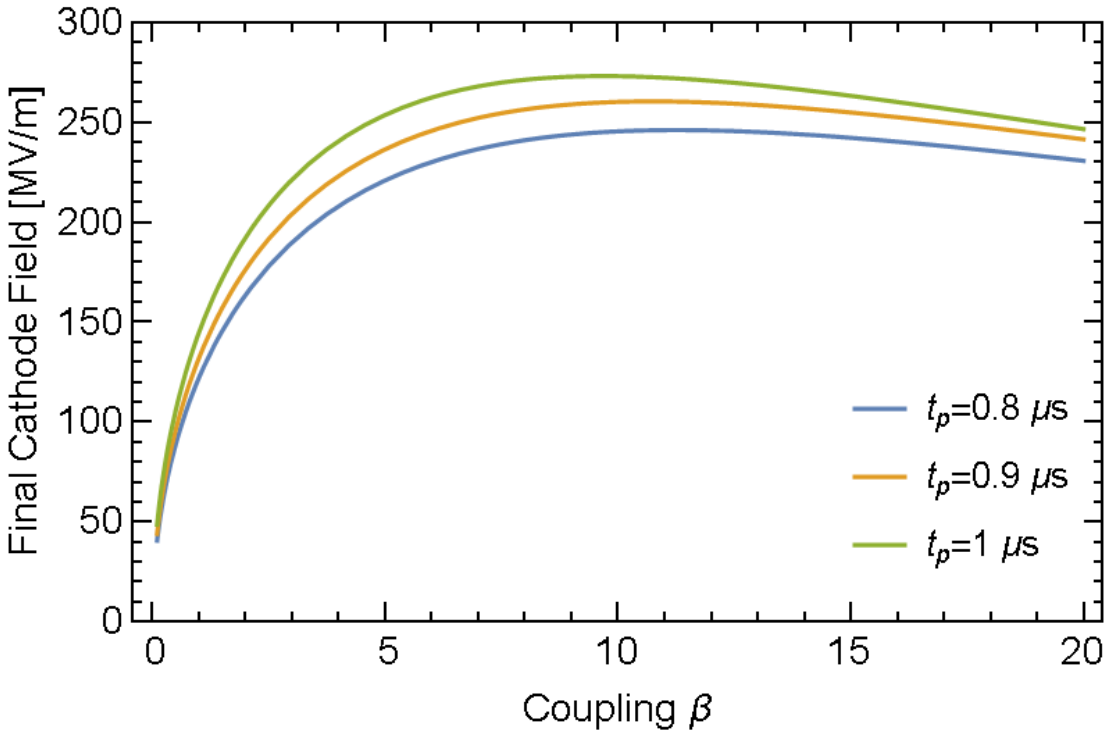

Figure 5.4: Cathode field calculated at the end of an input rf pulse of 50 MW. Three pulse lengths are shown with varying coupling beta.

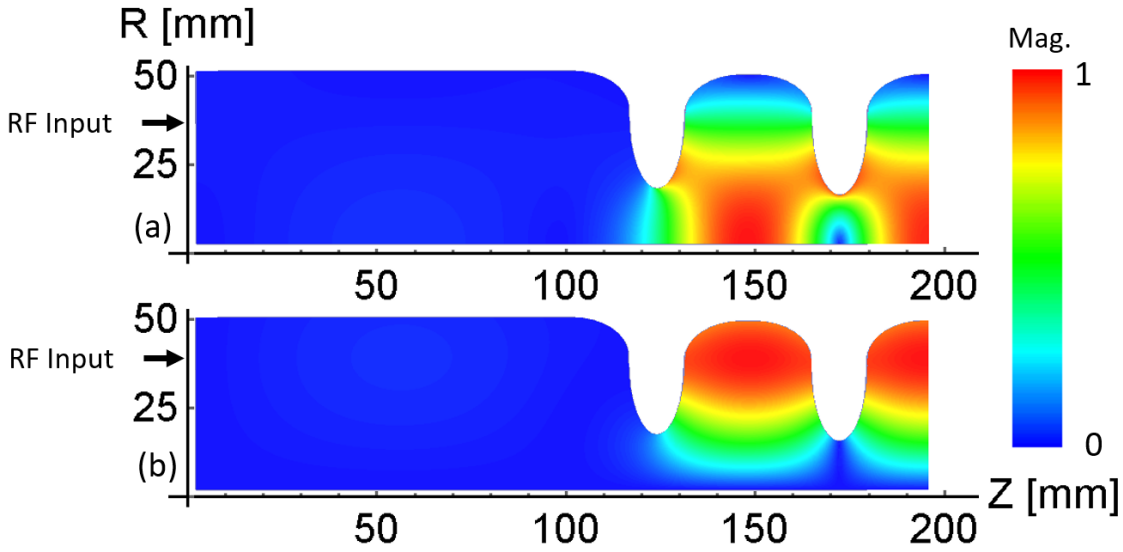

Figure 5.5: (a) electric and (b) magnetic fields for the TOPGUN. Fields are scaled to 250 MV/m on the cathode. Maximum E field is 250 MV/m, and maximum H field is 484 kA/m.

the rf properties for 27 K are listed in Table 5.1.

5.2.3 Thermal Considerations

As TOPGUN will operate at very low temperatures, heat removal from the system will be important. We consider here the amount of heat dissipated in the photoinjector at low temperatures. Again Equation 3.6 is used to find the electric fields inside the TOPGUN for an input square rf pulse. I used the same method as described in 3.5.2, except the input rf pulse was altered to remove the rf power from the TOPGUN quickly. After the input rf pulse is completed, and the field reaches 250 MV/m on the cathode, the phase of the input rf pulse is flipped by 180°. This serves to destructively interfere with the electromagnetic fields inside the cavity, removing power quickly. Figure 5.8 shows the instantaneous power deposited inside the cavity for a single rf pulse with this phase flip.

I calculated the thermal load at 6 different temperatures, 4 K, 20 K, 30 K, 40 K, 50 K, and 77 K. A room temperature analysis was also completed for comparison, however the peak field only reached 190 MV/m due to the reduced Q_0. I assumed the efficiency of the

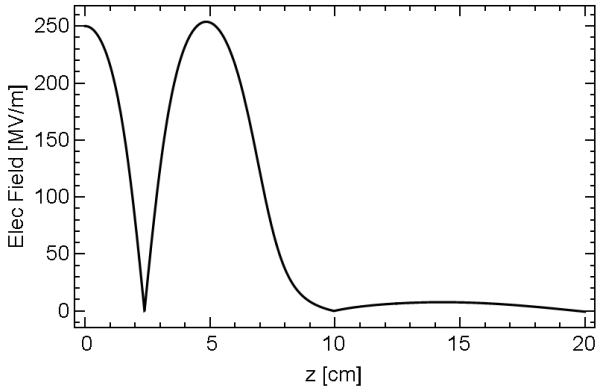

(a)

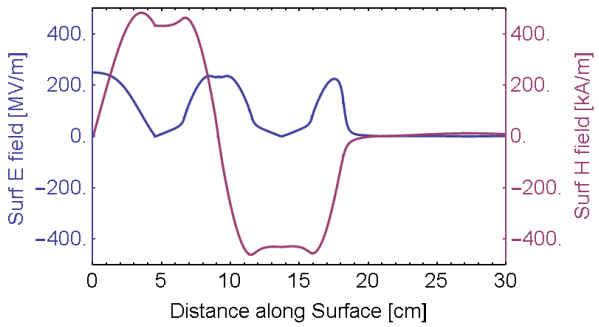

(b)

Figure 5.6: (a) On-axis electric field (b) surface electric (blue) and magnetic (purple) fields all scaled to 250 MV/m maximum electric field on the cathode. $Z = 0$ is at the cathode. Fields are calculated by SUPERFISH.

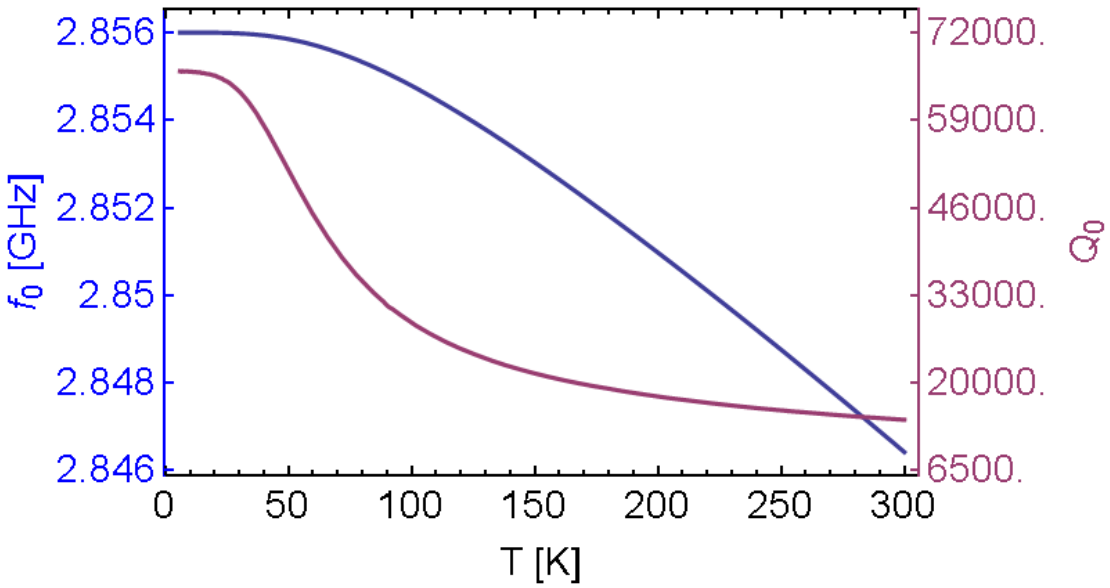

Figure 5.7: Expected temperature dependence of f_0 (blue) and Q_0 (purple) for the π mode frequency in the S-band cryogenic single cell structure. Expected Q_0 is adapted from the S-band cryogenic pillbox results. Expected f_0 is from the expected thermal expansion of copper.

f_0 (Resonant Frequency)	2.856 GHz
Q_0	66,240
Q_E	6,558
P_{in}	50 MW
Asymptotic P_{Refl}	33.47 MW
Asymptotic $P_{Diss.}$	16.53 MW
Max Cathode Electric Field	250 MV/m
Max Iris Electric Field	236 MV/m
Max Magnetic Field	484 kA/m
Mode Separation	19.8 MHz
Stored Energy	31.6 J

Table 5.1: RF parameters for the TOPGUN photogun at cryogenic temperatures. Normalized to 250 MV/m on cathode. The asymptotic P_{Refl} is the amount of power reflected in the steady state regime, and asymptotic $P_{Diss.}$ is the power dissipated in the cavity.

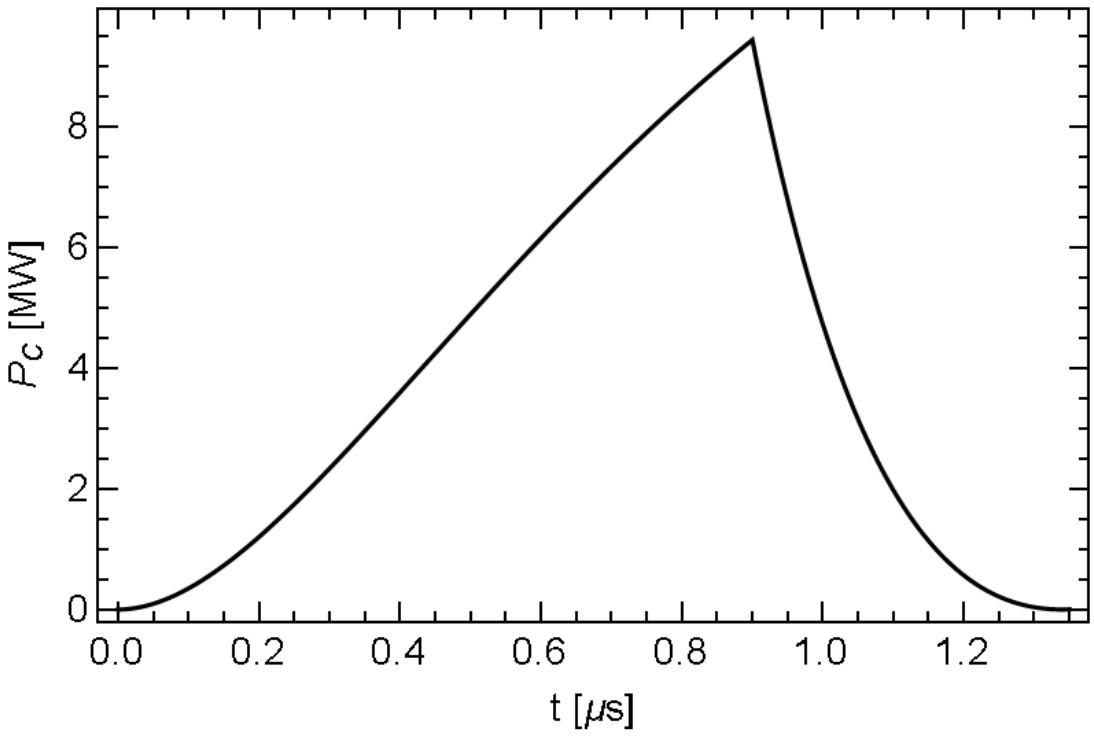

Figure 5.8: Power deposited inside the cavity for a single rf pulse, with pulse length 1.35μs, where the phase flip occurs at 0.9 μs, and a power of 50 MW.

Temp. (K)	4	20	30	40	50	77	300
Q_0	68,548	68,262	66,263	64,263	54,267	39,986	14,280
Coupling β	10.2	10.2	9.9	9.6	8.1	6.0	2.13
Pk. Elec. (MV/m)	257	257	257	257	254	249	217
P_{Avg}(W)	562	563	579	595	692	900	1,933
P_{Cryo} (kW)	239	45	30	22	20	15	2
ΔT (K)		8.62	7.52	7.92	9.61	20.63	23.05

Table 5.2: Coupling and Gradient reached at different temperatures for the S-band cryo accelerating structure. Also included are pulse heating and rf surface losses per pulse. Data for 15 MW 3.5 μs flat pulse

cryostat to be 17% of the Carnot value[15], which is a value seen for pulse tube refrigeration systems similar to the one currently used for cryogenic experiments at SLAC. The results are collected in Table 5.2. The numbers show that the amount of power dissipated in the cavity is very large, but we have found a quote from a company that can manufacture a cryocooler that can handle this thermal load. If the input power is increased to 65 MW the average power dissipated in the cavity can be decreased by a factor of around three by decreasing the rf pulse length.

5.2.4 Conceptual Layout

As of yet there are no engineering drawings of the TOPGUN experimental setup, however, there are ideas of the eventual layout. The setup will be similar to the drawings from the S-band cryogenic single cell structure, where the mode launcher is removed from the TOPGUN by over a meter. The solenoid will be placed around the cryostat. The cooling will be accomplished with liquid neon as the coolant. Figure 5.9 shows a first conceptual drawing.

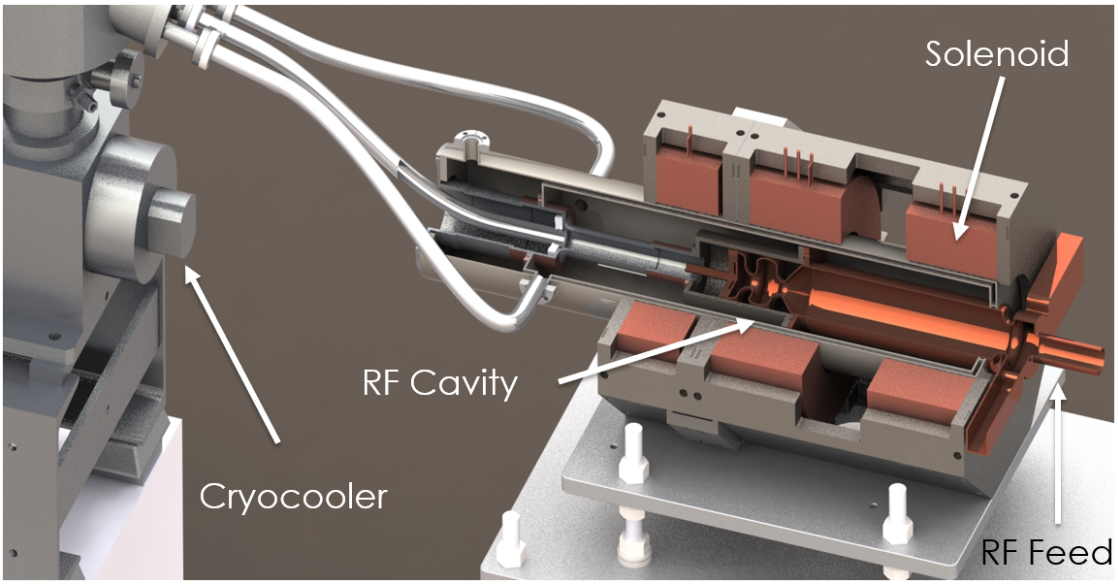

Figure 5.9: A conceptual drawing of the TOPGUN setup including the gun solenoid, mode launcher, and cryocooler.

5.2.5 C-Band TOPGUN

The operational frequency of the TOPGUN project is still being studied. An alternative TOPGUN design was completed for C-band (5.712 GHz). In C-band, the gradient conditions can be relaxed, where the field on the cathode will be designed for 250 MV/m, the same as the current S-band design. Since we are at a higher frequency, the fill time of the injector will be shorter, lessening the cryogenic load, as well as the constraints on the input klystron. I will show the first design of the C-band photoinjector in this section. The choice of the initial cell was set to $0.5\lambda/2$ for this case.

5.2.5.1 Choice of Coupling

This design will show rf properties at 27 K, the operational temperature.

We expect the Q_0 of a 5.712 GHz copper structure to increase by a factor of 5.11 from room temperature to 27 K by scaling the measured values at S-band and X-band using the scaling from Equation A.10. The frequency will also change by nearly 20 MHz as the temperature changes from 300 K to 27 K. For this iteration, I have set the resonant

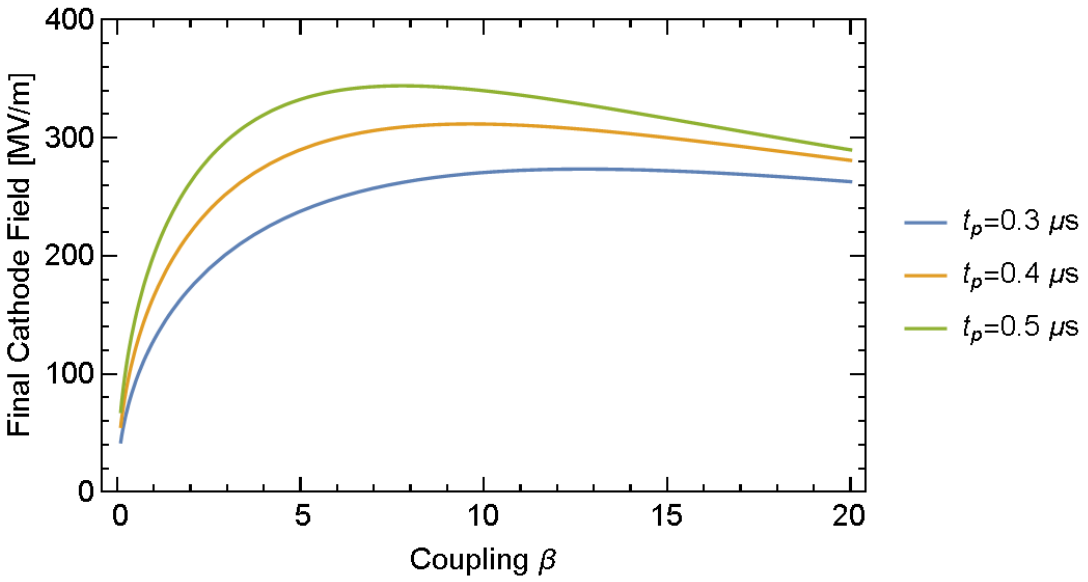

Figure 5.10: The final cathode field in the C-band photoinjector for a given coupling and input rf pulse length (t_p). A coupling of 4-5 was chosen for the design rf pulse length of 400 ns

frequency at 27 K to 5.712 GHz. Using the same method as described in 5.2.1.1, except changing the klystron input power to 20 MW, we can find the optimal coupling, which is shown in Figure 5.10. In this case an input pulse length of 400 ns was chosen, and a coupling was chosen so that $\beta = 5.11$ at 27 K, and thus the cavity is critically coupled at room temperature. Though the optimal bβ is closer to 8, a lower coupling was chosen to allow for more flexible operation at longer rf pulse lengths.

5.2.5.2 RF parameters and field maps

Given the choice of coupling β, the automating toolkit was used to create the C-band TOPGUN. The resulting coupling was slightly below the design β at 4.11, but this is within acceptable bounds. The rf parameters are summarized in Table 5.3. The field maps are shown in Figure 5.11 and surface and on-axis fields are presented in Figure 5.12. Figure 5.13 shows the temperature dependence of f_0 and Q_0 for the C-band TOPGUN design.

Q_0	53154
r/Q	192.894 Ohm
U_s	3.831 J
H_{max}	45.947 kA/m
$E_{max-iris}$	231 MV/m
P_c	2.6 kW
f_0	5.71193 GHz
β	4.11

Table 5.3: RF parameters from SUPERFISH and HFSS for C-band rf photoinjector. T=27 K and E_{Cath}=250 MV/m.

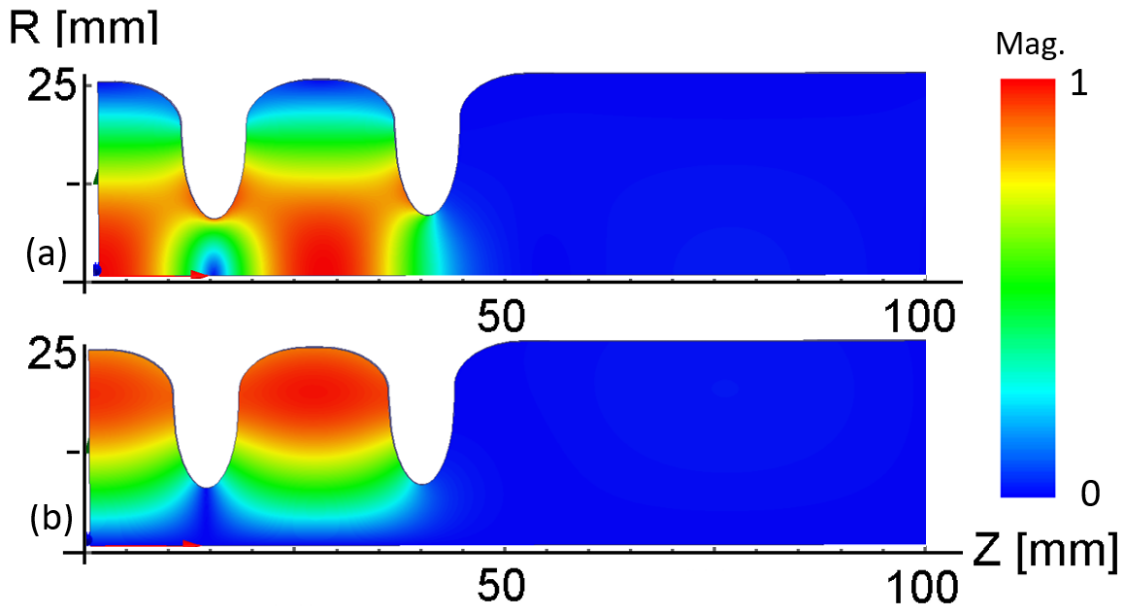

Figure 5.11: (a) Electric and (b) magnetic field maps for the C-band rf photoinjector scaled to 250 MV/m on the cathode. Maximum E field is 250 MV/m, and maximum H field is 46 kA/m.

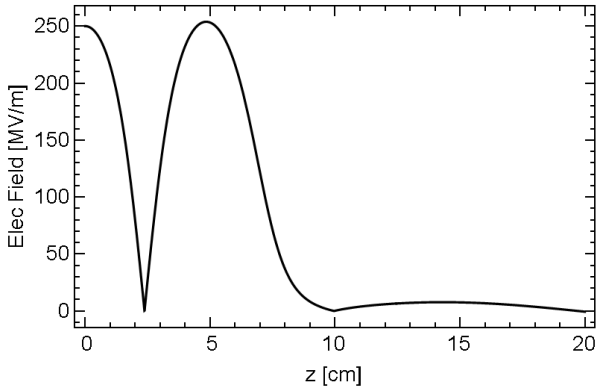

(a)

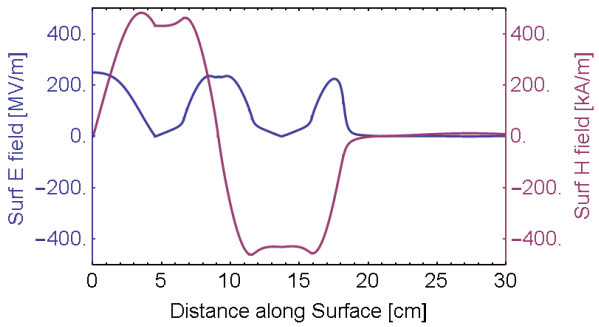

(b)

Figure 5.12: (a) On-axis electric field (b) surface electric (blue) and magnetic (purple) fields all scaled to 250 MV/m maximum electric field on the cathode. $Z = 0$ is at the cathode. Fields are calculated by SUPERFISH.

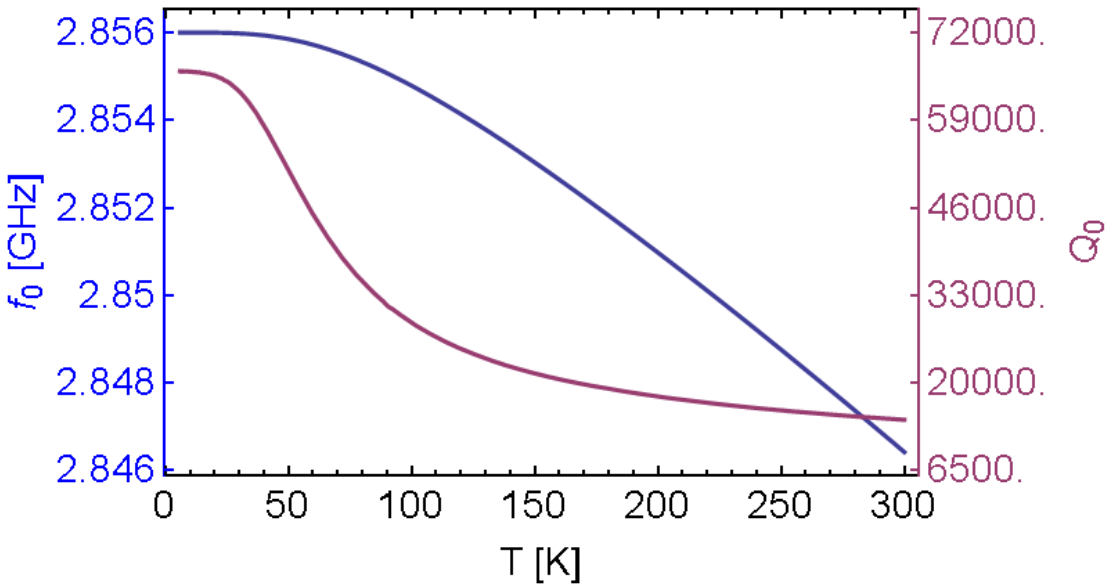

Figure 5.13: Expected temperature dependence of f_0 (blue) and Q_0 (purple) for the π mode frequency in the C-band cryogenic single cell structure. Expected Q_0 is adapted from the S-band cryogenic pillbox results. Expected f_0 is from the expected thermal expansion of copper.

5.3 Mode Launcher

To feed power into the cylindrical waveguide to the rf photogun, a mode converter is needed from TE_{01} rectangular waveguide to TM_{01} circular waveguide. To provide thermal isolation, the circular waveguide should be on the order of a meter long, and the room temperature mode converter needs to be separated from the accelerating structure. Fortunately, a design that accomplishes these constraints already exists, the TM_{01} mode launcher, however only at 11.424 GHz[105]. A problem with this design is a strong quadrupole field component, which will lead to undesirable emittance growth in the electron beams launched from the rf photoinjector [23]. In this section, I will show a modification to the original mode launcher that greatly reduces the quadrupole field component in the mode converter [172].

To keep the mode launcher design relatively compact, a dual-feed system was used in the following design. Our collaborators at INFN have also designed an alternate solution, a quadruple-feed mode launcher, which will have a larger footprint but the quadrupole component is fully removed by symmetry.

5.3.1 Original S-band Mode Launcher

I used the basic concept underlying the original mode launcher[105] to create a version at 2.856 GHz. Our mode launcher starts as a standard WR-284 rectangular waveguide fed directly into a cylindrical waveguide (radius of 45.974 mm) on one side, and a beam pipe on the other. The beam pipe radius (25 mm) is set so that the fundamental dipole mode in it is below cutoff. The device is matched using a rounded inductive iris in the rectangular waveguide. The device is matched using a rounded inductive iris in the rectangular waveguide and the match of the final design is -62dB at 2.856 GHz. See Figure 5.14 for the mode launcher geometry and fields, calculated by HFSS[156]. This design does not attempt to remove the quadrupole fields, but in applications without electron beams, this design is perfectly acceptable.

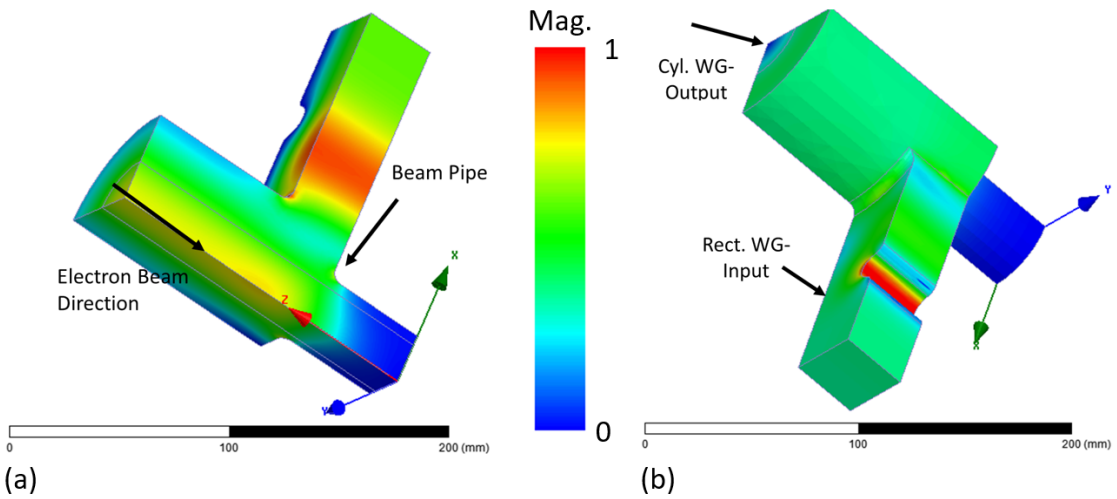

Figure 5.14: Electric (a) and magnetic (b) fields for one quarter of the S-band mode launcher. Fields are normalized to 50 MW input power in full mode launcher. The maximum E field is 8 MV/m and the max H field is 25 kA/m

5.3.2 Calculation of Quadrupole Kick

Now I would like to measure the quadrupole kick experienced by relativistic electron beams, to find the parameter that should be minimized in the rf design. I calculated the quadrupole kick by first integrating the longitudinal electric field, E_z, seen by a particle moving at the speed of light along the axis defined by the circular waveguide. The particles will only feel forces from the integrated longitudinal component. We assume that this particle is moving parallel to the center axis of the cylindrical waveguide, but is offset by a given radius r. The equation for the voltage $V_{\mp}$ is:

$$V_{\mp}(r,\theta) = \int_{z_{start}}^{z_{end}} E_z(r,\theta,z) e^{\mp i k_0 z} \mathrm{d}z, \tag{5.6}$$

where k_0 is the wavenumber of the input rf power and θ is the azimuthal angle. z_{start} should be chosen in the beam pipe where the fields are near zero, and z_{end} will be in the cylindrical waveguide after the quadrupole fields in the coupler have decayed (on the order of a diameter of the cylindrical waveguide past any perturbations). The plus or minus sign in the equation should be chosen based on direction of electron beam travel versus direction of rf power flow. Minus for electrons counterpropagating with the rf power in the cylindrical waveguide, and

plus for beams copropagating with the rf power. $V_{\mp}(r,\theta)$ is calculated for different θ but same r.

The quadrupole component of that integrated kick determined by taking the discrete Fourier transform versus θ_j of $V_{\mp}(r,\theta)$, where j is index of the sampled azimuthal angles;

$$M_{\mp,s}(r) = \frac{1}{\sqrt{n}}\Sigma_{j=1}^{n} V_{\mp}(r,\theta_j)e^{2\pi i(j-1)s/n}, \tag{5.7}$$

where n is the number of azimuthal variations calculated for $V_{\mp}(r,\theta_j)$, and $M_{\mp,s}$ is the mode being calculated, with index s. In this case $M_{\mp,0}$ is the monopole component and $M_{\mp,1}$ will be the dipole component, and the dipole component is identically zero due to symmetry of the model. The quadrupole voltage will be $M_{\mp,2}$.

5.3.2.1 Quadrupole Impedance

To characterize quadrupole voltage independent of rf power, I introduce the quadrupole Impedance, $Z_{Q,\mp}$ as

$$Z_{Q,\mp} = \frac{|M_{\mp,2}(r)|^2}{r^4 P}, \tag{5.8}$$

where P is the rf power transmitted through the mode launcher and the units for $Z_{Q,\mp}$ are Ω/m^4. The quadrupole impedance is independent of r for ultra relativistic electrons [172].

5.3.3 Minimized Quadrupole Field Mode Launcher

The quadrupole kick was canceled by adding two radial perturbations in the circular waveguide. These perturbations to create an opposite quadrupole kick, canceling that of the coupler. An rf splitter is included in the rf design, to that the mode launcher requires only a single rectangular waveguide input. The final reflection at 2.856 GHz is -71 dB. Figure 5.15 shows the geometry and fields for the quadrupole reduced mode launcher.

5.3.4 Comparison

Now I will compare the original S-band mode launcher with the optimized version to verify that the perturbations to reduce the quadrupole component do not degrade performance.

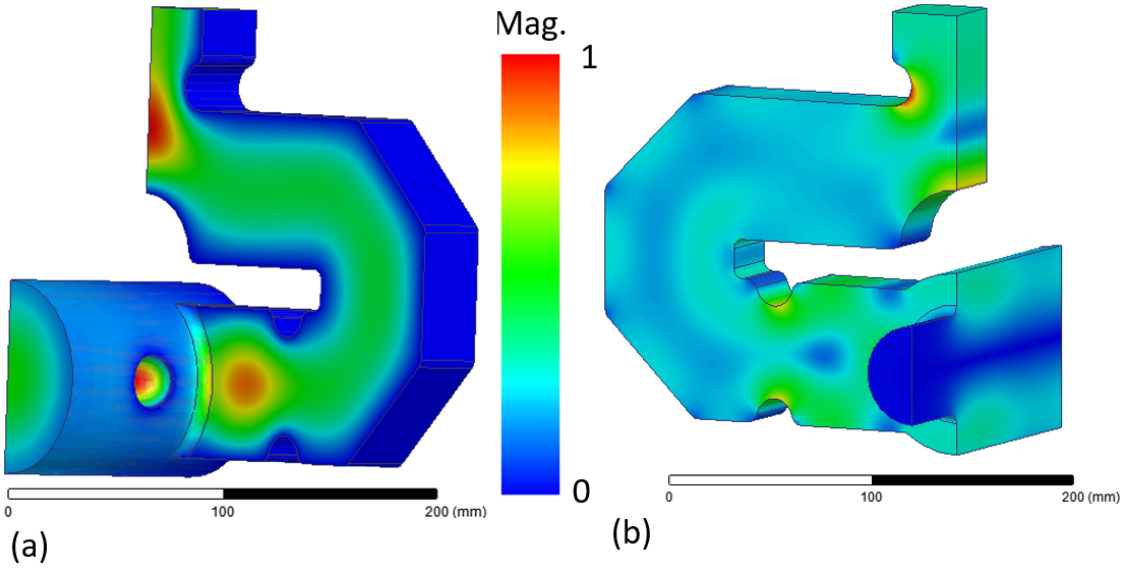

Figure 5.15: (a) Electric and (b) magnetic fields for the reduced quadrupole mode launcher. Fields are normalized to 50 MW input rf power. The maximum E field is 11 MV/m and the maximum H field is 40 kA/m.

First, I examined the electric field on axis. The fields in the perturbed model are not significantly increased. The electric field along the z-axis (the center axis of the cylindrical waveguide) are shown in Figure 5.16. The fields are plotted from the beginning of the beam pipe to the end of the cylindrical waveguide. The 20 dB bandwidth of the coupler decreased from 66 MHz to 44 MHz, but is still large enough for use in S-band high-power beam experiments.

Figure 5.17 shows $V_{-}(r,\theta)$ versus θ for $r = 10$ mm and integrated along the z direction (from the beginning of the beam pipe to the end of the cylindrical waveguide in our model).

The quadrupole impedance for the original S-band mode launcher is $Z_{Q,-}$=1850 MΩ/m^4, and the quadrupole impedance of the redesigned mode launcher is $Z_{Q,-}$=0.00018 MΩ/m^4. For this beams copropagating with the rf power will see a larger quadrupole kick: $Z_{Q,+}$=2011 MΩ/m^4 for the original mode launcher and $Z_{Q,+}$=2669 MΩ/m^4 for the redesign. In the final design, I have minimized the quadrupole field kick for beams counter-propagating with the rf power.

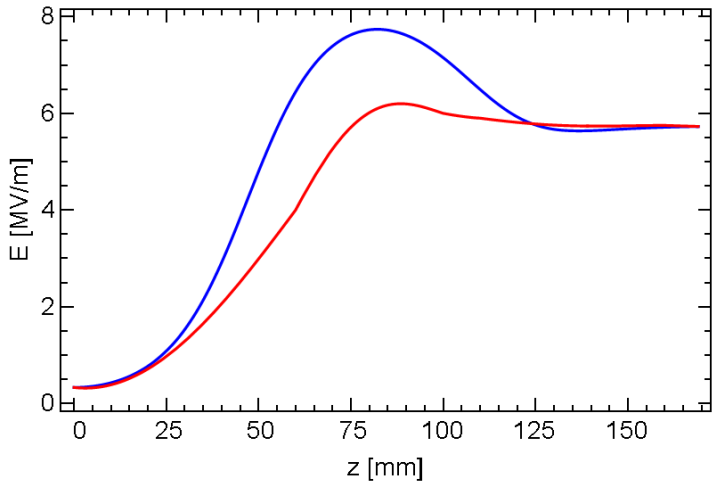

Figure 5.16: On axis fields in the cylindrical waveguide of the original mode launcher (red) and redesign (blue) with 50 MW input power. 0 mm starts at the beginning of the beam pipe.

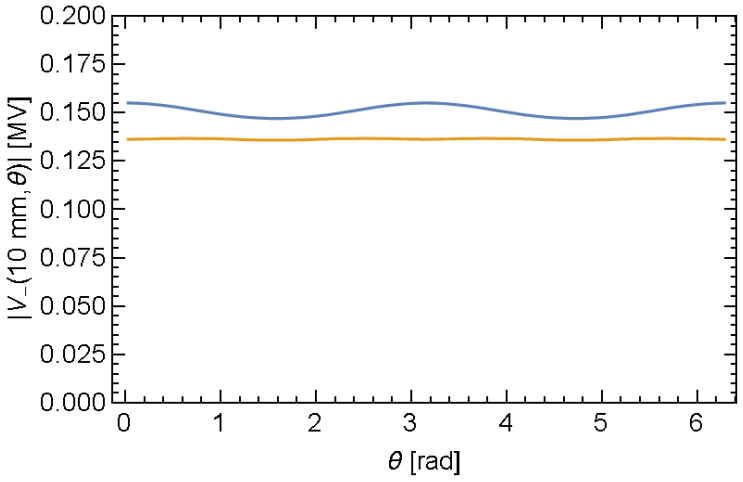

Figure 5.17: Example $V_{-}(r, \theta)$ in the mode launcher versus θ around the center axis of the cylindrical waveguide (beginning of the beam pipe to end of the cylindrical waveguide). Values are for 200 MW input for the whole mode launcher. The original design is in blue and new design is orange.

5.3.5 Engineering

5.3.5.1 Tolerance Analysis

To estimate the effects of manufacturing errors on the design, I simulated the structure with simulated errors for the important dimensions. For these dimensions I added and subtracted 25 μm to each in turn from the nominal values.

The quadrupole component is only significantly dependent on the two variables that describe the circular perturbations in the circular waveguide. Of those two, a 1 mil error in the position along the circular waveguide will lead to a 1 order of magnitude increase in the Quadrupole kick. This is acceptable, since the quadrupole kick is reduced already by seven orders of magnitude. Errors in the radius of the hemispherical perturbation will lead to more significant errors closer to nearly 3 orders of magnitude increasing from 0.00018 MΩ/m^4 to 0.1 MΩ/m^4. This still leads to a significant decrease in the quadrupole kick relative to the non quadrupole compensated design, and is thus deemed acceptable. All other dimension variables lead to smaller changes in the quadrupole impedance.

As for the transmission of the mode launcher, errors in either direction for non-radial variables keeps the reflection from the rectangular waveguide less than -50 dB. However, the four features that have radii, a 25 μm error in the radius leads to more significant changes in the input rf reflection. The tolerances should be half a mil for radii dimensions and one mil for all other dimensions.

5.3.5.2 Drawings

I have worked with mechanical engineers at SLAC to create a drawing package for this mode launcher, and it is currently being manufactured for use in the S-band cryogenic single cell accelerating structure experiment.

Figure 5.18 shows the CAD model of the mode launcher and Figure 5.19 shows a conceptual rendering of the TOPGUN with this mode launcher.

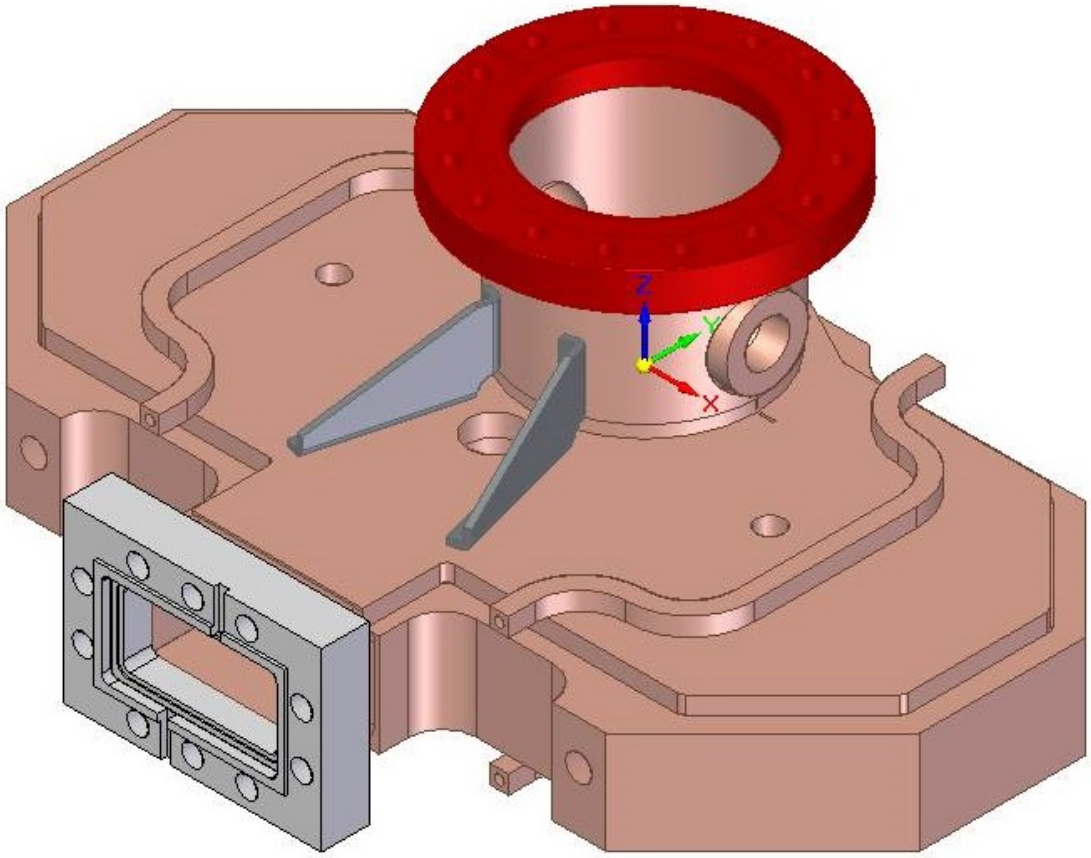

Figure 5.18: CAD drawing of the quadrupole kick reduced mode launcher for use in manufacturing.

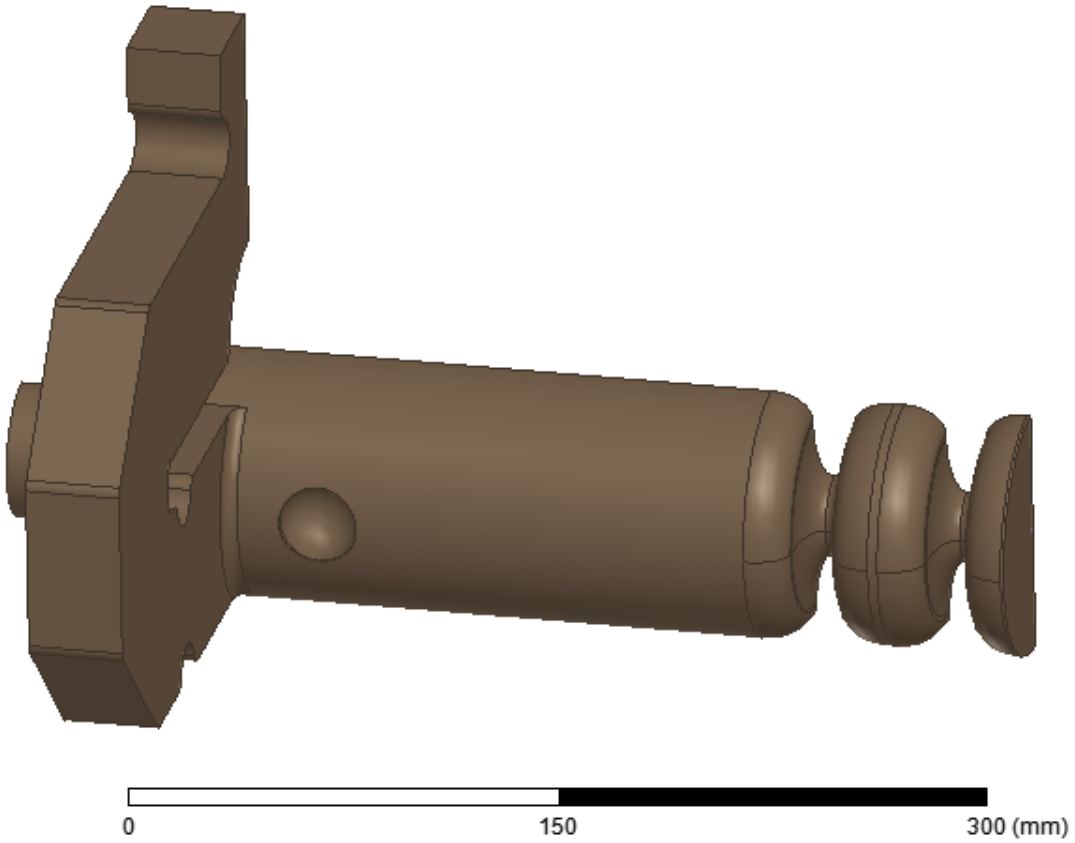

Figure 5.19: TOPGUN connected to the mode launcher. Fields are normalized to 250 MV/m at the cathode. In practice, the waveguide between the coupler and photogun will be on the order of a meter long.

5.4 Emittance Optimization with a Genetic Algorithm

To find optimal emittance performance of the ultra-high gradient rf photoinjector I have used a multi-objective genetic optimizer as developed at LBNL[173, 174]. This optimizer uses the NSGA-II genetic algorithm[175, 176] and Astra [177], a particle tracking code. The two objectives of the optimization are a small transverse emittance and a small bunch length. Pareto improvements were explored to maximize the peak brightness. Depending on the application, the maximum peak brightness might not be the best solution. For instance, in an FEL where compression is implemented downstream of the injector, a minimum emittance may be better to maximize the energy output of the FEL pulse. For a UED electron source, very short bunch length can be the primary goal. Full start-to-end simulations including possible degradation of the emittance are needed for deciding what is the best compromise between emittance and bunch length in the injector.

In this study I have explored changing the length of the cathode cell of the TOPGUN, as this will have large effects on the beam emittance. Using the framework that is laid out previously in this chapter, it is easy to redesign the gun in the matter of an hour to have a different cathode length. This will only minimally change the rf parameters stated above. In this study, I focused on the outliers in cathode cell length, and elected to explore a 1.4 cell and 1.6 cell rf gun geometry.

5.4.1 Simulation Setup

The electric field maps for the rf gun were generated in SUPERFISH [161], for 1.4, 1.45, 1.5, 1.55, and 1.6 cell geometries, each with the same overall shape as TOPGUN presented above, though only 1.4, 1.5, and 1.6 were used. Figure 5.20 shows the axial electric field for the varying geometries.

The variables for the simulation that control the injector setup are: the laser spot size and its temporal length; the initial rf phase relative to the laser; the solenoid position and maximum field; and the linac position, liac accelerating gradient, and its rf phase relative to the photoinjector rf phase. Figure 5.21 shows a diagram of the simulation setup. The initial

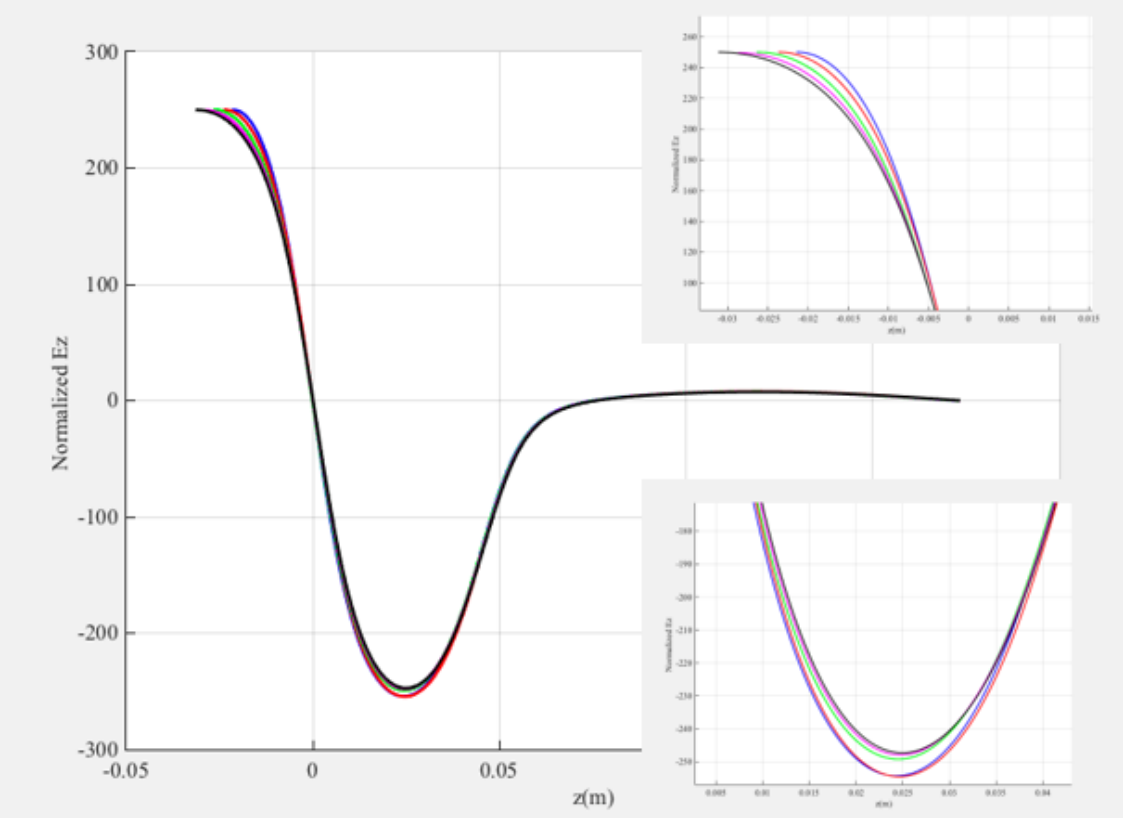

Figure 5.20: Axial electric fields for a 1.4, 1.45, 1.5, 1.55, and 1.6 cell rf photoinjector, scaled to 240 MV/m on the cathode. The varying magnitude of the full cell electric field is within our tolerance for the field balance.

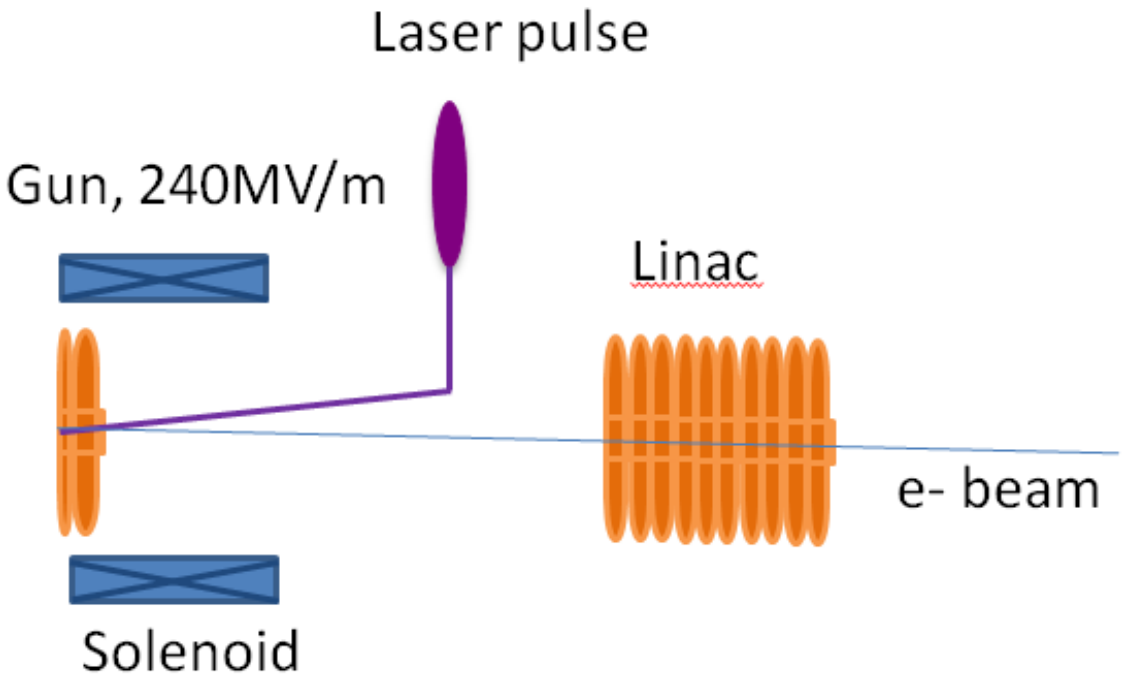

Figure 5.21: Setup of the ASTRA simulation. Initially, a laser is sent into the cavity to promote electrons. The electrons are accelerated by the photogun and focused by a solenoid. They reach an accelerating structure after propagating through in a drift section of adjustable length.

thermal emittance used for these simulations is 0.56 mm-mrad per rms mm of the laser spot size. The initial particle distributions create uniformly filled ellipsoids.

5.4.2 Genetic Optimizer

This section will explain how the optimizer works. The optimizer routine begins by generating a random set of initial points for the variables stated above. These initial points are used to propagate a beam through the simulated rf photoinjector, using Astra[177] to calculate the emittance and bunch length. The initial population is sorted by dominance, where any non-dominated solution, a solution where no others have an improvement in either objective without degrading the other objective, is given rank 1. Solutions that are dominated by only those in the first group are given rank 2 and so on [175]. Solutions are chosen, by minimizing dominance rank and maximizing the distance between solution points, to be the parents

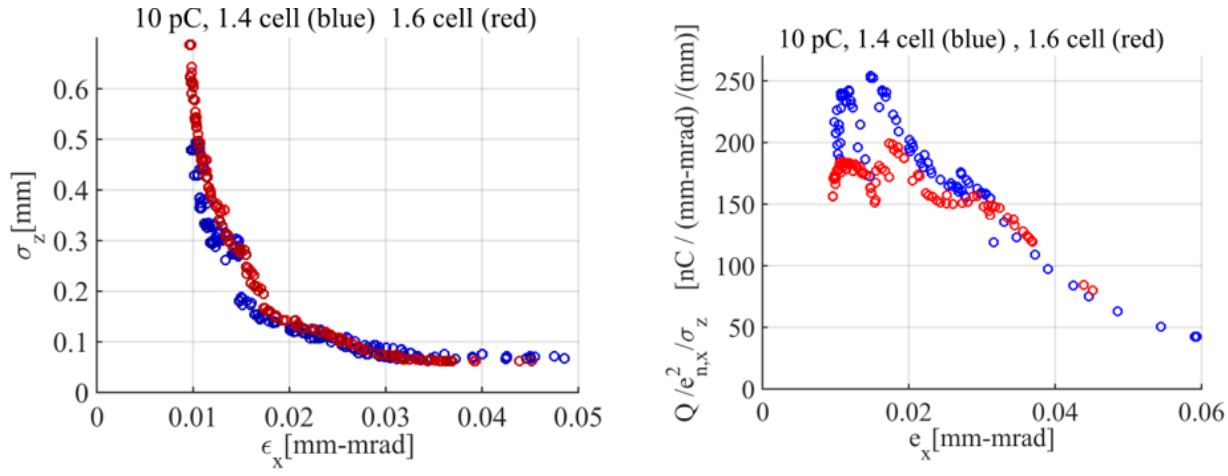

(a) (b)

Figure 5.22: (a) The optimal horizontal emittance and rms bunch length are plotted for 10 pC for 1.4 and 1.6 cell geometries. (b) Brightness vs transverse emittance. The shorter cathode cell leads to 20% larger beam brightness

to the next generation of solutions. This next generation is then created by crossover and mutation operators and simulated using Astra. The process continues until a diverse set of non-dominated solutions is found, giving the pareto plot that shows the trade-off between horizontal emittance and rms bunch length.

5.4.3 Emittance for Different Cathode Cell Lengths and Bunch Charges

The simulation was run for different bunch charges: 10 pC, 100 pC, and 1 nC. We focused on the two extremes of cathode cell length, simulating 1.4 and 1.6 cell rf photogun geometries.

5.4.3.1 10 pC

The results for a small bunch charge show horizontal emittance of 10 $nm \cdot rad$, and a peak brightness of 250 $nC/(mm \cdot mrad)^2/mm$. As can be seen in Figure 5.22, the difference between a 1.4 and 1.6 cell geometry is small but noticeable in emittance, and leads to a 20% increase in brightness for the 1.4 cell case relative to the 1.6 cell case.

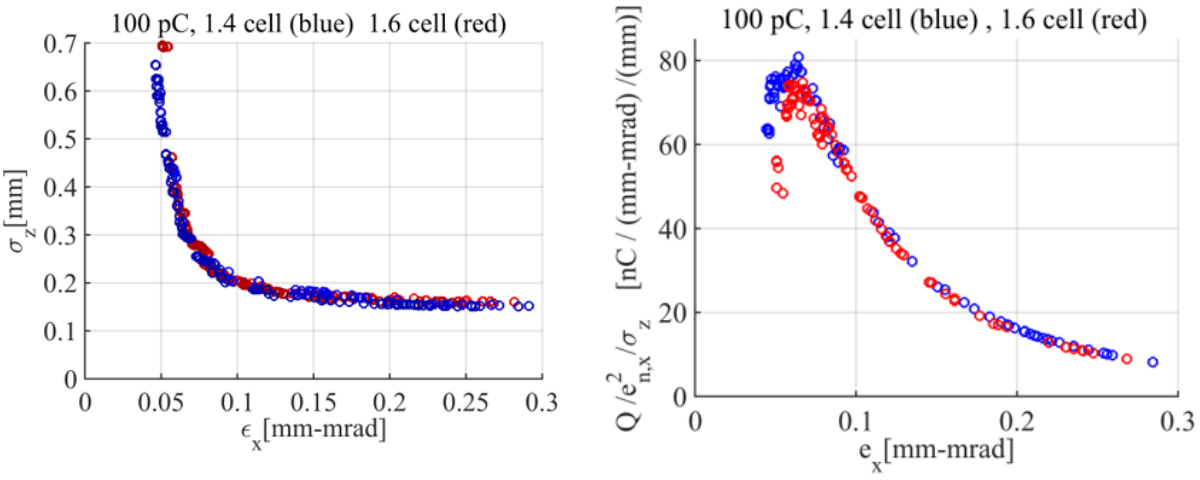

(a) (b)

Figure 5.23: (a) The optimal horizontal emittance and rms bunch length are plotted for 100 pC for 1.4 and 1.6 cell geometries. There is minimal difference between the two cases. (b) Beam brightness vs transverse emittance.

5.4.3.2 100 pC

For 100 pC there is very little difference in the optimal horizontal emittance and rms bunch length for two different cell lengths as can be seen in Figure 5.23. The maximum brightness is 80 $nC/(mm \cdot mrad)^2/mm$, and the horizontal emittance reaches 45 $nm \cdot rad$, which is smaller by 50% than the emittance in an optimized photoinjector with the S-Band gun operated at 120 MV/m [178].

5.4.3.3 1 nC

In the high charge case the brightness is larger when the cathode cell is longer, the 1.6 cell geometry has a peak beam brightness of 25 $nC/(mm \cdot mrad)^2/mm$ against 15 $nC/(mm \cdot mrad)^2/mm$ for the 1.4 cell geometry (see figure 6b). The transverse emittance for the longer geometry is 250 $nm \cdot rad$. Figure 5.24 shows the pareto plot and brightness for 1 nC.

In these simulations, there are two sections in the results: (1) where the linac was close to the rf gun exit at 0.6 m from the cathode, and (2) where the linac was 1.9 m downstream,

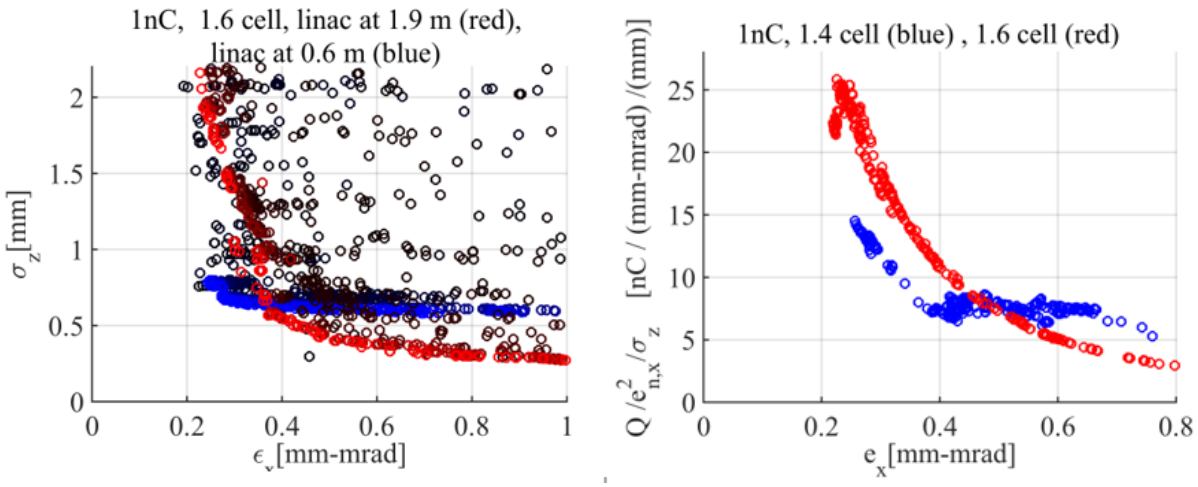

(a) (b)

Figure 5.24: (a) Optimal horizontal emittance and rms bunch length are plotted for a 1.6 cell geometry for two positions of the linac, close to the gun at 0.6 m and far from the gun at 1.9 m downstream.(b) The brightness versus transverse emittance. Beam brightness of the longer cathode cell is larger.

further from the rf gun. When the linac was close, the brightness was optimized, while when the linac was far, the electron beam reached very short bunch lengths, which is shown in Figure 5.24.(a). For the very high gradient, 240 MV/m, optimizing for brightness, it is important to have the linac close to minimize the time of space-charge expansion, also true for the two lower charge cases. However, if the linac is further from the rf gun for the high charge case, short bunch lengths can be created using velocity bunching while the electrons are at a relatively low energy.

In the 1.6 cell geometry, the electrons leave the gun at a phase where the defocusing kick is more linear [179]. This becomes important for a high charge bunch which is substantially elongated in time due to strong space charge forces. This is not as detrimental for low charge bunches which are short. This explains why the 1.6 cell gives smaller emittances than the 1.4 cell at 1 nC [180]. For lower charges the rf defocusing is not as important with reduced space-charge forces, while the larger accelerating gradient at the electron beam launch leads to a larger brightness.

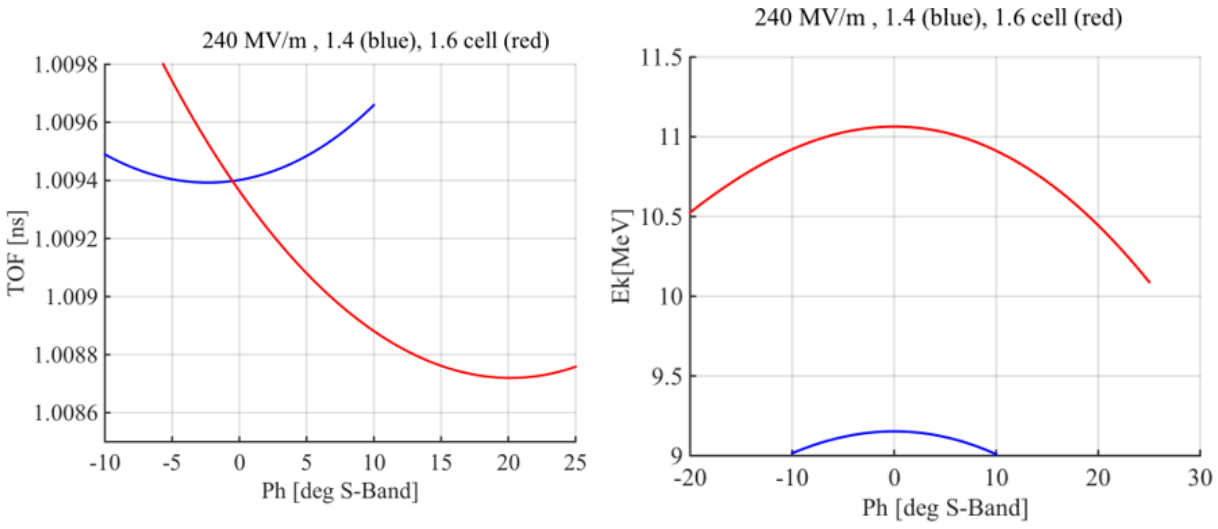

(a) (b)

Figure 5.25: (a) time of flight vs rf gun phase, where 0 deg is the maximum energy. (b) Energy at gun exit vs gun phase.

The results of these optimizations show brightness increases well over an order of magnitude larger than the LCLS photoinjector for similar bunch charges.

5.4.4 Time of Flight and Energy

Figure 5.25.(a) shows the time of flight and energy for the rf gun phase at the launch of the electron beam. The 1.4 cell geometry operates between -10 and -5 degrees, depending on charge and bunch length goals, where this injection phase will depend on the bunch charge. The 1.6 geometry operates between +5 and +10 degrees depending on goals. These phases are close to a phase of zero, where the variation in arrival time to change in phase is 7.9 fs/deg for the 1.4 cell gun and 65.6 fs/deg in the 1.6 cell geometry. This makes the 1.4 cell gun much more attractive for requirements on phase for arrival time stability, such as UED. In addition, the arrival time will vary with a change in voltage, 10 fs per 0.1 % change in voltage on the cathode. The shorter cathode cell is significantly more stable for arrival time.

Another difference between the 1.4 and 1.6 cell geometries is the beam energy at the gun

exit, as shown in Figure 5.25.(b). Since the energy is larger in the 1.6 cell geometry, the solenoid requires a larger field, around 0.81 T, while the shorter 1.4 cell geometry requires 0.66 T. Decreasing the solenoid requirements make the 1.4 cell geometry advantageous in this respect.

CHAPTER 6

Conclusion

I have shown the development and experimental results for numerous cryogenic high gradient accelerating structures. In these studies, I have focused both on understanding the physics of rf breakdowns, and the applications of the ultra-high accelerating gradients.

Measurements of rf surface resistance at low powers at both X-band, 11,4 GHz, and S-band, 2.85 GHz, showed agreement with the theory of the anomalous skin effect, which describes the rf surface impedance of conductors at low temperatures. The X-band measurements of rf surface resistance were in very close agreement, less than 5% larger than the theoretical model. The S-band cavity however, had measured values of rf surface resistance 10% larger than the theoretical model. The difference may have been caused by the coupling of the rf electromagnetic fields by antennae, which would change shape with the change in temperature, altering the measurement. The rf surface resistance will be measured with waveguide coupling in a later experiment with an S-band single cell accelerating structure.

Initial measurement of the single cell X-band cryogenic accelerating structure showed evidence of Q_0 degradation for peak rf surface electric fields greater than 300 MV/m. This effect was confirmed through an experimental program. I created a model that successfully fits the changing Q_0 and ω_0 using the measured dark current signals. This model was used to calculate the accelerating gradient, and the decrease in gradient was found to be minimal, less than 2%, even as the Q_0 decreases by 30%.

The amount of power dissipated is shown to be consistent with simulations of rf power being absorbed by field emission currents. This phenomenon is known as dark current beam loading

The high-power breakdown data was processed using the dynamic Q_0 model, and the

resulting breakdown rate is $2 * 10^{-4}/pulse/meter$ at 250 MV/m and 45 K, which is a larger accelerating gradient than in room-temperature single-cell structures for the same breakdown rate. The resulting conclusion is that cryogenic operation of copper accelerating structures decreases the rf breakdown rate. Since, at cryogenic temperatures, the copper hardness increases and rf pulsed heating stress decreases, the conclusion supports the current hypothesis that the immobilization of the dislocations and decreased cyclic mechanical stress decreases the breakdown rate.

In addition to experimenting on the cryogenic structures, I have worked with collaborators to create a promising design for a rf photoinjector, TOPGUN. This rf electron gun would be able to increase the electron beam brightness by over an order of magnitude past the current state of the art, as shown by beam dynamic simulations. This rf photoinjector has multiple possible applications, including free electron lasers, ultrafast electron diffraction, and dielectric wakefield accelerators.

6.1 Future Directions

The 1C-SW-A2.75-T2.0-Cryo-Cu-SLAC-#2 structure is currently in the process of being removed from the experimental setup to be cut open and the surface analyzed. The next structure, 1C-SW-A2.75-T2.0-Cryo-Cu-SLAC-#3, is already manufactured, has been rf tested at low power and room temperature, and is ready to be installed into the cryostat.

The first goal of the next experiment will be to confirm that the previous high gradient results are reproducible. The current experiment was limited to running in day-long increments and thus we were not able to accurately measure BDRs less than $\sim 10^{-5}$/pulse/m, which corresponds to a few breakdowns per day, due to a lack of statistics. The next installation will be operated continuously for many days and will be able to measure the BDR for lower gradients. This continuous operation will allow us to measure the exponent, ζ for the power law dependence BDR $\propto G^{\zeta}$ and repeat this measurement at different operating temperatures from 25 K to 77 K. This enables us to verify the theory proposed in [138], which predicts a stronger power law dependence between BDR and accelerating gradient for

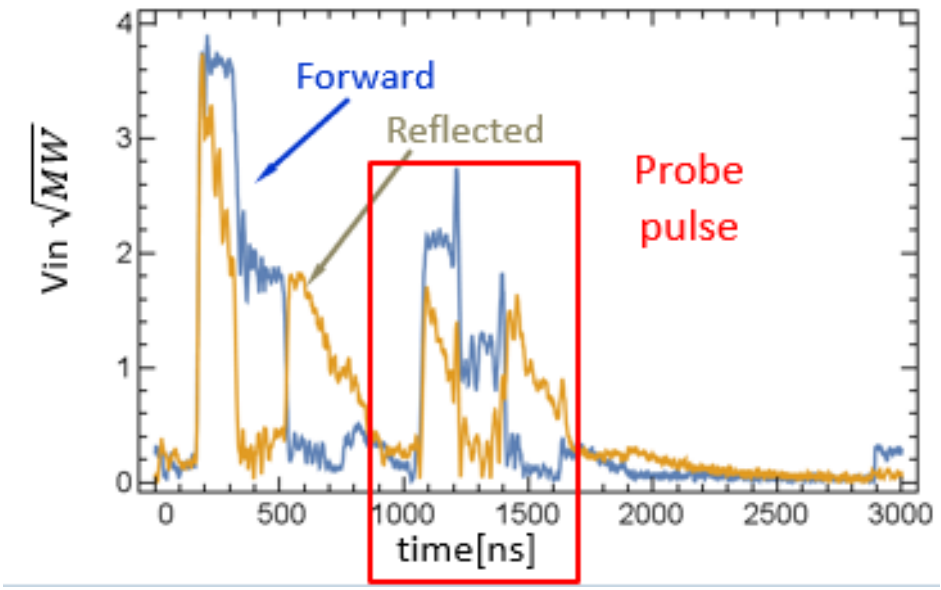

Figure 6.1: An example rf signal from a rf pump probe experiment. The initial rf pump pulse will cause the change in Q_0, and the probe pulse measures the Q_0 at a later time. The timing separation can be varied to find the full time-dependence of $Q_0(t)$.

both harder and colder structures.

The other focus will be further investigation of the Q_0 and ω_0 change, in particular the time scale of their return to the original values. Currently, a rf pump-probe experiment has been developed where a first large rf pulse (the pump) will cause the rf parameter movement, and a second smaller rf pulse (the probe) will measure the Q_0 value at a later point in time. By varying the separation of the two pulses, the time variation of the rf parameters can be determined. Figure 6.1 shows an example of this type of rf pulse.

Further in the future, new single cell structures will be tested, examining the behavior of other materials at cryogenic temperatures, particularly CuAg, which showed low breakdown rates at room temperature. In addition, expanding the single cell program to other frequencies will be pursued, including the S-band cryogenic single cell structure that has been presented in this work. This structure is currently being manufactured and will be installed within the next year.

The problem of large dark currents and the methods of reducing them will be considered.

The dark current could be reduced with novel surface treatments, coatings, or different bulk materials. Reduction of field emission currents will reduce dark current beam loading and thus may allow higher accelerating gradients. Low dark currents are also important for photoinjector designs, where the currents can easily be transported with the desired beam and among others effects degrade the magnets of undulators.

Advances in cryogenic accelerators will support the further investigation into cryogenic rf photoinjectors. In the future development of TOPGUN, specific paramters will be chosen depending on a target application. Once a electron gun is manufactured, then an experiment can be conducted to measure the ultra-high brightness capabilities of the ultra-high accelerating gradients in a cryogenic normal-conducting accelerating structure.

APPENDIX A

Skin Depth in Normal Conducting Metals

Early experiments by B. Pippard [145] found that surface resistances in normal conducting metals for MHz frequencies at cryogenic temperatures are not accurately predicted by the simple classical model; where electrons in the conductor are governed by Ohm's Law. The theory to explain this phenomenon, which was called the anomalous skin effect of metals, was then initially laid out by Reuter and Sondheimer [144]. A short overview of that theory is presented in this section.

For furture use, the Residual Resistivity Ratio (RRR) is defined as

$$\mathrm{RRR} \equiv \frac{\sigma_{c\ 4K}}{\sigma c\ 293K}. \tag{A.1}$$

A.1 Normal Skin Effect

First, I will examine the skin effect in room temperature conductors. I will consider a semi-infinite planar conductor, with $\mu = \mu_0$, and assume that electrons follow Ohm's Law,

$$\vec{J} = \sigma_c \vec{E}. \tag{A.2}$$

Further, I will assume that the time dependence of applied electromagnetic fields is $e^{-i\omega t}$. If the permeability, permittivity, and conductivity of the conductor do not vary in time or space, then the Maxwell's equations can be reduced to the diffusion equations in the conductor near the surface [164]:

$$\left(\nabla^2 - \mu_0 \sigma_c\right) \begin{cases} \vec{E}(z) \\ \vec{H}(z) \end{cases} = 0. \tag{A.3}$$

The solution to this equation shows that an incoming electromagnetic wave will penetrate the metallic surface and the magnitude will decrease exponentially as it travels farther into the metal. The exponential decay occurs with a characteristic length known as the skin depth (δ) [181]:

$$E_z/E_0 = H_z/H_0 = J_z/J_0 = \exp\left[-(1-i)\frac{z}{\delta}\right], \tag{A.4}$$

$$\delta(\omega) = \sqrt{\frac{2c}{Z_0\sigma_c\omega}}. \tag{A.5}$$

With the assumption that displacement currents are negligible, the Maxwell equation, $\epsilon_0\frac{\partial\vec{E}}{\partial t} = \vec{\nabla}\times\vec{H}$, can be used to find the surface impedance. The rf surface resistance is the reap part of the surface impedance. To accomplish this, I must assume that the variation of fields in the perpendicular direction is much larger than the variation along the surface of the metal and therefore, $\vec{\nabla} = -\vec{n}\frac{\partial}{\partial z}$[164]. This assumption will hold in good conductors such as copper. The resulting surface impedance, Z_s, is:

$$\begin{aligned} \vec{E} &= \frac{Z_s}{Z_0}[\vec{H}\times\vec{n}], \\ Z_s(\omega) &= \sqrt{\frac{\omega Z_0}{2c\sigma_c}}(1-i), \\ Re(Z_s) &= R_s. \end{aligned} \tag{A.6}$$

A.2 Anomalous Skin Effect

Now I will examine the behavior of electrons in low temperature conductors. As the temperature of the metal decreases the mean free path of electrons increases, described by:

$$l = \frac{\sigma_c Z_0 c v_f}{\omega_p^2}. \tag{A.7}$$

This is evidenced by experimental observations of the decreasing DC bulk conductivity [142]. In good conductors at low temperatures, the mean free path and the skin depth will approach the same order. Ohm's law requires that the electric field in the conductor does not vary over the free paths of electrons. Since the electric field now varies on the order of the skin depth, this assumption is no longer true and Ohm's law is invalid. To find the true electron

current the electric field will need to be integrated over the path of the electrons in the metal, which was done by [144], giving the following equations:

$$\begin{aligned}
\frac{4i\pi\omega}{c^2}\vec{J} &= \frac{d^2E}{dz^2}\vec{E} + \frac{\omega^2}{c^2}\vec{E}, \\
f &= f0 + f_1(\vec{v}, z), \\
f_0 &= \frac{1}{\exp[\frac{1}{2}m|v|^2 - \frac{\zeta}{k_BT}] + 1}, \\
f_1^{(1)} &= \frac{e}{mv_z}\frac{\partial f_0}{\partial v_x}\exp\left[-\frac{(1+i\omega\tau)z}{\tau v_z}\right]\int_0^z \vec{E}\exp\left[-\frac{(1+i\omega\tau)z}{\tau v_z}\right]dt, \\
f_1^{(2)} &= \frac{e}{mv_z}\frac{\partial f_0}{\partial v_x}\exp\left[-\frac{(1+i\omega\tau)z}{\tau v_z}\right] \\
&\quad \times\left(p\int_{-\infty}^z \vec{E}\exp\left[-\frac{(1+i\omega\tau)z}{\tau v_z}\right]dt + (1-p)\int_0^z \vec{E}\exp\left[-\frac{(1+i\omega\tau)z}{\tau v_z}\right]dt\right), \\
J_z(z) &= 2e\left(\frac{m}{h}\right)^3\int\int\int v_x f dv_x dv_y dv_z.
\end{aligned} \tag{A.8}$$

The first equation is directly from Maxwell's equations. The second equation gives the distribution function, and thus the probability that a given electron has a specific velocity. The Fermi function, f_0, describes the relaxed state where there is no electric applied electric field and f_1 describes the perturbation caused by the electric field. $f_1^{(1)}$ and $f_1^{(2)}$ are the particle distributions for the perturbation traveling towards and away from the metal boundary respectively. p is the ratio of specular to diffuse reflection from the boundary. This is a parameter that is left undefined, however, it does not have a strong effect on the final answer. The effect of magnetic fields was assumed to be much smaller than the electric field effects, and thus all terms related to the magnetic field were neglected. The equations A.8-A.9 were

then reduced by [182] to an simpler form (this form is taken from [183]).

$$\begin{aligned} Z_s(\omega) &= -\frac{i\omega l Z_0}{cF(\omega)}, \\ F(\omega) &= -\frac{1}{\pi} u \int_0^\infty \ln\left[1 + \frac{\eta + \xi\chi(t)}{t^2}\right] dt, \\ u &= 1 + i\frac{\omega l}{v_f}, \\ \eta &= -\frac{\omega^2 l^2}{c^2 u^2}, \\ \chi(t) &= 2t^{-3}[(1+t^2)\arctan(t) - t], \\ \xi &= i\alpha u^{-3}, \\ \alpha &= \frac{3}{2}\left(\frac{l}{\delta(\omega)}\right)^2. \end{aligned} \tag{A.9}$$

In the extreme limit where $\delta << l$, the cold temperature limit, there is a simplification as stated in [144]

$$Z_s(\omega) = \left(\frac{\sqrt{3}}{16\pi}\frac{c v_f}{\omega_p^2}\right)^{\frac{1}{3}} Z_0(1 - \sqrt{3}i)\left(\frac{\omega}{c}\right)^{2/3}. \tag{A.10}$$

In this extreme limit, we see that the rf surface resistance does not depend on the DC conductivity of the metal.

Figures A.1 and A.2 show calculations of the rf surface resistance for the NSE and ASE theories, and in the ASE theory for different frequencies.

A.2.1 Effective Skin Depth

The field dependence on depth into the metal is not necessary to calculate the surface impedance in A.9. As this field dependence is complicated to derive I will reference [144] for a full analysis.

The result shows that the field has two components: a short-range field that falls off exponentially, and a long-range field with a slower decrease. The short and long-range fields can be seen in Figure A.3 as well as a comparison to the theory of NSE exponential decrease in field magnitude.

I can then define an effective skin depth for the anomalous skin effect theory as the

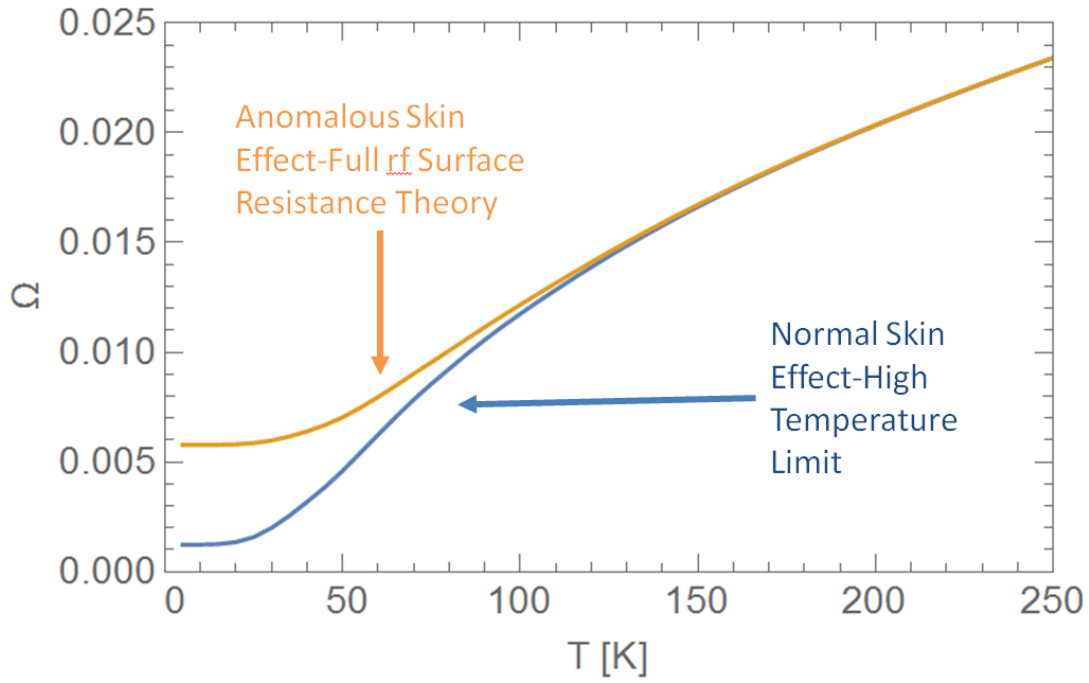

Figure A.1: Comparison of the normal skin effect surface resistance and anomalous skin effect surface resistance at 11.424 GHz in RRR=400 copper

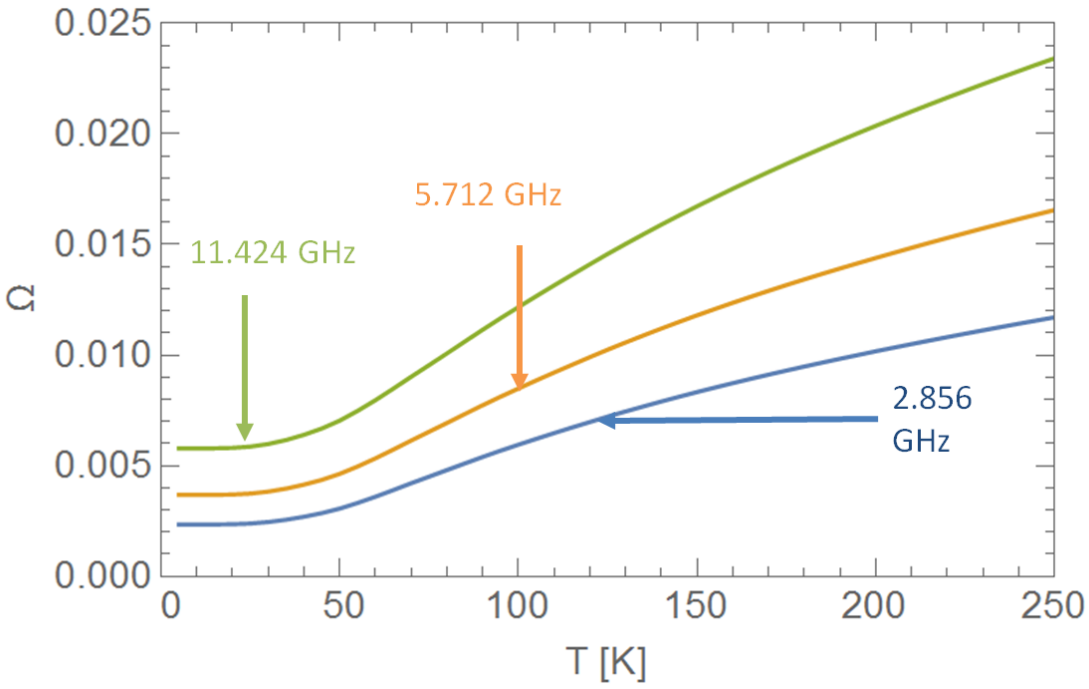

Figure A.2: Comparison of the anomalous skin effect surface resistance in RRR=500 Cu at 2.856, 5.712, and 11.424 GHz

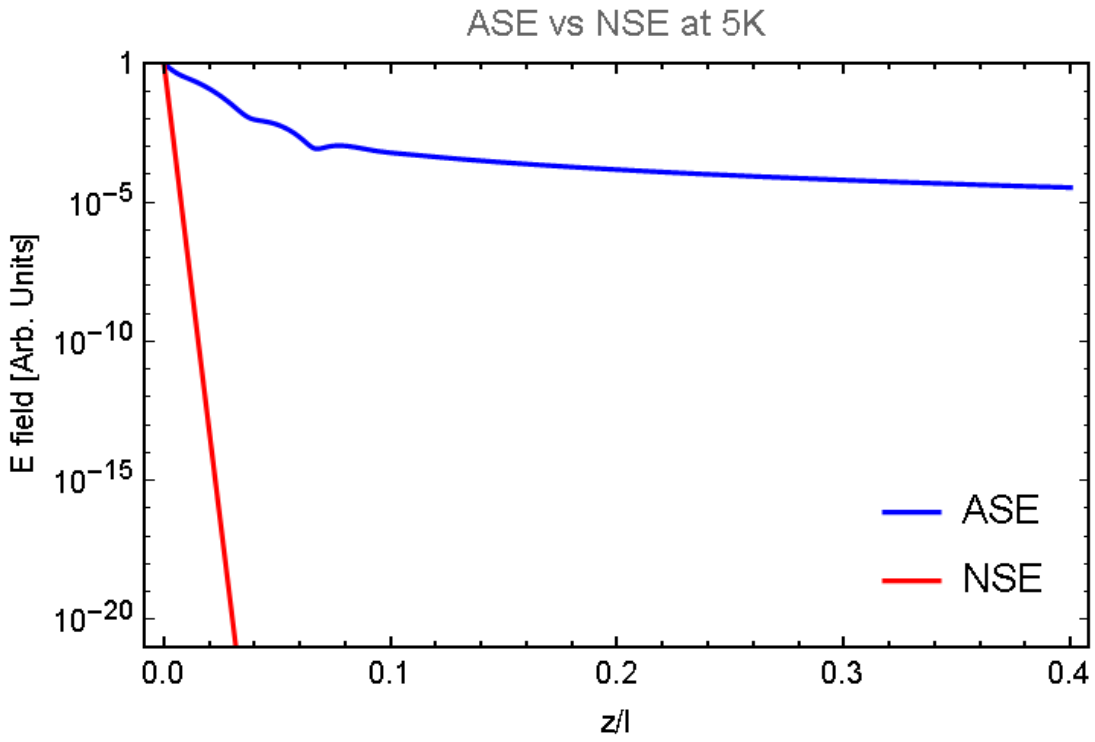

Figure A.3: Comparison of X-band electromagnetic field for normal skin effect and anomalous skin effect as they penetrate the surface of 4 K IACS 100% RRR=400 copper. The field is scaled to the value at the surface, and the distance is scaled to the electron mean free path in the metal.

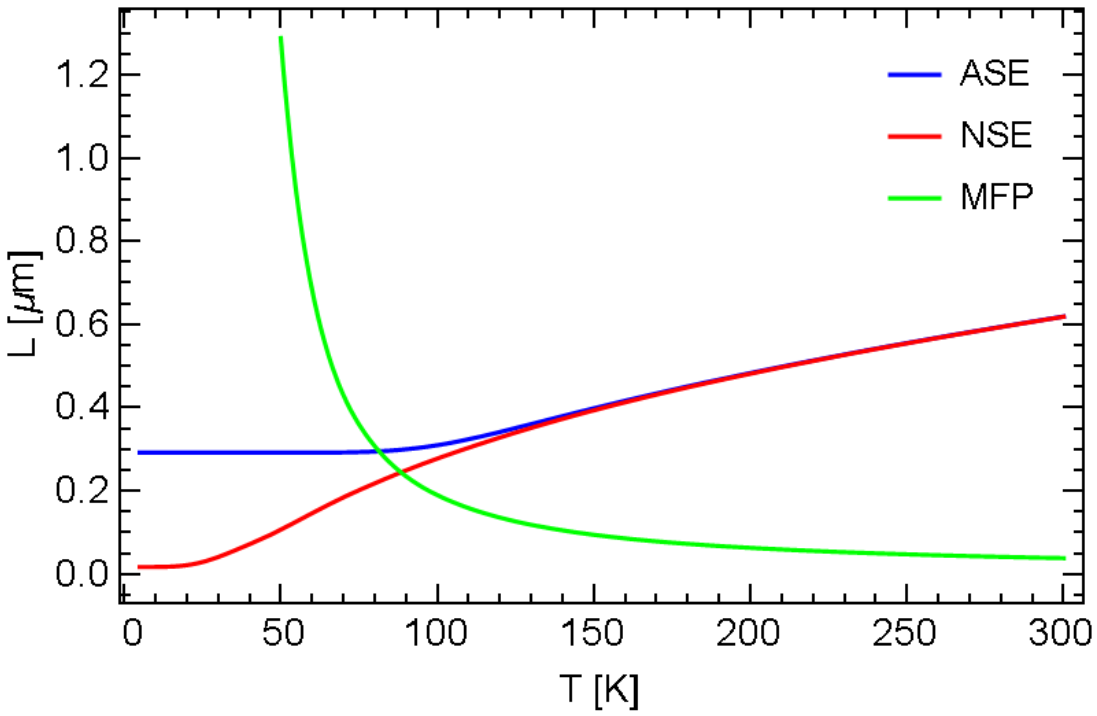

Figure A.4: The effective skin depth, normal skin depth, and mean free path of electrons for IACS 100%, RRR=400 copper at X-band.

distance it takes for the field to decrease by a factor of e. The result for X-band is shown in Figure A.4, along with the NSE skin depth and the mean free path of electrons in the metal. The effective skin depth and normal skin depth diverge when the mean free path approaches the same value.

A.2.2 Dependence on RRR

Another interesting consequence of the anomalous skin effect is that after a certain point, increasing the RRR does not improve the low temperature rf surface conductivity. As can be seen in the extreme limit, equation A.10, the rf surface resistance only depends on the Fermi velocity and the plasma frequency of a material, and not the DC resistivity. Figure A.5 shows, for X-band copper, that increasing the RRR does not decrease the low-temperature rf surface resistance..

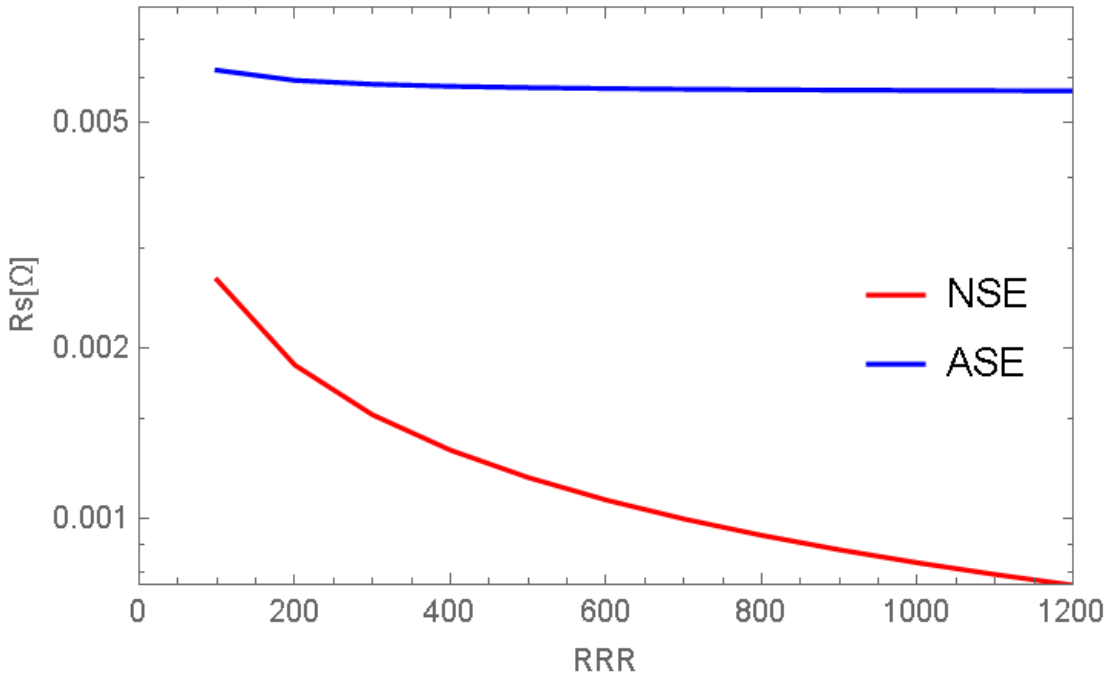

Figure A.5: R_s for 4 K, X-band, IACS 100 % copper with varying RRRs. Increasing the RRR does not significantly change the rf surface resistance at low temperatures.

APPENDIX B

Derivation of Fields in a Resonant Cavity

As the rf properties of the tested accelerating structures seem to vary in time, discussed in 4.1, a framework to calculate electromagnetic fields with time-dependent rf parameters needs to be developed. The resulting differential equation is used to calculate the electric field in the cryogenic accelerating cavity, as the Q_0 changes.

B.1 Definition of Basis Modes

I will consider at first a general fully closed resonant cavity with perfectly conductive walls. This resonant cavity will obey the source-less Maxwell's equations, which can be reduced to the steady-state electromagnetic wave equation

$$\left(\nabla^2 + k^2\right) \begin{cases} \vec{E}(\vec{r}) \\ \vec{H}(\vec{r}) \end{cases} = 0, \tag{B.1}$$

where k is the wave number, ω is the angular frequency, and $k = \omega/c$.

Then I will define a set of basis functions for a resonant cavity, where the basis functions, $\vec{E}_\lambda$ and $\vec{H}_\lambda$, are the eigenmodes of the cavity are solutions to the electromagnetic wave equation with eignennumbers k_λ:

$$\begin{aligned} \vec{E}(\vec{r},t) &= \sum_\lambda \vec{E}_\lambda(\vec{r}) e_\lambda(t), \\ \vec{H}(\vec{r},t) &= \sum_\lambda \vec{H}_\lambda(\vec{r}) h_\lambda(t), \end{aligned} \tag{B.2}$$

where e_λ and h_λ are the basis function field amplitudes. Non-degenerate solutions to equation B.1 are orthogonal and can be chosen to be orthonormal. Degenerate solutions can also

be orthogonalized if necessary. In this situation, I will not be concerned with any degenerate modes. The basis functions are defined such that

$$\begin{aligned} \vec{\nabla} \times \vec{E}_\lambda &= k_\lambda \vec{H}_\lambda, \\ \vec{\nabla} \times \vec{H}_\lambda &= k_\lambda \vec{E}_\lambda, \end{aligned} \tag{B.3}$$

where $k_\lambda = \omega_\lambda / c$ is the wave number of the resonant mode, and ω_λ is the angular frequency. Also, due to orthogonality

$$\begin{aligned} \vec{e}_\lambda(t) &= \int dV \vec{E}(\vec{r}, t) \cdot \vec{E}_\lambda(\vec{r}), \\ \vec{h}_\lambda(t) &= \int dV \vec{H}(\vec{r}, t) \cdot \vec{H}_\lambda(\vec{r}). \end{aligned} \tag{B.4}$$

These basis functions are for an ideal cavity, with perfectly conducting walls. In reality, the walls will be lossy, and the walls of the cavity require an opening for exciting fields inside the structure. These realities will be added as perturbations.

To accomplish this, I will take the dot product of Maxwell's curl equation, $\vec{\nabla} \times \vec{H} = \epsilon_0 \partial \vec{E} / \partial t$ with a basis function, $\vec{E}_\lambda$ and integrate over the cavity volume:

$$\begin{aligned} \int dV (\vec{\nabla} \times \vec{H}) \cdot \vec{E}_\lambda &= \epsilon_0 \int dV \frac{\partial \vec{E}}{\partial t} \cdot \vec{E}_\lambda \\ \int dV \vec{E} \cdot (\vec{\nabla} \times \vec{E}_\lambda) + \int dV \vec{\nabla} \cdot (\vec{H} \times \vec{E}_\lambda) &= \epsilon_0 \sum_\lambda \frac{de_{\lambda'}}{dt} \int dV \vec{E}_{\lambda'} \cdot \vec{E}_\lambda \\ \int dV \vec{E} \cdot (k_\lambda \vec{E}_\lambda) + \int dS \hat{n} \cdot (\vec{H} \times \vec{E}_\lambda) &= \epsilon_0 \sum_\lambda \frac{de_{\lambda'}}{dt} \delta_{\lambda\lambda'} \\ k_\lambda \vec{e}_\lambda + \int dS \hat{n} \cdot (\vec{H} \times \vec{E}_\lambda) &= \epsilon_0 \frac{de_\lambda}{dt}, \end{aligned} \tag{B.5}$$

where the integral is over the boundary to the resonant cavity volume and $\hat{n}$ is the unit vector that points outwards, perpendicular to that surface.

The same exercise can be performed for the magnetic field amplitude,

$$k_\lambda \vec{h}_\lambda + \int dS \hat{n} \cdot (\vec{E} \times \vec{H}_\lambda) = -\mu_0 \frac{dh_\lambda}{dt}. \tag{B.6}$$

Then the integrable surface is broken into two parts: for the finite conductivity walls, S_w, and the opening for the power input S_p. The equations to solve become:

$$
\begin{aligned}
k_\lambda \vec{e}_\lambda + \int_{S_w} dS\hat{n}\cdot(\vec{H}\times\vec{E}_\lambda) + \int_{S_p} dS\hat{n}\cdot(\vec{H}\times\vec{E}_\lambda) &= \epsilon_0 \frac{de_\lambda}{dt}, \\
k_\lambda \vec{h}_\lambda + \int_{S_w} dS\hat{n}\cdot(\vec{E}\times\vec{H}_\lambda) + \int_{S_p} dS\hat{n}\cdot(\vec{E}\times\vec{H}_\lambda) &= -\mu_0 \frac{dh_\lambda}{dt}.
\end{aligned} \tag{B.7}
$$

For simplicity I will assume that all fields have the same $e^{i\omega t}$ dependence; then:

$$
\begin{aligned}
\vec{E}(\vec{r},t) &= \tilde{E}(\vec{r},t)e^{i\omega t}, \\
\vec{E}(\vec{r},t) &= \tilde{E}(\vec{r},t)e^{i\omega t}, \\
\vec{e}(t) &= \tilde{e}(t)e^{i\omega t}, \\
\vec{h}(t) &= \tilde{h}(t)e^{i\omega t},
\end{aligned} \tag{B.8}
$$

where, $\tilde{E}, \tilde{H}, \tilde{e}$ and $\tilde{h}$ are all slowly-varying functions of time. ω, the frequency of the fields oscillatory behavior, is not necessarily the same as ω_λ, the frequency of the resonant mode. Using these relations, equation B.7 becomes:

$$
\begin{aligned}
k_\lambda \tilde{e}_\lambda + \int_{S_w} dS\hat{n}\cdot(\tilde{H}\times\vec{E}_\lambda) + \int_{S_p} dS\hat{n}\cdot(\vec{H}\times\vec{E}_\lambda) &= \epsilon_0 \frac{d\tilde{e}_\lambda}{dt} - i\omega\epsilon_0\tilde{e}_\lambda, \\
k_\lambda \tilde{h}_\lambda + \int_{S_w} dS\hat{n}\cdot(\tilde{E}\times\vec{H}_\lambda) + \int_{S_p} dS\hat{n}\cdot(\vec{E}\times\vec{H}_\lambda) &= -\mu_0 \frac{dh_\lambda}{dt} + i\omega\mu_0\tilde{h}_\lambda.
\end{aligned} \tag{B.9}
$$

B.2 Perturbation due to Skin Depth

I now change the previous assumption of the perfectly conducting walls to merely finite conductivity.

I define the ratio of the imaginary to real part of the rf surface impedance Z_S as

$$
\zeta_{im} \equiv -\frac{\mathrm{Im}(Z_s)}{\mathrm{Re}(Z_s)}. \tag{B.10}
$$

From A.2, ζ_{im} will vary from $\sqrt{3}$ at temperatures below 30 K to 1 at room temperature. Then,

$$
\tilde{E}|_{\mathrm{surf}} = R_s(1-\zeta_{im}i)(\tilde{H}_{\mathrm{surf}}\times\hat{n}) \tag{B.11}
$$

Then computing the surface wall integral, equation B.9

$$\begin{aligned}\int_{S_w} dS\hat{n}\cdot\tilde{E}\times\vec{H}_\lambda &= -\int_{S_w} dS\hat{n}\left[R_s(1-\zeta_{im}i)\hat{n}\times\tilde{H}\right]\vec{H}_\lambda \\ &= -\int_{S_w} dSR_s(1-\zeta_{im}i)\hat{n}\left[\hat{n}(\vec{H}_\lambda\cdot\tilde{H})-\tilde{H}(\hat{n}\cdot\vec{H}_\lambda)\right] \\ &= -\int_{S_w} dSR_s(1-\zeta_{im}i)\tilde{H}\cdot\vec{H}_\lambda\end{aligned} \tag{B.12}$$

From here we can define the internal quality factor as:

$$\frac{1}{Q_{0\lambda}} \equiv \int_{S_W} dS\frac{R_s}{2\mu_0\omega}|\vec{H}_\lambda|^2. \tag{B.13}$$

and substituting this back into B.12:

$$\begin{aligned}\int_{S_w} dS\hat{n}\cdot\tilde{E}\times\vec{H}_\lambda &= \tilde{h}_\lambda\int_{S_w} dSR_s(1-\zeta_{im}|\vec{H}_\lambda|^2 \\ &= \frac{(1-\zeta_{im})\mu_0\omega}{Q_{0\lambda}}\tilde{h}_\lambda.\end{aligned} \tag{B.14}$$

The other surface integral vanishes identically:

$$\int_{S_w} dS\hat{n}\cdot\tilde{H}\times\vec{E}_\lambda = -\int_{S_w} dS\tilde{H}\cdot\hat{n}\times\vec{E}_\lambda = 0. \tag{B.15}$$

B.3 Perturbation due to Coupling Waveguide

I assume now that there is a circular waveguide that is connected to the resonant cavity through a small coupling port. The fields in the waveguide can be completely defined by the fields perpendicular to the propagation axis, $\vec{E}_\perp\&\vec{H}_\perp$ [116]. A different set of orthogonal basis functions can be defined, $\vec{E}_{\perp a}\&\vec{H}_{\perp a}$, on a chosen plane normal to the propagation axis, $\hat{z}$, such that

$$\begin{aligned}\vec{E}_\perp(\vec{r},t) &= \sum_a \vec{E}_{\perp a}(\vec{r})V_a(t), \\ \vec{H}_\perp(\vec{r},t) &= \sum_a \vec{H}_{\perp a}(\vec{r})Z_{ca}I_a(t),\end{aligned} \tag{B.16}$$

where V_a and I_a are the expansion coefficients, and Z_{ca} is the characteristic impedance with $Z_{ca}\vec{H}_{\perp a} = \hat{z}\times\vec{E}_{\perp a}$. The basis functions follow the following orthogonal relations for an

arbitrary reference plane, S, in the waveguide:

$$\begin{aligned}
\int_S dS\vec{E}_{\perp a}\cdot\vec{E}_{\perp b} &= \delta_{ab} \\
\int_S dS\vec{H}_{\perp a}\cdot\vec{H}_{\perp b} &= \frac{\delta_{ab}}{Z_{ca}^2} \\
\int_S dS\vec{E}_{\perp a}\times\vec{H}_{\perp b} &= \frac{\delta_{ab}}{Z_{ca}}
\end{aligned} \tag{B.17}$$

Since I am interested in the overlap integrals between the electromagnetic fields in the waveguide and those in the resonant cavity, I define

$$\begin{aligned}
\vec{E}_{\perp\lambda}(\vec{r}) &= \sum_a \vec{E}_{\perp a}(\vec{r})V_{a\lambda}, \\
\vec{H}_{\perp\lambda}(\vec{r}) &= \sum_a \vec{H}_{\perp a}(\vec{r})Z_{ca}I_{a\lambda},
\end{aligned} \tag{B.18}$$

with

$$\begin{aligned}
V_{a\lambda} &= \int_S dS\vec{E}_\lambda(\vec{r})\cdot\vec{E}_{\perp a}(\vec{r}) \\
I_{a\lambda} &= Z_{ca}\int_S dS\vec{H}_\lambda(\vec{r})\cdot\vec{H}_{\perp a}(\vec{r})
\end{aligned} \tag{B.19}$$

Again, I assume that the time-dependence for all fields is $e^{-i\omega t}$ and that the slowly-varying amplitudes for the waveguide expansion coefficients are $\tilde{V}_a$ and $\tilde{I}_a$. Using these definitions, the other surface integral from equation B.9 can be calculated over the coupling waveguide surface S_p.

$$\begin{aligned}
\int_{S_p} dS\hat{n}\cdot\tilde{E}\times\vec{H}_\lambda &= \int_{S_p} dS\hat{n}\cdot\left[\sum_a \vec{E}_{\perp a}\tilde{V}_a\right]\times\left[\sum_b \vec{H}_{\perp b}Z_{cb}I_{b\lambda}\right] \\
&= -\sum_a\sum_b \tilde{V}_a Z_{cb}I_{b\lambda}\int_{S_p} dS\hat{z}\cdot\vec{E}_{\perp a}\times\vec{H}_{\perp b} \\
&= -\sum_a\sum_b \tilde{V}_a Z_{cb}I_{b\lambda}\frac{\delta_{ab}}{Z_{ca}} \\
&= -\sum_a \tilde{V}_a I_{a\lambda}
\end{aligned} \tag{B.20}$$

The other surface integral can be solved similarly to find

$$\int_{S_p} dS\hat{n}\cdot\tilde{H}\times\vec{E}_\lambda = \sum_a \tilde{I}_a V_{a\lambda}. \tag{B.21}$$

Since the choice of reference plane is arbitrary, I will choose a plane such that $V_{a\lambda} = 0$.

B.4 Derivation of Differential Equation

Having solved the surface integral perturbations due to the skin depth and coupling waveguide then equation B.9 becomes:

$$\begin{aligned} -\mu_0\frac{d\tilde{h}_\lambda(t)}{dt} + i\mu_0\omega\tilde{h}_\lambda(t) &= \frac{\omega_\lambda(t)\tilde{e}_\lambda}{c} + \frac{\mu_0(1-\zeta_{im}i)\omega}{Q_{0\lambda}(t)}\tilde{h}_\lambda(t) - \sum_a \tilde{V}_a I_{a\lambda} \\ \epsilon_0\frac{d\tilde{e}_\lambda(t)}{dt} - i\epsilon_0\omega\tilde{e}_\lambda(t) &= \frac{\omega_\lambda(t)\tilde{h}_\lambda}{c}, \end{aligned} \tag{B.22}$$

where the time dependencies of the mode amplitudes, $\tilde{e}_\lambda$ and $\tilde{h}_\lambda$, as well as the cavity properties Q_0 and ω_λ, are explicitly included. From here I solve for the electric field, by substituting the two equations of B.22 together, resulting in:

$$\begin{aligned} &-\epsilon_0\mu_0 c\frac{d}{dt}\left[\frac{1}{\omega_\lambda(t)}\left(\frac{d\tilde{e}_\lambda(t)}{dt} - i\omega\tilde{e}_\lambda(t)\right)\right] - \frac{\omega_\lambda(t)\tilde{e}_\lambda}{c} \\ = \;& \frac{\mu_0 c\epsilon_0(1-(\zeta_{im}+Q_{0\lambda})i)\omega}{Q_{0\lambda}(t)}\left[\frac{c}{\omega_\lambda(t)}\left(\frac{d\tilde{e}_\lambda(t)}{dt} - i\omega\tilde{e}_\lambda(t)\right)\right] - \sum_a \tilde{V}_a I_{a\lambda} \end{aligned} \tag{B.23}$$

which simplifies to

$$\begin{aligned} &\frac{d^2\tilde{e}_\lambda(t)}{dt^2} + \left[\frac{1}{\omega_\lambda(t)}\frac{d\omega_\lambda(t)}{dt} + \frac{\omega}{Q_{0\lambda}(t)} - i\omega\left(2 + \frac{\zeta_{im}}{Q_{0\lambda}(t)}\right)\right]\frac{d\tilde{e}_\lambda(t)}{dt} \\ &+ \left[\omega_\lambda^2(t) - \omega^2\left(1 + \frac{\zeta_{im}}{Q_{0\lambda}}\right) + i\omega\left(\frac{1}{\omega_\lambda(t)}\frac{d\omega_\lambda(t)}{dt} - \frac{\omega}{Q_{0\lambda}(t)}\right)\right]\tilde{e}_\lambda(t) \\ &= -c\omega_\lambda(t)\sum_a \tilde{V}_a I_{a\lambda} \end{aligned} \tag{B.24}$$

Here, I make two assumptions. First, that the resonant frequency of the excited mode, ω_λ will not vary by more than a bandwidth. For the experiment presented: $\omega_\lambda \sim 10^{10}$, $Q_0 \sim 10^5$, and the pulse length over which the change in ω_λ occurs is less than $1\mu s$. Therefore, $\omega\omega_\lambda/Q_0 \sim 10^{15}$ and $\Delta\omega_\lambda\Delta t < 10^{11}$, giving the following inequality:

$$\left|\frac{d\omega_\lambda}{dt}\right| << \frac{\omega\omega_\lambda}{Q_{0\lambda}}. \tag{B.25}$$

Second, since the field amplitude $\tilde{e}_\lambda(t)$ is slowly varying I can assume that

$$\left|\frac{d^2\tilde{e}_\lambda(t)}{dt^2}\right| << \omega^2\tilde{e}_\lambda(t). \tag{B.26}$$

Using these assumptions, I arrive at:

$$\left[\frac{1}{Q_{0\lambda}(t)} - i\left(2 + \frac{\zeta_{im}}{Q_{0\lambda}(t)}\right)\right]\frac{d\tilde{e}_\lambda(t)}{dt} + \left[\frac{\omega_\lambda^2(t)}{\omega} - \omega\left(1 + \frac{\zeta_{im}}{Q_{0\lambda}}\right) - \frac{i\omega}{Q_{0\lambda}(t)}\right]\tilde{e}_\lambda(t) = -\frac{c\omega_\lambda(t)}{\omega}\sum_a \tilde{V}_a I_{a\lambda} \tag{B.27}$$

Next, I want to express $\sum_a \tilde{I}_a V_{a\lambda}$ in terms of the electric field amplitude. In the waveguide, I assume the primary mode is TM, in which case I can write:

$$\tilde{H}_\perp = \tilde{H}_\lambda = \sum_a \vec{H}_{\perp a} Z_{ca} \tilde{I}_a(t) = \sum_\lambda \vec{H}_\lambda \tilde{e}_\lambda. \tag{B.28}$$

I will assume that there is only one waveguide mode exciting one resonant mode. By taking the dot product on both sides with the waveguide mode $\vec{H}_{\perp 1}$, then I arrive at:

$$\tilde{I}_1(t) = I_{1\lambda}\tilde{h}_\lambda(t) \tag{B.29}$$

The waveguide expansion coefficients can be split into forward and backward propagating components:

$$\begin{aligned}\tilde{V}_1 &= \tilde{V}_1^+ + \tilde{V}_1^- \\ \tilde{I}_1 &= \tilde{I}_1^+ + \tilde{I}_1^-,\end{aligned} \tag{B.30}$$

with the relation

$$Z_{ca}\tilde{I}_a^\pm = \pm\tilde{V}_a^\pm \tag{B.31}$$

$$\begin{aligned}\tilde{V}_1 &= 2Z_{c1}\tilde{I}_1^+ - Z_{c1}\tilde{I}_1 \\ &= 2\tilde{V}_1^+ - Z_{c1}I_{1\lambda}\tilde{h}_\lambda(t)\end{aligned} \tag{B.32}$$

I define the external quality factor,

$$\frac{1}{Q_{E\lambda}} \equiv \frac{I_{1\lambda}^2 Z_{c1}}{\mu_0 \omega_\lambda}. \tag{B.33}$$

The rf power, P_{in}, that is incident to the resonant cavity from the waveguide can be represented as:

$$\tilde{V}_1^+ = \sqrt{2P_{in}Z_{c1}} \tag{B.34}$$

By multiplying through by $I_{1\lambda}$ and substituting $\tilde{h}_\lambda$ from equation B.22:

$$\begin{aligned}\tilde{V}_1 I_{1\lambda} &= 2V_1^+ I_{1\lambda} - Z_{c1} I_{1\lambda}^2 \tilde{h}_\lambda(t) \\ \tilde{V}_1 I_{1\lambda} &= \sqrt{\frac{8P_{in}\mu_0\omega_\lambda}{Q_{E\lambda}}} - \frac{\epsilon_0 c\mu_0}{Q_{E\lambda}}\left(\frac{d\tilde{e}_\lambda(t)}{dt} - i\omega\tilde{e}_\lambda(t)\right)\end{aligned} \tag{B.35}$$

This definition from the previous equation is substituted back into equation B.27

$$\begin{aligned}\left[\frac{1}{Q_{0\lambda}(t)} - i\left(2 + \frac{\zeta_{im}}{Q_{0\lambda}(t)}\right)\right]\frac{d\tilde{e}_\lambda(t)}{dt} &+ \left[\frac{\omega_\lambda^2(t)}{\omega} - \omega\left(1 + \frac{\zeta_{im}}{Q_{0\lambda}}\right) - \frac{i\omega}{Q_{0\lambda}(t)}\right]\tilde{e}_\lambda(t) \\ &= -\frac{1}{\omega}\sqrt{\frac{8P_{in}\omega_\lambda^3}{\epsilon_0 Q_{E\lambda}}} - \frac{\omega_\lambda}{\omega Q_{E\lambda}}\left(\frac{d\tilde{e}_\lambda(t)}{dt} - i\omega\tilde{e}_\lambda(t)\right)\end{aligned} \tag{B.36}$$

which finally simplifies to:

$$\begin{aligned}&\left[\frac{\omega}{Q_{0\lambda}(t)} + \frac{\omega_\lambda}{Q_{E\lambda}} - i\omega\left(2 + \frac{\zeta_{im}}{Q_{0\lambda}(t)}\right)\right]\frac{d\tilde{e}_\lambda(t)}{dt} \\ &+ \left[\omega_\lambda^2(t) - \omega^2\left(1 + \frac{\zeta_{im}}{Q_{0\lambda}(t)}\right) - i\omega\left(\frac{\omega}{Q_{0\lambda}(t)} + \frac{\omega_\lambda}{Q_{E\lambda}}\right)\right]\tilde{e}_\lambda(t) = -\sqrt{\frac{8P_{in}\omega_\lambda^3}{\epsilon_0 Q_{E\lambda}}}\end{aligned} \tag{B.37}$$

This is the full equation for the electric field inside a resonant cavity.

Before moving on further, it is important to analyze this equation. If the cavity parameters are constant and I define:

$$\frac{1}{Q_{T\lambda}} \equiv \frac{1}{Q_{0\lambda}} + \frac{1}{Q_{E\lambda}}, \tag{B.38}$$

and drive the resonant cavity at

$$\omega = \frac{\omega_\lambda}{\sqrt{1 + \frac{\zeta_{im}}{Q_{0\lambda}}}}, \tag{B.39}$$

then the differential equation B.37 reduces to (ignoring terms of $1/Q^2$

$$\frac{d\tilde{e}_\lambda(t)}{dt}\left[\frac{1}{Q_{T\lambda}} - 2i\right] - \tilde{e}_\lambda(t)\left[\frac{i\omega_\lambda}{Q_{T\lambda}}\right] = -\sqrt{\frac{8P_{in}\omega_\lambda}{\epsilon_0 Q_{E\lambda}}}. \tag{B.40}$$

This equation has a relatively simple solution with the initial condition $e_\lambda(0) = 0$:

$$e_\lambda(t) = -iQ_{T\lambda}\sqrt{\frac{8P_{in}}{\omega_\lambda\epsilon_0 Q_{E\lambda}}}\left(1 - e^{it/\tau_p}\right)e^{-i\omega t}, \tag{B.41}$$

with ω defined as in equation B.39 and $\tau_p \equiv 2Q_{T\lambda}/\omega_\lambda$. What is important to draw from this equation is that the resonance frequency has been shifted from ω_λ by the skin depth of the

resonant cavity. In particular the terms that cause the frequency shift are those with the from $\zeta_{im}/Q_{0\lambda}(t)$.

In the experiment presented in this work the frequency shift may not only be caused by the skin depth, as it is here. Therefore, I will ignore this frequency shift and fit the frequency change separately. To this end I can simplify even further by assuming $Q_0 >> 1$:

$$\begin{aligned} & \left[\frac{\omega}{Q_{0\lambda}(t)} + \frac{\omega_\lambda(t)}{Q_{E\lambda}} - 2i\omega\right]\frac{d\tilde{e}_\lambda(t)}{dt} \\ + & \left[\omega_\lambda^2(t) - \omega^2 - i\omega\left(\frac{\omega}{Q_{0\lambda}(t)} + \frac{\omega_\lambda(t)}{Q_{E\lambda}}\right)\right]\tilde{e}_\lambda(t) = -\sqrt{\frac{8P_{in}\omega_\lambda^3(t)}{\epsilon_0 Q_{E\lambda}}} \end{aligned} \tag{B.42}$$

The solution for this differential equation no longer has the frequency shift mentioned above due to the skin depth. The frequency shift is instead contained explicitly in $\omega_\lambda(t)$.

B.5 Constant Cavity Parameters

In a different exercise I will now quickly re-derive the differential equation with constant cavity parameters. In this case I use a Fourier and inverse Fourier transform, as in [116], without adopting the assumed slowly-varying functions in time, starting from equation B.8, the I arrive at:

$$\begin{aligned} -\mu_0\frac{dh_\lambda(t)}{dt} &= \frac{\omega_\lambda}{c}e_\lambda(t) + \mu_0\omega_\lambda\frac{1-i\zeta_{im}}{Q_0}h_\lambda(t) - \sqrt{\frac{8P_{in}\mu_0\omega_\lambda}{Q_E}}e^{-i\omega_d t} + \frac{\mu_0\omega_\lambda}{Q_E}h_\lambda(t) \\ \epsilon_0\frac{de_\lambda(t)}{dt} &= \frac{\omega_\lambda}{c}h_\lambda(t) \end{aligned} \tag{B.43}$$

Solving for $e_\lambda(t)$

$$\begin{aligned} -\frac{\epsilon_0 c\mu_0}{\omega_\lambda}\frac{d^2e_\lambda(t)}{dt^2} &= \frac{\omega_\lambda}{c}e_\lambda(t) + \mu_0 c\epsilon_0\frac{1-i\zeta_{im}}{Q_0}\frac{de_\lambda(t)}{dt} - \sqrt{\frac{8P_{in}\mu_0\omega_\lambda}{Q_E}}e^{-i\omega_d t} + \frac{\epsilon_0 c\mu_0}{Q_E}\frac{de_\lambda(t)}{dt} \\ -\frac{1}{c\omega_\lambda}\frac{d^2e_\lambda(t)}{dt^2} &= \frac{\omega_\lambda}{c}e_\lambda(t) + \frac{1}{c}\frac{1-i\zeta_{im}}{Q_0}\frac{de_\lambda(t)}{dt} - \sqrt{\frac{8P_{in}\mu_0\omega_\lambda}{Q_E}}e^{-i\omega_d t} + \frac{1}{cQ_E}\frac{de_\lambda(t)}{dt} \end{aligned} \tag{B.44}$$

If I solve for the real and imaginary parts separately, and define $1/Q_L = 1/Q_0 + 1/Q_E$,

$$\left[\frac{d^2}{dt^2} + \frac{\omega_\lambda}{Q_L}\frac{d}{dt} + \omega_\lambda^2\right]e_\lambda(t) = -\sqrt{\frac{8P_{in}\omega_\lambda^3}{\mu_0 Q_E}}e^{-i\omega_d t} \tag{B.45}$$

This final differential equation is analogous to a damped driven harmonic oscillator. The next section will show that a driven LRC circuit arrives at the same differential equation, and equivalent circuits become a strong tool for resonant cavities as explained in **??**.

APPENDIX C

Equivalent Circuit Theory

As shown in B.5, a resonant cavity behaves as a driven harmonic oscillator when the rf parameters are constant in time. The behaviorof an LRC circuit is also defined by a differential equation analogous to the damped driven harmonic oscillator. Therefore, analogous circuits can be created to reveal some aspects of the behavior in resonant cavities. Equivalent circuit theory will also be very important for extracting the rf parameters from a VNA measurement.

C.1 LRC circuit

I will consider a driven shunt LRC circuit as shown in Figure C.1.

The differential equation for the voltage in the LRC circuit is [7]:

$$\left(\frac{d}{dt^2} + \frac{d}{dt}\frac{1}{RC} + \frac{1}{LC}\right) V(t) = \frac{\dot{I}}{C}, \tag{C.1}$$

where the voltage generator supplies the current $I(t)$. Then the analogous values between the resonant cavity and the circuit are:

$$\begin{aligned} \mathrm{Q}_0 &= \omega_0 RC, \\ \omega_0 &= \frac{1}{\sqrt{LC}}, \\ \beta &= \frac{R}{Z_L}, \end{aligned} \tag{C.2}$$

where Z_L is the impedance of the line to the generator.

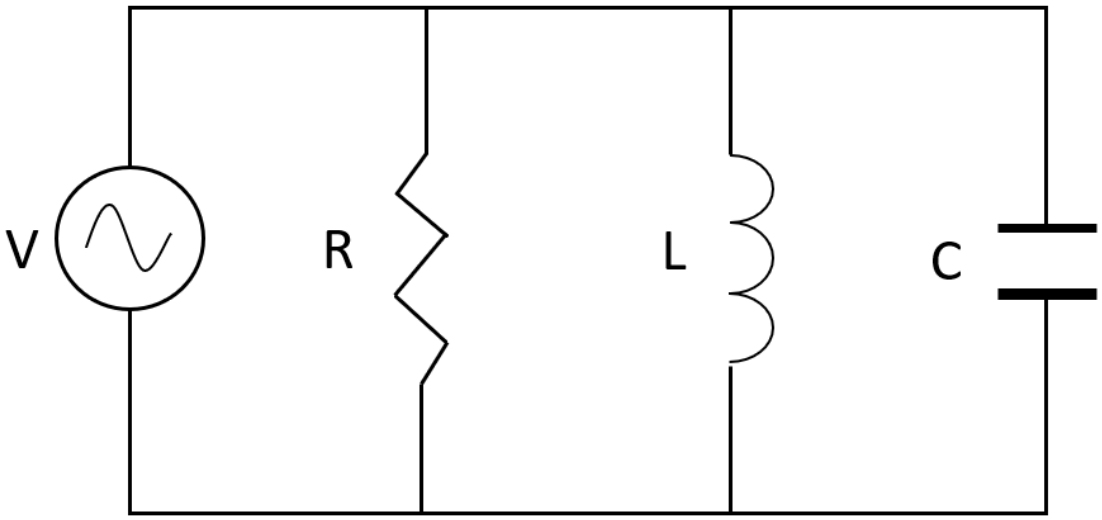

Figure C.1: Circuit diagram for a LRC circuit

C.2 Impedance

Using this analogous circuit, the complex impedance is:

$$Z_c(\omega) = \frac{1}{\frac{1}{R} + i\omega C + \frac{1}{i\omega L}}. \tag{C.3}$$

Which can be reduced to

$$\begin{aligned} Z_c(\omega) &= \frac{R}{1 + i\mathrm{Q}_0\delta}, \\ \delta &= \frac{\omega}{\omega_0} - \frac{\omega_0}{\omega} = \frac{f}{f_0} - \frac{f_0}{f}. \end{aligned} \tag{C.4}$$

To find the reflection coefficient I use the equation:

$$\Gamma = \frac{Z_c - Z_L}{Z_c + Z_L}. \tag{C.5}$$

Inputting equation C.4 into C.5, the reflection is:

$$\Gamma(\omega) = \frac{(\beta - 1)\omega\omega_0 - i\mathrm{Q}_0(\omega^2 - \omega_0^2)}{(1 + \beta)\omega\omega_0 + i\mathrm{Q}_0(\omega^2 - \omega_0^2)}. \tag{C.6}$$

Using this calculated reflection coefficient, the expected reflected amplitude from an arbitrary input to the cavity is found using $V^- = \Gamma[\omega]V^+$. Given a reflected amplitude and the input

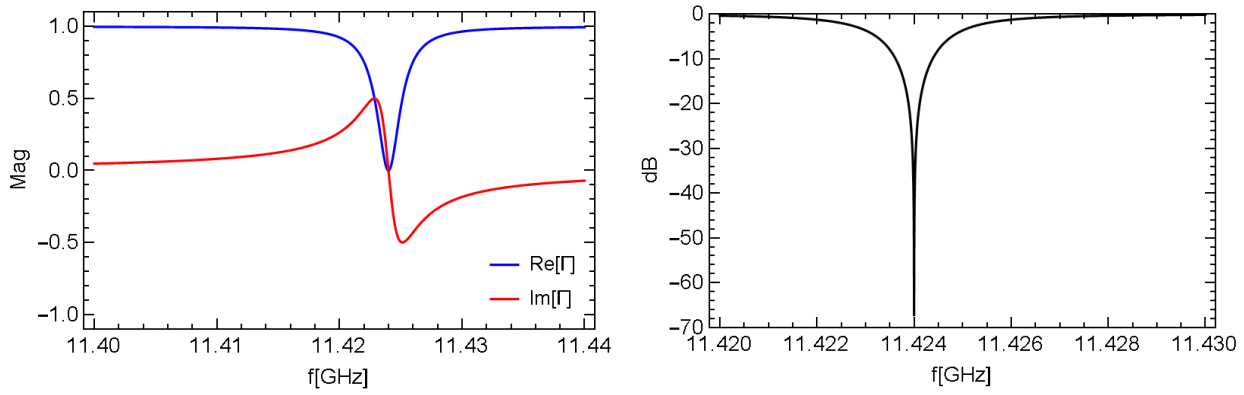

(a) (b)

Figure C.2: Reflection coefficient for a resonant cavity with $Q_0 = 10,000$, $\beta = 1$, and $f_0 = 11.424$ GHz.(a) real and imaginary parts, and (b) dB.

wave that created the reflection that is measured, I can fit and find Q_0, ω_0, and β for the cavity by matching the measurement with the result of C.6. Figure C.2 shows an example of the reflection coefficient of a resonant cavity.

The gradient inside the resonant cavity is analogous to the voltage across the LRC circuit, V_{LRC}. To calculate the gradient I use the effective shunt impedance r and length as defined in 1.2.1. The analogy to the circuit for power lost in the cavity, P_{cav}, and input power, P_{in} is:

$$\begin{aligned} P_{cav} &= \frac{|V_{LRC}|^2}{2R} \\ P_{in} &= \frac{|V^+|^2}{2Z_L}. \end{aligned} \tag{C.7}$$

The voltage across the circuit, and thus the accelerating gradient, in the steady state regime can be found by:

$$\begin{aligned} V_{LRC} &= V^+ + V^- = V^+(1+\Gamma) \\ P_{cav} &= P_{in}|1+\Gamma|^2\frac{Z_L}{R} \\ G(\omega) &= \sqrt{\frac{r}{L}}\frac{2\sqrt{\beta}\omega\omega_0}{(1+\beta)\omega\omega_0 + i\mathrm{Q}_0(\omega^2-\omega_0^2)}\sqrt{P_{in}} \end{aligned} \tag{C.8}$$

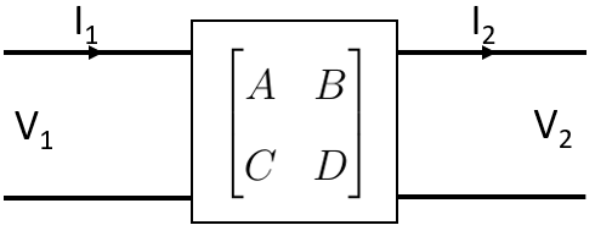

Figure C.3: An arbitrary two-port equivalent circuit with ABCD matrix.

C.3 ABCD Matrix Cascading

So far, I have only considered the equivalent circuit of a one-port cavity, which is described by its reflection coefficient when observing from the outside, or the voltage across the circuit. Now I would like to consider two-port rf elements, such as a waveguide. Since I am also interested creating equivalent circuits out of multiple elements, I will use the formalism known as ABCD matrices that are well-suited for this application.

An ABCD matrix for an arbitrary two-port matrix shown in Figure C.3, is

$$\begin{bmatrix} V_1 \\ I_1 \end{bmatrix} = \begin{bmatrix} A & B \\ C & D \end{bmatrix} \cdot \begin{bmatrix} V_2 \\ I_2 \end{bmatrix}. \tag{C.9}$$

In this formalism, to find the effect of consecutive two-port rf elements, the matrices are simply multiplied together as matrices [184].

Since I will be using equivalent circuits to examine the reflection from resonant cavities I need a way to find the total reflection of a two-port matrix cascaded with a cavity as in the example shown in Figure C.4. The resulting impedance is (where the components of the ABCD matrix can depend on ω):

$$Z_{\mathrm{Tot}}(\omega) = \frac{A(\omega)Z_C(\omega) + B(\omega)}{C(\omega)Z_C(\omega) + D(\omega)} \tag{C.10}$$

and the reflection can be found by applying equation C.5.

C.3.1 VNA model for Waveguide Connection

A VNA measures the reflection coefficient of the resonant cavity. Equation C.6 is used to fit that data and extract, β, ω_0 and Q_0. However, to reach a more accurate result measurement,

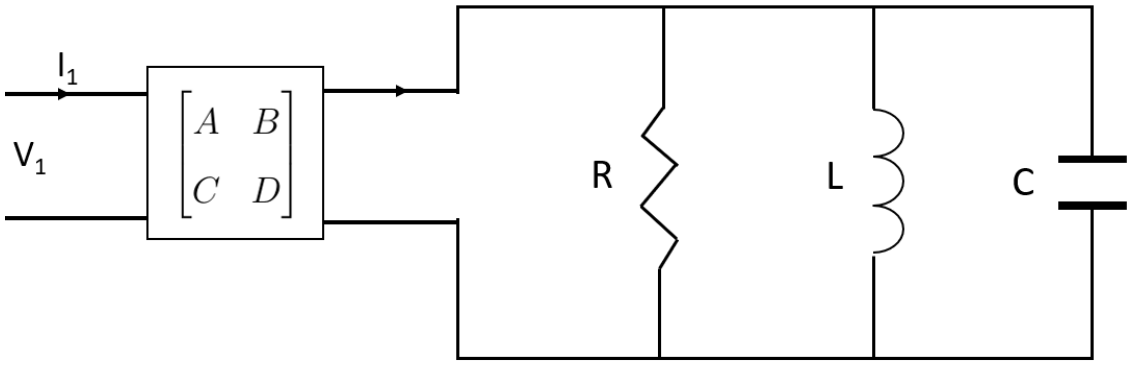

Figure C.4: An arbitrary two-port equivalent circuit with ABCD matrix attached to a resonant LRC circuit.

we should add some complexity to the equivalent circuit to more accurately represent the system. To do this I include the effect of the transmission from the cavity to the VNA via a rectangular waveguide.

According [184], the ABCD matrix for a lossy rectangular waveguide is

$$\begin{aligned}\begin{bmatrix} A & B \\ C & D \end{bmatrix} &= \begin{bmatrix} \cosh\gamma_W(\omega)L_W & Z_L\sinh\gamma_W(\omega)L_W \\ \frac{1}{Z_L}\sinh\gamma_W(\omega)L_W & \cosh\gamma_W(\omega)L_W \end{bmatrix} \\ \gamma_W(\omega) &= \frac{\alpha_W}{\sqrt{1-\left(\frac{\omega_c}{\omega}\right)^2}} + i\frac{\omega}{c}\sqrt{1-\left(\frac{\omega_c}{\omega}\right)^2}, \end{aligned} \tag{C.11}$$

where α_W is the attenuation constant of the waveguide, L_W is the length, and ω_c is the cutoff frequency.

The resulting reflection coefficient is then, where I have changed from angular frequency to frequency:

$$\Gamma(f) = e^{i\theta}e^{-2\alpha_W L_W\left(1-\left(\frac{f_c}{f}\right)^2\right)^{-\frac{1}{2}}}e^{-2i\frac{L_W}{cf}(f+f_c)(f-f_c)\left(1-\left(\frac{f_c}{f}\right)^2\right)^{-\frac{1}{2}}}\frac{1-i\left(\frac{1}{Q_e}-\frac{1}{Q_0}\right)\frac{f}{f_0}-\left(\frac{f}{f_0}\right)^2}{-1-i\left(\frac{1}{Q_0}+\frac{1}{Q_e}\right)\frac{f}{f_0}+\left(\frac{f}{f_0}\right)^2}. \tag{C.12}$$

The first factor is an arbitrary phase of the transmission, the second factor is attenuation in the waveguide, and the third factor is a dispersion term. For the VNA measurement I only consider a relatively small frequency window around the target frequency $f = f_0 + \delta f$, therefore we can use a Taylor expansion to simplify this expression. For this exercise

$(f_c/f_0)^2 \sim 1/3$. First looking specifically at the dispersion term:

$$\begin{aligned} & e^{-2i\frac{L_W}{c}(f-\frac{f_c^2}{f})\left(1-\frac{1}{3}\frac{1}{1+\left(\frac{\delta f}{f_0}\right)^2}\right)^{-\frac{1}{2}}} \\ = \; & e^{-2i\frac{L_W}{c}(f_0+\delta f-(\frac{1}{3}\frac{f_0}{1+\frac{\delta f}{f_0}}))\left(1-\frac{1}{3}(1-\left(\frac{\delta f}{f_0}\right)^2)\right)^{-\frac{1}{2}}} \\ = \; & e^{-i\frac{4}{3}\sqrt{\frac{2}{3}}\frac{L_W}{c}(f_0+2\delta f-\frac{3}{4f_0}\delta f^2)}. \end{aligned} \tag{C.13}$$

Similarly, the attenuation term becomes:

$$e^{-2\alpha_W L_W\left(1-\frac{1}{3}\frac{1}{1+\left(\frac{\delta f}{f_0}\right)^2}\right)^{-\frac{1}{2}}}$$

$$= e^{-2\alpha_W L_W\left(1-\frac{1}{4}\left(\frac{\delta f}{f_0}\right)^2\right)} \tag{C.14}$$

$$= e^{-2\alpha_W L_W}\left(1+\frac{\alpha_W L_W}{2}\left(\frac{\delta f}{f_0}\right)^2\right) \tag{C.15}$$

The model has been simplified to fit the data:

$$\Gamma(f) = A_c e^{i\theta} e^{i\gamma_l(f-f_0)} e^{i\gamma_q(f-f_0)^2} \frac{1-i\left(\frac{1}{Q_e}-\frac{1}{Q_0}\right)\frac{f}{f_0}-\left(\frac{f}{f_0}\right)^2}{-1-i\left(\frac{1}{Q_0}+\frac{1}{Q_e}\right)\frac{f}{f_0}+\left(\frac{f}{f_0}\right)^2} \tag{C.16}$$

In this model A_c collects the attenuation of the system from the lossy components in the RF network, and the frequency dependent attenuation is disregarded, as it is second order in $\delta f/f_0 << 1$. γ_l, and γ_q are the linear and quadratic dispersion terms. These terms are split to allow more freedom, since the transmission is not a perfect waveguide. θ collects the frequency independent rotation angle in a single variable, from drift in the network analyzer and length of transmission lines. Figure C.5 shows an example reflection coefficient for this system. The dispersion terms are exaggerated to show their effects.

C.3.2 Equivalent Circuit for High Voltage Coaxial Feedthrough

In the experiment described in 3.4, equation C.16 does not accurately describe the data. This is most likely due to the coaxial high voltage feedthrough into the cryostat. In [184],

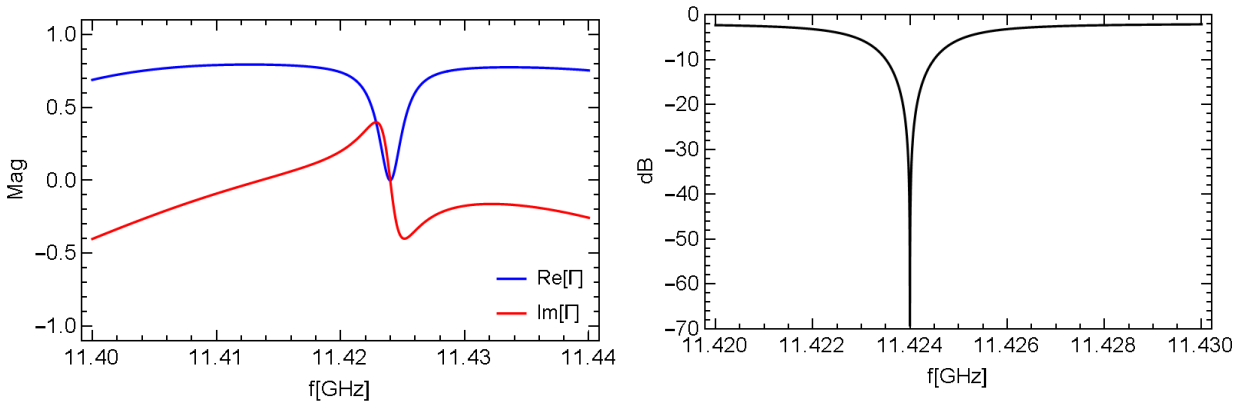

(a) (b)

Figure C.5: Reflection coefficient for a resonant cavity with $Q_0 = 10,000$, $\beta = 1$, and $f_0 = 11.424$ GHz and a lossy waveguide with $A_c = 0.8$, $\gamma_l = 201/GHz$, and $\gamma_q = 10^3 1/GHz^2$.(a) real and imaginary parts, and (b) dB.

there are multiple equivalent circuit discontinuities that could exist in a coaxial transmission line. The one that worked the best for this situation was a shunt capacitance discontinuity, which can be described by the ABCD matrix:

$$\begin{bmatrix} A & B \\ C & D \end{bmatrix} = \begin{bmatrix} 1 & 0 \\ i\omega D_0 & 1 \end{bmatrix},$$

where D_0 describes the capacitance of the discontinuity.

For this model I also used a lossy coaxial transmission line rather than lossy waveguide, which is described as:

$$\begin{aligned} \begin{bmatrix} A & B \\ C & D \end{bmatrix} &= \begin{bmatrix} \cosh \gamma_{\text{coax}}(\omega) L_{\text{coax}} & Z_L \sinh \gamma_{\text{coax}}(\omega) L_{\text{coax}} \\ \frac{1}{Z_L} \sinh \gamma_{\text{coax}}(\omega) L_{\text{coax}} & \cosh \gamma_{\text{coax}}(\omega) L_{\text{coax}} \end{bmatrix} \\ \gamma_{\text{coax}}(\omega) &= \alpha_{\text{cx}} + i\beta_{\text{cx}}\omega, \end{aligned} \tag{C.17}$$

where L_{coax} is the length of the coaxial lines, α_{coax} is the attenuation, and β_{coax} describes the oscillation in phase.

After cascading a coaxial line, the capacitor discontinuity, and another coaxial line with

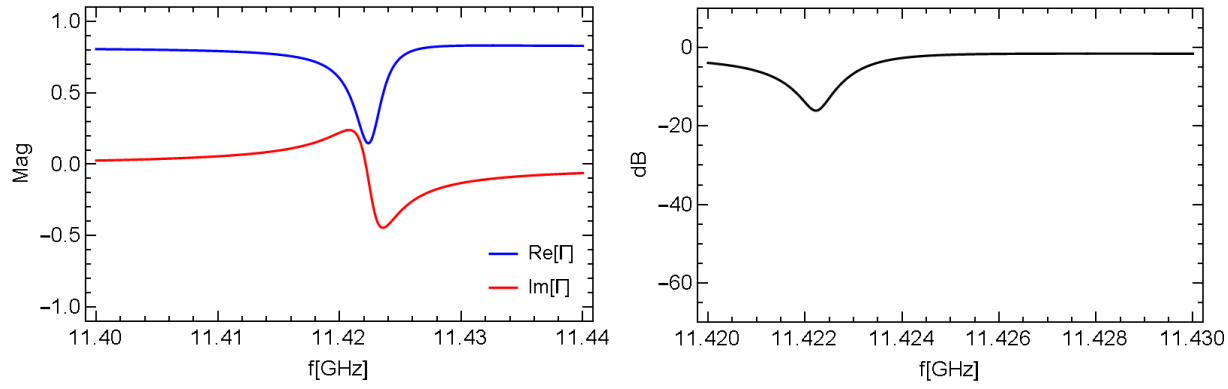

(a) (b)

Figure C.6: Reflection coefficient for a resonant cavity with $Q_0 = 10,000$, $\beta = 1$, and $f_0 = 11.424$ GHz and a lossy waveguide with $\alpha_{\rm cx} = 0.01$, $\gamma_l = 0.031/GHz$, and $D_0 = 0.251/GHz$.(a) real and imaginary parts, and (b) dB.

the resonant cavity I simplify the resulting reflection coefficent by gathering variables:

$$\Gamma(f) = e^{i\theta}\frac{\left[e^{-(\alpha_{\rm cx}+i\gamma_l(f-f_0))}(D_0+\frac{2i}{f})(i\delta+(\frac{1}{Q_0}-\frac{1}{Q_E}))-D_0(i\delta+(\frac{1}{Q_E}+\frac{1}{Q_0}))\right]}{\left[e^{(\alpha_{\rm cx}+i\gamma_l(f-f_0))}(D_0-\frac{2i}{f})(i\delta+(\frac{1}{Q_0}+\frac{1}{Q_E}))-D_0(i\delta-(\frac{1}{Q_E}-\frac{1}{Q_0}))\right]} \tag{C.18}$$

Figure C.6 shows an example of this model. The attenuation, dispersion, and capacitance are exaggerated. The capacitance, will shift the value of the frequency resonance.

C.4 Time-Varying Fields

One method for calculating the time-dependent reflection or fields inside a resonant cavity, or a rf system with an arbitrary impedance, is to use a Fourier transform method. The method is as follows:

- Take the Fourier Transform of the input voltage
- Multiply with the impedance of the rf system
- Take the Inverse Fourier Transform of the result

The result will be the reflected signal from the rf system. If I instead multiply by equation C.8, instead of the impedance, the result will be the field inside the resonant

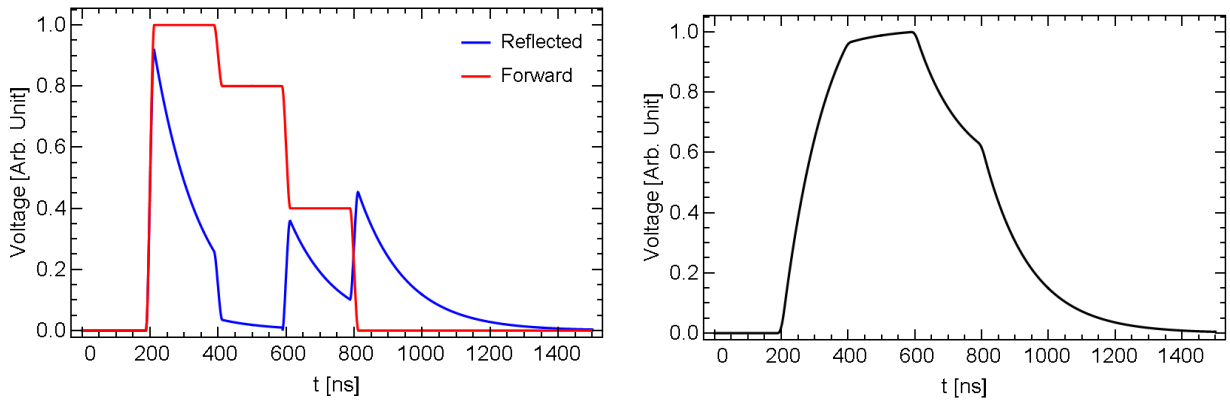

(a) (b)

Figure C.7: (a) The forward voltage signal and the calculated reflected voltage signal, and (b) the voltage inside the cavity. Cavity is $Q_0 = 10,000$, $\beta = 1$, and $f_0 = 11.424$ GHz

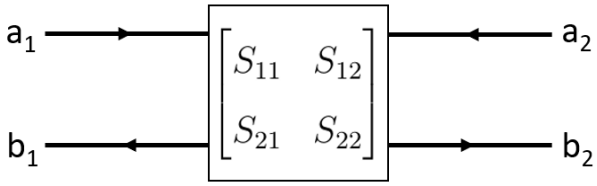

Figure C.8: An arbitrary two-port equivalent circuit with S-matrix.

cavity. An example of the reflected signal and voltage inside the cavity from an arbitrary input voltage is shown in Figure C.7.

C.5 Full RF System Model

To model the full rf system, I will use a different framework than ABCD matrices. Instead I will use scattering matrices for the individual components of the high power rf circuit. For this formalism I consider a two-port element again, and define a forward and backward wave at each port, as depicted in Figure C.8. Then the S-matrix is defined as:

$$\begin{bmatrix} b_1 \\ b_2 \end{bmatrix} = \begin{bmatrix} S_{11} & S_{12} \\ S_{21} & S_{22} \end{bmatrix} \begin{bmatrix} a_1 \\ a_2 \end{bmatrix} \tag{C.19}$$

S-matrices generalize to larger n×n dimensions for n ports.

A method for creating a S-matrix from multiple rf components is as follows and is taken from [184]. For a diagram of the circuit used for high power experiments, see Figure 3.11.

The method to create an overall scattering matrix is to start by creating a block diagonal matrix, A_S, from the S-matrices for each rf component. Along the diagonal, after the S-matrices of the rf components, add a zero for each external port of the system. In this model I will include: the klystron as a 1-port element, a rectangular waveguide (2-ports), circular waveguide (2-ports), 3dB hybrid (4 ports), directional coupler (4-ports), a second rectangular waveguide section (2-ports), and the resonant cavity (1-port). The system has four external ports, two on the 3dB hybrid, and two on the directional coupler. Then in total, the block diagonal matrix is 20×20 matrix.

the second step is to create a symmetric matrix, B_{conn} that encodes the connections of the system. Number each individual port of all the components sequentially from 1-16 for this system, and then for any two ports m and n that are connected place a 1 at position (m, n) and (n, m) in this connection matrix. Do the same thing for where the external ports are connected, that will be numbered 17-20. The external ports are connected to ports 7, 8, 11, and 12. The resulting matrix should be non-singular with Det(B_{conn})=1.

Next, define

$$W = B_{\text{conn}} - A_S, \tag{C.20}$$

and define a n-dimension vector $\vec{X}$ that defines the input to the system. For example, for the case where power is inputted to the system from the klystron into the first waveguide section at port 2,

$$\vec{X} = \begin{bmatrix} 0 \\ 1 \\ 0 \\ \vdots \end{bmatrix} \tag{C.21}$$

To find the resulting output vector, $\vec{F}$, for the entire system:

$$B_{\text{conn}} \cdot \vec{Y} = \vec{F}, \tag{C.22}$$

where $\vec{Y}$ is the solution to $W \cdot \vec{Y} = \vec{X}$.

With this framework I can solve the behavior of the system. I will now discuss the models used for each component.

The klystron is modeled with $S_{11} = -0.69$ [185]. I used the following to model both types of waveguide, circular and rectangular:

$$\begin{aligned} S_{12} = S_{21} &= \frac{1}{\sinh\left((\alpha_W + i\beta_W(f, f_c))L_W\right) + \cosh\left((\alpha_W + i\beta_W(f, f_c))L_W\right)} \\ S_{11} = S_{22} &= 0 \\ \beta_W(f, f_c) &= \frac{2\pi f}{c}\sqrt{1 - \left(\frac{f_c}{f}\right)^2}. \end{aligned} \tag{C.23}$$

The attenuation is small enough to ignore for the circular waveguide, and $\alpha = 0.12 dB/m$ for the rectangular waveguide. The length of the circular waveguide was fitted to be 16.847. The first rectangular waveguide near the klystron was 9.3m long, and the second was 0.1 m. The rectangular waveguides add more dispersion to the system than the circular waveguide.

The 3dB hybrid was modeled as a splitter that sent -3.5 dB to each arm and the external ports were assumed to be connected to loads with no reflection. The directional coupler was measured with the VNA, and the sampling arms had about -45.5 dB output. The input loss was -0.28 dB and the directivity was 25 dB. The VNA measurements were also used for the resonant cavity.

The results are discussed in 3.3.4.

Bibliography

[1] D Brandt, H Burkhardt, M Lamont, S Myers, and J Wenninger, "Accelerator physics at LEP", Reports on Progress in Physics **63**, 939 (2000).

[2] K. L. F. Bane et al., "Measurements and modeling of coherent synchrotron radiation and its impact on the linac coherent light source electron beam", Phys. Rev. ST Accel. Beams **12**, 030704 (2009).

[3] G Ising, "Prinzip einer Methode zur Herstellung von Kanalstrahlen hoher Voltzahl", Ark. Mat. Astron. Fys. **18**, 1 (1924).

[4] R. Widerøe, "Über ein neues prinzip zur herstellung hoher spannungen", Archiv für Elektrotechnik **21**, 387 (1928).

[5] SgBeer, CC BY-SA 3.0, https://commons.wikimedia.org/w/index.php?curid=9371904.

[6] D. H. Sloan and E. O. Lawrence, "The production of heavy high speed ions without the use of high voltages", Phys. Rev. **38**, 2021 (1931).

[7] T. Wangler, *Rf linear accelerators* (Wiley, 1998).

[8] L. W. Alvarez, "The production of heavy high speed ions without the use of high voltages", Phys. Rev. **70**, 799 (1946).

[9] L. W. Alvarez et al., "Berkeley proton linear accelerator", Review of Scientific Instruments **26**, 111 (1955).

[10] E. L. Ginzton, W. W. Hansen, and W. R. Kennedy, "A linear electron accelerator", Review of Scientific Instruments **19**, 89 (1948).

[11] M. Chodorow, E. L. Ginzton, W. W. Hansen, R. L. Kyhl, R. B. Neal, and W. K. H. Panofsky, "Stanford high-energy linear electron accelerator (Mark III)", Review of Scientific Instruments **26**, 134 (1955).

[12] R. B. Neal (ed.), D. W. Dupen, H. A. Hogg, and G. A. Loew, *The stanford two mile accelerator*, SLAC-REPRINT-1968-001 (W.A. Benjamin, Inc., New York, 1968), p. 1169.

[13] J. G. Navarro, "Breakdown studies for high gradient RF warm technology in: CLIC and hadrontherapy linacs", PhD thesis (Universitat de Valencia, 2016).

[14] S. Carnot, *Reflections on the motive power of fire* (Bachelier, Paris, France, 1824).

[15] R. Radebaugh, "Commissioning results of the LCLS injector", in Proc. of Institute of Refrigeration, Vol. 96 (2000).

[16] N. Valles and M. Liepe, "The superheating field of niobium: theory and experiment", in Proc. of SRF11, Chicago (2011).

[17] V. Shemelin, "Optimal choice of cell geometry for a multicell superconducting cavity", Phys. Rev. ST Accel. Beams **12**, 114701 (2009).

[18] D. B. Liarte, S. Posen, M. K. Transtrum, G. Catelani, M. Liepe, and J. P. Sethna, "Theoretical estimates of maximum fields in superconducting resonant radio frequency cavities: stability theory, disorder, and laminates", Superconductor Science and Technology **30**, 033002 (2017).

[19] X. Xu, "A review and prospects for nb3sn superconductor development", Superconductor Science and Technology **30**, 093001 (2017).

[20] M. Aicheler et al., *A multi-TeV linear collider based on CLIC technology: CLIC conceptual design report*, tech. rep. (CERN, 2012).

[21] M. Ferrario et al., "New design study and related experimental program for the LCLS RF photoinjector", in Particle accelerator. Proceedings, 7th European Conference, EPAC 2000, Vienna, Austria, June 26-30, 2000. Vol. 1-3 (2000), pp. 1642–1644.

[22] A. Sørensen, *Liouville's theorem and emittance*, tech. rep. (CERN, 1989).

[23] D. T. Palmer, "The Next Generation Photoinjector", PhD thesis (STANFORD UNIVERSITY, 1998).

[24] A. Cahill et al., "Rf design for the TOPGUN photogun: a cryogenic normal conducting copper electron gun", Nucl. Instr. and Meth. A **865**, Physics and Applications of High Brightness Beams 2016, 105 (2017).

[25] E. Pirez, D. Alesini, J. Maxson, and P. Musumeci, "New 1.4 Cell RF Photoinjector Design for High Brightness Beam Generation", in Proc. of north american particle accelerator conference (NAPAC'16), Chicago, IL, USA, October 9-14, 2016, 3 (2017), pp. 1083–1086.

[26] M. Cornacchia and P. Emma, "Transverse to longitudinal emittance exchange", Phys. Rev. ST Accel. Beams **5**, 084001 (2002).

[27] A. Valloni et al., "An asymmetric emittance electron source for the GALAXIE dielectric-laser accelerator injector", AIP Conference Proceedings **1507**, 762 (2012).

[28] J. B. Rosenzweig et al., "The GALAXIE all-optical fel project", AIP Conference Proceedings **1507**, 493 (2012).

[29] A. D. Cahill et al., "TOPGUN: an ultra-high gradient cryogenic rf photoinjector", American Workshop on Linear Colliders, 2017.

[30] B. Carlsten, "New photoelectric injector design for the Los Alamos National Laboratory XUV FEL accelerator", Nucl. Instr. and Meth. A **285**, 313 (1989).

[31] T. Rao and D. H. Dowell, "An Engineering Guide To Photoinjectors", (2014).

[32] L. Serafini and J. B. Rosenzweig, "Envelope analysis of intense relativistic quasilaminar beams in rf photoinjectors:ma theory of emittance compensation", Phys. Rev. E **55**, 7565 (1997).

[33] M. Ferrario, J. E. Clendenin, D. T. Palmer, J. B. Rosenzweig, and L. Serafini, "Homdyn Study for the Lcls RF Photo-Injector", in The physics of high brightness beams, edited by J. Rosenzweig and L. Serafini (2000), pp. 534–563.

[34] M. Ferrario et al., "Direct measurement of the double emittance minimum in the beam dynamics of the sparc high-brightness photoinjector", Phys. Rev. Lett. **99**, 234801 (2007).

[35] J. B. Rosenzweig et al., "Next generation high brightness electron beams from ultra-high field cryogenic radiofrequency photocathode sources", Arxiv:1603.01657, "In Submission", 2016.

[36] O. J. Luiten, S. B. van der Geer, M. J. de Loos, F. B. Kiewiet, and M. J. van der Wiel, "How to Realize Uniform Three-Dimensional Ellipsoidal Electron Bunches", Phys. Rev. Lett. **93**, 094802, 094802 (2004).

[37] D. Filippetto, P. Musumeci, M. Zolotorev, and G. Stupakov, "Maximum current density and beam brightness achievable by laser-driven electron sources", Phys. Rev. ST Accel. Beams **17**, 024201 (2014).

[38] K. Batchelor, J. Sheehan, and M. Woodle, *Design and modelling of a 5 mev radio frequency electron gun*, tech. rep. (BNL, 1988).

[39] J. S. Fraser, R. L. Sheffield, E. R. Gray, and G. W. Rodenz, "High-brightness photoemitter injector for electron accelerators", IEEE Tr. Nucl. Sci. **32**, 1791 (1985).

[40] B. E. Carlsten, "Space charge induced emittance compensation in high brightness photoinjectors", Part. Accel. **49**, 27 (1995).

[41] A. Fukusawa, H. Badakov, B. O'Shea, E. Hemsing, and J. B. Rosenzweig, "The finder photoinjector", in 22nd Particle Accelerator Conference (PAC 07) (2007), pp. 1260–1262.

[42] C. Pellegrini et al., "Initial operation and beam characteristics of the UCLA S-band rf photo-injector", in Proceedings of international conference on particle accelerators, Vol. 4 (1993), pp. 3216–3218.

[43] E. Colby et al., "Experimental Testing of the TTF RF Photoinjector", in Proc. of particle accelerator conference (pac'97), vancouver, canada, 12–16 may, 1997, 8 (1997), pp. 2873–2875.

[44] G. D'Auria et al., "The new photoinjector for the Fermi project", in 22nd Particle Accelerator Conference (PAC 07) (2007), p. 974.

[45] D. Alesini et al., "New technology based on clamping for high gradient radio frequency photogun", Phys. Rev. ST Accel. Beams **18**, 092001 (2015).

[46] R. Akre et al., "Commissioning the linac coherent light source injector", Phys. Rev. ST Accel. Beams **11**, 030703 (2008).

[47] F. Stephan et al., "Detailed characterization of electron sources yielding first demonstration of European X-ray free-electron laser beam quality", Phys. Rev. ST Accel. Beams **13**, 020704 (2010).

[48] J. G. Marmouget, A Binet, P Guimbal, and J. L. Coacolo, "Present Performance of the Low-emittance, High-bunch Charge ELSA Photo-injected Linac", in Proc. of EPAC 2002 (2002), pp. 1795–1797.

[49] W. Cornelius, S. Bender, K. Meier, L. Thode, and J. Watson, "The Los Alamos High-Brightness Accelerator FEL (HIBAF) facility", Nucl. Instr. and Meth. A **296**, 251 (1990).

[50] R. A. Marsh et al., "Modeling and design of an x-band rf photoinjector", Phys. Rev. ST Accel. Beams **15**, 102001 (2012).

[51] D. H. Dowell et al., "First operation of a photocathode radio frequency gun injector at high duty factor", Applied Physics Letters **63**, 2035 (1993).

[52] H. L. Andrews et al., "First Operation of the LANL/AES Normal Conducting Radio Frequency Photoinjector", Conf. Proc. **C110328**, 2498 (2011).

[53] F. Sannibale et al., "Advanced photoinjector experiment photogun commissioning results", Phys. Rev. ST Accel. Beams **15**, 103501 (2012).

[54] SLAC, *Zeroth-order design report for the next linear collider*, tech. rep. (SLAC, 1996).

[55] R. Ruber, V. Ziemann, T. Ekelöf, A. Palaia, W. Farabolini, and R. Corsini, "The CTF3 two-beam test stand", Nucl. Instr. and Meth. A **729**, 546 (2013).

[56] F. V. Hartemann and F. Albert, *Design of a 2 MeV Compton scattering gamma-ray source for DNDO missions*, tech. rep. (Lawrence Livermore National Lab, 2009).

[57] I. Gadjev et al., "An inverse free electron laser acceleration-driven compton scattering x-ray source", In Preparation, 2017.

[58] O. Adriani et al., *Technical Design Report EuroGammaS proposal for the ELI-NP Gamma beam System*, tech. rep. (Extreme Light Infrastructure, 2014).

[59] G. D'Auria, "X-band technology applications at FERMI@Elettra FEL project", Nucl. Instr. and Meth. A **657**, X-Band Structures, Beam Dynamics and Sources Workshop (XB-10), 150 (2011).

[60] J. Beijers et al., "Zfel: a compact, soft x-ray fel in the netherlands", in Proc. of FEL2010, Malmo, Sweden (2010), pp. 163–164.

[61] U. Amaldi et al., "Cyclinacs: Fast-Cycling Accelerators for Hadrontherapy", arXiv:0902.3533, 2009.

[62] P. Maxim, B. Loo, and S. Tantawi, *Pluridirectional high-energy agile scanning electron radiotherapy (PHASER): extremely rapid treatment for early lung cancer*, tech. rep. (Stanford University, 2014).

[63] P. McIntosh et al., "Realization of an X-Band RF System for LCLS", in In Proc. of PAC05, Knoxville, Tennesee, USA (2005).

[64] G. Roberts, "Slac physicists help design, build cargo x-ray scanners [press release]", 2013.

[65] V.A. Dolgashev, "X-Band Deflectors", Presented at ICFA Beam Dynamics Mini-Workshop on Deflecting/Crabbing Cavity Applications in Accelerators Cockcroft Institute, 1-3 September 2010, 2010.

[66] V. A. Dolgashev et al., "Design and application of multimegawatt x-band deflectors for femtosecond electron beam diagnostics", Phys. Rev. ST Accel. Beams **17**, 102801 (2014).

[67] P. Craievich et al., "Implementation of radio-frequency deflecting devices for comprehensive high-energy electron beam diagnosis", IEEE Tr. Nucl. Sci. **62**, 210 (2015).

[68] S.G. Tantawi and others, "Application of the Balanced Hybrid Mode in Overmoded Corrugated Waveguides to Short Wavelength Dynamic Undulators", in Proceedings of IPAC2011, San Sebastian, Spain (2011), pp. 3328–3330.

[69] S. Tantawi et al., "Experimental demonstration of a tunable microwave undulator", Phys. Rev. Lett. **112**, 164802 (2014).

[70] C. Bostedt et al., "Linac coherent light source: the first five years", Rev. Mod. Phys. **88**, 015007 (2016).

[71] J. Stohr et al., *Linac Coherent Light Source II*, tech. rep. (SLAC, 2011).

[72] M. Altarelli et al., *European x-ray free electron laser*, tech. rep. (DESY, 2006).

[73] M. Xie, "Design optimization for an X-ray free electron laser driven by SLAC LINAC", Conf. Proc. **C950501**, 183 (1996).

[74] P. Schmüser, M. Dohlus, J. Rossbach, and C. Behrens, *Free-electron lasers in the ultraviolet and x-ray regime* (Springer International Publishing, Switzerland, 2014).

[75] R. Alley et al., "The design for the LCLS RF photoinjector", NIMA **429** (1999).

[76] S. Chen et al., *SXFEL design report*, tech. rep. (Shanghai Institute of Applied Physics, 2007).

[77] R. Ganter et al., *SwissFEL conceptual design report*, tech. rep. (Paul Scherrer Institut, 2012).

[78] M. Yabashi et al., *XFEL/SPring-8 beamline technical design report*, tech. rep. (SACLA, 2008).

[79] J. Han, "Beam Commissioning of PAL-XFEL", in Proc. of International Particle Accelerator Conference (IPAC'16), Busan, Korea, May 8-13, 2016, 7 (2016), pp. 6–10.

[80] B D. O'Shea et al., "Observation of acceleration and deceleration in gigaelectron-volt-per-metre gradient dielectric wakefield accelerators", Nature Communications **7**, 12763 (2016).

[81] W. Gai et al., "Experimental demonstration of wake-field effects in dielectric structures", Phys. Rev. Lett. **61**, 2756 (1988).

[82] S. Antipov et al., "Experimental demonstration of wakefield effects in a THz planar diamond accelerating structure", Appl. Phys. Lett. **100**, 132910 (2012).

[83] S. P. Weathersby et al., "Mega-electron-volt ultrafast electron diffraction at SLAC National Accelerator Laboratory", Review of Scientific Instruments **86**, 073702 (2015).

[84] P. Musumeci, J. Moody, and C. Scoby, "Relativistic electron diffraction at the ucla pegasus photoinjector laboratory", Ultramicroscopy **108**, 1450 (2008).

[85] J. W. Wang, "Rf properties of periodic accelerating structures for linear colliders", SLAC-REPORT-339, PhD thesis (Stanford University, 1989).

[86] W. Wuensch, *Advances in the Understanding of the Physical Processes of Vacuum Breakdown*, tech. rep. (CERN, Geneva, 2013).

[87] V. A. Dolgashev and S. G. Tantawi, "Rf breakdown in x-band waveguides", in Proc. of EPAC 2002, Paris, France (2002), pp. 2139–2141.

[88] G. A. Loew and J. W. Wang, "RF Breakdown Studies in Room Temperature Electron LINAC Structures", in 13th International Symposium on Discharges and Electrical Insulation in Vacuum Paris, France, June 27-30, 1988 (1988).

[89] J. Wang, S. Tantawi, V. Dolgashev, and J. Neilson, "Rf breakdown and it's limitation", Muon Collider 2011, 2011.

[90] V. A. Dolgashev, S. G. Tantawi, C. D. Nantista, Y. Higashi, and T. Higo, "Rf breakdown in normal conducting single-cell structures", in Proc. of IEEE PAC 2005, Knoxville, Tennessee (2005), pp. 595–599.

[91] V. Dolgashev et al., "High gradient, x-band and above, metallic rf structures", 2nd European Advanced Accelerator Concepts Workshop (EAAC 2015), 2015.

[92] S. Parviainen, F. Djurabekova, H. Timko, and K. Nordlund, "Electronic processes in molecular dynamics simulations of nanoscale metal tips under electric fields", Computational Materials Science **50**, 2075 (2011).

[93] J. W. Kovermann, "Comparative Studies of High-Gradient RF and DC Breakdowns", PhD thesis (RWTH Aachen University, 2010).

[94] F. Djurabekova et al., "Crater formation by single ions, cluster ions and ion "showers"", Nucl. Instr. and Meth. B **272**, Proceedings of the 17th Internation Conference on Ion Beam Modifications of Materials (IBMM 2010), 374 (2012).

[95] V. A. Dolgashev, S. G. Tantawi, C. D. Nantista, Y. Higashi, and T. Higo, "High power tests of normal conducting single cell structures", in Proc. of IEEE PAC 2007, Albuquerque, New Mexico (2007), pp. 2430–2432.

[96] V. E. Balakin, O. N. Brezhnev, A. V. Novokhatsky, and Yu. I. Semenov, *Accelerating structure of a colliding linear electron-positron beam (VLEPP). investigation of the maximum attainable acceleration rate*, tech. rep. (Institute of Nuclear Physics, Novosibirsk, USSR, 1978).

[97] J. Wang, "Research of rf high gradient physics and its application in accelerator structure development", in *High gradient accelerating structure*, edited by W. Gai (World Scientific Publishing Co. Pte. Ltd., Oxford, 2015), pp. 17–30.

[98] C. Adolphsen et al., "Processing studies of x-band accelerator structures at the nlcta", in Proceedings of the 2001 Particle Accelerator Conference, Vol. 1 (2001), pp. 478–480.

[99] L. L. Laurent, "High Gradient RF Breakdown Studies", PhD thesis (University of California, Davis, 2002).

[100] C. Adolphsen et al., "RF processing of X band accelerator structures at the NLCTA", in Proc. of the 20th International Linac Conference, Monterey, USA, August 21-25 (2000).

[101] V. Dolgashev and S. Tantawi, "Effect of rf parameters on breakdown limits in high-vacuum x-band structures", in Aip conf. proc. 691, 151 (2003), pp. 151–165.

[102] S. Dobert et al., "High gradient performance of NLC/GLC x-band accelerating structures", in Proceedings of the 2005 particle accelerator conference (2005), pp. 372–374.

[103] C. Adolphsen, "Normal-conducting rf structure test facilities and results", in Proceedings of the 2003 particle accelerator conference, Vol. 1 (2003), 668–672 Vol.1.

[104] W. Wuensch, "Observations about rf breakdown from the clic high-gradient testing program", AIP Conference Proceedings **877**, 15 (2006).

[105] C. Nantista, S. Tantawi, and V. A. Dolgashev, "Low-field accelerator structure couplers and design techniques", PRST-AB **7** (2004).

[106] S. Döbert, *Gradient Limitations for High-Frequency Accelerators*, tech. rep. (SLAC, Menlo Park, CA USA).

[107] V. A. Dolgashev, "Progress on high-gradient structures", AIP Conference Proceedings **1507**, 76 (2012).

[108] A. Grudiev, S. Calatroni, and W. Wuensch, "New local field quantity describing the high gradient limit of accelerating structures", Phys. Rev. ST Accel. Beams **12**, 102001 (2009).

[109] J. Wang et al., "Fabrication Technologies of the High Gradient Accelerator Structures at 100MV/m Range", in Proc. of the 1st International Particle Accelerator Conference (IPAC'10): Kyoto, Japan, May 23-28 (2010).

[110] T. Higo et al., "Advances in X-band TW Accelerator Structures Operating in the 100 MV/m Regime", in Proceedings, 1st International Particle Accelerator Conference (IPAC'10): Kyoto, Japan, May 23-28, 2010 (2010).

[111] W. Wuensch, "Ultimate Field Gradient in Metallic Structures", in Proc. of International Particle Accelerator Conference (IPAC17), Copenhagen, Denmark, 14-19 May, 8 (2017), pp. 24–29.

[112] E. Senes et al., "Results of the Beam-Loading Breakdown Rate Experiment at the CLIC Test Facility CTF3", in Proc. of International Particle Accelerator Conference (IPAC'17), Copenhagen, Denmark, 14-19 May, 2017, 8 (2017), pp. 1348–1351.

[113] A. Degiovanni, W. Wuensch, and J. Giner Navarro, "Comparison of the conditioning of high gradient accelerating structures", Phys. Rev. Accel. Beams **19**, 032001 (2016).

[114] W. Wuensch et al., "Statistics of vacuum breakdown in the high-gradient and low-rate regime", Phys. Rev. Accel. Beams **20**, 011007 (2017).

[115] V. A. Dolgashev et al., "Study of Basic Breakdown Phenomena in High Gradient Vacuum Structures", in Proc. of LINAC 2010, Tsukuba, Japan (2010), pp. 1043–1047.

[116] D. Pritzkau, "RF pulsed heating", PhD thesis (STANFORD UNIVERSITY, 2001).

[117] D. P. Pritzkau and R. H. Siemann, "Experimental study of rf pulsed heating on oxygen free electronic copper", Phys. Rev. ST Accel. Beams **5**, 112002 (2002).

[118] L. Laurent et al., "Experimental study of rf pulsed heating", Phys. Rev. ST Accel. Beams **14** (2011) 10.1103/PhysRevSTAB.14.041001.

[119] S. Heikkinen, "Study of high power rf induced thermal fatigue in the high gradient accelerating structures", PhD thesis (Helsinki University of Technology, Finland, 2008).

[120] *US High Gradient Research Collaboration Workshop 2011*, 2011.

[121] *Solid edge*, Siemens.

[122] V. Dolgashev, "Progress on high gradient structures", 15th Advanced Accelerator Concepts Workshop (AAC 2012), 2012.

[123] V. Dolgashev, S. Tantawi, Y. Higashi, and B. Spataro, "Geometric dependence of radio-frequency breakdown in normal conducting accelerating structures", APPL PHYS LETT **97**, 171501 (2010).

[124] J. Shi et al., "New Quantity Describing the Pulse Shape Dependence of the High Gradient Limit in Single Cell Standing-Wave Accelerating Structures", in Proc. of International Particle Accelerator Conference (IPAC'16), Busan, Korea, May 8-13, 2016, 7 (2016), pp. 3878–3880.

[125] V. Dolgashev et al., "Status of high power tests of normal conducting short sw structures", in Mopc071, proceedings of ipac2011, san sebastian, spain (2011).

[126] V. Dolgashev et al., "Status of High Power Tests of Normal Conducting Single-Cell Standing Wave Structures ", in Proc. of ipac 2010, kyoto, japan (2010), pp. 3810–3812.

[127] Y. Saito, "Breakdown phenomena in vacuum", in Proc. of 1992 linear accelerator conference, International Particle Accelerator Conference (1992), p. 575.

[128] V. Dolgashev, S. Tantawi, Y. Higashi, and T. Higo, "Status of high power tests of normal conducting single-cell structures", in Proc. of EPAC 2008, Genoa, Italy (2008), pp. 742–744.

[129] M. Haouaoui, I. Karaman, K. T. Harwig, and H. J. Maier, "Microstructure evolution and mechanical behavior of bulk copper obtained by consolidation of micro- and nanopowders using equal-channel angular extrusion", Metallurgical and Materials Transactions A **35**, 2935 (2004).

[130] V. Dolgashev et al., "Recent high gradient tests at slac", CLIC 2016 Workshop, 2016.

[131] J. Haimson and B. Mecklenburg, "Design features and initial rf performance of a gradient hardened 17 ghz tw linac structure", AIP Conference Proceedings **1086**, 464 (2009).

[132] V. Dolgashev et al., "Recent high gradient tests at slac", 3rd International Workshop on Breakdown Science and High Gradient Technology (HG13), 2013.

[133] V. Dolgashev et al., "High power tests of an electroforming cavity operating at 11.424 ghz", Jour. of Inst. **11** (2016).

[134] B. Spataro et al., "High-power comparison among brazed, clamped and electroformed X-band cavities", Nucl. Instr. and Meth. A **A657**, 88 (2011).

[135] W. Wuensch et al., "Fabrication and High-Gradient Testing of an Accelerating Structure Made From Milled Halves", in Proc. of Linear Accelerator Conference (LINAC'16), East Lansing, MI, USA, 25-30 September 2016, 28 (2017), pp. 845–848.

[136] T. Higo and T. Abe, "High gradient result update from Nextef", Tenth International Workshop on High-Gradient Acceleration (HG2017), 2017.

[137] A. D. Yeremian et al., "Dual mode acclerating cavity to test rf breakdows dependance on rf magnetic fields", in Proceedings of IPAC2011, San Sebastian, Spain (2011), pp. 247–249.

[138] K. Nordlund and F. Djurabekova, "Defect model for the dependence of breakdown rate on external electric fields", Phys. Rev. ST Accel. Beams **15** (2012) 10.1103/PhysRevSTAB.15.071002.

[139] A. Descoeudres, F. Djurabekova, and K. Nordlund, *DC breakdown experiments with cobalt electrodes*, tech. rep. CERN-OPEN-2011-029. CLIC-Note-875 (CERN, Geneva, 2009).

[140] E. Engelberg and Y. Ashkenazy, "Stochastic model of breakdown nucleation under intense electric fields", 6th International Workshop on Mechanisms of Vacuum Arcs, 2017.

[141] Y. Ashkenazy, E. Engelberg, I. Popov, I. Nachshon, and A. Yashar, "Bd nucleation as a critical transition in dislocation population", 6th International Workshop on Mechanisms of Vacuum Arcs, 2017.

[142] R. A. Matula, "Electrical resistivity of copper, gold, palladium, and silver", Journal of Physical and Chemical Reference Data **8**, 1147 (1979).

[143] N. J. Simon, E. S. Drexler, and R. P. Reed, *Properties of copper and copper alloys at cryogenic temperatures*, tech. rep. (Boulder, CO, 1992).

[144] G. Reuter and E. Sondheimer, "The theory of the anomalous skin effect in metals", P ROY SOC A-MATH PHY **195**, 336 (1948).

[145] B. Pippard, "The surface impedance of superconductors and normal metals at high frequencies ii. the anomalous skin effect in normal metals", P Roy. Soc. A-Math Phy. **191**, 385 (1947).

[146] T. Tanaka et al., "Characterization of Cold Model Cavity for Cryocooled C-Band 2.6-Cell Photocathode RF Gun at 20 K", in Proc. of International Particle Accelerator Conference (IPAC'17), Copenhagen, Denmark, 14–19 May, 2017, 8 (2017), pp. 518–521.

[147] A. Iino et al., "High-power test of c-band accelerating structure at 20 k", in Proc. of 13th annual meeting of part. accel. soc. of japan (2016), pp. 863–866.

[148] F. Biquard and A. Septier, "Amelioration de la conductivite superficielle du cuivre et de l'aluminium en hyperfrequences, par abaissement de temperature", Nuclear Instruments and Methods **44**, 18 (1966).

[149] J. Benard, N. H. E. Minyawi, and N. T. Viet, "Reduction of RF losses at 35 GHz in high purity copper resonant cavities by cooling to cryogenic temperature", Revue de Physique Appliquee **13**, 483 (1978).

[150] J. Guo, S. Tantawi, D. Martin, and C. Yoneda, "Cryogenic rf material testing with a high-q copper cavity", AIP Conference Proceedings **1299**, 330 (2010).

[151] A. J. Saversky and I. S. Shchedrin, "Measurement of Microwave Properties of X-Band Accelerating Structure Under Pulsed High-Power Operation at Liquid Nitrogen Temperature", in 1993 15th ieee particle accelerator conference (1994), p. 1030.

[152] A. Cahill et al., "Measurements of Copper RF Surface Resistance at Cryogenic Temperatures for Applications to X-Band and S-Band Accelerators", in Proc. of International Particle Accelerator Conference (IPAC'16), Busan, Korea, May 8-13, 2016, 7 (2016), pp. 487–490.

[153] A. H. McEuen, P. Lui, E. Tanabe, and V. Vaguine, "High-power operation of accelerator structures at liquid nitrogen temperature", IEEE Tr. Nucl. Sci. **32**, 2972 (1985).

[154] R. A. Kishek, Y. Y. Lau, L. K. Ang, A. Valfells, and R. M. Gilgenbach, "Multipactor discharge on metals and dielectrics: historical review and recent theories", Physics of Plasmas **5**, 2120 (1998).

[155] H. H. Braun, S. Döbert, I. Wilson, and W. Wuensch, "Frequency and temperature dependence of electrical breakdown at 21, 30, and 39 ghz", Phys. Rev. Lett. **90**, 224801 (2003).

[156] *High frequency structural simulator*, HFSS.

[157] C. W. Steele, "A nonresonant perturbation theory", IEEE Transactions on Microwave Theory and Techniques **14**, 70 (1966).

[158] D. Yeremian, *Choke flange for high power rf components excited by TE01 mode*, tech. rep. (SLAC, 2009).

[159] V. A. Dolgashev et al., "Prelimiary results of high power tests of normal conducting cryo cavity", Presented at HG2015 (2015).

[160] D. Pozar, *Microwave engineering* (Wiley, 2004).

[161] K. Halbach and R. Holsinger, "SUPERFISH-a computer program for evaluation and design techniques", in (1976).

[162] A. Cahill, M. D. Forno, and V. Dolgashev, "Automated Design for Standing Wave Electron Photoguns: TOPGUN RF Design", in Proc. of International Particle Accelerator Conference (IPAC'16), Busan, Korea, May 8-13, 2016, 7 (2016), pp. 3999–4001.

[163] A. Jensen et al., "25 year performance review of the SLAC 5045 S-Band Klystron", in Proceedings, 2nd International Particle Accelerator Conference (IPAC 2011): San Sebastian, Spain, September 4-9, 2011 (2011), pp. 409–411.

[164] J. Jackson, *Classical electrodynamics* (Wiley, 1975).

[165] G. Bowden, *Rf guide cryogenic heat loads*, tech. rep. (SLAC, 2016).

[166] P. Wilson, *High energy electron linacs: applications to storage ring RF systems and linear colliders*, tech. rep. (SLAC, 1991).

[167] K. Ko et al., "Advances in Parallel Electromagnetic Codes for Accelerator Science and Development", in Proceedings, 25th International Linear Accelerator Conference, LINAC2010: Tsukuba, Japan, September 12-17, 2010 (2011), pp. 1028–1032.

[168] R. Bossart, J. Godot, H. Kugler, J. Madsen, A. Riche, and J. Strode, "Rf-gun construction, tuning and high power tests", in Proceedings, 3rd european particle accelerator conference, epac92: berlin germany (1992), pp. 1026–1028.

[169] R. Alley et al., "The design for the lcls rf photoinjector", NUCL INSTRUM METH A **429**, 324 (1999).

[170] S. G. Anderson et al., "Commissioning of a high-brightness photoinjector for compton scattering x-ray sources", in 2007 IEEE Particle Accelerator Conference (PAC) (2007), pp. 1242–1244.

[171] L. Faillace, R. Agustsson, P. Frigola, and A. Verma, "Status of the FERMI II RF Gun at Sincrotrone Trieste", in Proceedings, 27th Linear Accelerator Conference, LINAC2014: Geneva, Switzerland, August 31-September 5, 2014 (2014), pp. 692–694.

[172] A. Cahill, M. D. Forno, and V. Dolgashev, "TM01 Mode Launcher for Use in High Brightness Photoguns", in Proc. of International Particle Accelerator Conference (IPAC'16), Busan, Korea, May 8-13, 2016, 7 (2016), pp. 491–493.

[173] C. Papadopoulos et al., "Rf injector beam dynamic optimization for lcls-ii", in Proc. of International Particle Accelerator Conference (IPAC'14), Dresden, Germany, May 8-13, 2014 (2014), pp. 1974–1976.

[174] J. Qiang, C. Mitchell, and A. Qiang, "Tuning of an adaptive unified differential evolution algorithm for global optimization", in 2016 IEEE Congress on Evolutionary Computation (CEC) (2016), pp. 4061–4068.

[175] K. Deb, A. Pratap, S. Agarwal, and T. Meyarivan, "A fast and elitist multiobjective genetic algorithm: nsga-ii", IEEE Transactions on Evolutionary Computation **6**, 182 (2002).

[176] A. Hofler et al., "Innovative applications of genetic algorithms to problems in accelerator physics", Phys. Rev. ST Accel. Beams **16**, 010101 (2013).

[177] K. Floettmann, "Astra: a space charge tracking algorithm", in ().

[178] H. Qian, D. Filippetto, and F. Sannibale, "S-Band Photoinjector Investigations by Multiobjective Genetic Optimizer", in Proc. of International Particle Accelerator Conference (IPAC'16), Busan, Korea, May 8-13, 2016, 7 (2016), pp. 3979–3982.

[179] K.-J. Kim, "Rf and space-charge effects in laser-driven rf electron guns", Nuclear Instruments and Methods in Physics Research Section A: Accelerators, Spectrometers, Detectors and Associated Equipment **275**, 201 (1989).

[180] A. Cahill, A. Fukasawa, C. Limborg, W. Qin, and J. Rosenzweig, "Optimization of Beam Dynamics for an S-Band Ultra-High Gradient Photoinjector", in Proc. of International Particle Accelerator Conference (IPAC'17), Copenhagen, Denmark, 14–19 May, 2017, 8 (2017), pp. 1626–1629.

[181] B. Podobedov, "Resistive wall wakefields in the extreme anomalous skin effect regime", Phys. Rev. ST Accel. Beams **12**, 044401 (2009).

[182] R. G. Chambers, "The anomalous skin effect", P Roy. Soc. A-Math Phy. **215**, 481 (1952).

[183] G. Stupakov, K. L. F. Bane, P. Emma, and B. Podobedov, "Resistive wall wakefields of short bunches at cryogenic temperatures", Phys. Rev. ST Accel. Beams **18**, 034402 (2015).

[184] K. Gupta, R. Garg, and R. Chadha, *Computer-aided design of microwave circuits*, Artech Microwave Library (Artech, 1981).

[185] *Personal communication with Aaron Jensen*, 2016.